# Analysis of recent atmospheric methane trends using models and observations

Joe Ramu McNorton

Submitted in accordance with the requirements for the degree of Doctor of Philosophy

The University of Leeds
School of Earth and Environment
March 2016

# Declaration of Authorship

The candidate confirms that the work submitted is his own, except where work which has formed part of jointly-authored publications has been included. The contribution of the candidate and the other authors to this work has been explicitly indicated below. The candidate confirms that appropriate credit has been given within the thesis where reference has been made to the work of others.

A large portion of the results from Chapter 4 of the thesis are based on an ACPD paper on which the candidate is first author. The observations were made by several of the co-authors and the model code was initially written and developed by many others. The candidate performed the model simulations, manipulated the driving data for the model and performed the comparison of the model output with the observations. All plots and evaluations performed are the candidates own work.

Title: "Role of OH variability in the stalling of the global atmospheric $CH_4$ growth rate from 1999 to 2006" - ACP-2015-1029

Authors: **J. McNorton, M. P. Chipperfield, M. Gloor, C. Wilson, W. Feng, G. D. Hayman, M. Rigby, P. B. Krummel, S. O'Doherty, R. G. Prinn, R. F. Weiss, D. Young, E. Dlugokencky and S. A. Montzka**

# Abstract

Over the past two decades the growth rate of methane has shown large variability on multi-year timescales, the reasons for which are not well understood. The JULES land surface model, TOMCAT 3-D chemical transport model and observations have been used to investigate causes for these variations, with a specific focus on wetland emissions and atmospheric loss.

The role of atmospheric variability in the recent methane trends was investigated using TOMCAT, driven by variations in global mean hydroxyl concentrations derived from methyl chloroform observations. Results show that between 1999 and 2006, a stall in the atmospheric methane growth rate was, in part, caused by changes in the atmospheric loss. This was due largely to relatively small changes in global mean hydroxyl concentrations over time, with minor contributions from variations in atmospheric transport and temperature.

Methane emissions from various wetland inventories were evaluated using TOMCAT and observations, and recent trends in emissions were investigated. Emissions calculated by JULES were spatially and temporally similar to a top-down emission inventory and produced good agreement with satellite observations when used in TOMCAT ($R = 0.84$). Emissions derived for the period 1993 – 2012 show a statistically significant (95%-level) positive trend of 0.43 Tg/yr. This suggests a long-term positive trend in wetland emissions that may continue. During the stall in methane growth (1999-2006) modelled wetland emissions were 0.4 Tg/yr lower than average. This suggests that a decrease in wetland emissions contributed to the observed stall in methane growth.

The wetland methane processes within JULES were developed to include transport, oxidation, sulphate suppression, unsaturated production and methane storage pools. The parameters required for the additional processes were derived using a perturbed parameter ensemble to optimise the fit with observed fluxes. This slightly increased model performance at flux sites from $R = 0.32$ in the standard model to $R = 0.34$ in the updated model. The new version of JULES was tested using TOMCAT and satellite observations, and model agreement improved from $R = 0.84$ to $R = 0.87$, additionally the root-mean-squared-error reduced from 17.17 ppb to 15.09 ppb. This suggests the optimised additional model processes slightly improved model performance.

# Acknowledgements

I would like to express an immense amount of thanks to my three supervisors, Martyn Chipperfield, Manuel Gloor and Garry Hayman. All work presented within this thesis is a result of their supportive guidance and advice.

I would like to express my thanks to Chris Wilson for essentially acting as a fourth supervisor by providing guidance throughout my PhD and for being my TOMCAT oracle. All members of team TOMCAT including Georgio, Richard, Ryan, Sandip, Sarah and Wuhu provided so much help throughout. I'd particularly like to thank Erin for the challenges, Nigel for all his help with IDL and The Guardians of the Troposphere (Hannah and Tim). Within the school I have also received an immense amount of help from Richard Rigby and the ICT team. I would like to acknowledge everyone involved in the school 5-a-side and the board game crew (Leighton, Douglas, Ben, Dan etc.), for keeping it fun.

In the wider community I would like to thank everyone at CEH including Nic, Eleanor and Eddy for all their advice with anything JULES related. Matt Rigby and Steve Montzka provided much needed assistance at various points.

I would like to acknowledge the financial assistance I received from the National Centre for Earth Observation and the Centre for Ecology and Hydrology.

Special thanks goes to Alpa for her continued support throughout my PhD and for her wise words of advice.

Finally, David, Sooriya, Luke, Jack, Bob and my entire family have provided me with not only a place to live but also unconditional support throughout the entire process from start to finish. Thank you.

# Contents

# List of Figures

# List of Tables

# Abbreviations

| | |
|---|---|
| **AGAGE** | **A**dvanced **G**lobal **A**tmospheric **G**ases **E**xperiment |
| **BIO** | **BIO**mass |
| **CNRM** | **C**entre **N**ational de **R**echerches **M**étéorologiques |
| **CTM** | **C**hemical **T**ransport **M**odel |
| **DPM** | **D**ecomposable **P**lant **M**aterial |
| **ECMWF** | **E**uropean **C**entre for **M**edium-Range **W**eather **F**orecasts |
| **EDGAR** | **E**mission **D**atabase for **G**lobal **A**tmospheric **R**esearch |
| **ENSO** | **E**l **N**iño **S**outhern **O**scillation |
| **ESM** | **E**arth **S**ystem **M**odel |
| **ESRL** | **E**arth **S**ystem **R**esearch **L**aboratory |
| **GCM** | **G**eneral **C**irculation **M**odel |
| **GFED** | **G**lobal **F**ire **E**missions **D**atabase |
| **GIEMS** | **G**lobal **I**nundation **E**xtent from **M**ulti-**S**atellites |
| **GOSAT** | **G**reenhouse gases **O**bserving **SAT**ellite |
| **GRACE** | **G**ravity **R**ecovery **A**nd **C**limate **E**xperiment |
| **GWP** | **G**lobal **W**arming **P**otential |
| **HALOE** | **HAL**ogen **O**ccultation **E**xperiment |
| **HUM** | **HUM**us |
| **HWSD** | **H**armonised **W**orld **S**oil **D**atabase |
| **IASI** | **I**nfrared **A**tmospheric **S**ounding **I**nterferometer |

| | |
|---|---|
| **IPCC** | **I**ntergovernmental **P**anel on **C**limate **C**hange |
| **JULES** | **J**oint **U**K **L**and **E**nvironment **S**imulator |
| **LSM** | **L**and **S**urface **M**odel |
| **MAPE** | **M**ean **A**bsolute **P**ercentage **E**rror |
| **MOSES** | **M**et **O**ffice **S**urface **E**xchange **S**cheme |
| **NCAR** | **N**ational **C**enter for **A**tmospheric **R**esearch |
| **NDACC** | **N**etwork for the **D**etection of **A**tmospheric **C**omposition **C**hange |
| **NOAA** | **N**ational **O**ceanic and **A**tmospheric **A**dministration |
| **PBL** | **P**lanetary **B**oundary **L**ayer |
| **PFTs** | **P**lant **F**unctional **T**ype**s** |
| **RMSE** | **R**oot **M**ean **S**quare **E**rror |
| **RPM** | **R**esistant **P**lant **M**aterial |
| **SCIAMACHY** | **SC**anning **I**maging **A**bsorption spectro**M**eter for **A**tmospheric **CH**artography |
| **TANSO** | **T**hermal **A**nd **N**ear-infrared **S**ensor for carbon **O**bservation |
| **TCCON** | **T**otal **C**arbon **C**olumn **O**bserving **N**etwork |
| **TOPMODEL** | **TOP**ography-based hydrological **MODEL** |
| **TRIFFID** | **T**op-down **R**epresentation of **I**nteractive **F**oliage and **F**lora **I**ncluding **D**ynamics |
| **UNEP** | **U**nited **N**ations **E**nvironment **P**rogramme |
| **VMR** | **V**olume **M**ixing **R**atio |
| **WETCHIMP** | **WET**land and wetland **$CH_4$** **I**nter-comparison of **M**odels **P**roject |
| **WFDEI** | **W**ATCH-**F**orcing-**D**ata-**E**RA-**I**nterim |

# 1 Introduction

## 1.1 Motivation

Global surface temperatures over the last three decades have been successively warmer than any decade since 1850. A linear trend applied to observations shows a warming of 0.85 °C from 1880 to 2012, which is expected to continue in the future (Hartmann *et al.*, 2013). Long-lived greenhouse gases, such as carbon dioxide ($CO_2$) and methane ($CH_4$), have contributed to the increase in temperature by producing a warming effect on the Earth's climate system (e.g. Hartmann *et al.*, 2013). This occurs because greenhouse gases absorb and re-emit long-wave infra-red radiation, which ultimately leads to a positive total radiative forcing. Human activities, such as the burning of fossil fuels, changes in agricultural practices and waste management have contributed to the observed increase in atmospheric greenhouse gases through an increase in emissions. The Earth's climate system is likely to undergo further changes in the coming decades in response to changes in atmospheric composition, which could lead to a greater increase in temperatures. This will have an impact on natural and human systems globally.

To be able to comprehend past trends and to predict future changes in the Earth's climate a clear understanding of the system is required. Computer models are needed which describe the physical, chemical and biological processes controlling part or all of the system. For example, land surface models can provide estimates of biogenic emissions of greenhouse gases, which can then be used by atmospheric models to investigate changes in composition. However, the accuracy of all models is limited by the process description within the model and by the information used to drive the model. Hindcasting can be used to test models against observations; this identifies potential weaknesses in the models and leads to improved understanding of past events. Overall the development and use of these models, alongside observations, is essential for understanding the Earth's climate system both past and future.

For greenhouse gases, and $CH_4$ in particular, emission estimates have large uncertainties. Wetlands are the largest single source of $CH_4$ globally and both their distribution and the

processes controlling their emissions remain poorly understood (e.g. Melton *et al.* 2013). Additionally, there remains uncertainty in the variability of the major atmospheric sink, reaction with atmospheric OH (Holmes *et al.*, 2013). These uncertainties lead not only to gaps in knowledge about recent trends in atmospheric $CH_4$ but also limit predictions of future climate change.

## 1.2 The Role of Methane in Climate Change

$CH_4$, like $CO_2$, is a greenhouse gas because it absorbs and emits radiation in the infra-red range of the spectrum, thus producing a warming effect on the Earth's surface. It is the second most important anthropogenic greenhouse gas after $CO_2$, directly contributing 0.48±0.05 $Wm^{-2}$ of the 2.63 $Wm^{-2}$ of total radiative forcing by long-lived greenhouse gases (Myhre *et al.*, 2013). Figure 1.1 compares $CH_4$ to other radiative forcing agents. Radiative forcing is a measure of an agent's influence on the Earth's radiation balance (Myhre *et al.*, 2013). The effective radiative forcing displayed represents the change in radiative flux after considering changes in temperatures, water vapour and clouds. The relative abundance of $CH_4$ (~1.775 parts per million by volume (ppm)) compared to $CO_2$ (~400 ppm) is small; however on a per molecule basis its global warming potential (GWP) is approximately 26 times larger. This is because it absorbs atmospheric radiation more efficiently than $CO_2$; meaning that small changes in atmospheric $CH_4$ could play a large role in changes to the total radiative forcing. Once emitted into the atmosphere $CH_4$ has a relatively short atmospheric lifetime of 9.1±0.9 years (e.g. Prather *et al.*, 2012) in contrast to $CO_2$, which does not have an atmospheric sink. The lifetime of atmospheric $CO_2$ is determined by surface removal with different rates of uptake by multiple removal processes and is somewhere between 50 and 200 years (Archer *et al*., 2009).

In addition to the direct effects already mentioned, $CH_4$ can lead to indirect radiative forcing effects of approximately 0.2 $Wm^{-2}$ following its oxidation in the atmosphere (Hansen and Sato, 2001). Approximately half of this indirect radiative forcing is a result of $CH_4$ oxidation causing an increase in tropospheric ozone. The other half is through the production of $H_2O$ in the stratosphere (Hansen *et al*., 2000).

Recent variations in the concentration of atmospheric $CH_4$ have highlighted uncertainties in its emissions and/or sinks, which must be reduced so that more accurate future predictions can be made regarding changes in concentration (Dlugokencky *et al.*, 2011). The assessment of changes in emissions and/or sinks can be made using two different approaches, top-down and bottom-up. The top-down approach uses atmospheric measurements of $CH_4$ in an inversion of atmospheric

transport to calculate emissions. This method provides an estimate for the global $CH_4$ emissions, assuming the atmospheric loss is well understood (Kirschke *et al.*, 2013). The bottom-up approach generates emissions based on modelled process descriptions, which often leads to a large range in estimates because of a lack of understanding regarding emission processes (Lamarque *et al.*, 2013). This thesis uses top-down emission estimates to scale bottom-up inventories and compares those with observations using a chemical transport model (CTM). This is to investigate the time period between 1999 and 2006 when the atmospheric growth of $CH_4$ paused, described in more detail in Chapter 2.

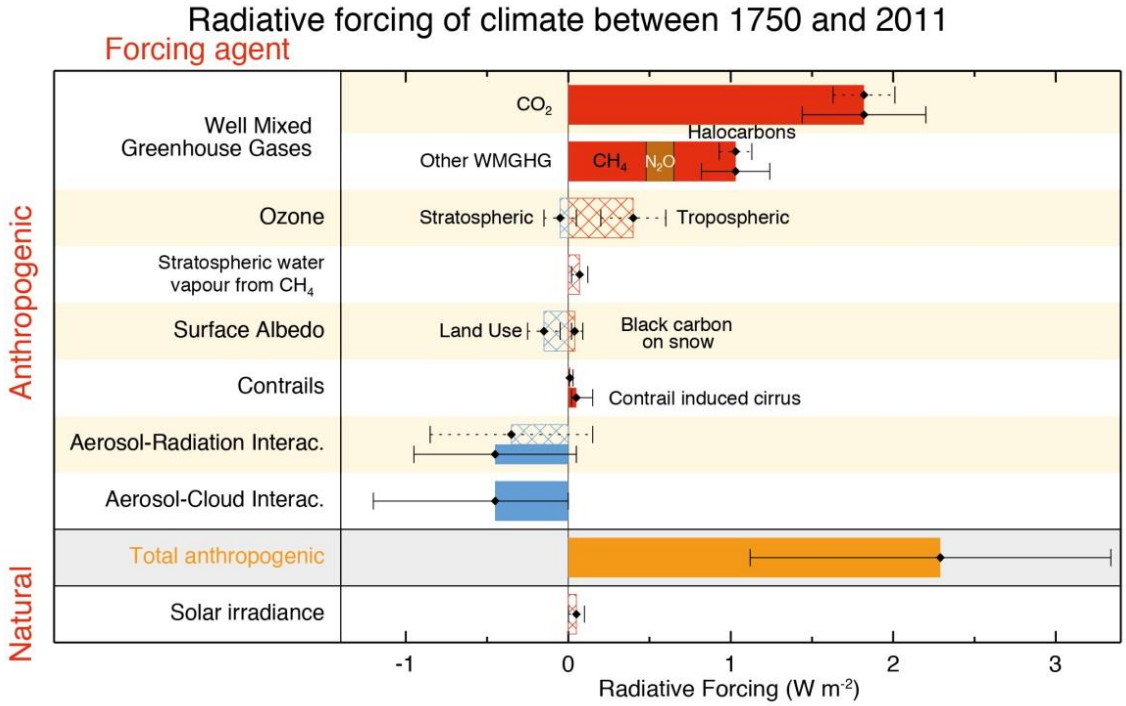


*Figure 1.1 The radiative forcing (hatched) and effective radiative forcing (solid) for various processes for the period 1750-2011. Note effective radiative forcing represents the forcing change after accounting for changes in atmospheric temperature, water vapour and clouds. From Myhre et al. (2013).*

Wetlands are the largest single source of $CH_4$ to the atmosphere and are the main drivers of the global interannual variability in $CH_4$ emissions (e.g. Ciais *et al.*, 2014). Processes governing wetland emissions are poorly understood and $CH_4$ fluxes are not well constrained. A possible feedback between climate change and wetland $CH_4$ emissions has been hypothesised but the sign and amplitude of this feedback remain unknown (Ringeval *et al.*, 2011). This suggests that a detailed understanding of processes controlling wetland emissions is required for a better understanding of likely future changes in atmospheric $CH_4$.

## 1.3 Thesis Aims

An overall aim of this thesis is to improve our understanding of atmospheric $CH_4$, including the sinks, transport and sources. More specifically, the study uses models and observations to analyse recent trends in atmospheric $CH_4$ growth rates and develop a more detailed description of the wetland emission processes in the JULES (Joint UK Land Environment Simulator) model. The specific thesis aims are:

- **Assess the role of atmospheric processes in the pause in $CH_4$ growth between 1999 and 2006.**

  1. What is the role of meteorology on the global atmospheric $CH_4$ growth pause?

  2. How much of a role did variations in OH play $CH_4$ growth pause?

The pause in the $CH_4$ growth rate between 1999 and 2006 has been well documented in observations (Dlugokencky *et al*., 2003); however there exists no clear consensus regarding the cause. Previous studies have investigated possible changes in emissions but not changes in the atmospheric sink (Bousquet *et al*., 2006; Kai *et al.*, 2011). This study aims to use $CH_3CCl_3$-derived OH to investigate the atmospheric contribution to the pause in growth. If the impact of OH variability is observable in the $CH_4$ trend then it highlights the need for possible variations in OH to be considered when investigating the global $CH_4$ growth rate.

- **Use a global atmospheric chemistry transport model, TOMCAT, and observations to investigate limitations of current wetland $CH_4$ emissions models.**

  1. How much of the wetland $CH_4$ model uncertainty originates from parameter uncertainty and how much is from process uncertainty?

  2. When various bottom-up emission inventories are compared with each other, which regions show the largest range in $CH_4$ emissions and do the inventories provide accurate regional emission estimates as deduced from atmospheric observations?

  3. Can a long-term trend in wetland emissions be detected in bottom-up and top-down emissions inventories?

Wetland $CH_4$ emissions from land surface models have uncertainties in both the structural processes described by the model and the parameter values used (Melton *et al.*, 2013). This study uses an existing wetland emission inventory and generates a further two, all of which follow a similar process description but have different driving parameters. By using these inventories in

TOMCAT and comparing the output with observations, the inventories can be evaluated. This analysis is performed on a spatial and temporal scale.

- **Improve understanding of processes which drive wetland $CH_4$ emissions and use this in the development of the JULES land surface model.**

  1. Can the representation of modelled wetland emissions be improved by adding in more complex processes?

  2. Does model tuning using local flux measurements improve the global representation of modelled emissions?

  3. Can the new wetland model and time-varying OH fields capture the observed $CH_4$ growth rate variability?

It is hypothesised that differences in TOMCAT simulations and observations will be largely because of uncertainties in the process description of the modelled wetland emissions. The development of a more complex process description in the wetland model aims to improve the representation of wetland emissions. Flux measurements are first used to tune the model processes, which are then up-scaled to the global domain for use in TOMCAT. By incorporating multiple versions of the wetland model in TOMCAT, and comparing them with observations, key structural components, such as $CH_4$ transport and oxidation, can be analysed.

## 1.4 Thesis Layout

This thesis has seven chapters, in total. Chapter 2 reviews key literature relevant to this work, providing background information about the sources, sinks and recent trends in atmospheric $CH_4$. Chapter 2 also provides information on the observation techniques used in this work and how they have been used in previous studies. Chapter 3 provides a description of the land surface and atmospheric modelling tools used in this thesis. The two main models, TOMCAT and JULES, are discussed, including their history and formulation. Chapter 4 uses TOMCAT to investigate the role of OH variability on the pause in the $CH_4$ growth rate between 1999 and 2006 using $CH_3CCl_3$-derived OH. Chapter 5 investigates the limitations of existing wetland $CH_4$ models by using multiple emissions inventories to drive TOMCAT, with a particular focus on parameter uncertainties. Chapter 6 develops the wetland $CH_4$ component of JULES through the use of flux measurements. These developments are then evaluated using TOMCAT and observations. Chapter 7 summarises the results of the thesis within the context of the original aims.

# 2 Atmospheric Methane

## 2.1 Introduction

This chapter reviews key literature relevant to the research questions outlined in Chapter 1. A clear understanding of wetland $CH_4$ processes and atmospheric chemistry is required to develop further knowledge of the recent and future trends in atmospheric $CH_4$.

Section 2.2 summarises the physical and chemical structure of the atmosphere, both in the troposphere and stratosphere, and gives an overview of the $CH_4$ distribution. Section 2.3 describes the sinks of atmospheric $CH_4$, including the chemical loss pathways. Section 2.4 summarises the major sources of atmospheric $CH_4$. The section also describes the significance of wetlands in the global $CH_4$ budget, outlining the key driving processes. Section 2.5 provides an overview of observation techniques from multiple instruments, exploring the recent history and development of $CH_4$ measurements. Section 2.6 outlines our current understanding of the recent variation in $CH_4$ growth, exploring the possible explanations. This section also discusses the significance of these recent trends in relation to predictions of future $CH_4$ levels.

## 2.2 Structure of the Atmosphere

### 2.2.1 Physical Structure of the Atmosphere

This section provides a brief overview of atmospheric physics; more details can be found in various textbooks (e.g. Wallace and Hobbs, 2006; Seinfeld and Pandis, 2012). The atmosphere is defined as the layer of gases which surround the Earth. An understanding of the physical and chemical structure of the atmosphere is required to help understand the role of greenhouse gases within the Earth system.

The vertical structure of the atmosphere is controlled by the balance of the gravitational force of the Earth and the pressure gradient force. The balance between these two opposing forces, known as hydrostatic equilibrium, is shown in equation 2.1, where $p$ is pressure, $z$ is height, ρ is density and $g$ is the acceleration due to gravity. Atmospheric pressure decreases almost exponentially with height, though variations in atmospheric temperature prevent this from being a truly exponential relationship, because of the influence of temperature on pressure.

$$\frac{dp}{dz} = -\rho g \qquad \textbf{(2.1)}$$

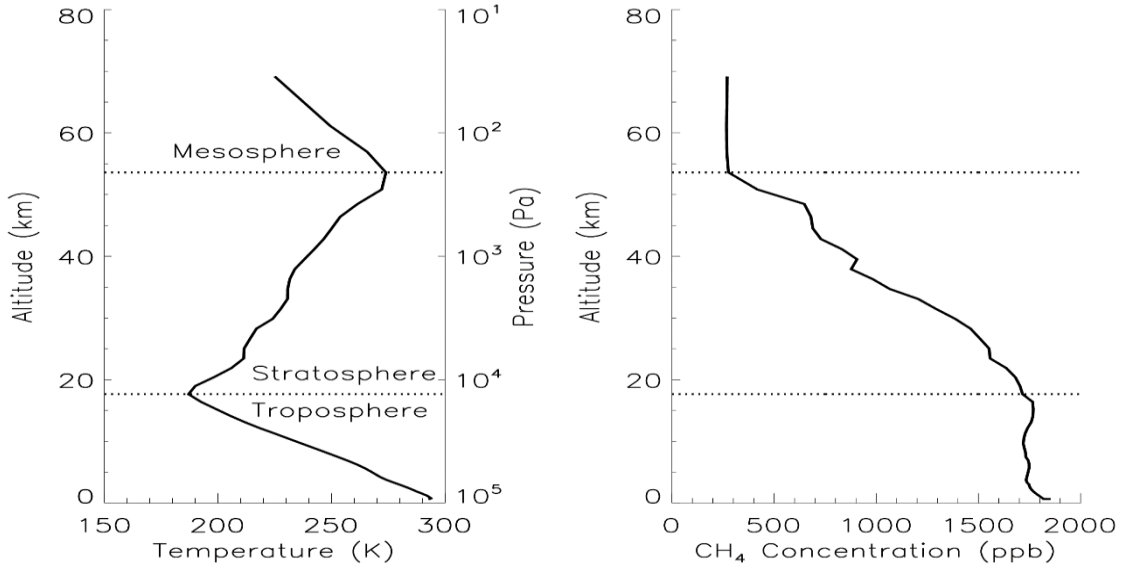


*Figure 2.1 Typical vertical profiles of temperature (left) and $CH_4$ (right) from a TOMCAT simulation at the equator.*

The vertical structure of the lower and middle atmosphere is shown in Figure 2.1. This domain can be broken down in to three regions, defined by a change in temperature gradient. A planetary boundary layer (PBL) exists at the base of the lowest region, the troposphere. The PBL can extend up to a few kilometres and is defined as a region of turbulent mixing governed by interactions with the surface. The troposphere extends from the relatively warm surface up to ~17 km at the equator and ~9 km at the poles. It is typically considered to be a well-mixed region and contains around three quarters of the mass of the atmosphere. The tropopause is at the top of the troposphere, where there is a temperature minimum. Above this altitude is the stratosphere, which is defined by an increasing vertical temperature due to the presence of the ozone layer. The stratosphere extends up to around 50 km and is vertically stable because warm air is found above cold air, which slows vertical mixing of chemical species. The troposphere and stratosphere collectively contain 99.9% of the mass of the atmosphere and a majority of the key processes which determine climate. The stratopause is the boundary at the top of the stratosphere where

there is a temperature maximum, after which the temperatures once again decrease through the mesosphere. Further atmospheric layers, including the thermosphere and exosphere, continue above the mesosphere.

### 2.2.2 Composition and Chemistry of the Atmosphere

Summaries of the composition of the atmosphere can be found in textbooks such as Wayne (1993) and Seinfeld and Pandis (2012). Briefly, the atmosphere is mainly composed of nitrogen (78% by volume) and oxygen (21% by volume). Excluding water vapour, trace gases make up the remaining 1% of the atmospheric composition. Although these trace gases are low in concentration, they can have large impacts on air quality, climate change and ozone-depletion. $CH_4$ is the fifth most abundant trace gas in the atmosphere, making up less than 0.0002% (~1800 ppb). In the lower atmosphere $CH_4$ is ubiquitous with relatively small variations in the horizontal plane. An exception to this is in source regions, where $CH_4$ levels can be elevated to over 2000 ppb. Long-lived trace gases in the troposphere are typically well mixed vertically; this is also the case for $CH_4$. In the stratosphere $CH_4$ concentrations decrease with height due to slow vertical mixing and stratospheric chemical loss, as shown in Figure 2.1.

## 2.3 Methane Sinks

After being emitted, $CH_4$ is transported throughout the lower atmosphere by advection, boundary layer mixing and convection. $CH_4$ can be removed from the atmosphere either through chemical loss pathways or oxidation by methanotrophic bacteria in soils. The largest of these sinks is the oxidation of $CH_4$ by the hydroxyl radical (OH) in the atmosphere, which is governed by a temperature-dependent reaction with loss rate, $k_{OH}$, shown in reaction 2.1 (e.g. Prather *et al*., 2012).

$$CH_4 + OH \xrightarrow{k_{OH}} CH_3 + H_2O \qquad \textbf{(R2.1)}$$

OH is highly reactive in the atmosphere and as a result has a relatively small atmospheric concentration of approximately $1x10^6$ molecules $cm^{-3}$ and a lifetime of about 1 s. The main loss pathways for OH are through reactions with carbon monoxide (CO) and $CH_4$. The primary formation of OH is controlled by ozone ($O_3$) and involves photolysis by UV radiation to form a single oxygen, which can react with a water molecule to produce OH. OH can also be recycled through reactions with nitrogen oxides ($NO_x$) to form $O_3$, which subsequently produces OH. Figure 2.2 shows the primary and recycled pathways for the formation of OH in the atmosphere

highlighting two regimes which alter the recycling process, $NO_x$ enriched/depleted. The OH concentration ([OH]) is controlled by production, through changes in $O_3$ and UV radiation, and loss, through reactions with atmospheric species including $CH_4$, CO, sulphur dioxide ($SO_2$) and nitrogen dioxide ($NO_2$).

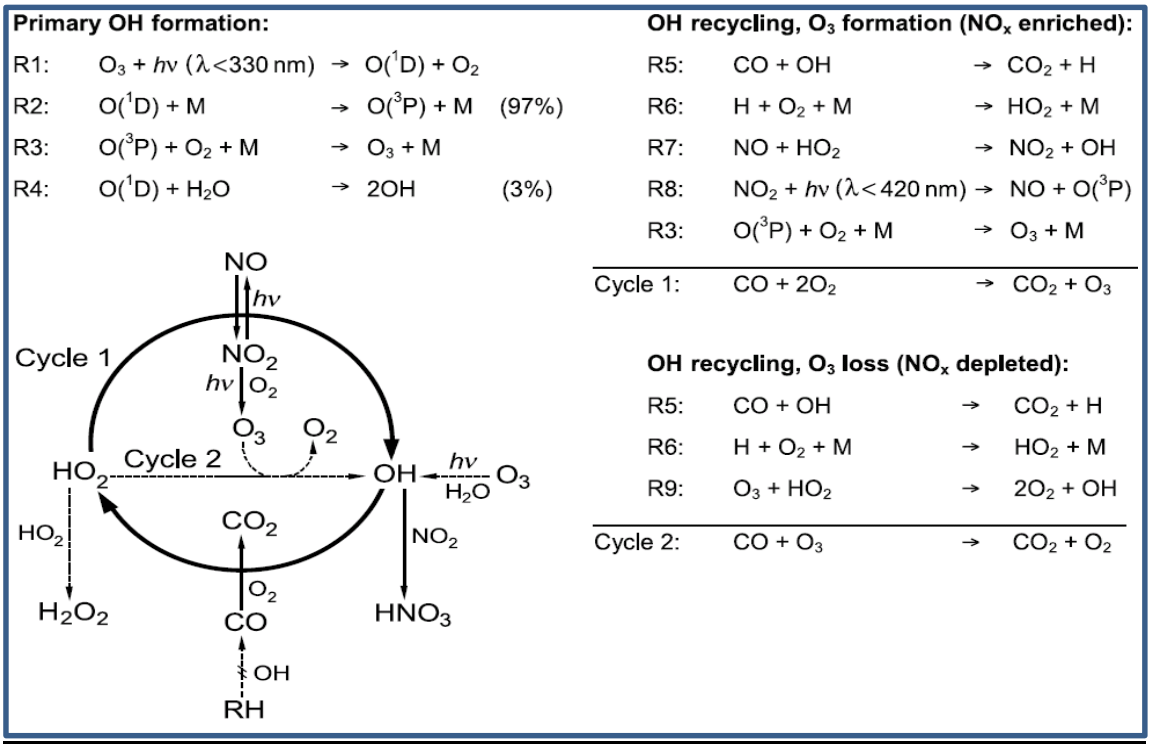


*Figure 2.2 Reaction cycles of OH as determined by reactions with CO and $NO_x$. RH represents hydrocarbons, mainly $CH_4$. M represents an air molecule which collides with the species and dissipates excess energy. From Lelieveld et al. (2002).*

Around 90% of all surface-emitted $CH_4$ is lost through reactions with OH, despite OH only having an atmospheric lifetime of a few seconds. This equates to an annual loss through OH of 9% of the total burden (4700 to 4900 Tg) (Voulgarakis *et al.*, 2013). The atmospheric [OH] is influenced by several factors discussed previously; one factor is the atmospheric concentration of $CH_4$ itself. An increase in atmospheric $CH_4$ causes a decrease in the [OH], which in turn affects the $CH_4$ lifetime. This is an indirect effect of $CH_4$ changes. Additionally, the reaction of $CH_4$ with OH can eventually lead to the formation of CO via the formation of formaldehyde ($CH_2O$). Following reaction 2.1 the formation of $CH_2O$ is summarised by reactions 2.2, 2.3 and 2.4 (Seinfeld and Pandis, 2006).

$$CH_3 + O_2 + M \rightarrow CH_3O_2 + M \qquad \textbf{(R2.2)}$$

$$CH_3O_2 + NO \rightarrow CH_3O + NO_2 \qquad \textbf{(R2.3)}$$

$$CH_3O + O_2 \rightarrow CH_2O + HO_2 \qquad \textbf{(R2.4)}$$

$CH_2O$ then undergoes photolysis reactions to form CO (reaction 2.5) or HCO (reaction 2.6), which further reacts with $O_2$ to form CO (reaction 2.7) (Seinfeld and Pandis, 2006).

$$CH_2O + hv \rightarrow H_2 + CO \qquad \textbf{(R2.5)}$$

$$CH_2O + hv \rightarrow HCO + H \qquad \textbf{(R2.6)}$$

$$HCO + O_2 \rightarrow HO_2 + CO \qquad \textbf{(R2.7)}$$

On a several-month timescale CO further depletes atmospheric OH and reacts to form $CO_2$, given by reaction 2.8 (Seinfeld and Pandis, 2006).

$$CO + OH \underset{O_2}{\rightarrow} CO_2 + HO_2 \qquad \textbf{(R2.8)}$$

In high-$NO_x$ conditions the oxidation of $CH_4$ has a theoretical maximum yield of 5 $O_3$ molecules, given by reaction 2.9; however, due to competing reactions this is almost never achieved (Seinfeld and Pandis, 2006).

$$CH_4 + 10O_2 \rightarrow CO_2 + H_2O + 2OH + 5O_3 \qquad \textbf{(R2.9)}$$

In low-$NO_x$ conditions, as a contrast to the production of ozone via the oxidation pathways shown above, ozone can be consumed to produce $CO_2$, $H_2O$ and $H_2$ (Cicerone and Oremland, 1988). Two example net reactions (2.10 and 2.11) show how ozone can be consumed in these conditions (McElroy, 2002).

$$CH_4 + 3O_3 \rightarrow CO_2 + H_2O + 2HO_2 + O_2 \qquad \textbf{(R2.10)}$$

$$CH_4 + O_3 + 2O_2 \rightarrow CO_2 + H_2O + 2HO_2 \qquad \textbf{(R2.11)}$$

Several smaller sinks of $CH_4$ contribute to the remaining 10% of $CH_4$ loss. Approximately 5% of atmospheric loss occurs through reactions with tropospheric and stratospheric chlorine (Cl) and oxygen radicals ($O^1D$) (Prather *et al.*, 2012).

$$CH_4 + O(^1\mathrm{D}) \xrightarrow{k_{O^1D}} CH_3 + OH \qquad \textbf{(R2.12)}$$

$$CH_4 + Cl \xrightarrow{k_{Cl}} CH_3 + HCl \qquad \textbf{(R2.13)}$$

$CH_4$-oxidising bacteria, known as methanotrophs make up the remaining sink for atmospheric $CH_4$ (~5%). The chemical processes by which this occurs are discussed in detail in Section 2.4.2.

Any net positive difference between emissions and sinks results in an increase in the atmospheric burden, and therefore positive growth rates. Conversely, if the loss processes are larger than the sources, the atmospheric burden will fall. The combined sinks, discussed in this section, lead to

$CH_4$ having a relatively short atmospheric lifetime, 9.1±0.9 years (Prather *et al*., 2012), compared to $CO_2$. $CO_2$ removal includes extremely long time-scale processes, of 5-200 years, which means a single, characteristic atmospheric lifetime value is not applicable (Ciais *et al.*, 2014). Climate change effects caused by a reduction in emissions of $CH_4$ would be observed on a decadal timescale, due to a large decrease in the atmospheric burden. This would lead to a decrease in radiative forcing and an improvement in global air quality through the role of $CH_4$ in tropospheric ozone production.

## 2.4 Methane Emissions

Emissions of $CH_4$ originate from a combination of natural (~218 Tg$CH_4$/yr) and anthropogenic (~335 Tg/yr) sources (Ciais *et al*., 2014). The most recent estimates of current $CH_4$ emission sources are given in Table 2.1. The processes that lead to the emission of $CH_4$ can be placed into three categories, biogenic, pyrogenic and thermogenic (e.g. Neef *et al*., 2010). $CH_4$ emissions from animals, rice agriculture, waste and wetlands are all driven by biogenic processes, which occur in anaerobic conditions and involve the conversion of organic matter into $CH_4$. Emissions from biofuel and biomass burning occur as a result of incomplete combustion, and are known as pyrogenic processes. Emissions from coal, natural gas and oil are typically associated with thermogenic processes, which occur under high temperature and/or pressure over geological timescales.

Since the beginning of the industrial era the total sources and sinks of $CH_4$ have been imbalanced, with the source term being larger, resulting in the observed atmospheric growth. This imbalance has been estimated to be as much as 30 Tg/yr between 1980 and 1989 (Ciais *et al*., 2014), with the sum of the sources at 541 Tg/yr and the sinks 511 Tg/yr. It is estimated that the imbalance was reduced to 3 Tg/yr between 2000 and 2009 (Kirschke *et al.*, 2013; Ciais *et al*., 2014). The ranges of uncertainties for source and sink terms vary greatly, as shown in Table 2.1. For this reason, certain individual sources and sinks should be targeted to reduce the overall emission uncertainties.

By examining the data provided in Table 2.1 it is clear that source and sink estimates vary considerably between top-down and bottom-up estimates, both of which have their individual merits. Bottom-up estimates tend to follow a more process-based approach, which provides details of individual sources. A poor understanding of the processes governing emissions and challenges associated with upscaling, leads to the range of emissions being much larger in bottom-up estimates. Ciais *et al.* (2014) compared bottom-up global source inventories (678 Tg/yr) with

sink inventories (632 Tg/yr) (Lamarque *et al*., 2013) to show an imbalance of 45 Tg/yr from 2000 to 2009. This is greater than the observed growth of 3 Tg/yr even allowing for atmospheric loss. Top-down estimates based on observations and inverse models are constrained by OH fields. For this reason top-down estimates are used in this study when assessing the global $CH_4$ budget. The emission inventories used in this study are described in more detail in Chapters 4, 5 and 6, and are scaled to the top-down emission estimates provided in Table 2.1. The remainder of this section focuses on individual sources of $CH_4$, detailing their size, processes, interannual variability, uncertainty and, spatial and temporal distribution.

| | Top-Down Estimate | Bottom-Up Estimate |
|---|---|---|
| **Source** | **Annual $CH_4$ Source from 2000-2009 (Tg/yr)** | |
| Natural | 218 (179-273) | 347 (238-484) |
| Wetlands | 175 (142-208) | 217 (177-284) |
| Other | 43 (37-65) | 130 (61-200) |
| Freshwater | | 40 (8-73) |
| Wild Animals | | 15 |
| Wildfires | | 3 (1-5) |
| Termites | | 11 (2-22) |
| Geological (including oceans) | | 54 (33-75) |
| Hydrates | | 6 (2-9) |
| Permafrost | | 1 (0-1) |
| Anthropogenic | 335 (273-409) | 331 (304-368) |
| Biomass Burning | 30 (24-45) | 35 (32-39) |
| Fossil Fuels | 96 (77-123) | 96 (85-105) |
| Agriculture and Waste | 209 (180-241) | 200 (187-224) |
| Rice | | 36 (33-40) |
| Ruminants | | 89 (87-94) |
| Landfills and Waste | | 75 (67-90) |
| **Sink** | **Annual $CH_4$ Sink from 2000-2009 (Tg/yr)** | |
| Soil | 32 (26-42) | 28 (9-47) |
| Atmospheric Chemical Loss | 518 (510-538) | 604 (483-738) |
| Tropospheric OH | | 528 (454-617) |
| Stratospheric Loss | | 51 (16-84) |
| Tropospheric Cl | | 25 (13-37) |
| **Total** | | |
| Sum of Sources | 553 (526-569) | 678 (542-852) |
| Sum of Sinks | 550 (514-560) | 632 (592-785) |
| Imbalance | 3 (-4-19) | 45 |

*Table 2.1 Estimated sources and sinks for global $CH_4$ for 2000-2009, based on top-down and bottom-up inventories. Adapted from Ciais et al. (2014), using estimates from various contributors (Sanderson, 1996; Sugimoto et al., 1998; Andreae and Merlet, 2001; Dickens, 2003; Bastviken et al., 2004; Hoelzemann et al., 2004; Ito and Penner 2004; van der Werf, 2004; Dentener et al., 2005; Allan et al., 2007; Curry, 2007; Denman et al., 2007; Walter et al., 2007; Etiope et al., 2008; Bergamaschi et al., 2009; EDGAR4-database, 2009; Pison et al., 2009; Rhee et al., 2009;* Anderson *et al*., 2010*; Mieville et al., 2010; Neef et al., 2010; Shakhova et al., 2010; van der Werf et al., 2010; Bastviken et al., 2011; Bousquet et al., 2011; EPA, 2012; Hodson et al., 2011; Ringeval et al., 2011; Spahni et al., 2011; Wiedinmyer et al., 2011; Spahni et al., 2011; Ito and Inatomi, 2012; Williams et al., 2012; Voulgarakis et al., 2013). Note that emission ranges are shown in brackets.*

## 2.4.1 Anthropogenic Emissions

**Fossil Fuels**

Anthropogenic consumption of fossil fuels, predominantly natural gas, leads to $CH_4$ being emitted into the atmosphere. Fugitive emissions make up the bulk of this source via leaks in either the extraction method or in the transport of the fuel. Incomplete combustion of fossil fuels leads to an additional source of emissions. Fossil fuel operations, including extraction, are generally well documented and therefore the estimates of $CH_4$ from this sector are well constrained at around 96 Tg/yr (77-123 Tg/yr) (Ciais *et al*., 2014). Fossil fuel emissions have only a small interannual variation, as shown in Figure 2.3 based on the Emission Database for Global Atmospheric Research (EDGAR) version 4.0 inventory (2009). Emissions from fossil fuels have remained relatively constant from 1975 to 2000, with a small positive trend. The EDGAR 4.0 inventory shows that between 2000 and 2005 global fossil fuel-related $CH_4$ emissions increased by 20 Tg/yr relative to pre-2000 values.

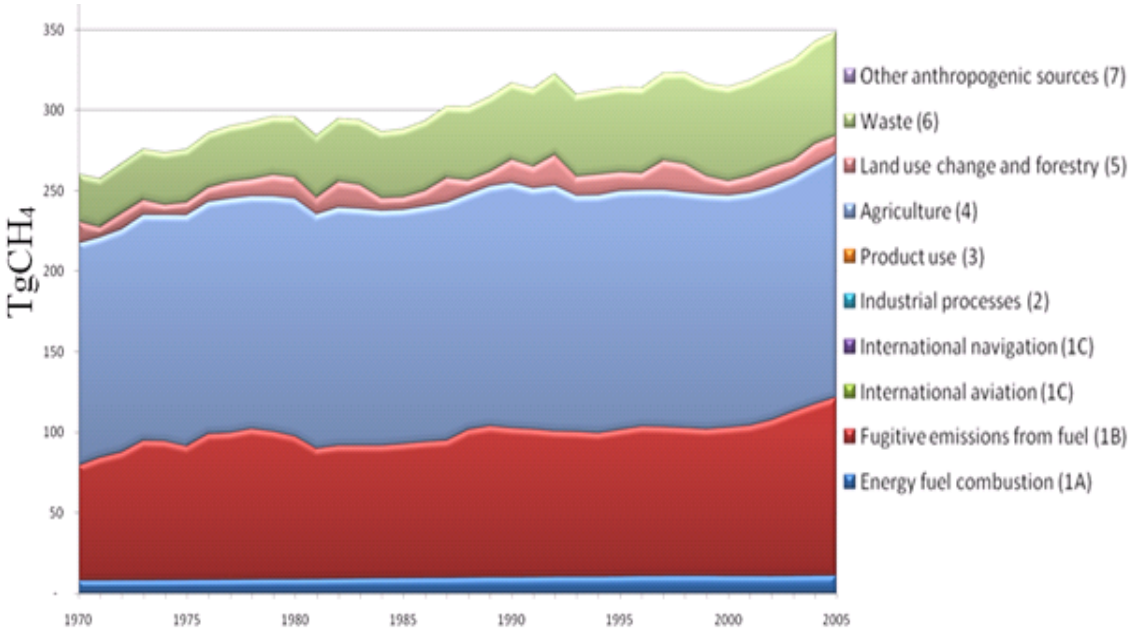


*Figure 2.3 Annual global anthropogenic $CH_4$ emissions (Tg/yr) for 1970-2005 (EDGAR 4.0, 2009).*

**Ruminants**

The term ruminant is given to mammals that ferment food in their rumen, a large section of their stomach. Large livestock, such as sheep, goats and cows are ruminants and generate $CH_4$ as a waste product within their fermentation system. Methanogens within the fermentation system produce the $CH_4$ through anaerobic respiration; this process is discussed in more detail in Section

2.4.2. Several factors control the $CH_4$ emissions from ruminants, including the quantity (Shibata *et al*., 1993) and the type of feed (Blaxter and Clapperton, 1965). Emission prediction models can be created by using feeding characteristics (Johnson and Johnson, 1995). Emission estimates from ruminants are well constrained in the 5th IPCC report because livestock data is well documented (Ciais *et al*., 2014). These range from 87-94 Tg/yr, making them comparable with emissions from fossil fuels.

**Rice Agriculture**

Emissions of $CH_4$ from rice cultivation occur from the same biogenic processes that are responsible for $CH_4$ emissions from wetlands, discussed in more detail in Section 2.4.2. The majority of global rice emissions originate from East and South-East Asia, as highlighted in Figure 2.4. Regional and global emissions are well constrained with estimates ranging from 33-40 Tg/yr. The small range in values likely originates from the variety of models used to derive the estimates and the techniques used to upscale the emissions to a global value (Huang *et al*., 2006). Previously rice cultivation emissions have been modelled as wetland emissions (Bloom *et al*., 2012); although agricultural treatments could cause a change in the $CH_4$ producing biogenic processes. Kai *et al.* (2010) suggested a possible declining trend in $CH_4$ emissions from rice agriculture between 1982 and 2007. This is thought to be due to changes in agricultural practices, increased inorganic fertiliser use, improved crop yields and decreases in the rice production area. Global $CH_4$ emissions from rice agriculture exhibit a strong seasonal cycle due to the growing seasons in rice production.

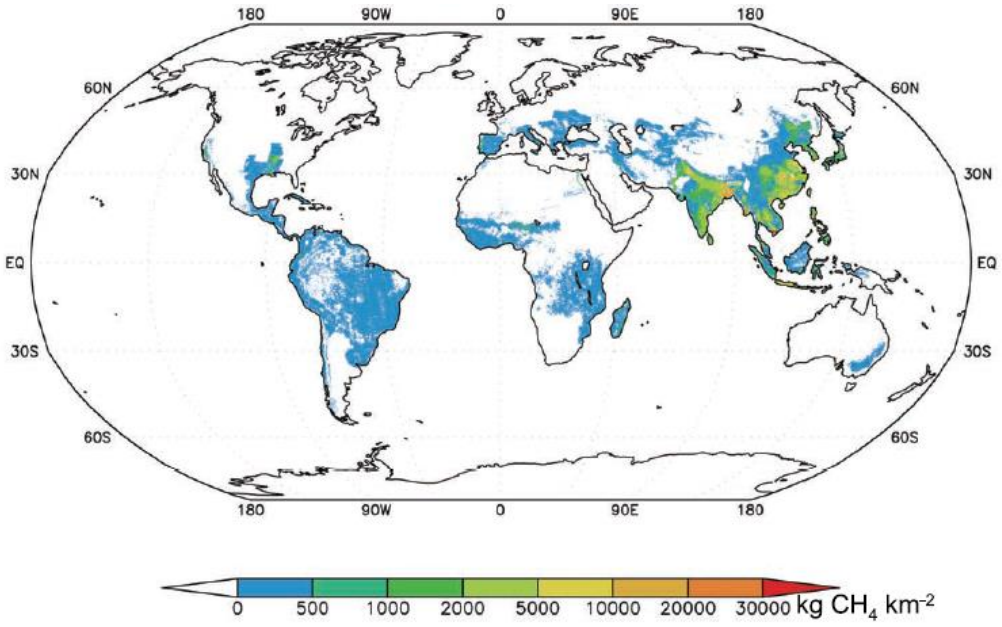


*Figure 2.4 Estimated annual $CH_4$ emissions in kg $km^{-2}$ from rice agriculture (Yan et al. 2009).*

**Biomass Burning**

Pyrogenic $CH_4$ emission from biomass burning can be a result of both anthropogenic and naturally occurring events, and are the result of incomplete combustion. The temperature, composition of matter and rate of temperature change all contribute to the amount of $CH_4$ emitted from a biomass burning event (Koppmann *et al*., 2005). The range of emission estimates are well constrained at 24-35 Tg/yr for biomass burning events, based on top-down studies, and 1-5 Tg/yr for wildfires, based on bottom-up studies. The interannual variability of both the frequency and magnitude of biomass burning events can be large during intensive fire periods (Simpson *et al*., 2006). This is particularly evident during strong El Niño events when tropical emissions are observed to increase (van der Werf *et al*., 2004). There is a strong spatial pattern to biomass burning $CH_4$ emissions, with around 85% originating from tropical regions (Hao and Ward, 1993). Of these regions tropical Asia and Africa are the most dominant, as shown in Figure 2.4. Bottom-up process-based models for predicting $CH_4$ emissions from biomass burning are not yet at a stage where they can accurately reproduce the timing of emissions (Thonicke *et al.*, 2010). More accurate estimates of past emissions are available using a combination of a biogeochemical model and satellite observations of burned area, plant productivity and active fire detection (van der Werf *et al*., 2010). This approach relies on emission factors being applied to convert dry matter to $CH_4$ emissions, for example peat fires are estimated to emit approximately 20.8 $gCH_4$ for every Kg of dry matter, whereas Savanna fires only emit around 1.94 $gCH_4$ per Kg (Akagi *et al.*, 2011). CO is also emitted from biomass burning events and influences the atmospheric lifetime of $CH_4$ through reactions with OH. Based on Akagi *et al.* (2011) the relative emission factors for CO are around 10 to 30 times larger than those for $CH_4$, depending on the fire type.

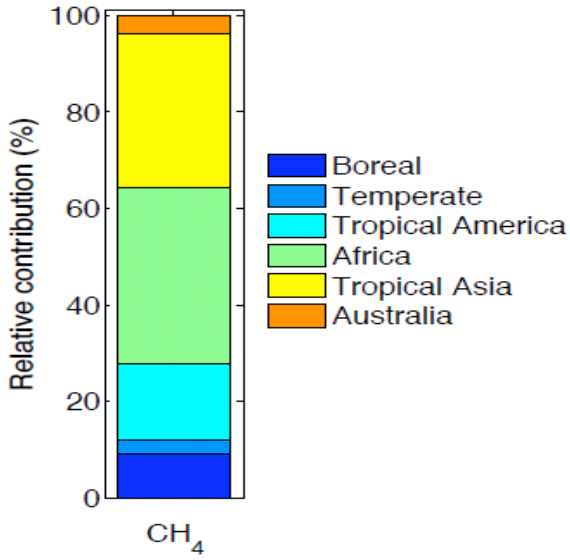


*Figure 2.4 Relative contribution of $CH_4$ biomass burning emissions from different regions for the period 1997 to 2009. Adapted from van der Werf et al. (2010).*

**Landfills and Waste**

Emissions of $CH_4$ from landfills and waste follow a similar biogenic pathway to rice emissions discussed above and wetland emissions discussed in Section 2.4.2. Buried degradable carbon at landfill sites undergoes a series of microbial transformations, which first lead to the production of species such as acetic acid, $CO_2$ and hydrogen ($H_2$). Then, through acetate consumption or reduction of $CO_2$ with $H_2$, microorganisms, known as methanogens, produce $CH_4$. This is then either emitted to the atmosphere or oxidised, as discussed in more detail in Section 2.4.2. Landfill and waste emissions are estimated to be between 67 and 90 Tg/yr. These emission estimates are typically based on measured or estimated waste generation, fraction of waste that is anaerobically biodegradable, the organic carbon content of the waste and an estimate of the amount of oxidation of $CH_4$ that occurs (Bogner and Matthews, 2003). The range in emission estimates provided in the IPCC report (67 to 90 Tg/yr) is in part due to the lack of waste data available from many countries (Ciais *et al.*, 2014). Landfill and waste emissions have increased since 1970 (see Figure 2.3).

## 2.4.2 Natural Emissions

**Wetlands**

Wetlands are the largest single source of $CH_4$ to the atmosphere, with top-down estimates of 175 Tg/yr (~30% of global total). Wetlands, such as bogs, fens, marshes and swamps, are defined as areas where the soil is saturated, either permanently or seasonally. Nearly half of all wetlands can be found in high northern latitudes (OECD, 1996), most of which are seasonal due to winter time freezing. The remaining wetlands in tropical and sub-tropical regions are more often permanent. The largest wetland regions can be found in the Amazon River Basin, The Congo, The Pantanal and the West Siberian Plain. The distribution of wetlands is dependent on several factors, including the topography, soil properties and precipitation. Wetland distribution alone does not dictate the global biogenic emission of $CH_4$ from wetlands, and several other parameters play a key role in $CH_4$ production and transport to the atmosphere. There is a large uncertainty in global $CH_4$ emissions, ranging from 142 to 208 Tg/yr based on top-down estimates and 177 to 284 Tg/yr based on bottom-up estimates. The range in existing estimates comes from uncertainty in the processes that lead to emissions from wetlands. There is also a large interannual variability in wetland emissions. This is discussed in more detail in Chapters 5 and 6.

$CH_4$ emission from wetlands can be broken down into three parts; production, transport and oxidation. The $CH_4$ is first produced in the soils, then either transported out into the atmosphere or oxidised within the soil or water column. $CH_4$ is produced via a process known as methanogenesis by methanogens in the anaerobic wetland environments. Methanogens are microorganisms that use two different metabolic pathways to produce $CH_4$ as a by-product. Prior to the production of $CH_4$, biological polymers are broken down into simpler chemicals, such as $H_2$, $CO_2$, acetate and formate (Le Mer *et al*., 2001). Hydrolysis of biological polymers into monomers (fatty acids, amino acids) is followed by acidogenesis to form organic acids, alcohols, $H_2$ and $CO_2$. At this point the $H_2$ and the $CO_2$ can be consumed by methanogens to form $CH_4$ or can undergo acetogenesis to form acetate, which is then consumed by methanogens (Le Mer *et al*., 2001). The two most common final steps in the formation of wetland $CH_4$ are from acetic acid and $CO_2$ reduction by $H_2$, summarised by reactions 2.14 and 2.15.

$$CH_3COOH \rightarrow CH_4 + CO_2 \qquad \textbf{(R2.14)}$$

$$CO_2 + 4H_2 \rightarrow CH_4 + 2H_2O \qquad \textbf{(R2.15)}$$

The formation of $CH_4$ by methanogens is dependent on several biological, chemical and physical factors. The biological dependence originates from the microbial community structure of the wetland. Methanogens require other members of the microbial community to first break down more complex carbon substrates, which are known as complementary interactions in the microbial food web (Cicerone and Oremland, 1988). A separate chemical and biological dependence comes from the nitrate and sulphate composition of the wetland. Nitrate and sulphate reducing bacteria typically outcompete methanogens for acetate and $H_2$, which reduces the total $CH_4$ production. A separate chemical dependence comes from the soil carbon. Wetland $CH_4$ emissions are not only affected by the quantity of soil carbon but also by its quality. Easily degradable carbon can quickly be converted and emitted as $CO_2$ and $CH_4$. Methanogens are sensitive to soil pH, with an optimum range between 5.5 and 7.0 (Dunfield *et al*., 1993). Temperature is the major physical factor in the control of $CH_4$ production by methanogens. Below 0 °C the ground is frozen and there is very low production. As the temperature increases above 0 °C the rate of methanogenesis also increases. The optimum temperature for methanogenesis varies depending on the production process; acetate-consuming methanogens were found to have an optimum temperature at 20 °C, whilst hydrogen oxidisers had an optimum at 28 °C (Svensson *et al*., 1984). The optimum values will vary between wetlands but are almost never reached. Methanogens, and even more so the microorganisms involved in the complementary reactions, are responsible for the observed decrease in $CH_4$ emissions with a decreasing temperature (Conrad *et al*., 1987). The strong links to temperature suggest that a positive climate change feedback loop might be present with wetland $CH_4$ emissions (Gedney *et al.*, 2004). The change in precipitation under a changing climate might

have a positive or negative feedback on wetland emissions (Trenberth *et al.*, 2011). Methanogens similar to the ones described here can also be found in ruminants and landfill sites.

$CH_4$ present in the soil and water column can be oxidised by methantrophic microorganisms. These bacteria require $O_2$ to consume $CH_4$ in the oxidised soil layer. As $CH_4$ escapes the anaerobic soil layer up to 90 % can be oxidised in these aerobic zones (Oremland *et al*., 1992). Atmospheric $CH_4$ can also be oxidised and as a sink term this accounts for around 32 Tg/yr. As with methanogens, methanotrophs are dependent on a range of biological, chemical and physical factors.

Methanogenesis in wetlands typically occurs in the soils below the water column. For $CH_4$ to be emitted into the atmosphere it must first be transported through both the soil and water column. The three most common transport pathways are ebullition, diffusion and plant-mediated transport (see Figure 2.6). The ebullition pathway involves the release of $CH_4$ through gas bubbles. An increase in methanogen activity within a wetland leads to a build-up of $CH_4$ in the water column, when the concentration is large enough bubbles form, which ascend in the water column, releasing the $CH_4$ into the atmosphere. A recent study suggests that sudden ebullition events triggered by changes in atmospheric pressure can contribute as much as 64% of total $CH_4$ emissions from peatlands (Tokida *et al*., 2007). Ebullition fluxes typically occur as pulses in response to changes in atmospheric pressure, temperature or water table depth (Tokida *et al*., 2007).

The diffusion of $CH_4$ from wetland soils and water occurs as a result of a concentration gradient between the surface and atmosphere. The proportion of $CH_4$ lost via the diffusion pathway depends on the wetland type because the diffusion process is quicker through porous soils than through compact soils. Diffusion of $O_2$ from the atmosphere into the soil column enhances the oxidation rate of $CH_4$, suppressing the amount emitted into the atmosphere. Diffusion through the water column is slower than through soil, therefore a high water table can limit the diffusion of $CH_4$ into the atmosphere.

Plant-mediated emission of $CH_4$ relies on transport through air-filled cavities in plants, known as aerenchyma, which allow for the transport of gases around the plant. $CH_4$ in the soils can enter in through the roots of the plants and be transported up into the stem via diffusion (Colmer, 2003). The $CH_4$ can then be released into the atmosphere from the plant. As with the previous two transport pathways, the proportion of total emissions that occur as a result of plant-mediated transport varies depending on the wetland. Studies show plant-mediated transport can contribute up to 90% of the total emissions (Cicerone and Shetter, 1981; Nouchi *et al*., 1990). As with the

diffusion pathway, $O_2$ in the plant can cause oxidation of the $CH_4$ before it is emitted into the atmosphere.

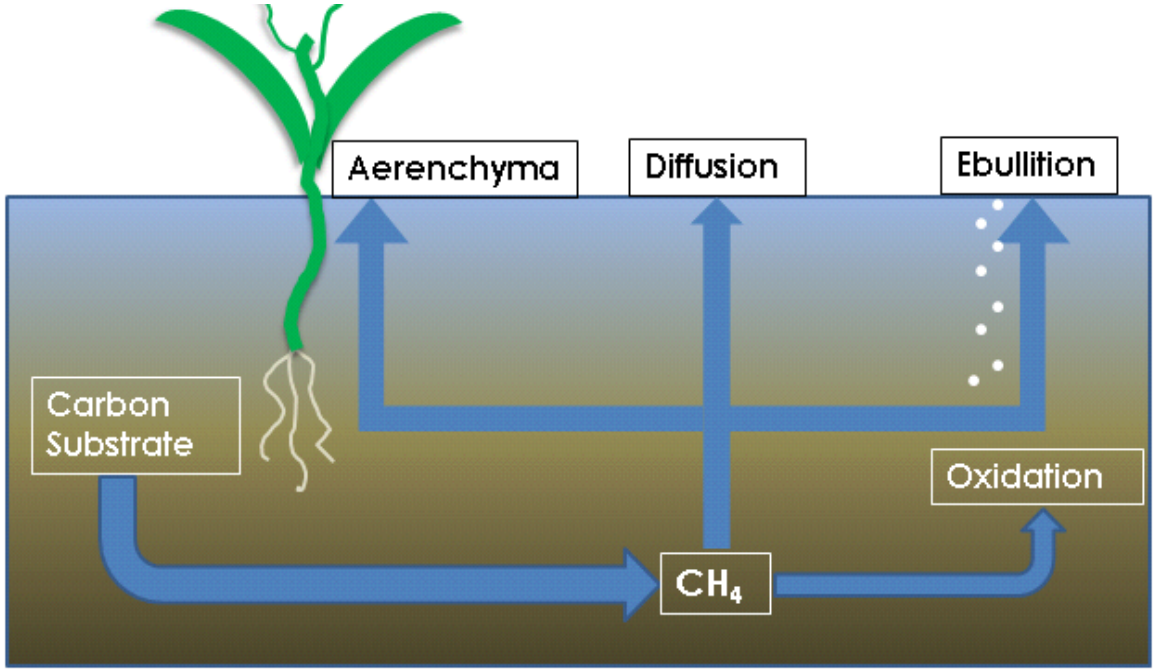


*Figure 2.6 Simple schematic showing the production, transport and oxidation pathways of wetland $CH_4$.*

**Termites**

Termites account for a relatively small fraction of biogenic $CH_4$ emissions (2 to 22 Tg/yr). As with ruminants, the emissions originate in the gut of the termite and vary dependent on several factors. There are three main dietary types of termite, soil-feeding, wood-feeding and fungus-growing (Sanderson *et al*., 1996). Each type emits $CH_4$ at different rates and there are uncertainties in the spatial distribution of each (Sugimoto *et al*., 1998). Termite $CH_4$ emissions have been found to have a strong seasonal cycle, with emissions 3.5 times higher in the wet season compared to the dry season (Jamali *et al*., 2011). This is mostly due to a large increase in biomass during the wet season.

**Hydrates and Oceans**

Both hydrate and ocean emissions are emitted from the surface of the ocean. Hydrate $CH_4$ is trapped in crystalline water molecules found in the deep ocean formed under conditions of low temperature and high pressure. Changes in pressure and temperature can trigger the release of the $CH_4$ from the gas hydrate. Hydrates are most commonly found in coastal regions, with high concentrations in the northern high-latitudes. There is a large uncertainty of the total $CH_4$ trapped

in hydrate and several factors play a role in emissions firstly, the formation, and secondly, the release of $CH_4$ from hydrates. When considering the formation of $CH_4$ hydrates a clear understanding of the accumulation of organic carbon on the seafloor, the seafloor microbial community, the thickness of the hydrate stability zone, the $CH_4$ solubility, sediment compaction and transport is required (Wallmann *et al*., 2012). The process complexity, which includes carbon accumulation and microbial kinetics, and the lack of measurement data restrict the accuracy of $CH_4$ hydrate emissions (Wallmann *et al.*, 2012). Future changes in sea temperatures and circulation might lead to changes in hydrate emissions and possibly lead to a positive climate change feedback (Archer *et al*., 2007). Currently hydrate emissions are estimated to be between 2 and 9 Tg/yr.

Newly formed $CH_4$ from the ocean can be emitted from the ocean surface. In this study these ocean emissions are considered separately from hydrate emissions. As in wetland ecosystems, some aquatic environments consist of methanogens and methanotrophs. $CH_4$ is typically produced in anoxic zones of the ocean, such as the deep ocean or in the sediment layers. Most of this $CH_4$ is then consumed in the oxygenated regions of the ocean (Conrad, 2009). If surface waters become supersaturated then $CH_4$ can outgas into the atmosphere. Without analysis of isotopic signatures it is difficult to distinguish between emissions that originate from hydrates and more newly formed $CH_4$ emissions. However, total marine emissions are estimated to be around 20 Tg/yr (Ciais *et al*., 2014).

**Geological**

Geological sources of $CH_4$, which includes geothermal activity and mud volcanoes, have been estimated at 53 Tg/yr using a combination of top-down estimates based on radiocarbon ($^{14}C$) and bottom-up estimates of $CH_4$ in the lithosphere (Etiope *et al*., 2008). This value includes the marine emissions previously mentioned (20 Tg/yr). The $CH_4$ trapped in the Earth's crust is formed through thermogenic and biogenic processes. The $CH_4$ is then transported up into the atmosphere by mud volcanoes, faults, fractures and volcanic activity (Kvenvolden and Rogers, 2005). The spatial distribution of geological emission sites is poorly constrained and the total emission estimates vary from 13 to 80 Tg/yr (Etiope *et al*., 2008).

## 2.5 Atmospheric $CH_4$ Observations

Atmospheric measurements of $CH_4$ are being increasingly used to gain insights into the change in emissions, sinks and growth of $CH_4$. The three main methods for the measurement of

atmospheric $CH_4$ concentrations are *in-situ* flasks, ground-based Fourier Transform Spectrometers and satellites. All three are used in this study, with the basic retrieval methods discussed in this section and further model comparison details provided in Chapters 3 and 5.

## 2.5.1 Surface Observations

Ground based *in-situ* measurements provide the longest record of recent atmospheric $CH_4$ concentrations. The National Oceanic and Atmospheric Administration (NOAA) has provided surface $CH_4$ measurements since 1983 (Mauna Loa, Hawaii) through the cooperative air sampling network. The network has continuously expanded from just a few stations and now provides monthly mean flask $CH_4$ data from 92 sites. The monthly mean data are averaged from approximately weekly measurements (Dlugokencky *et al.*, 2015). The data have a relatively good global coverage, although there are only a few tropical sites. As a result the horizontal distribution of surface $CH_4$ in the tropics is poorly captured in the observation network. It is important to note that although the relative length, accuracy (0.2%), spatial coverage and temporal coverage of the flask based measurements are good, they are restricted by only being able to provide surface measurements. The samples taken are sent to Boulder, Colorado, where the measurements are made. This is done by first injecting standard air samples into a gas chromatograph. Packed columns are used to separate the $CH_4$ out from the sample before flame ionisation is used for detection (Dlugokencky *et al.*, 2015).

The Advanced Global Atmospheric Gases Experiment (AGAGE) network also measures surface $CH_4$ but *in-situ* using real-time flame ionisation detectors. The data provided by AGAGE offers a coarser spatial resolution because there are only 5 sampling sites used. In addition to the $CH_4$ measurements made by both NOAA and AGAGE, the two sampling networks also provide measurements of $CH_3CCl_3$. These data can be used to derive atmospheric OH concentrations and this is further discussed in more detail in Chapter 4.

## 2.5.2 Ground-based Column Observations

The Total Carbon Column Observing Network (TCCON) measures atmospheric $CH_4$ using ground-based Fourier Transform Spectrometers (Wunch *et al*., 2011). First established in 2004, the TCCON network contains 26 sites, of which 24 are operational. The spatial coverage is biased to the northern hemisphere with noticeable gaps in Africa, Asia and South America, as shown in Figure 2.7. The TCCON dataset therefore lacks the spatial coverage and, with the time series only

commencing in 2004, the duration of the surface *in-situ* measurements. The advantage of TCCON is that it measures predominantly tropospheric column profiles, providing a vertical column of $CH_4$, with an accuracy of <0.25%. TCCON instruments use the shortwave infrared spectral region, with central wavenumbers at 5938, 6002, 6076 $cm^{-1}$, to record direct solar spectra (Wunch *et al.*, 2011). The shortwave infrared frequency range is selected because it includes temperature-independent absorption bands of $CH_4$, with high sensitivity in the lower troposphere. Further details of TCCON vertical sensitivities are provided in Chapter 5.

The accuracy of measurements is expected to improve in the future with the increasing use of proxy species, such as hydrogen fluoride, to remove the contribution of stratospheric variability of $CH_4$ (Saad *et al.*, 2014). To compare TCCON measurements with other datasets requires the application of an averaging kernel; these are discussed in more detail in Chapter 5.

In addition to TCCON, the Network for the Detection of Atmospheric Composition Change (NDACC) also provides atmospheric $CH_4$ measurements from ground-based Fourier Transform Spectrometers (Sepúlveda *et al.*, 2014). NDACC has a similar global coverage to TCCON, with 15 stations located at a large range of latitudes. The time series length of NDACC stations is typically longer than the TCCON stations, with some extending back to 1989. The majority of data from NDACC sites are not continuous and contain gaps in their record. In addition to these gaps, several sites are no longer operational, resulting in missing data for the past few years. For these reasons NDACC data are not used in this study.

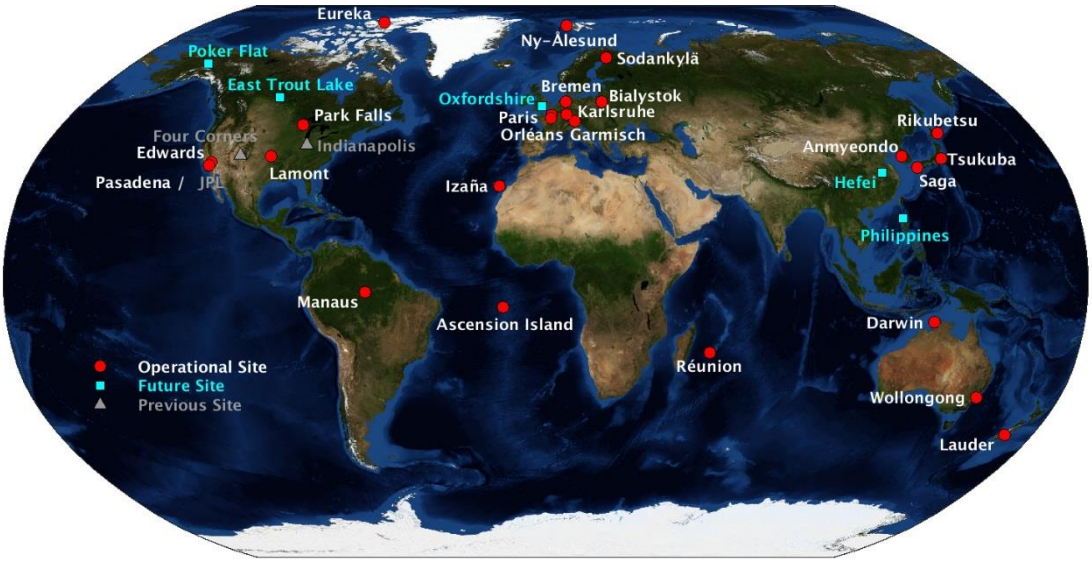


*Figure 2.7 Map showing spatial distribution of TCCON measurement sites. Circles show currently operational sites and squares show planned sites (tccon.ornl.gov, 2016).*

## 2.5.3 Satellite Observation

Satellite remote sensing of lower tropospheric $CH_4$ was pioneered with the launch of the SCanning Imaging Absorption spectroMeter for Atmospheric CHartographY (SCIAMACHY) in 2002 (Bovensmann *et al.*, 1999). Previous upper atmosphere observations are available from The HALogen Occultation Experiment (HALOE) (Russell *et al.*, 1993), which retrieved limb viewing profiles; however, observations only extended down to the tropopause, making the data unsuitable for use with surface flux estimates.

Early missions capable of global coverage $CH_4$ retrievals, such as IMG/ADEOS operated in the thermal infrared (3 - 8μm) (Kobayashi et al., 1999). Thermal infrared observations have a maximum sensitivity in the mid-troposphere, with low sensitivity in the lower troposphere (Buchwitz et al., 2005). This makes thermal infrared retrievals less suited to the detection of surface methane fluxes.

Tropospheric $CH_4$ retrievals from nadir viewing short-wave infrared (1.4-3 μm) instruments began with SCIAMACHY. The short-wave infrared measurements taken from SCIAMACHY are sensitive to low altitude levels, including the lower troposphere and boundary layer, making them better suited for estimating surface fluxes (Buchwitz et al., 2005). These retrievals required validation from ground stations but provided global coverage at a high spatial and temporal resolution for the first time. The passive spectrometer on-board SCIAMACHY measured backscattered, reflected, transmitted or emitted radiation from the surface and atmosphere. Until April 2012 SCIAMACHY provided global measurements of trace gases, including $CH_4$ from the 1.66 μm band (Schneising et al., 2009).

Following on from the success of SCIAMACHY, the Infrared Atmospheric Sounding Interferometer (IASI) and the Greenhouse gases Observing SATellite (GOSAT) were launched. The main difference between IASI and the other two satellites (GOSAT and SCIAMACHY) is the wavelength of operation. IASI operates in the mid-infrared, which allows for day and night coverage, land and ocean coverage and sensitivity to $CH_4$ in the mid to upper troposphere. Both GOSAT and SCIAMACHY operate in the shortwave infrared, allowing for lower troposphere retrievals. IASI operates using a Michelson interferometer in the mid-infrared to provide total column-integrated $CH_4$ content with a horizontal resolution of 100 km and an accuracy of 10%.

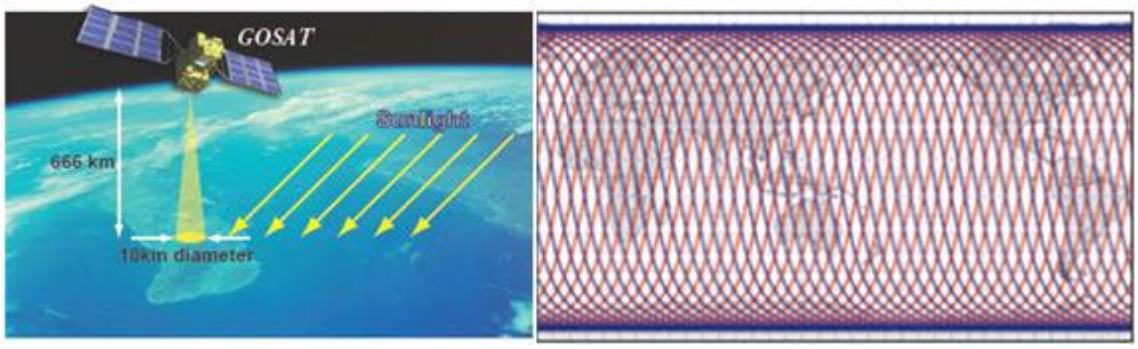


*Figure 2.8 (Left) Schematic illustrating GOSAT observational method. (Right) The three-day GOSAT footprint (gosat.nies.go.jp, 2015)*

GOSAT is the first satellite dedicated purely to greenhouse gas retrievals; this is done using the Thermal And Near-infrared Sensor for carbon Observation (TANSO). The Fourier Transform Spectrometer is part of TANSO and operates in a similar way to the interferometer on IASI. Incoming radiation is split into two optical paths, which creates an optical path difference. A Fourier transform is applied to the measured interference, which provides a spectrum. The absorption of radiation by surface waters makes atmospheric $CH_4$ difficult to measure over lakes and oceans. Two of the four TANSO bands are used to target the retrieval of $CH_4$, band 2 and band 4, with spectral coverages at 1.56-1.72 and 5.56-14.3 μm, respectively. This study uses GOSAT data because of the near surface sensitivity, which is explored in more detail in Chapter 5.

## 2.6 Trends in Atmospheric $CH_4$

### 2.6.1 Long-term Trends

From 1000 to 1750 globally-averaged atmospheric $CH_4$ had no clear trend with concentrations varying by about 40 ppb from a mean of 695 ppb (Etheridge *et al*., 1998). Since the pre-industrial era global mean $CH_4$ concentrations have increased by a factor of 2.5, from approximately 722 ppb in 1750 to 1803 ppb in 2011 (Etheridge *et al*., 1998; Dlugokencky *et al*., 2005). Figure 2.9 shows this notable increase in $CH_4$ concentration over this time period. This long-term increase has been attributed to a rise in anthropogenic emissions from fossil fuel exploitation, agriculture, waste management and biomass burning. Emissions more than doubled from a pre-industrial value of approximately 250 Tg/yr to a 2000 to 2010 value of 553 Tg/yr (Etheridge *et* al., 1998; Dlugokencky *et al*., 2011; Ciais *et al*., 2014).

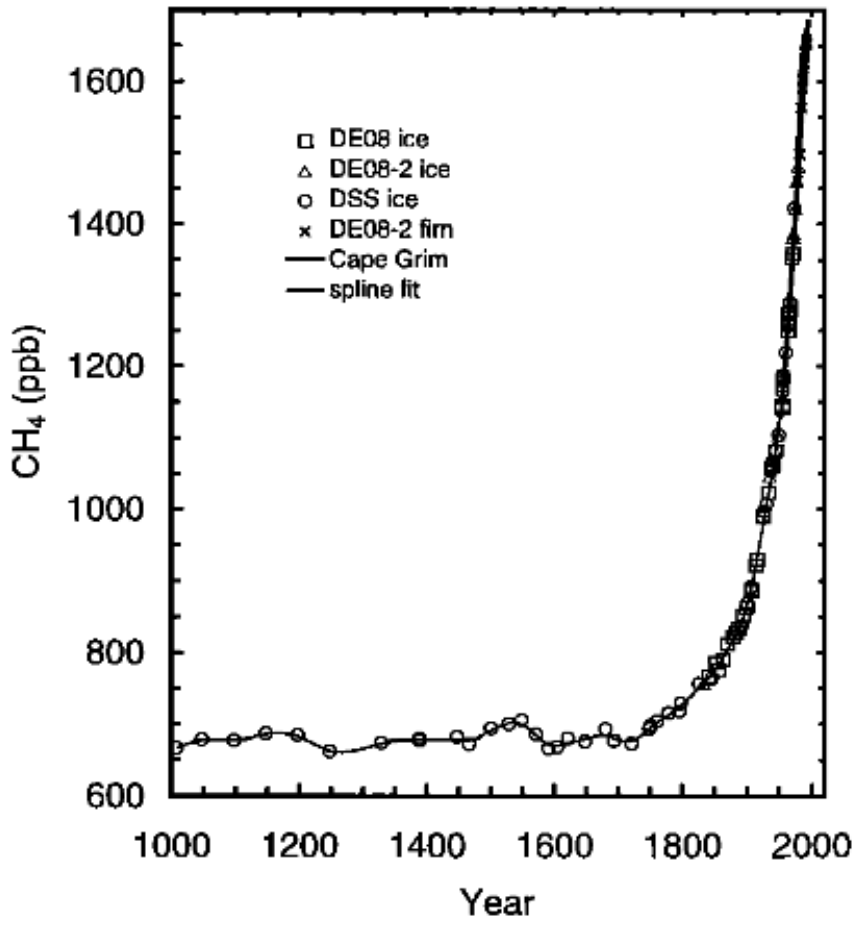


*Figure 2.9 Atmospheric $CH_4$ concentrations over the last 1000 years, based on various ice core samples (Etheridge et al., 1998).*

## 2.6.2 Recent trends

The relatively short atmospheric life-time of $CH_4$, compared to $CO_2$, means that interannual changes in sources and sinks are easily detectable in observations. The relatively smooth increase in globally-averaged atmospheric $CH_4$ on an inter-decadal timescale since the pre-industrial era is less apparent on a more recent interannual (0 – 10 year) timescale. Since continuous flask measurements became available in the mid-1980s, the rate of increase of atmospheric $CH_4$ has been observed to slow down (Dlugokencky *et al.*, 2011). Figure 2.10 shows deviations from a steady growth, using observations from University of California, Irvine (UCI), AGAGE and NOAA surface sampling sites.

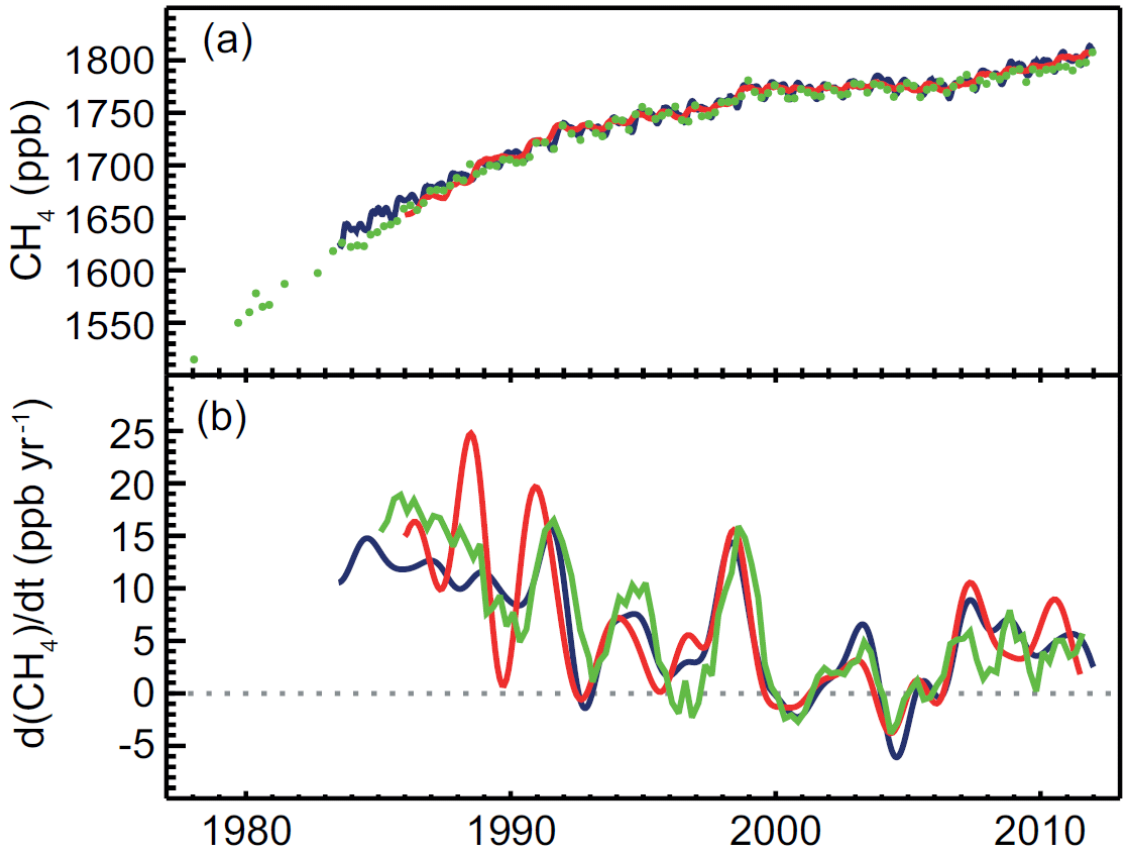


*Figure 2.10 (a) Averaged global surface $CH_4$ from the University of California, Irvine (green), AGAGE (red) and NOAA (blue) networks. (b) 12-month smoothing of growth rate in ppb/yr for averaged global $CH_4$ using same colours as (a) (Hartmann et al. 2013).*

The atmospheric $CH_4$ growth rate, shown in Figure 2.10, can be split into several phases. Firstly; from the mid-1980s until 1991 the rate of growth steadily decreased from 12 ppb/yr to approximately 8 ppb/yr. This steady decline has been attributed to a long-term gradual decrease in anthropogenic emissions, with large interannual variability in wetland emissions during this period (Bousquet *et al.*, 2006). During this period the AGAGE observation network observed a large growth anomaly, which has been attributed to a sharp decrease in destruction by OH in the tropics (Bousquet *et al.*, 2006). This anomaly is likely less apparent in other networks due to the spatial distribution of the measurement sites.

The second noticeable deviation occurred between 1991 and 1993 when there was a sharp increase followed by a drop in the atmospheric growth rate, reaching a rate of 0 ppb/yr, observed by all networks. These were likely caused by two major events, the eruption of Mount Pinatubo in June 1991 and the collapse of the Soviet Union (Dlugokencky *et al.*, 1994). Following the Pinatubo eruption volcanic aerosols caused a reduction in ultraviolet radiation reaching the troposphere. This lowered the concentration of species, like OH, which lead to a decrease in the photochemical loss of $CH_4$ (Dlugokencky *et al.*, 1996), explaining the initial growth in $CH_4$ after

mid-1991. In the months after the eruption a reduction in direct solar radiation also caused a drop in global temperatures; for example just over a year after the eruption northern hemisphere temperatures had decreased by 0.7°C (Dutton and Christy, 1992). As wetland $CH_4$ emissions are temperature dependent this caused a decrease in emissions which is partly responsible for the decrease in the growth rate in 1992. Prior to the collapse of the Soviet Union there existed large-scale inefficiency in the extraction and transport of natural gas, resulting in emissions of 29 to 50 Tg/yr (Reshetnikov *et al*., 2000). A majority (>80%) of extracted gas originated in the West-Siberian gas fields and had to be transported long distance through ageing pipelines, which led to a large loss of $CH_4$. Following the collapse, new investment allowed for the construction of pipelines, which were maintained with more generous funding (Reshetnikov *et al*., 2000). This resulted in a decrease in emissions of 10 Tg/yr, helping to explain some of the observed decrease in growth in 1992 and 1993 (Dlugokencky *et al*., 2003).

From 1993 $CH_4$ growth resumed at a steady rate until 1997 when a strong El Niño event caused a large increase in the growth rate. An El Niño event is characterised as the Pacific warm phase of the El Niño Southern Oscillation (ENSO), the cause of which is poorly understood (Trenberth, 1997; Guilyardi *et al.*, 2012). ENSO events lead to a shift in the atmospheric Walker circulation due to changes in ocean circulation. This causes changes in temperatures and rainfall patterns globally, which influences both wetland and biomass burning $CH_4$ emissions (van der Werf *et al.*, 2006; Hodson *et al.*, 2011). The overall global shift in wetland $CH_4$ emissions during an ENSO event is poorly understood, with a recent study suggesting an overall decrease during the warm phase and an increase during the cool phase (La Niña) (Hodson *et al.*, 2011). During the warm phase, like the El Niño event in 1997 and 1998, drought in equatorial Asia and Central and South America caused an increase in fire activity (van der Werf *et al.*, 2006). It has been suggested that the large increase in atmospheric $CH_4$ growth in 1997/1998 is due to the increased biomass burning emissions (Bousquet *et al.*, 2006). In addition to $CH_4$ emissions, changes in other chemical species, such as CO, during ENSO events are likely to influence OH concentration and therefore the loss rate of $CH_4$.

After the sharp increase in the $CH_4$ growth rate in 1997/1998 there followed a stagnation period of nearly zero growth from 1999 to 2006. The cause of this stagnation period is not well understood and it is investigated in this thesis (Chapter 4). Several hypotheses have been proposed to explain the stagnation including a drop in anthropogenic emissions, a drop in wetland emissions and a change in atmospheric conditions (Warwick *et al.*, 2002; Bousquet *et al.*, 2006; Chen and Prinn, 2006). There remains a lack of consistency between studies with some suggesting that anthropogenic emissions continued to increase (Olivier *et al*., 2005) and others showing much more uncertainty in the role of wetland emissions (Pison *et al*., 2013). Kai *et al.* (2011) used trends

isotopic measurements from Niwot Ridge to provide an alternative hypothesis that a change in agricultural practices caused a reduction in emissions from rice paddies. Levin *et al.* (2012) used a more comprehensive dataset and found a much smaller trend in the isotopic signature; results that were not consistent with Kai *et al.* (2011). The role of changes in atmospheric conditions over this period has not been studied in detail and serves as motivation for Chapter 4.

It had been previously suggested that the observed stagnation between 1999 and 2006 might be a trend towards a steady state, especially considering the slowdown in growth in the preceding years (Dlugokencky *et al*., 2003). Since 2007 there has been renewed growth observed globally, suggesting either an increase in emissions or a reduction in the sinks that had been responsible for the observed temporary steady state. The renewed growth was particularly evident in tropical regions, with studies suggesting an increase in wetland emissions in 2007/2008 (Dlugokencky *et al.*, 2009; Bousquet *et al.*, 2011). In a similar way to the stagnation period most studies have focused on the potential changes in emissions, with less investigation into the potential changes in sinks. By investigating the causes of recent trends in $CH_4$ growth a better understanding and prediction can be made for future changes in $CH_4$.

## 2.7 Summary

The overall global atmospheric $CH_4$ budget is well constrained by top-down emission inventories (Kirschke *et al*., 2013). There is, however, considerable uncertainty in the spatial and temporal distribution of emissions from individual sources, most notably wetlands. To improve predictions of future changes in emissions these uncertainties need to be addressed. Wetlands account for the largest single source of $CH_4$ to the atmosphere, the largest interannual variability and the largest uncertainty in emissions. This highlights the importance of developing a better understanding of the distribution of wetlands and the processes controlling emissions from them.

There is consistency in the observed highly variable growth rate between observation networks over the past three decades, which is poorly understood (Hatermann *et al.*, 2013). Previous studies suggest that the interannual variability in wetland and biomass burning emissions play a large part in the observed variability in $CH_4$ growth (Dlugokencky *et al.*, 2009; Bousquet *et al.*, 2011). Part of this hypothesis can be tested using detailed bottom-up wetland $CH_4$ inventories, atmospheric models and observations. Variations in atmospheric conditions are also a possible reason for the observed variability in $CH_4$ growth.

# 3 Modelling Tools

## 3.1 Introduction

This chapter details the modelling approaches used in Chapters 4, 5 and 6. Mathematical computer models, which describe both chemical and physical processes, are a numerical representation of our understanding of a system. They are essential tools used in conjunction with observations to improve and test our understanding of the Earth system. They are also used to provide predictions of the future based on predicted scenarios, for example to estimate future changes in temperature in response to variations in atmospheric gas concentrations.

Section 3.2 summarises the development of wetland $CH_4$ emissions models, with a focus on JULES (Clark *et al.*, 2011), which is used to simulate land surface processes. Section 3.3 describes the TOMCAT CTM, which is used to simulate chemical and physical interactions within the atmosphere. This includes a brief overview of the history of TOMCAT and examples of studies where it has been used. Section 3.4 discusses the findings of previous studies, which have compared modelled $CH_4$ with observations. This includes flux measurements which are typically compared directly with wetland $CH_4$ models and atmospheric observations which are compared with CTMs. Section 3.5 provides an overall conclusion to the present state of land surface and atmospheric modelling.

## 3.2 Land Surface Models

Land surface models (LSMs) are used to describe the complex interactions between the Earth surface and atmosphere. The land surface is typically split into grid cells, which can then be further divided into subgrid scale surface types, plant functional types (PFTs) and soil layers, as shown in Figure 3.1. LSMs typically include equations describing the energy balance, hydrology, carbon cycle and vegetation. Each of these processes interacts with each other to provide a

detailed framework of the whole ecosystem. For instance, changes in the hydrology might influence vegetation growth, which in turn would affect the surface energy budget.

The complexity of LSMs can be varied to suit the problem being studied and our understanding of any particular process. Disabling certain processes can also influence both the computing time and model uncertainties. For example if the model fails to estimate vegetation accurately the model can be forced by prescribed vegetation. Often additional model modules, like wetland $CH_4$ processes, can be coupled to a LSM to simulate processes that are not usually required in standard simulations (e.g. Wania *et al*., 2010; Riley *et al.*, 2011). Section 2.3.1 describes wetland $CH_4$ models, some of which are in-built to LSMs some that are used as attachments and some that are stand alone.

LSMs are often coupled with atmosphere and ocean models to produce Earth system models (ESMs), which can then be used to provide climate change projections. They can also be used in "stand-alone" mode, which requires the use of meteorological forcing data to drive the model. The LSM output can then be input into an atmospheric model in a subsequent experiment. This thesis adopts this approach and uses LSMs and CTMs in "stand-alone" mode.

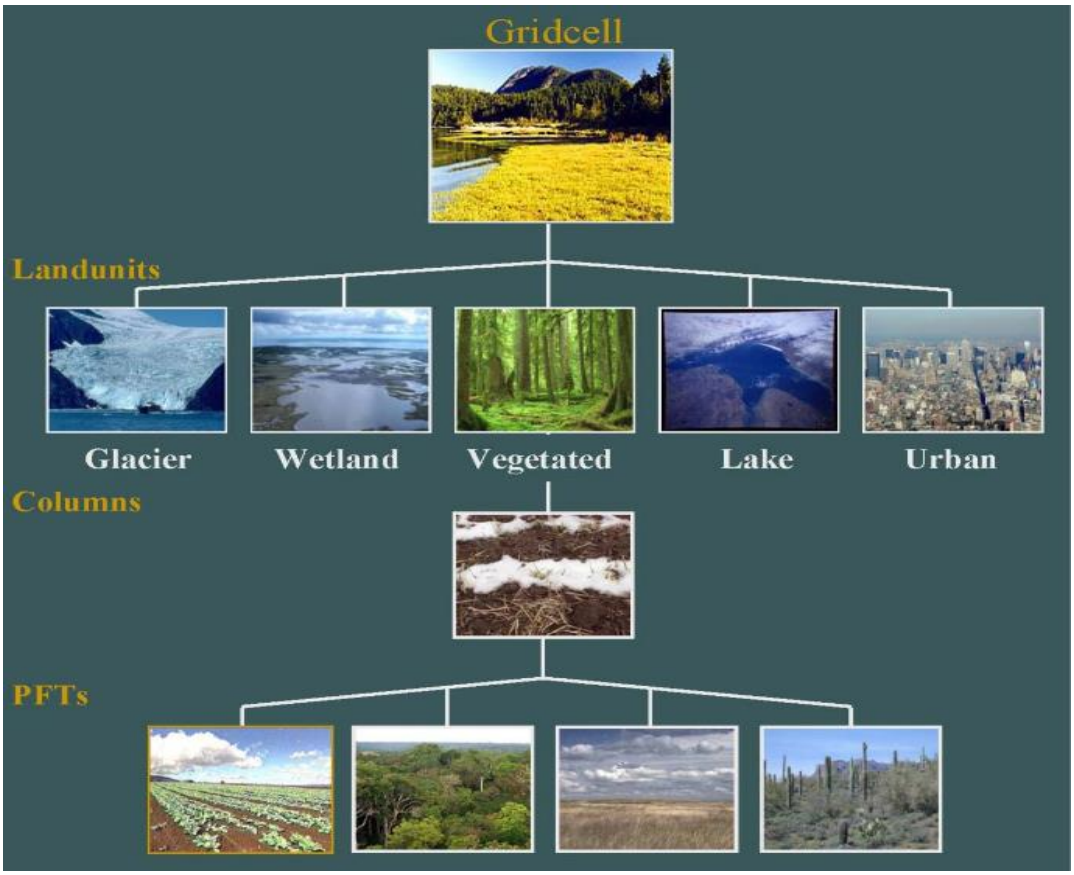


*Figure 3.1 Subgrid hierarchy within the Community Land Surface model, showing the surface types, soil layers and plant functional types (PFTs) (Oleson et al., 2010).*

### 3.2.1 Wetland $CH_4$ Emission Models

Global-scale modelling of wetland $CH_4$ emissions began with Matthews and Fung (1987). That model relied on prescribed vegetation, soil properties and fractional inundated area datasets to generate global $CH_4$ emission datasets, with an estimate of ~110 Tg/yr (Matthews and Fung, 1987). These emission estimates were based on upscaling from local flux measurements to the global scale. Without the use of land surface models or time-varying wetland fractions, these early attempts to quantify wetland emissions did not capture the temporal variation in emissions.

Process-based modelling of wetland $CH_4$ introduced time-varying emissions (Fung *et al*., 1991). These were initially dependent on the time-invariant inundation product from Matthews and Fung (1987) but introduced a basic representation of surface $CH_4$ oxidation and soil layers (Christensen and Cox, 1995). Studies also began to include vegetation models to estimate $CH_4$ emissions, which allowed for a soil carbon representation (Christensen and Cox, 1995). Following on from earlier studies, substrate availability, wetland fraction and soil temperature emerged as the dominant controls of wetland $CH_4$ emission and were used as prescribed parameters to generate emissions (Cao *et al*., 1996).

All methods mentioned above relied on a prescribed inundation area and were not coupled to LSMs. As a result the hydrology in the models was fixed and they could not be tested for climate sensitivity. After these initial models, wetland $CH_4$ modelling development began to split into two directions. The first is discussed in more detail in Chapter 6 and involved a detailed process description at a local scale (Walter *et al.*, 1996; Zhuang *et al.*, 2004). The second involved simpler process descriptions with time-varying hydrology at a global scale (Gedney *et al*., 2004; Wania *et al.*, 2010; Riley *et al.*, 2011). By using topographic indices and soil property information land surface models began to develop more advanced hydrology schemes which aimed to better capture the seasonal and interannual variability in wetland fraction. Global LSMs typically use a semi-empirical fit of parameters, such as soil temperature, to simulate wetland $CH_4$ emissions which are then scaled to a global value based on inversion estimates (Gedney *et al*., 2004). An alternative method involves scaling up from site flux measurements (Wania *et al.*, 2010; Riley *et al.*, 2011). As a result the total emissions over a defined period are fixed by the scaling factor, but this can be used to perform a transient climate simulation to predict future changes in wetland emissions (Gedney *et al*., 2004). There are large uncertainties in the future emissions of wetland $CH_4$, but studies suggest that emissions are likely to increase (Gedney *et al*., 2004; O'Connor *et al.*, 2010). These uncertainties are a result of unknown temperature feedbacks, changes in wetland

distribution and permafrost carbon storage. Figure 3.2 shows a model-simulated future wetland $CH_4$ emission scenario, which suggests an almost doubling of wetland $CH_4$ emissions by 2100.

The major challenges facing current wetland $CH_4$ modelling have been outlined in a recent multi-model intercomparison study (Melton *et al.*, 2013). That study highlighted the differences between current LSM estimates, stating that they were a result of a combination of parameter and structural uncertainty. This suggests that the problem can be split into two subsections, the difference in the parameters that control wetland emissions (e.g soil temperature) and the complexity of the wetland process within the models. Chapter 5 investigates how multiple models with similar processes perform using different parameter sets, with wetland fraction being the largest control on emission differences. Melton *et al.*, (2013) showed large differences in the wetland fraction of different land surface models (see Figure 3.3). Chapter 6 focuses on how adding in more complex processes affects the accuracy of wetland models. Current assessments of LSMs typically involve comparisons with surface flux measurements; one aim of this thesis is to upscale the comparisons to a global scale by incorporating the fluxes in a CTM.

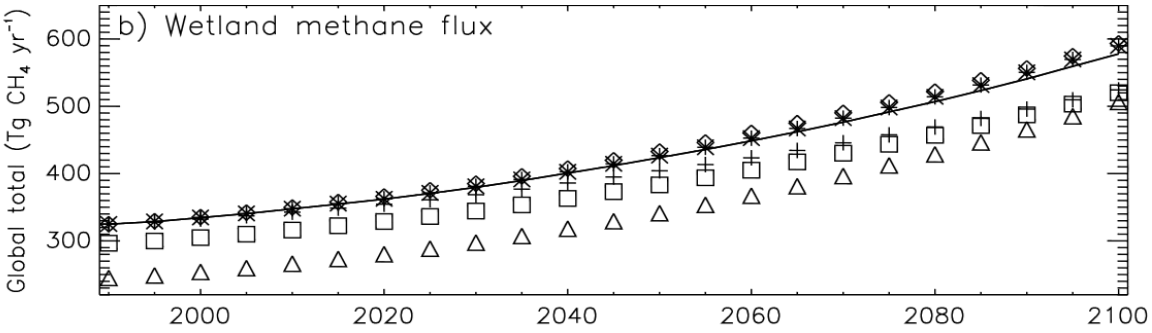


*Figure 3.2 Simulated future wetland $CH_4$ emissions in Tg/yr based on a suite of different temperature sensitivities as given by JULES (Gedney et al., 2004).*

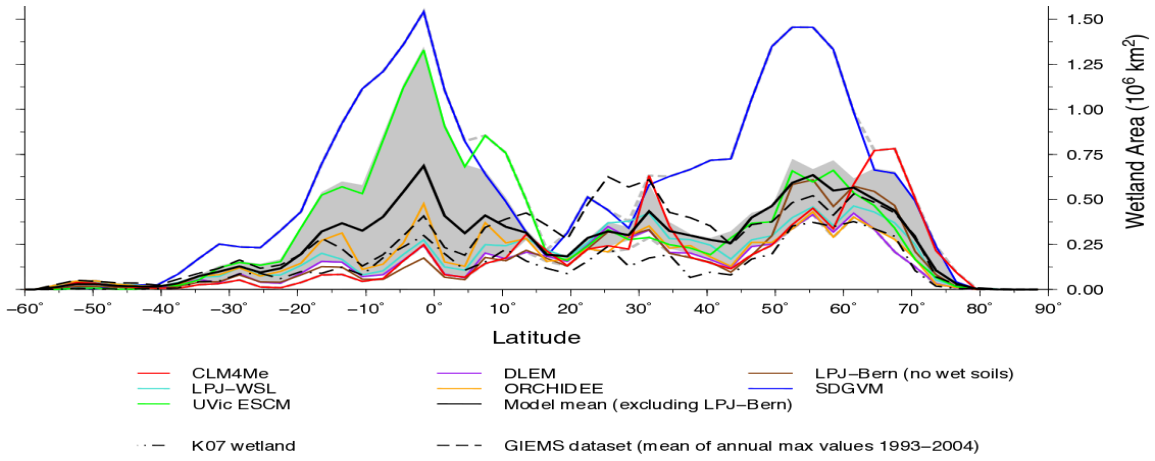


*Figure 3.3 Zonal sum of mean annual maximal wetland area from 1993 to 2004 from different land surface models. K07 and GIEMS lines are based on observations (Melton* et al., *2013).*

### 3.2.2 JULES Model Description

JULES, the primary LSM used in this study, was developed as a community land surface model from the Met Office Surface Exchange Scheme (MOSES), which was originally designed as the land surface component for Earth system and weather forecasting models (Cox *et al.*, 1999). JULES contains multiple land surface modules that interact with each other, including surface radiation, vegetation, hydrology and soil processes. Each process can be simulated with various different complexities, dependent on the user requirements. For this study JULES is run globally at 0.5° by 0.5° with daily output. To simulate $CH_4$ emissions the current version of JULES uses modelled soil carbon, soil temperature and wetland fraction (Gedney *et al*., 2004).

For soil carbon, vegetation information is first required. All simulations in this thesis use the dynamic vegetation model Top-down Representation of Interactive Foliage and Flora Including Dynamics (TRIFFID), which includes simulated plant growth for 5 plant functional types (PFTs): broadleaf trees, needle leaf trees, $C_3$ grasses, $C_4$ grasses and shrubs. The vegetation dynamics allow for litterfall which enters the soil carbon model, RothC (Coleman and Jenkinson, 1999). Soil carbon in the RothC model is split into four pools: decomposable plant material (DPM), resistant plant material (RPM), biomass (BIO) and humus (HUM). Total soil carbon is increased by litterfall and decreased by soil respiration. The respiration rate varies for each pool and the pool allocation is dependent on the type of litterfall and interactions between the pools.

JULES uses soil temperature in the calculation of soil respiration and the production of $CH_4$ by methanogenesis. Soil thermodynamics in JULES simulates both surface and subsurface soil temperature. Surface soil temperatures, used in the simulation of $CH_4$, are calculated in the surface exchange module. This module requires various data including incoming longwave and shortwave radiation, surface grid cell type and soil thermal conductivity properties. Thermal diffusion, which is dependent on soil moisture and various soil properties in JULES, is used to produce subsurface soil temperatures.

Within the surface hydrology module of JULES The TOPography-based hydrological MODEL (TOPMODEL) (Bevan *et al.*, 1984) is used to represent soil hydrology, which determines wetland fraction. TOPMODEL is required to simulate surface fluxes and runoff in each grid cell and is dependent on a topographic index, which is an amalgamation of various elements which can define the hydrological surface dynamics. By providing a representation for drainage and runoff the topographic index controls the tendency for a grid cell to become saturated. This study uses a recently developed topographic index to drive TOPMODEL within JULES (Marthews *et al.*, 2015). Previous versions of JULES failed to capture the spatial distribution of wetland fraction

when compared to observations (Hayman *et al.*, 2014). The new topographic index is used in Chapters 4, 5 and 6.

## 3.3 Atmospheric Models

Atmospheric observations provide essential information about $CH_4$ concentrations in the present day and recent past. However to develop a better understanding of the distribution of sources and sinks numerical models are required. A 3-D model simulates the physical and chemical processes controlling one or more chemical species in the atmosphere. This is done by solving the continuity equations for mass conservation of the species. These are shown in equation 3.1 which describes the transport of a species in 3-dimensional space, where $F$ is the flux vector, $n$ is the number density of the species, $t$ is time, $x$, $y$ and $z$ are the directions, and $\nabla \cdot F$ is the flux divergence measuring net flow.

$$\frac{\partial n}{\partial t} = -\frac{\partial F_x}{\partial x} - \frac{\partial F_y}{\partial y} - \frac{\partial F_z}{\partial z} = -\nabla \cdot F \qquad \textbf{(3.1)}$$

Grid cell concentrations ($C_t$) of chemical species within a model are provided by balancing the concentration at the previous time step ($C_{t-1}$), a grid cell flux (F) and chemical loss or production, which is often dependent on other species (Y) and temperature (T), shown in equation 3.2.

$$[C_t] = [C_{t-1}] + F + f([Y], T, [C_{t-1}]) \qquad \textbf{(3.2)}$$

By comparing the results of CTM simulations with observations, underlying processes can be better understood. CTMs require meteorological inputs because they do not simulate atmospheric dynamics unlike general circulation models (GCM). The advantages of using CTMs over GCMs are that they are less computationally expensive, easier to run and can be easily compared with observations. An off-line CTM does not include chemical feedbacks into the driving meteorology. In the past few decades CTMs have been increasingly used to create global $CH_4$ budgets (Fung *et al.*, 1991; Dlugokencky *et al.*, 2011; Kirschke *et al.*, 2013). Two methods are commonly used in most atmospheric modelling studies, forward and inverse.

### 3.3.1 Forward Chemical Transport Models

Forward CTMs, like that used in this thesis, require emission estimates and loss fields of chemical species. Emissions come from a wide range of sources described in Chapter 2, including national

inventories, land surface models and satellite proxy methods. CTMs can be split into two categories; Lagrangian models use a local air-parcel-following frame of reference, whereas Eulerian models contain gridboxes with fluxes in and out. This makes Eulerian models more suitable for understanding global budgets. Eulerian models typically comprise of multiple horizontal and vertical levels, the emissions are input at the surface level and are transported around the model gridboxes via advection, convection and boundary layer mixing. Once in the atmosphere, loss fields are applied to the species, these can either be calculated or specified. Calculated loss fields are defined by fully interactive chemistry where equations are solved for each species. Specified loss fields use prescribed data from elsewhere, the advantages and disadvantages of both methods are discussed further in Chapter 4. For the soil sink, the loss can be applied as a negative emission field. The spatial variation in emissions, loss fields and transport plays a key role in the removal of $CH_4$. If, for example, large quantities of $CH_4$ were emitted and remained in poorly sunlit regions due to no mixing or transport being simulated, then the lifetime of $CH_4$ would increase due to the limited availability of OH. Results in Patra *et al.* (2011) show how forward models can be used to investigate emissions, transport and loss fields by comparing models not only with each other but also with observations. Their results show that differences exist within forward model predictions but they generally agree well with observations.

### 3.3.2 Inverse Chemical Transport Models

Inverse modelling techniques use observations of atmospheric concentrations of $CH_4$ to estimate a surface emission flux, e.g. Wilson *et al.* (2014). This top-down approach provides a good spatial coverage for emission estimates, but like forward modelling requires accurate modelling of transport. Previous studies suggest the lack of spatial coverage of observations and inaccuracy in model transport hinder the accuracy of inferred emission estimates from inversions (Dentener *et al.*, 2003; Mikaloff Fletcher *et al.*, 2004; Chen and Prinn, 2005). Additionally, inverse modelling requires a prior estimate of emissions and an estimate of the error.

### 3.3.3 TOMCAT Model Description

TOMCAT is an off-line Eulerian CTM, which was originally created to study the polar stratosphere in the early 1990s at the Centre National de Recherches Météorologiques (CNRM) in Toulouse (Chipperfield *et al.*, 1993). A related model, SLIMCAT, was later created from TOMCAT to improve simulations of the stratosphere using a different vertical level system (Chipperfield *et al.*, 1996). The two models were later combined to create a newer version of

TOMCAT, described by Chipperfield (2006), that has been used in many tropospheric studies (e.g. Dhomse *et al.* 2011; Hossaini *et al.*, 2015). The version of TOMCAT used in this study has a horizontal resolution of 2.8° by 2.8° with 60 vertical levels from surface to ~60km. The model levels use a hybrid vertical coordinate ($\sigma$-$p$), with terrain-following levels near the surface ($\sigma$) and pressure levels in the upper atmosphere ($p$). The pressure of a model half-level ($p_{k+1/2}$), or interface, is given by equation 3.3, where $p_0$ is a reference pressure of 100,000 Pa and $p_s$ is the surface pressure (see Chipperfield *et al.*, 2006).

$$p_{k+1/2} = Ap_0 + Bp_s \quad \textbf{(3.3)}$$

Transport in the TOMCAT model used in this study is controlled by separate advection, convection and planetary boundary layer schemes. Advection in the model is represented by equation 3.1. Convection within the model is based on a scheme developed by Tiedtke (1989) and described by Stockwell and Chipperfield (1999). Planetary boundary layer mixing is based on a scheme developed by Holtslag and Boville (1993) and described by Wang *et al.*, (1999). TOMCAT can be used in full chemistry mode, which includes multiple chemical species; however for the purpose of this study a simplified chemistry is used which is explained in more detail in Chapter 4. The TOMCAT simulations used in this thesis are forced by winds and temperatures from the 6-hourly European Centre for Medium-Range Weather Forecasts (ECMWF) ERA-Interim reanalyses (Dee et al., 2011). These are transformed onto the model grid prior to use in the model simulations and the model is updated on 30-minute time steps.

TOMCAT has been previously used to investigate the impact of meteorology on the interannual growth rate of $CH_4$ in the atmosphere using an offline OH field (Warwick *et al.*, 2002). A similar simplified chemistry scheme used in this thesis has also been previously used in TOMCAT to show good model agreement with observed atmospheric $CH_4$ concentrations (Patra *et al.*, 2011).

## 3.4 Comparisons with Observations

Previous studies have compared land surface and atmospheric model output of $CH_4$ with observations to aid in model development and improve process understanding. Fung *et al.*, (1991) combined a wetland $CH_4$ model, a CTM and observations to generate geographical and seasonal emission distributions. This study highlighted uncertainties because of the unknown magnitude of individual sources and the limited measurement data. The study concluded that, based on the data available, a global methane budget could not be estimated. On a site-specific scale wetland models were developed to have good agreement with observations (Walter *et al.*, 1996). At the

same time global wetland models were developed but not tested against observations (Cao *et al.*, 1996). Walter *et al.* (2000) introduced additional surface processes to an earlier study by Walter *et al.* (1996) and generated a model that could be, but had not yet been, used on the global scale. Wania *et al.* (2010) and Riley *et al.* (2011) carried out model comparisons, which showed good agreement with surface flux measurements; however they did not compare their results with atmospheric measurements using a forward CTM. Wania *et al.* (2010) showed that the model can be tuned at individual sites to capture the seasonality observed in flux observations. The model is then tuned to one single parameter set that is used across all sites. Some sites show a large reduction in model performance whilst others appear almost unchanged (see Figure 3.4).

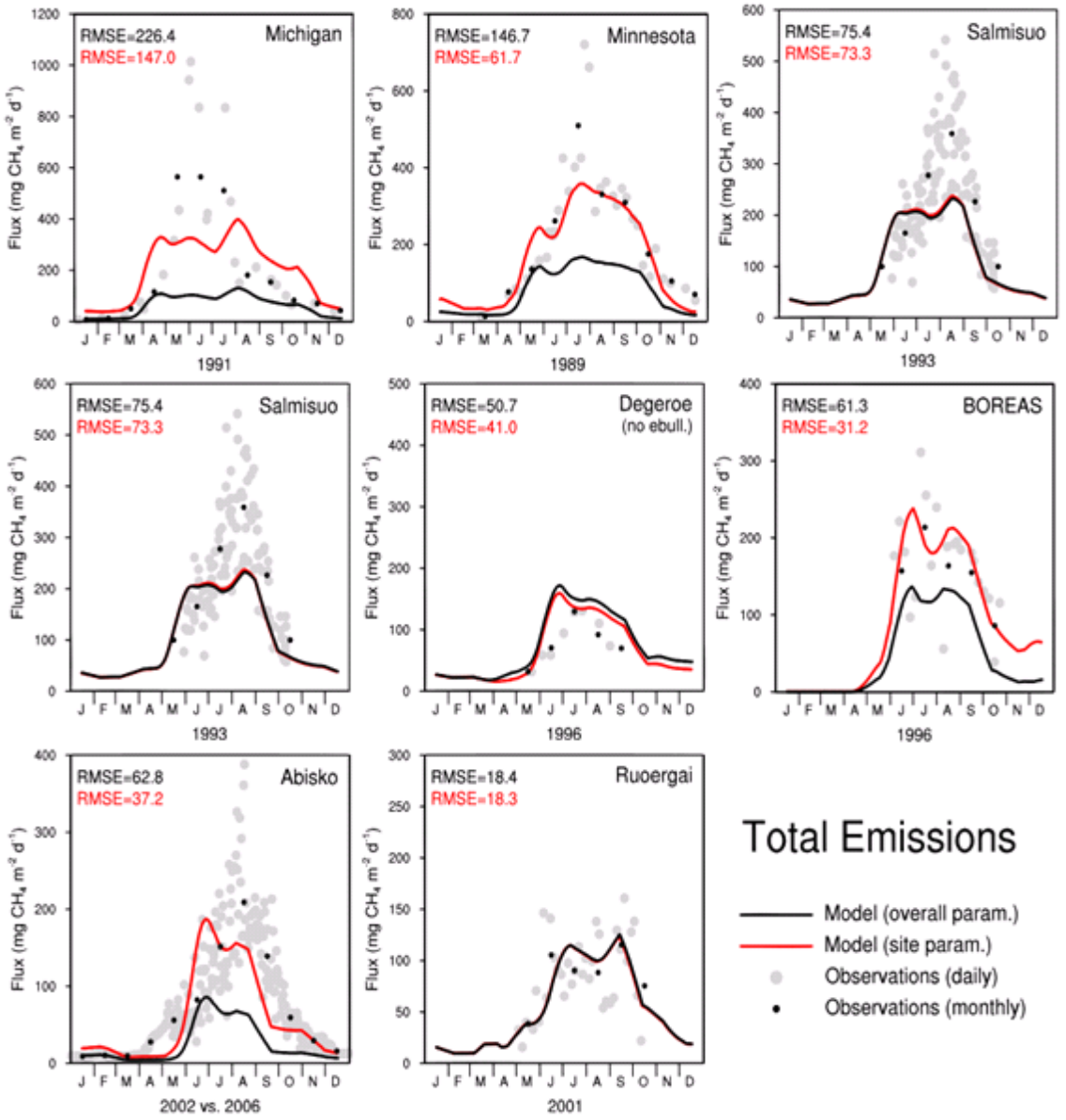


*Figure 3.4 Modelled $CH_4$ emissions compared with flux observations for seven northern hemisphere sites. Results are plotted with the RMSE value relative to the observation for the model tuned for the individual site (red line) and model tuned for all sites (black line) (Wania et al., 2010).*

Atmospheric observations can be compared with CTM results to assess the model, the estimated sources and sinks, and the meteorological fields. Chen and Prinn (2005) compared modelled and flask measurements of atmospheric $CH_4$ between 1996 and 2001 to show that the model captures some, but not all, of the seasonality in the observations. The interannual variability was not tested because repeating yearly emission and loss fields were used. Patra *et al.* (2011) used multiple emission inventories in multiple CTMs and compared the output with data at 8 surface sites. They found that the seasonal cycle was well captured at most sites, but not at high latitudes. These initial comparisons suggest that surface $CH_4$ is well captured by the models in most regions; however the spatial distribution of the surface observations used is poor.

Initial comparison studies with satellite-retrieved data showed a model agreement within 5-10% of SCIAMACHY $CH_4$ columns (Buchwitz *et al.*, 2005). The errors in the SCIAMACHY retrieval, although relatively small, are on a similar scale to predicted spatial variation in $CH_4$ fluxes. It can therefore be reasoned that in order to accurately detect spatial variations in $CH_4$ concentration these errors must be reduced. This thesis aims to show that by using more recent satellite data from GOSAT and IASI, both of which have more accurate instruments, these errors will be reduced to a suitable level. Investigations into the spatial variation in emission inventories using SCIAMACHY show tropical emissions are generally underestimated in the inventories, highlighting wetlands as a key area of concern (Bergamaschi *et al.*, 2007). Hayman *et al.*, (2014) used an ESM with three different bottom-up wetland emission inventories and compared the results with SCIAMACHY and surface observations between 1999 and 2007. One wetland dataset used annually repeating emissions from Fung *et al.*, (1991). The second used the JULES process description with prescribed soil carbon. The third used the JULES process description with prescribed soil carbon and wetland fraction. They found a total offset of 50 ppb between the model and SCIAMACHY and found large spatial differences between the model simulations.

Parker *et al.* (2011) found good agreement between CTM predictions and GOSAT measurements. That study not only shows high hemispheric gradient correlation values ($R = 0.93 - 0.99$) between model and satellite data but also good regional correlations ($R = 0.71 – 0.97$). Results shown elsewhere suggest that the regional correlation between GOSAT and the GEOS-Chem CTM is lower ($R = 0.11 – 0.90$) (Fraser *et al.*, 2013). Both these studies use top-down emission estimates of wetland $CH_4$ and do not test the accuracy of bottom-up wetland inventories (Bloom *et al.*, 2012). From the two studies shown in Figure 3.5, Parker *et al.* (2011) and Fraser *et al.* (2013), it can be concluded that although variation in comparison methods remain, satellite data can provide an accurate assessment of model results.

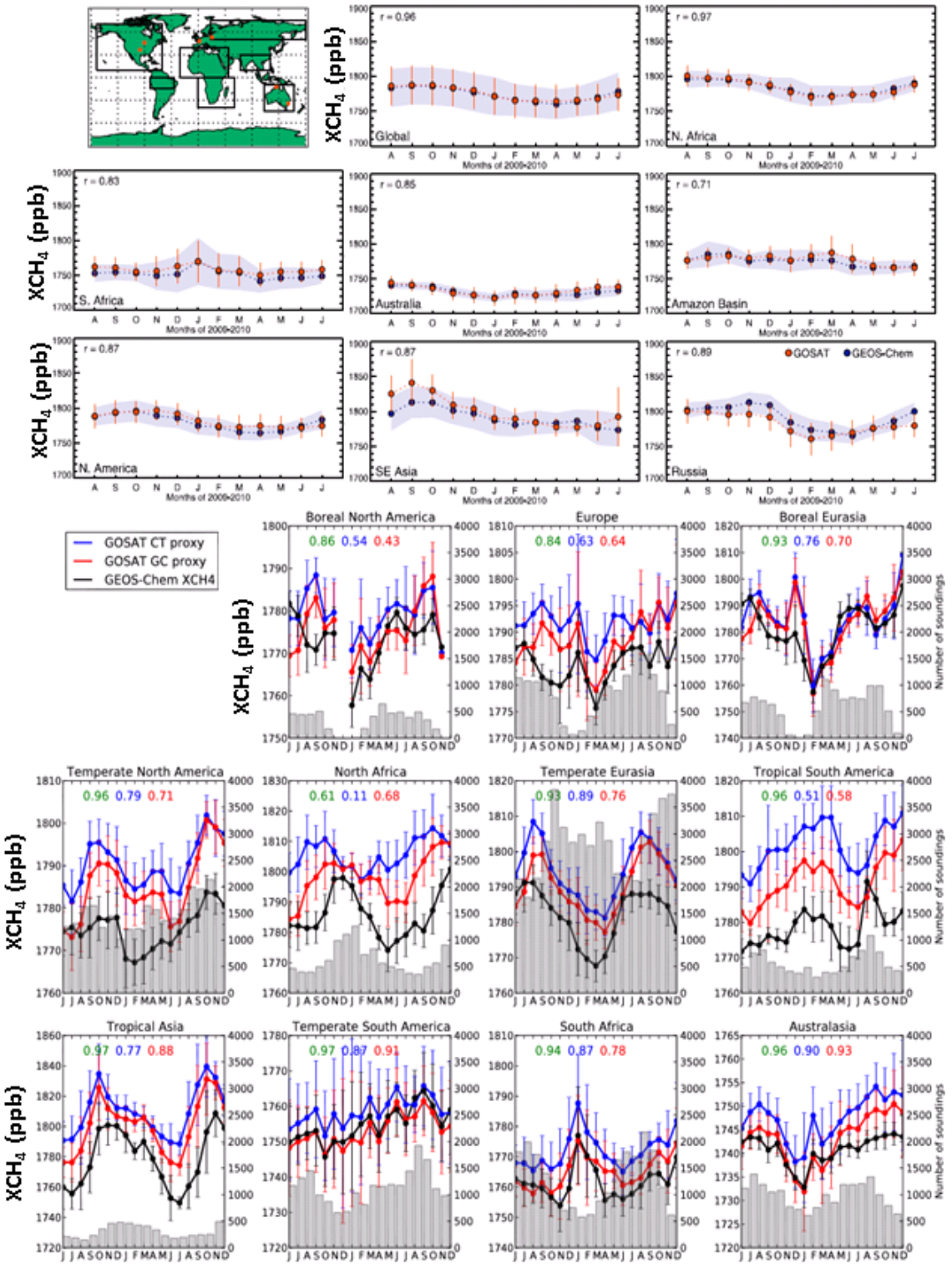


*Figure 3.5 Top - Time-series of the GOSAT and GEOS-Chem column-average $CH_4$ dry-air mixing ratios ($XCH_4$) between August 2009 and July 2010 globally and for the 7 regions outlined on the map. (Parker et al., 2011). Bottom – Time-series of the GOSAT and GEOS-Chem $XCH_4$ between June 2009 and December 2010. The inset numbers are the correlation coefficients between the two GOSAT proxies (green), the Carbon Tracker proxy and GEOS-Chem $XCH_4$ (blue), and the Geos-Chem proxy and GEOS-Chem $XCH_4$ (red) (Fraser et al., 2013).*

## 3.5 Summary

Recent developments of LSMs have provided simulated global wetland fraction, soil temperature and carbon substrate for the first time. These are the three key parameters that drive wetland $CH_4$ emissions and, as a result, bottom-up emission inventories can now be compared against top-down estimates and observations. Studies have shown that, on a site-specific scale, tuned bottom-up model predictions agree well with flux measurements (Walter *et al.*, 1996; Wania *et al.*, 2010; Riley *et al.*, 2011). CTMs and SCIAMACHY have been used to test bottom-up models of $CH_4$ on a global scale (Buchwitz *et al*., 2005; Hayman *et al.*, 2014). More recent observations (GOSAT and IASI) provide more accurate measurements that can be compared with the latest version of the bottom-up wetland models. Analysis of multiple wetland $CH_4$ inventories can be made using CTMs to aid in the development of both the process and parameter description within the bottom-up models. These comparisons can be made seasonally, interannually, regionally and globally using a suite of observation techniques.

# 4 Atmospheric Contribution to Recent Trends in $CH_4$

## 4.1 Introduction

This chapter evaluates the role of atmospheric variability in the recent trends in $CH_4$ growth. Nisbet *et al*. (2014) used NOAA flask data to show that between 1984 and 1992 atmospheric $CH_4$ increased at ~12 ppb/yr, after which the growth rate slowed to ~3 ppb/yr. In 1999 a period of near-zero growth began which continued until 2007. In 2007 this stagnation period ended and since then average growth has increased again to ~6 ppb/yr (Rigby et al., 2008). These trend variations are discussed in more detail in Chapter 2.

Most previous attempts to explain the pause in $CH_4$ growth between 1999 and 2006 have focused on changes in emissions (e.g. Bousquet *et al.*, 2006; Chen and Prinn, 2006; Kai *et al.*, 2011). Here, it is hypothesised that variations in atmospheric chemistry also played a role in the recent variability in growth. Variations in OH, the major atmospheric sink of atmospheric $CH_4$, might have contributed to the decreased growth rate. Additionally, it is hypothesised that reaction rate changes due to changes in atmospheric temperature or changes in atmospheric transport produce a noticeable effect. For example Warwick *et al.* (2002) investigated the impact of meteorology on atmospheric $CH_4$ growth rates from 1980 to 1998, i.e. well before the observed recent pause. They concluded that atmospheric conditions, e.g. transport and temperature, could be an important driver in the interannual variability of atmospheric $CH_4$.

Some previous studies have suggested that an increase in atmospheric [OH] may have been at least partly responsible for a decrease in the $CH_4$ growth rate at certain times (Lelieveld *et al.*, 2004; Fiore *et al.*, 2006). Atmospheric OH production rates are determined by the intensity of UV radiation and the abundance of $O_3$, which is controlled by $O_3$-producing species, such as $NO_x$. The destruction of atmospheric OH is dependent on the abundance of species, such as $CH_4$, CO and $SO_2$. Several suggestions have been made as to why atmospheric [OH] was elevated during

the $CH_4$ stagnation period. Fiore *et al.* (2006) attributed a possible change to an increase in lightning $NO_x$. Prinn *et al.* (2005) suggested major global wildfires and ENSO events could influence [OH] variability through changes to CO. This would imply a reduction in these events during the $CH_4$ stagnation. A third theory, not yet tested, is the role of volcanic activity on downward UV radiation limiting OH production. A period of low volcanic activity would lead to a decrease in stratospheric aerosol, which would increase the amount of UV radiation reaching the troposphere. This would increase the photolysis rate, which would increase [OH]. This hypothesis is dependent on a reduction in volcanic activity in the period prior to and during the stagnation. Figure 4.1 shows that reduced volcanic activity caused an increase in incoming shortwave radiation during the $CH_4$ stagnation in agreement with previous work (Carn *et al.*, 2015; Mills *et al.*, under review).

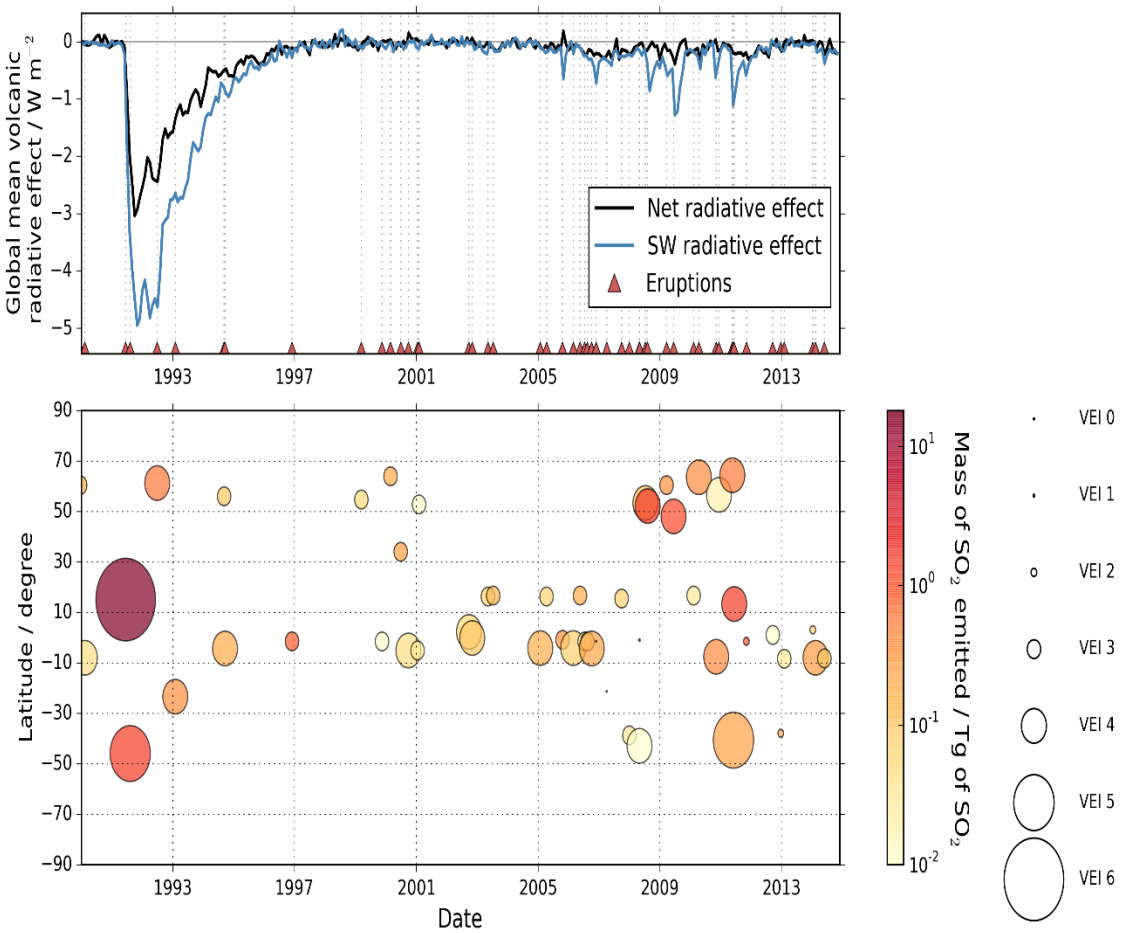


*Figure 4.1 The top panel shows the model-simulated global mean net radiative effect (black line) and short-wave radiative effect (blue line) due to volcanic eruptions (red triangles) between 1990 and 2014. The simulations are described in Mills et al. (2016) and the bottom panel shows the latitude and amount of sulphur dioxide ($SO_2$) emitted for each eruption. VEI = Volcanic Explosivity Index, which is an estimate of the magnitude of an eruption (Newhall & Self, 1982). Figure courtesy of Anja Schmidt.*

Section 4.2 describes the $CH_3CCl_3$ and $CH_4$ observations used here. Section 4.3 provides information about a simple one-box model used to derive atmospheric [OH] and investigate variations in $CH_4$ emissions. Section 4.4 gives a background to the TOMCAT model set-up. This includes a description of the emission inventories, the various tracers and the loss fields used. Section 4.5 shows comparisons of one-box model and TOMCAT simulations with previous studies and observations. Section 4.6 summarises the results, highlighting the role of atmospheric variability in the recent trends in $CH_4$ growth, particularly between 1999 and 2006.

## 4.2 $CH_3CCl_3$ and $CH_4$ Observations

NOAA and AGAGE surface observations of both $CH_3CCl_3$ and $CH_4$ have been used to constrain and evaluate 15 TOMCAT simulations between 1993 and 2009. The data are taken from 22 sites shown in Table 4.1 and Figure 4.2, a majority of which (19) are part of the NOAA Earth System Research Laboratory (ESRL) Global Monitoring Division (Dlugokencky *et al*., 2015). The AGAGE $CH_4$ data are measured *in-situ* at 4 sites, which have limited global coverage (Prinn *et al*., 2000; Cunnold *et al*., 2002; Prinn *et al*., 2005). Vardag *et* al. (2014) showed good agreement between the X2004 scale (NOAA) and the Tohoku University scale (AGAGE) used for $CH_4$ measurements, and the GLOBALVIEW-CH4 multiplier factor between networks is less than 0.05% (Masarie *et al.*, 2001). Global $CH_4$ concentration estimates for both networks are derived by interpolating the measurements across 180 latitude bins, which are then weighted by surface area.

$CH_3CCl_3$ emission sources include refrigeration and air conditioning. It is an ozone-depleting substance that is regulated under the Montreal Protocol. This has resulted in a large decrease in emissions of $CH_3CCl_3$ from 1997 onwards. Montzka *et al*. (2000) showed that since the reduction in emissions the distribution of atmospheric $CH_3CCl_3$ is primarily controlled by atmospheric removal, which is mainly through reaction with OH. Therefore, [OH] variability can be derived by analysing anomalies in $CH_3CCl_3$ decay. For example, assuming zero emissions, constant transport and temperature, a smooth decay curve of $CH_3CCl_3$ concentrations would suggest that OH concentrations are constant. Measurements of $CH_3CCl_3$ taken between 1997 and 2009 are used to derive [OH] anomalies, which are then applied to the [OH] field used in TOMCAT and also to evaluate $CH_3CCl_3$ in TOMCAT. Further details of the methods used to create a time-varying [OH] field for use in TOMCAT are discussed in Sections 4.3 and 4.4.2. Measurements are taken from 7 NOAA and 5 AGAGE sites between 1997 and 2009, where available, and used to create two global $CH_3CCl_3$ records by averaging across all sites (Montzka *et al.*, 2011; Rigby *et al.*, 2013).

| Site Code | Site Name | Latitude | Longitude | Altitude (km) | $CH_4$ | $CH_3CCl_3$ | Start Date |
|---|---|---|---|---|---|---|---|
| ABP | Arembepe, Brazil | -12.77 | -38.17 | 0 | NOAA | | 27/10/2006 |
| ALT | Alert, Canada | 82.45 | -62.51 | 0.2 | NOAA | | 10/06/1985 |
| ASC | Ascension Island, UK | 7.97 | -14.4 | 0.09 | NOAA | | 11/05/1983 |
| BRW | Barrow, USA | 71.32 | -156.61 | 0.01 | NOAA | NOAA | 06/04/1983 |
| CGO | Cape Grim, Australia | -40.68 | 144.69 | 0.09 | NOAA/ AGAGE | AGAGE | 19/04/1984 |
| HBA | Halley Station, UK | -75.61 | -26.21 | 0.03 | NOAA | | 17/01/1983 |
| ICE | Storhofdi, Iceland | 63.4 | -20.29 | 0.12 | NOAA | | 02/10/1992 |
| KUM | Cape Kumukahi, USA | 19.5 | -154.8 | 0.02 | - | NOAA | - |
| LEF | Park Falls, USA | 45.9 | -90.3 | 0.47 | - | NOAA | - |
| MHD | Mace Head, Ireland | 53.33 | -9.9 | 0.01 | NOAA/ AGAGE | AGAGE | 03/06/1991 |
| MLO | Mauna Loa, USA | 19.54 | -155.58 | 3.4 | NOAA | NOAA | 06/05/1983 |
| NWR | Niwot Ridge, USA | 40.05 | -105.59 | 3.52 | NOAA | NOAA | 21/06/1983 |
| PAL | Pallas-Sammaltunturi, Finland | 67.97 | 24.12 | 0.56 | NOAA | | 21/12/2001 |
| PSA | Palmer Station, USA | -64.92 | -64 | 0.01 | NOAA | | 01/01/1983 |
| RPB | Ragged Point, Barbados | 13.17 | -59.43 | 0.02 | NOAA/ AGAGE | AGAGE | 14/11/1987 |
| SEY | Mahe Island, Seychelles | -4.68 | 55.53 | 0 | NOAA | | 12/05/1983 |
| SMO | Tutuila, American Samoa | -14.25 | -170.56 | 0.04 | NOAA | NOAA/ AGAGE | 23/04/1983 |
| SPO | South Pole, USA | -89.98 | -24.8 | 2.81 | NOAA | NOAA | 20/02/1983 |
| STM | Ocean Station M, Norway | 66 | 2 | 0 | NOAA | | 29/04/1983 |
| SUM | Summit, Greenland | 72.6 | -38.42 | 3.21 | NOAA | | 23/06/1997 |
| THD | Trinidad Head, USA | 41.1 | -124.1 | 0.1 | AGAGE | AGAGE | 09/1995 |
| ZEP | Ny-Alesund, Norway & Sweden | 78.91 | 11.89 | 0.47 | NOAA | | 11/02/1994 |

*Table 4.1 List of NOAA and AGAGE stations which provide $CH_4$ and $CH_3CCl_3$ observations with their site code, latitude, longitude, altitude and start date. Note the $CH_4$ and $CH_3CCl_3$ columns show which network provides the data.*

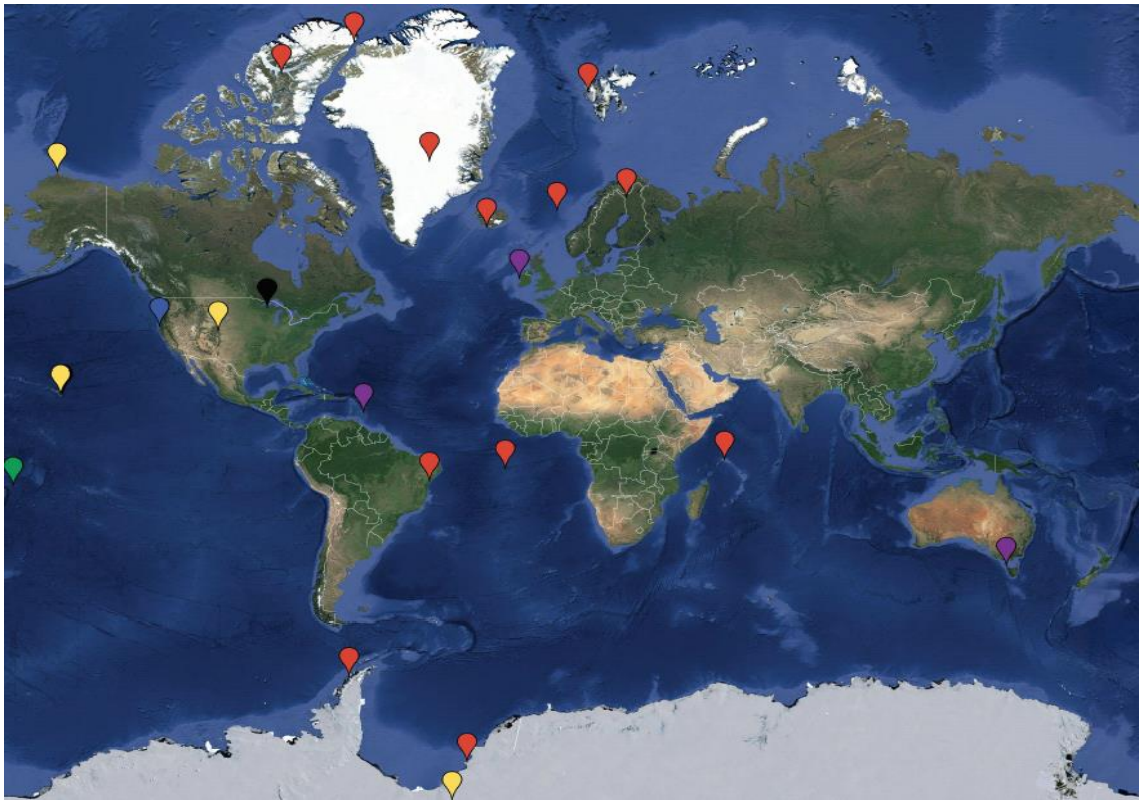

*Figure 4.2 Map showing distribution of the 22 surface stations which provide data used in this study. These are marked in red (NOAA $CH_4$), yellow (NOAA $CH_4$ and $CH_3CCl_3$), purple (NOAA and AGAGE $CH_4$), purple (AGAGE $CH_3CCl_3$), black (NOAA $CH_3CCl_3$), blue (AGAGE $CH_4$ and $CH_3CCl_3$) and green (NOAA $CH_4$ and, NOAA and AGAGE).*

## 4.3 One-box model

A simple one-box model has been developed to investigate emissions of $CH_4$ and derive anomalies in global atmospheric [OH] using $CH_3CCl_3$ observations. This model permits a first-order understanding of the factors which govern the variation in global growth rate and the relative contribution of emissions and loss to that growth. Additionally, this model is much less computationally expensive to run than a full 3-D simulation. The model integrates the global mean burden of either $CH_4$ or $CH_3CCl_3$ (*X)* based on annual emissions (*E*, g/yr) and chemical loss (*L*, g/yr) through the reaction of *X* with OH. The modelled atmospheric burden of X ($X_t$, g) can be integrated over a 1-month period ($\Delta t$) (equation 4.3), where *k* ($cm^3$ $molecule^{-1}$ $month^{-1}$) is the rate constant for the reaction of *X* with OH (e.g. Sander *et al*., 2011). The reaction rate constants for $CH_4$ and $CH_3CCl_3$ loss are given by equations 4.1 and 4.2, where *T* (K) is temperature (Sander *et al*., 2011).

$$CH_4 : \ k = 2.45\text{x}10^{-12}e^{\frac{-1775}{T}} \qquad \textbf{(4.1)}$$

$$CH_3CCl_3 : k = 1.64\text{x}10^{-12}e^{\frac{-1520}{T}} \quad \textbf{(4.2)}$$

$$\frac{1}{\Delta t}(X_{t+\Delta t} - X_t) = E - L = E - k[OH][X] \quad \textbf{(4.3)}$$

Global [OH] is calculated from $CH_3CCl_3$ measurements by rearranging equation 4.3. This requires global atmospheric temperatures, global $CH_3CCl_3$ concentrations and emission estimates.

To estimate the temperature value appropriate for $CH_4$ and $CH_3CCl_3$ loss, two methods were used based on fields from ECMWF ERA-interim (Dee et al., 2011). The first used a time varying annual temperature mean for each grid box in TOMCAT, described in Chapter 3. These temperatures were averaged into a global temperature that is weighted by the [OH] in the grid box. The OH concentrations were taken from a prescribed OH field, described in more detail in Section 4.4. The second used the same method, except the temperature was also averaged over time, giving a global mean value of 272.9 K.

NOAA and AGAGE observations of $CH_3CCl_3$ were used to create a time series of global [OH] concentrations. NOAA observations (Table 4.1) were aggregated into three boxes, one in the southern hemisphere and two in the northern (Montzka *et al.*, 2011). These were used to produce a global average concentration for use in equation 4.3. The AGAGE network contains fewer $CH_3CCl_3$ sites, so these were directly averaged to give an estimated global concentration (Rigby *et al.*, 2013). Global observations were smoothed across a 12-month period.

Two sets of $CH_3CCl_3$ emissions were used in equation 4.3. The first, taken from Montzka *et al.* (2011), provides annual emissions up until 2000 after which 20% decay/yr is assumed. These emission estimates were originally taken from global and regional industry data and measurements of polluted air in industrial regions (Prinn *et al.*, 2005). The second, taken from Rigby *et al.* (2013), provides annual emissions from 1997 to 2009 and is an updated version of those used by Prinn *et al.* (2005) based on United Nations Environment Programme (UNEP) consumption estimates. Both emission datasets were assumed to have no seasonal variability and were equally divided into monthly time steps. A comparison of [OH] anomalies derived from the one-box model with previous studies is made in section 4.5.2

For $CH_4$ emission estimates, equation 4.3 is used with both annually repeating and derived [OH] anomalies, the same two temperature fields as described above and surface NOAA observations. To calculate the global average $CH_4$ concentrations, data from the 19 surface sites were interpolated across 180 latitude bins, which were then weighted by surface area. As with $CH_3CCl_3$, OH is the major sink of $CH_4$ in the atmosphere. By estimating or assuming constant emissions of $CH_4$ (553 Tg/yr) and using concentration measurements, a required [OH] anomaly can be calculated using equation 4.3.

## 4.4 TOMCAT Model Set-up

Simulations of $CH_4$ and $CH_3CCl_3$ were performed using TOMCAT between 1993 and 2009. The model was spun-up from 1980 using initialisation fields taken from Patra *et al.* (2011). The global concentrations on January 1st 1993 were scaled so that the global average concentration equalled that of the $CH_4$ and $CH_3CCl_3$ concentrations derived from NOAA surface observations.

TOMCAT simulations were performed using 3 different meteorological fields, 1 with varying winds and temperature (simulations labelled *VTVW), 1 with varying winds and fixed temperature (*FTVW) and 1 with fixed winds and temperature (*FTFW) (Table 4.2). Fixed wind runs used repeating 1996 winds. Fixed temperature runs used a 2-D (latitude-height) zonal mean temperature from 1993 to 2009. Each TOMCAT run included 5 tracers for both $CH_4$ and $CH_3CCl_3$, which used a different [OH] field (labelled RE*, AP*, AL*, NP* and NL*). These [OH] fields are described further in Section 4.4.2. The model resolution and forcing data are described in Chapter 3. 12-hourly output has been used for surface $CH_4$ and $CH_3CCl_3$ comparisons.

| Run | [OH] Time Variation | Meteorology[b] | |
|---|---|---|---|
| | | Winds | Temperature |
| RE_FTFW | Repeating[a] | Fixed | Fixed |
| RE_FTVW | Repeating[a] | Varying | Fixed |
| RE_VTVW | Repeating[a] | Varying | Varying |
| AP_FTFW | AGAGE (Rigby et al., 2013) | Fixed | Fixed |
| AP_FTVW | AGAGE (Rigby et al., 2013) | Varying | Fixed |
| AP_VTVW | AGAGE (Rigby et al., 2013) | Varying | Varying |
| AL_FTFW | AGAGE (one-box model) | Fixed | Fixed |
| AL_FTVW | AGAGE (one-box model) | Varying | Fixed |
| AL_VTVW | AGAGE (one-box model) | Varying | Varying |
| NP_FTFW | NOAA (Montzka et al., 2011) | Fixed | Fixed |
| NP_FTVW | NOAA (Monztka et al., 2011) | Varying | Fixed |
| NP_VTVW | NOAA (Montzka et al., 2011) | Varying | Varying |
| NL_FTFW | NOAA (one-box model) | Fixed | Fixed |
| NL_FTVW | NOAA (one-box model) | Varying | Fixed |
| NL_VTVW | NOAA (one-box model) | Varying | Varying |

*Table 4.2 Summary of the $CH_4$ and $CH_3CCl_3$ tracers in the TOMCAT 3-D CTM simulations. (a) Annually repeating OH taken from Patra et al. (2011). (b) Varying winds and temperatures are from ERA-Interim. Fixed winds using repeating ERA-Interim winds from 1996. Fixed temperatures use zonal mean ERA-Interim temperatures averaged over 1993-2009.*

## 4.4.1 $CH_4$ Emission Inventories

The TOMCAT simulations in this chapter are intended to investigate the atmospheric loss contribution to recent $CH_4$ trends and not the influence of variation in emissions. Repeated yearly $CH_4$ emissions are therefore used, which are scaled to IPCC estimates outlined in Chapter 2 (553 Tg/yr). Annually-repeating anthropogenic emissions, excluding biomass burning, were calculated from averaging the EDGAR v3.2 (2001) inventory from 1993 to 2009. Biomass burning emissions were averaged from the Global Fire Emissions Database (GFED) v3.1 inventory, which extends from 1997 to 2009 (van der Werf *et al.*, 2010). JULES was used to calculate interannual variations in wetland emissions between 1993 and 2009 (see Chapter 5), which was then used to produce a scaled mean annual cycle. Annually-repeating rice (Yan et al., 2009), hydrate, mud volcano, termite, wild animal and ocean (Matthews and Fung, 1987) emissions were taken from the TransCom $CH_4$ study (Patra et al., 2011). All emissions are input into TOMCAT at a 1° by 1° resolution and are then averaged onto the larger model grid (2.8° by 2.8°).

To evaluate the performance of annual [OH] anomalies, described in section 4.4.2, equivalent $CH_3CCl_3$ tracers were included which used the same configuration as the $CH_4$ tracers (Table 4.2). These can then be compared to the observations described in section 4.2. Although this method appears somewhat cyclic, the overall aim is to assess whether a global annual OH anomaly that is derived from $CH_3CCl_3$ observations can be applied to a CTM to replicate the spatial and temporal distribution of $CH_3CCl_3$ observations. The $CH_3CCl_3$ emissions used in TOMCAT between 1988 and 1998 are taken from EDGAR v3.2 and linearly adjusted using methods described by McCulloch and Midgley (2001). From 1999 onwards emissions are taken from Patra *et al.* (2011), which assumes a 20% exponential decay after 2002.

## 4.4.2 Hydroxyl and Other Loss Fields

A simplified description of atmospheric chemistry is used in the TOMCAT simulations discussed here, and is based on specified loss fields. Losses of $CH_4$ and $CH_3CCl_3$, through reactions with OH, are calculated using prescribed [OH] values and the rate constant derived from equations 4.1 and 4.2. This loss is then directly applied to the concentration of both species within the grid cell as given by equation 4.4, where L is loss in molecules $s^{-1}$. Five different prescribed global latitude-height [OH] fields are used (RE*, AP*, AL*, NP* and NL*), all originally based on the annually repeating OH used in Patra *et al.* (2011). This was a development of a previous field derived from a combination of semi-empirically calculated tropospheric distributions (Spivakosvky *et al.*, 2000; Huijnen *et al.*, 2010).

$$L = k[OH][X] \quad \textbf{(4.4)}$$

The first [OH] field, RE, is for a control tracer that uses the annually repeating OH field from Patra *et al.* (2011). Any interannual anomalies in the $CH_4$ or $CH_3CCl_3$ concentrations in these simulations cannot be due to changes in [OH]. The second field, AP, uses published AGAGE annual global OH anomalies from Rigby *et al.* (2013), which are applied to RE between 1997 and 2009. These anomalies were derived from UNEP emission estimates and observations of $CH_3CCl_3$ from the 5 AGAGE sites using a 12-box model. The third field, AL, uses the same $CH_3CCl_3$ observations and emission estimates, but with the one-box model described in section 4.3 to produce monthly global anomalies. These were then averaged into global anomalies, which were applied to RE between 1997 and 2009. The fourth field, NP, uses published NOAA annual global [OH] anomalies from Montzka *et al.* (2011), which are applied to RE between 1997 and 2007. These were derived using slightly older emission estimates, which estimate a 20% exponential decay after 2000, observations of $CH_3CCl_3$ from 7 NOAA sites and a simple one-box model, similar to the one used here (Rigby *et al.*, 2008; Montzka *et al*., 2011). The fifth field, NL, repeats the method used for AL except using NOAA observations between 1997 and 2007. Both AL- and NL- derived [OH] anomalies using varying temperatures in the one-box model. For consistency between the model experiments, all yearly anomalies were scaled so that the mean [OH] between 1997 and 2007 (the overlap period where NOAA and AGAGE anomalies are both available) equalled the RE [OH] value.

Two other $CH_4$ loss fields are annually repeating with seasonal cycles and the same for all 15 model simulations. $CH_4$ loss through reactions with Cl and $O(^1D)$ radicals in the stratosphere are based on the Cambridge 2-D model (Velders, 1995), previously used by Patra *et al.* (2011). The surface soil sink, previously described in Chapter 2, is applied as a negative surface flux in TOMCAT. The soil sink field provided by Patra *et al.* (2011), was originally derived using an atmospheric $CH_4$ inversion model (Bousquet *et al.*, 2006). Interannual variability in the Cl, $O(^1D)$ and soil sinks are not accounted for in this study.

## 4.5 TOMCAT-Observation Comparisons

### 4.5.1 Correlation of Observed $CH_4$ with OH and temperature

The loss rate of $CH_4$ by reaction with OH is temperature dependent (equation 4.1) and so changes in atmospheric temperature can affect $CH_4$ concentrations. Figure 4.3 shows the zonally averaged

ERA-Interim temperature between 30°N and 30°S at 700 hPa for 1993-2011. This pressure level and latitude range was selected to represent mean conditions of the atmospheric region where most $CH_4$ removal occurs, based on analysis of TOMCAT runs. The temperature fluctuations in 1997/1998 and 2010 can be explained by El Niño Southern Oscillation (ENSO) events. For $CH_4$ it is important to consider that ENSO events affect not only atmospheric removal, but also sources via variations in wetland and biomass burning emissions through changes in temperature and precipitation (Hodson *et al.*, 2011). These variations will not be captured in the TOMCAT simulations which use annually repeating emissions. In relation to the $CH_4$ stagnation period, between 2001 and 2006 the temperature is an average of 0.3 K warmer than the temperature between 1993 and 1997, and 0.1 K warmer than the average temperature between 2007 and 2011.

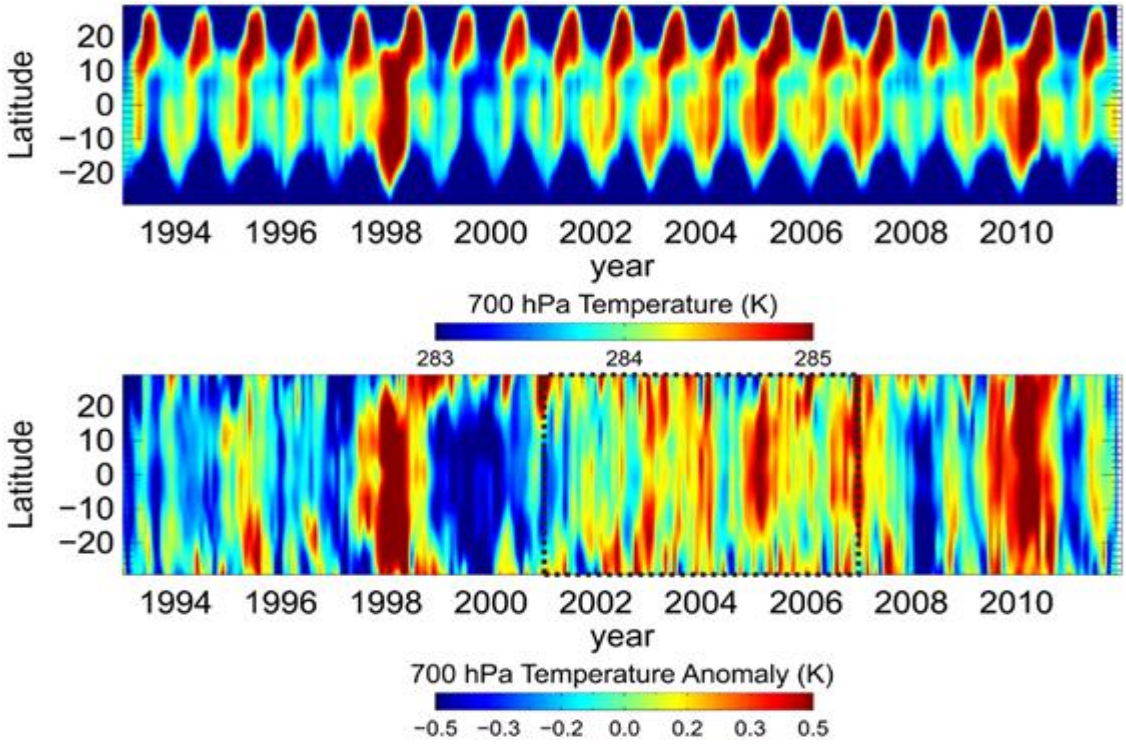


*Figure 4.3 (Top) Latitude-time plot of zonal mean temperature (K) between 30°N and 30°S at 700 hPa from ERA-Interim reanalyses between 1993 and 2011. This altitude and latitude region is the location of the largest $CH_4$ loss in the 3-D model. (Bottom) Temperature anomalies (K) for the same time and region as top panel. The dashed box indicates the anomalously warm period of 2001-2006.*

Figure 4.4 shows a comparisons of the global $CH_4$ growth rate and the average temperature in the main loss region (loss-weighted mean over all TOMCAT grid boxes). Over the entire time series temperature shows only a slight negative correlation with $CH_4$ growth rate, with Pearson's correlation coefficient (R) values of -0.24 for NOAA -0.07 for AGAGE. This is likely, in part, due to changes in wetland and biomass burning emissions in ENSO years balancing out the change in atmospheric loss. The sensitivity of the $CH_4$ loss rate due to the temperature variation

of the $CH_4$ + OH reaction can be estimated from equation 4.5, which assumes [OH] is independent of temperature. This relationship, shown in Figure 4.4, shows a variation in *k* of about 2%/K feeds through into similar relative changes in the $CH_4$ loss rate. The 0.3 K observed temperature increase during the stagnation period has an equivalent of a 3.9 Tg/yr emissions decrease, equating to a 0.72 ppb/yr decrease in growth. The effect of temperature is already accounted for in the derivation of the OH anomaly based on atmospheric data, therefore the main analysis of these results focuses on simulations with fixed temperatures (*_FTVW).

$$\frac{dL}{dT} = \frac{d}{dT}k[OH]CH_4 = [OH]CH_4\frac{1775}{T^2}7.73 \times 10^{-5}e^{-1775/T} \qquad \textbf{(4.5)}$$

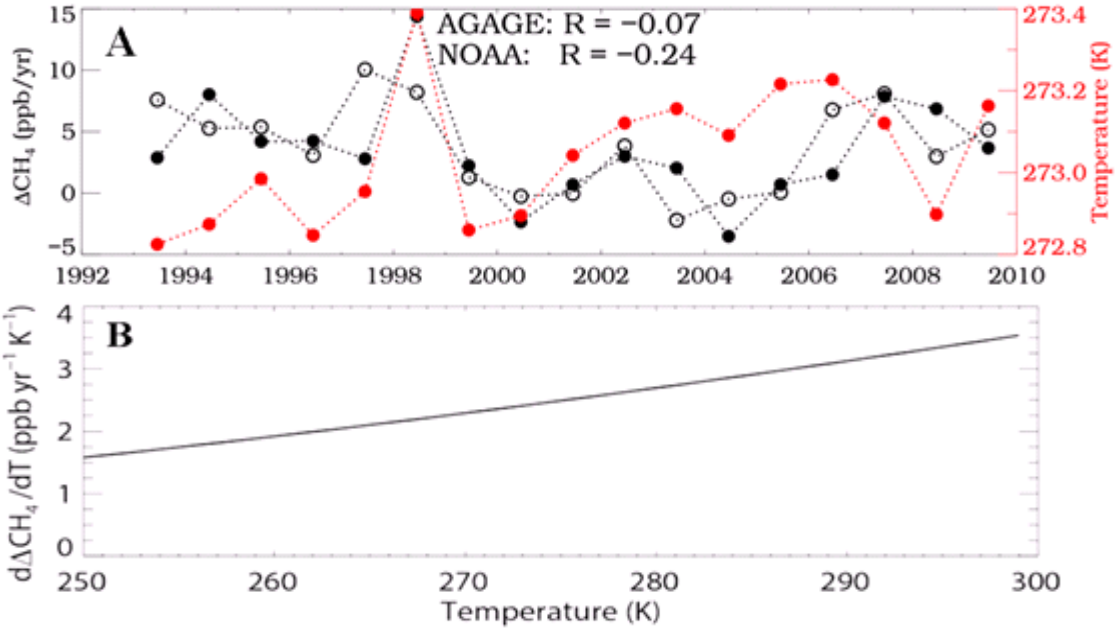


*Figure 4.4 (a) Annual global $CH_4$ growth rate (ppb/yr) derived from NOAA (filled black circles) and AGAGE (open black circles) data (left hand y-axis), and annual mean temperature (K) weighted by $CH_4$ loss rate in TOMCAT (red circles) (right hand y-axis). (b) Relative growth rate change with respect to temperature for representative OH ($0.99\times10^6$ molecules $cm^{-3}$) and $CH_4$ (1770 ppb) values.*

Figure 4.5 shows the published NOAA-derived and AGAGE-derived global [OH] anomalies along with the annual $CH_4$ growth rate estimated from the NOAA and AGAGE measurements. The two [OH] series show the similar behaviour of negative anomalies around 1997 and 2006/7, and an extended period of more positive anomalies in between. For the time periods covered by the NOAA (1997-2007) and AGAGE (1997-2009) $CH_3CCl_3$ observations, the two derived [OH] time series show negative correlations with the $CH_4$ growth from NOAA (R = -0.32) and AGAGE (R = -0.64). Only the AGAGE [OH] correlation, from the longer time series, is statistically significant at the 90% level.

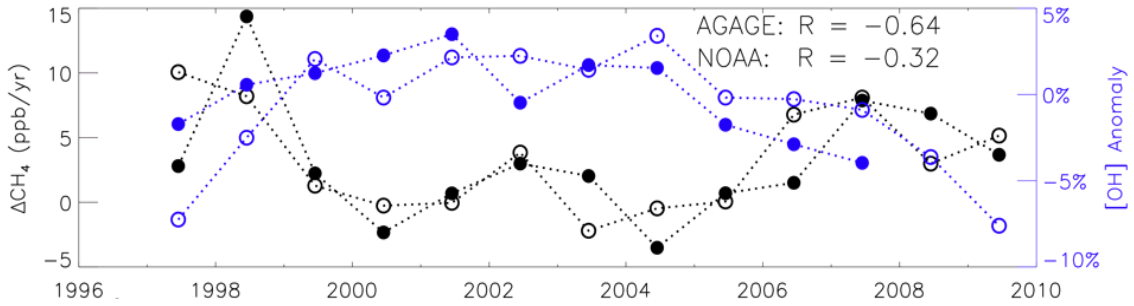


*Figure 4.5 Annual global $CH_4$ growth rate (ppb/yr) derived from NOAA (filled black circles) and AGAGE (open black circles) data (left hand y-axis), and published annual global [OH] anomalies derived from NOAA (filled blue circles, 1997-2007) and AGAGE (open blue circles, 1997-2009) $CH_3CCl_3$ measurements (right hand y-axis).*

## 4.5.2 $CH_3CCl_3$ and Hydroxyl Comparisons

The global one-box model was used to estimate the [OH] variations required to fit the observed global $CH_4$ growth rate variations, assuming constant emissions and temperature. This allows a simple assessment of the potential for variations in [OH] to affect the $CH_4$ growth rate. Figure 4.6 shows the model output compared to the published derived OH concentrations from NOAA and AGAGE $CH_3CCl_3$ observations. The derived concentration percentage anomalies have been converted to global mean concentrations using the one-box model average concentration. The results are consistent with a previous study which performed a similar analysis of the NOAA $CH_4$ data (Montzka *et al*., 2011). The required OH change rarely exceeds the $CH_3CCl_3$-derived interannual variability range (±2.3%) presented by Montzka *et al.* (2011). Moreover, the relative interannual variations in [OH] required to fit the $CH_4$ observations match the $CH_3CCl_3$-derived [OH] variations in many years, for example from 1998-2002 (see Montzka et al., 2011). Some of the derived variations in [OH] exceed that required to match the $CH_4$ growth, with larger negative anomalies in the early and later years and some slightly larger positive anomalies in between.

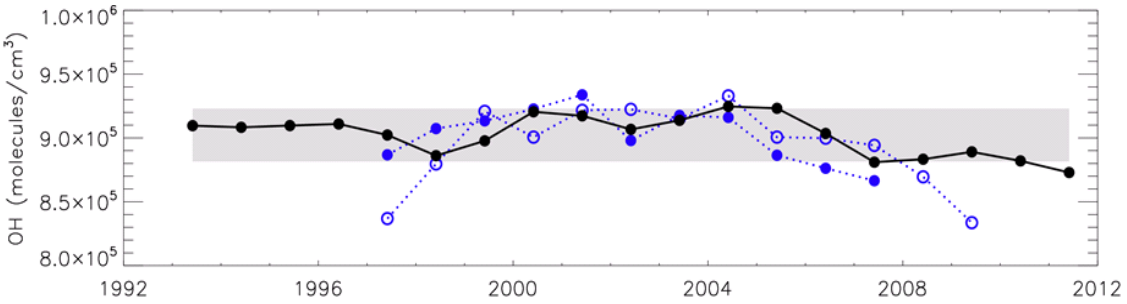


*Figure 4.6 Annual mean [OH] (molecules $cm^{-3}$) required for global box model to fit variations in NOAA $CH_4$ observations assuming constant emissions and temperature, based on Montzka et al. (2011) (solid black line). Shaded region denotes [OH] deviation of ±2.3% from the mean. Also shown are the NOAA- (filled) and AGAGE- (open) derived [OH] anomalies applied to an assumed mean OH taken from the box model (blue circles).*

The one-box model was used to derive [OH] based on $CH_3CCl_3$ observations from NOAA (NL) and AGAGE (AL). These are based on two emission scenarios and varying or repeating temperature. UNEP emission estimates and estimates derived from an assumed 20% exponential decay in emissions since 2002 are both used. These are then compared with the published NOAA and AGAGE anomalies (Montzka *et al.*, 2011; Rigby *et al.*, 2013). The results (see Figure 4.7) demonstrate the small impact of using different observations and emission assumptions. In later years the choice of observations has a bigger impact than the choice of emissions on the derived [OH]. For AGAGE-derived values, the one-box model estimates agree well with the published values of Rigby *et al*. (2013) despite the simplicity of the one-box model compared to their more sophisticated 12-box model. In contrast, the one-box model shows poor agreement with the NOAA-derived [OH] variability published by Montzka *et al*. (2011), despite both studies using box models. In particular, around 2002-2003 the one-box model used here overestimates the positive anomaly in [OH]. The one-box model estimates a much more negative OH anomaly in 1997 compared to Montzka *et al*. (2011). This suggests a large uncertainty in the inferred low 1997 OH value, when emissions of $CH_3CCl_3$ were decreasing rapidly, although reasons why atmospheric [OH] might have been low were discussed by Prinn *et al.* (2005). The treatment of emissions and the method by which the observations and emissions are smoothed results in the observed difference in anomalies. Figure 4.7 also demonstrates the influence of temperature changes on the loss anomaly is negligible.

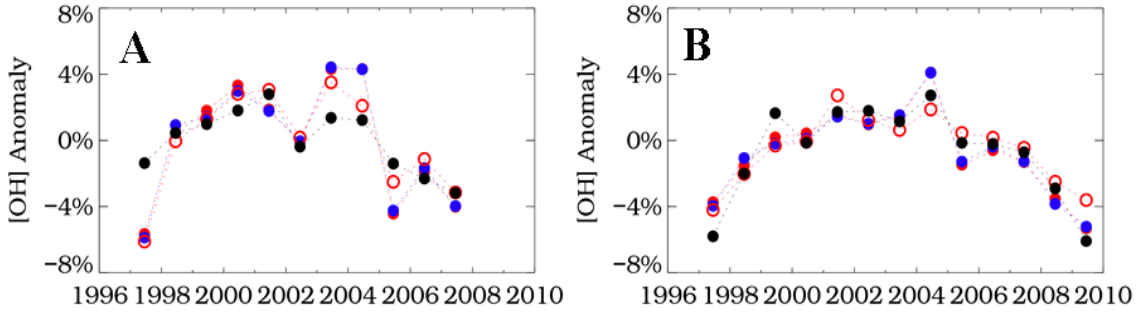


*Figure 4.7 Estimates of OH derived from (a) NOAA and (b) AGAGE $CH_3CCl_3$ observations calculated using an one-box model using repeating (blue) and varying (red) annual mean temperature. $CH_3CCl_3$ emission scenarios are taken from UNEP (2015) (filled circles) and Montzka et al. (2011) (open circles) based on (Prinn et al. 2005). Also shown are (a) published NOAA-derived values (Montzka et al., 2011) and (b) AGAGE-derived values (Rigby et al., 2013) (black).*

The TOMCAT simulations have been compared to global $CH_3CCl_3$ observations from both NOAA and AGAGE networks. If the model reproduces the observed magnitude and variability of $CH_3CCl_3$ decay accurately then this gives confidence in the approach of using a global [OH] field, scaled by derived anomalies. Figure 4.8 shows that the model, with the imposed [OH] field,

simulates the global decay of $CH_3CCl_3$ better than the model using a repeating [OH] field. This supports the use of an 'offline' [OH] field in favour of a coupled 'online' [OH] field. 'Online' fields calculated with an interactive tropospheric chemistry scheme can, in principle, capture interannual variability. However, they show a large uncertainty in the absolute global [OH], which then influences the lifetimes of gases such as $CH_3CCl_3$. For example, Voulgarakis *et al.*, (2013) analysed the global mean [OH] predicted by various models and found a range of $0.55 \times 10^6$ to $1.34 \times 10^6$ molecules $cm^{-3}$.

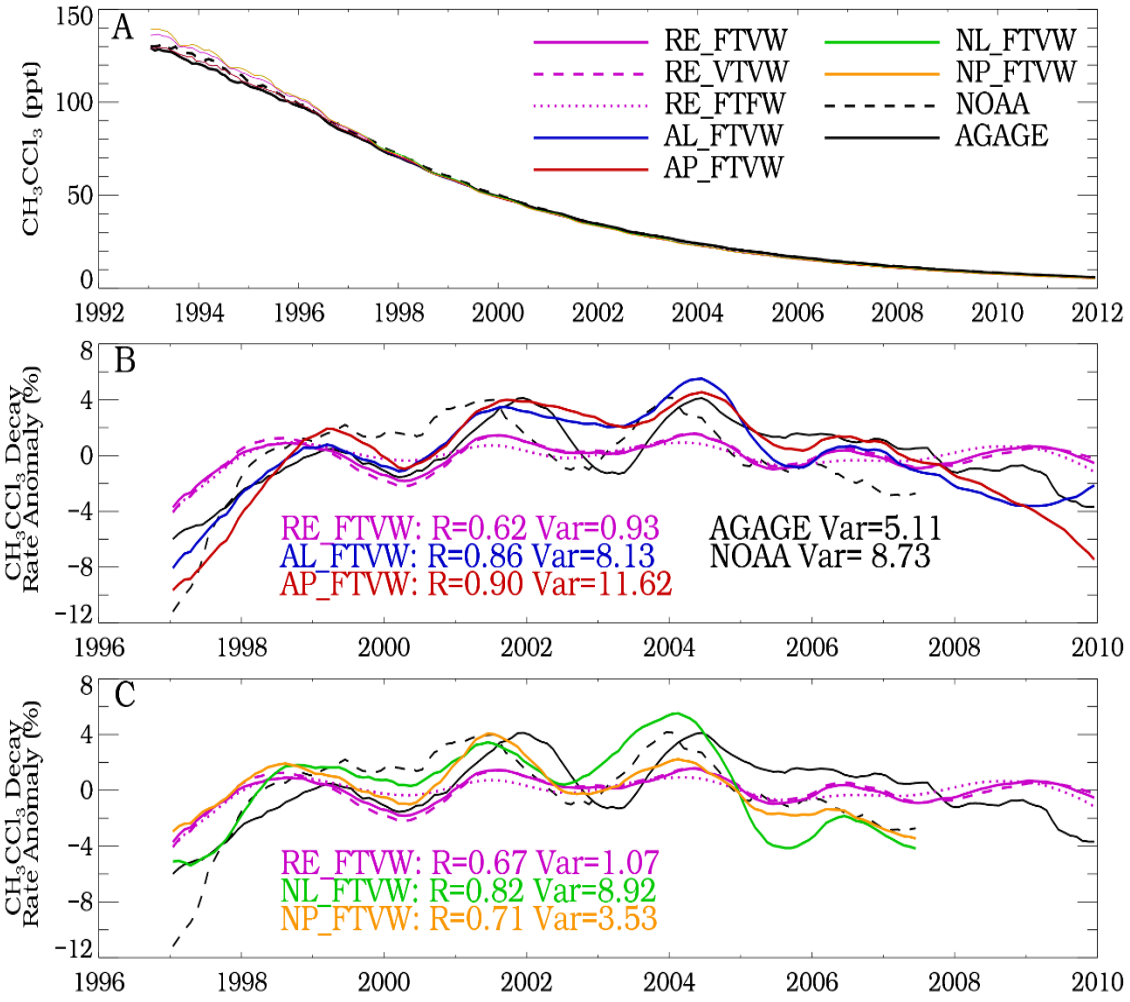


*Figure 4.8 (a) Global mean surface $CH_3CCl_3$ (ppt) from NOAA (black dashed) and AGAGE (black solid) observations from 1993 to 2012. Also shown are results from seven TOMCAT simulations (see Table 4.2). (b) Global surface CH3CCl3 decay rate anomalies from NOAA and AGAGE along with model runs RE_FTFW, RE_VTVW, RE_FTVW, AL_FTVW and AP_FTVW (solid lines). Results from runs RE_FTFW and RE_VTVW are shown as equivalent dotted lines and dashed lines, respectively. Observation and model anomalies are smoothed with a 12-month running average. Values given represent correlation coefficient when compared to AGAGE observations and variance. (c) As panel (b) but for model runs RE_FTFW, RE_VTVW, RE_FTVW, NL_FTVW and NP_FTVW with correlation coefficients for comparison with NOAA observations.*

Figure 4.8a shows that the global mean $CH_3CCl_3$ from the NOAA and AGAGE networks differ by ~2.5 ppt around 1993-1996, since then the difference has become smaller both in absolute and relative terms. The observed and modelled $CH_3CCl_3$ decay rates show a faster decay (more positive anomaly) in the middle period, with slower decay at the start and end (see Figures 4.8b and 4.8c). The comparisons show a phase difference of 3 months between the two observation networks, previously noted by Holmes *et al.* (2013). The reason for this is unknown, although when the model is sampled at the site locations the lag is not observed, which suggests it is not an issue with the spatial distribution of NOAA and AGAGE sites. The model runs with varying winds generally capture these periodic variations with correlation coefficients ranging from 0.60 – 0.86. The correlation coefficients for the runs using varying [OH] are all higher than the runs using repeating OH (RE_FTVW = 0.62 – 0.67, AL_FTVW = 0.86, AP_FTVW = 0.90, NL_FTVW = 0.82, NP_FTVW = 0.71). As previously noted by Montzka *et al.* (2011), there are only small differences between the simulations which use varying temperature (*FTVW) and the corresponding runs which use fixed temperature (*VTVW). This shows that the largest contribution from the $CH_3CCl_3$ decay rate anomaly comes from variations in atmospheric [OH], rather than atmospheric temperature. The simulations with repeating winds show less variability in the $CH_3CCl_3$ decay rate, particularly in the period 1999-2004.

The $CH_3CCl_3$-derived [OH] fields used a global annual decay anomaly. This means that anomalies derived might no longer represent the observed monthly anomalies at individual sites, suggesting the approach might be too simple. To test this the simulations are compared with $CH_3CCl_3$ observations at individual sites in Figure 4.9. The results show comparisons from four selected stations, two from the NOAA network and two from the AGAGE network. The agreement at individual sites is improved by the inclusion of interannually varying [OH] fields. Although varying [OH] fields derived from $CH_3CCl_3$ decay anomalies provide a better agreement than the repeat OH fields, they still fail to capture some of the anomaly events observed at certain sites. For example, the AGAGE site at Cape Grim observed a large negative anomaly in 2008, this is not replicated in any of the TOMCAT simulations.

In summary, results from $CH_3CCl_3$ comparisons show that the global [OH] fields that are derived from $CH_3CCl_3$ decay anomalies perform well applied to TOMCAT, both globally and at individual sites. Although, the interannual variability in global mean [OH] has been derived from these $CH_3CCl_3$ observations, the results show that the reconstructed model [OH] fields perform well in simulating $CH_3CCl_3$ within TOMCAT. These results suggest that the [OH] fields used here are suitable for testing the impact of [OH] variability on the $CH_4$ growth rate, as discussed in the following section.

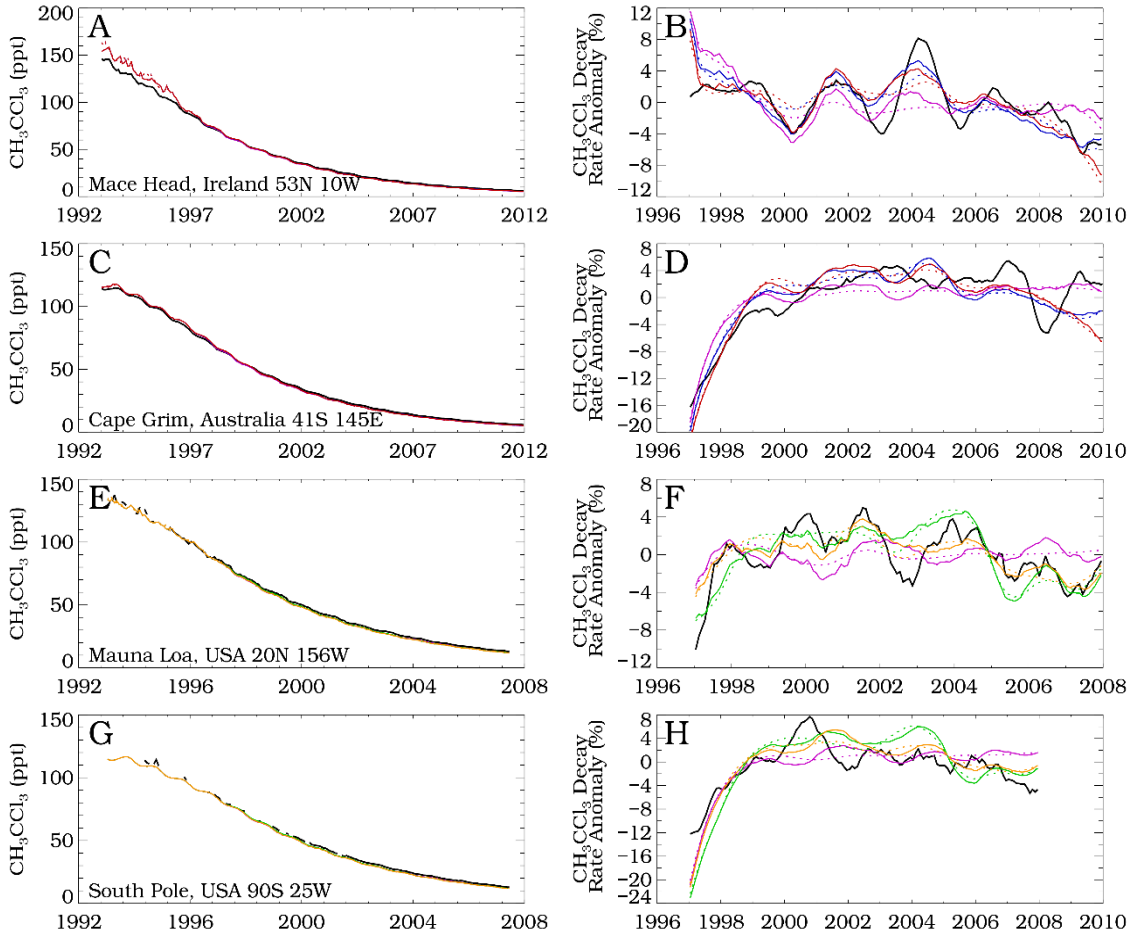


*Figure 4.9 (Left) Observed mean surface $CH_3CCl_3$ (ppt) (black line) from (a) Mace Head (AGAGE), (c) Cape Grim (AGAGE), (e) Mauna Loa (NOAA) and (g) South Pole. Also shown are results from TOMCAT simulations, using the same colour scheme as Figure 4.8. (Right) Surface $CH_3CCl_3$ decay rate anomalies at the same sites as the corresponding left column plot for observations (black), TOMCAT simulations with varying winds and fixed temperatures (solid coloured lines), varying winds and temperatures (dashed coloured lines) and fixed winds and temperatures (dotted coloured lines), using the same colour scheme as Figure 4.8. Note that observations at NOAA (AGAGE) sites show only comparisons with runs using NOAA (AGAGE)-derived OH, along with repeating OH.*

## 4.5.3 $CH_4$ Comparisons

The one-box model described in Section 4.3 has been used to estimate global $CH_4$ emissions using various temperature and OH conditions. The simple one-box model shows reasonable comparison with $CH_4$ observations on an inter-decadal timescale, when assuming constant emissions, temperature and loss (see Figure 4.10a). The model was initialised with the de-seasonalised January 1993 global mean $CH_4$ value from the NOAA sampling sites (1730 ppb; for comparison the AGAGE mean was 1728 ppb). The integrations used a temperature (272.9 K) based on the mean ERA-Interim data and a constant mean [OH] of $0.99\times10^6$ molecules $cm^{-3}$. The model results show a good fit with NOAA and AGAGE observations (R = 0.96 for both and root mean square

error (RMSE) = 6.8 and 5.6 ppb, respectively). This shows that in the absence of any changes in sources or sinks, $CH_4$ is tending towards a steady-state with zero growth rate at a value of 1806 ppb. Indeed, Dlugokencky *et al.*, (2003) suggested that $CH_4$ was approaching a steady state through 2002. The additional years of data in Figure 4.10a show significant perturbations to the balance of sources and sinks since that time. Either, there was an abrupt change to the $CH_4$ steady state at the end of the stagnation period around 2006, or $CH_4$ continued to approach a steady-state through 2012 with periods of deviation from that curve around 1999 and 2006. The shaded region in Figure 4.10a shows the effect of a constant ±2.3% change in [OH], indicative of the mean 1998-2007 interannual variability (Montzka *et al.*, 2011). This illustrates the large leverage that relatively small variations in global mean [OH], which are difficult to diagnose with $CH_3CCl_3$, have on $CH_4$ growth rates.

The one-box model has been used to estimate the annual $CH_4$ emissions required to match the observed concentrations based on several atmospheric conditions shown in Figures 4.10b and 4.10c. For the calculation that uses a mean temperature (272.9 K) and a mean [OH] ($0.99\times10^6$ molecules $cm^{-3}$) the required emissions during the stagnation period are 546.2 Tg/yr, 5.5 Tg/yr less than the 1993-1997 mean of 551.7 Tg/yr. The simulation with varying temperature and mean [OH] requires average emissions of 548.4 Tg/yr during the stagnation period, this is 2.2 Tg/yr larger than the simulation with mean temperature and [OH]. The stagnation period shows a 4.1 Tg/yr decrease from 552.5 Tg/yr before the stagnation. For the same stagnation period, using the mean the temperature and varying [OH] requires average annual emissions of 549.7 – 553.8 Tg/yr. This corresponds to a change in emissions of -22.0 - +5.0 Tg/yr when compared to the 1997-1998 averages. After 2006 emissions do not always need to increase to capture the observed increase in growth rate (see Table 4.3). The simple one-box model therefore suggests that [OH] variations alone can account for some of the observed decrease in $CH_4$ growth.

| [OH] | Temperature | Mean Required Annual Emissions (Tg/yr) | | |
|---|---|---|---|---|
| | | 1993-1998* | 1999-2006 | 2007-2011* |
| RE | Varying | 552.5 | 548.4 | 567.7 |
| RE | Fixed | 551.7 | 546.2 | 565.6 |
| AP | Fixed | 531.5 | 553.5 | 541.6 |
| AL | Fixed | 540.9 | 551.6 | 540.2 |
| NP | Fixed | 554.7 | 549.7 | 544.2 |
| NL | Fixed | 541.2 | 553.8 | 538.7 |

*Table 4.3 Required $CH_4$ emissions to fit observations derived using a simple one-box model between 1993 and 1998, 1999 and 2006, and 2007 and 2012 based on various atmospheric conditions detailed in Table 4.2. *Where [OH] data are available.*

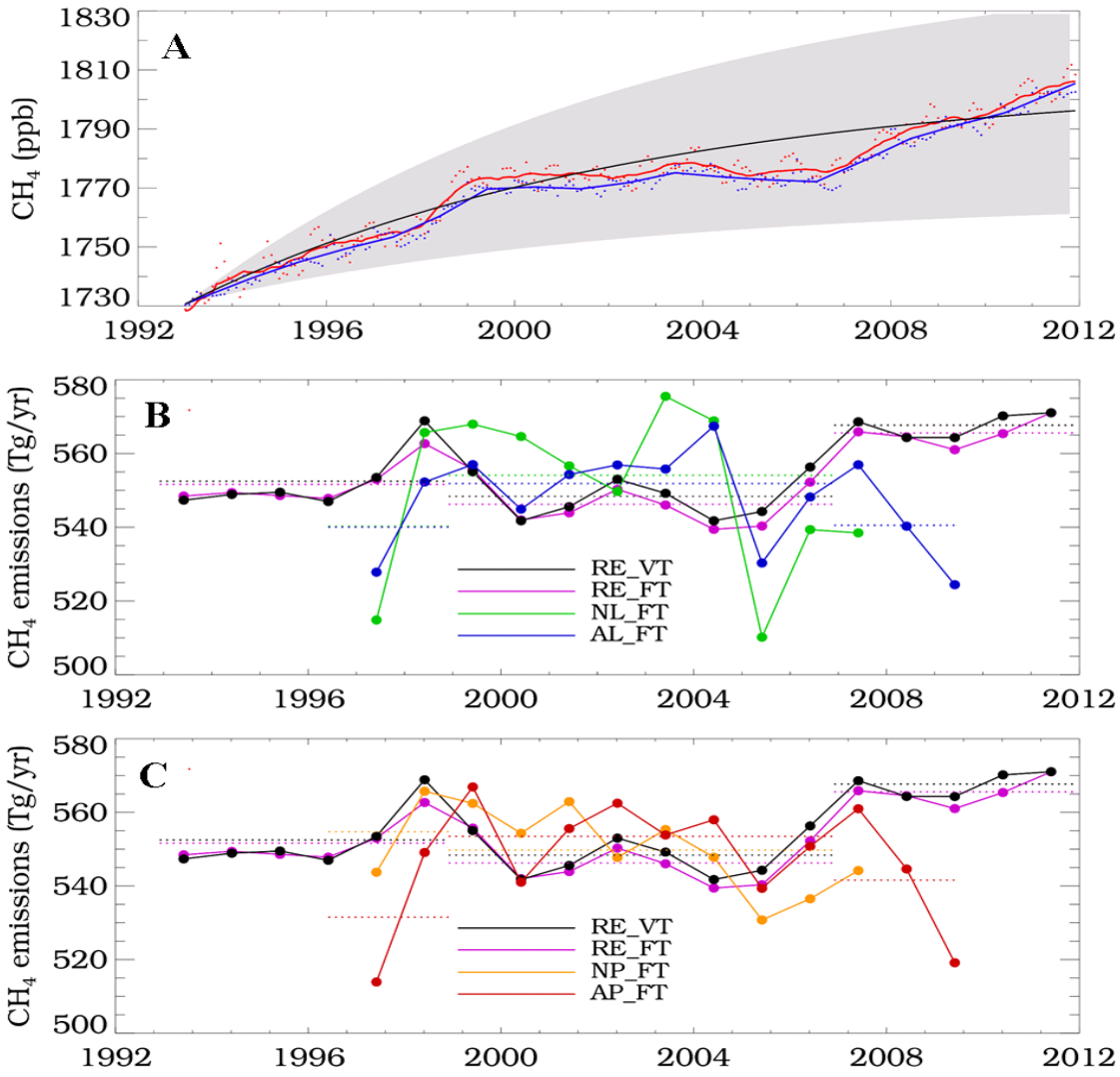


*Figure 4.10 (a) $CH_4$ mixing ratio calculated by a global box model (mean emissions E=553 Tg/yr, temperature T=272.9 K and [OH] = $0.99\times10^6$ molecules $cm^{-3}$) initialised in 1993 with global average $CH_4$ observations between 1993 and 2011 (black line). The shaded region illustrates the range of calculated $CH_4$ for mean [OH] variations of ±2.3%. Monthly global average $CH_4$ observations for the NOAA (blue circles) and AGAGE (red circles) networks, with lines showing 12-month smoothing. (b) Derived annual $CH_4$ emissions (Tg/yr) required for global box model to fit yearly variations in NOAA $CH_4$ observations for annually varying temperature and repeating [OH] (black), annually repeating temperature for repeating [OH] (pink), varying [OH] based on NOAA $CH_3CCl_3$ observations and the one-box model (green), and varying [OH] based on AGAGE $CH_3CCl_3$ observations and the one-box model (blue) between 1993 and 2012 where data are available. (c) Same as (b) except using published [OH] anomaly data from Montzka et al. (2011) (orange) and Rigby et al. (2013) (red) between 1993 and 2012 where data are available. Note the dashed lines on (b) and (c) indicate the average emissions required before (1993-1998), during (1999-2006) and after (2007-2011) the $CH_4$ stagnation period, where data are available.*

For a more detailed and realistic evaluation of the role of [OH] and transport on the growth rate of $CH_4$ the results of the TOMCAT model simulations have been compared with *in-situ*

observations. Figure 4.11 shows deseasonalised modelled surface $CH_4$ from TOMCAT simulations compared with observations from a high-latitude station (Alert), two tropical stations (Mauna Loa and Tutuila), a southern high-latitude station (South Pole) and the global average of NOAA and AGAGE stations. In 1993, at the end of the model spin-up, the simulations capture the global mean $CH_4$ level well, along with the observed values at a range of latitudes. The exception is at high northern latitudes. However, these differences are not important when investigating the change in the global growth rate. The global change in atmospheric $CH_4$ in the simulations with varying winds for 1993 to the end of 2009 is between 75 and 104 ppb, compared to 56 and 66 ppb in the observations.

Model run RE_FTFW does not include interannual variations in atmospheric transport or $CH_4$ loss. Therefore, the modelled $CH_4$ gradually approaches a steady state value of ~1830 ppb (see Figure 4.11f). The rate of $CH_4$ growth decreases from 7.9 ppb/yr (1993-1998) to 1.4 ppb/yr (2007-2009). Compared to run RE_FTFW, the other simulations introduce variability on this $CH_4$ evolution.

Run RE_FTVW includes interannual variability in wind fields which alter the transport of $CH_4$ from the source to the sink regions. The largest difference between RE_FTFW and RE_FTVW occurs after 2000 (see Figure 4.11f). During the stagnation period run RE_FTVW has a smaller growth rate of 3.5 ppb/yr compared to 4.1 ppb/yr in run RE_FTFW, showing that variations in atmospheric transport made a small contribution to the slowdown in global mean $CH_4$ growth.

Compared to run RE_FTVW, runs AP_FTVW, AL_FTVW, NP_FTVW and NL_FTVW include $CH_3CCl_3$-derived interannual variations in [OH] which introduce large changes in modelled $CH_4$, which are more in line with the observations (see Figure 4.11e). These runs produce turnarounds in the $CH_4$ growth in 2001/2 (becomes negative) and 2005/6 (returns to being positive). For AGAGE-derived [OH] (runs AP_FTVW, AL_FTVW) the large negative anomaly in OH in 1997 produces a significant increase in $CH_4$ prior to the turnaround in 2001.

Table 4.4 summarises the change in global mean $CH_4$ over different time periods defined by the key dates in the observed record, before during and after the growth stagnation. Comparison of Figure 4.11 and Table 4.4 shows, however, that the timing of the largest modelled change in growth rate do not necessarily coincide with those dates. That is understandable if other factors not considered here, e.g. emission changes, are contributing to the change in global $CH_4$ concentration. It does mean that the summary values in Table 4.4 do not capture the full impact of the changes in [OH] and winds within the stagnation period.

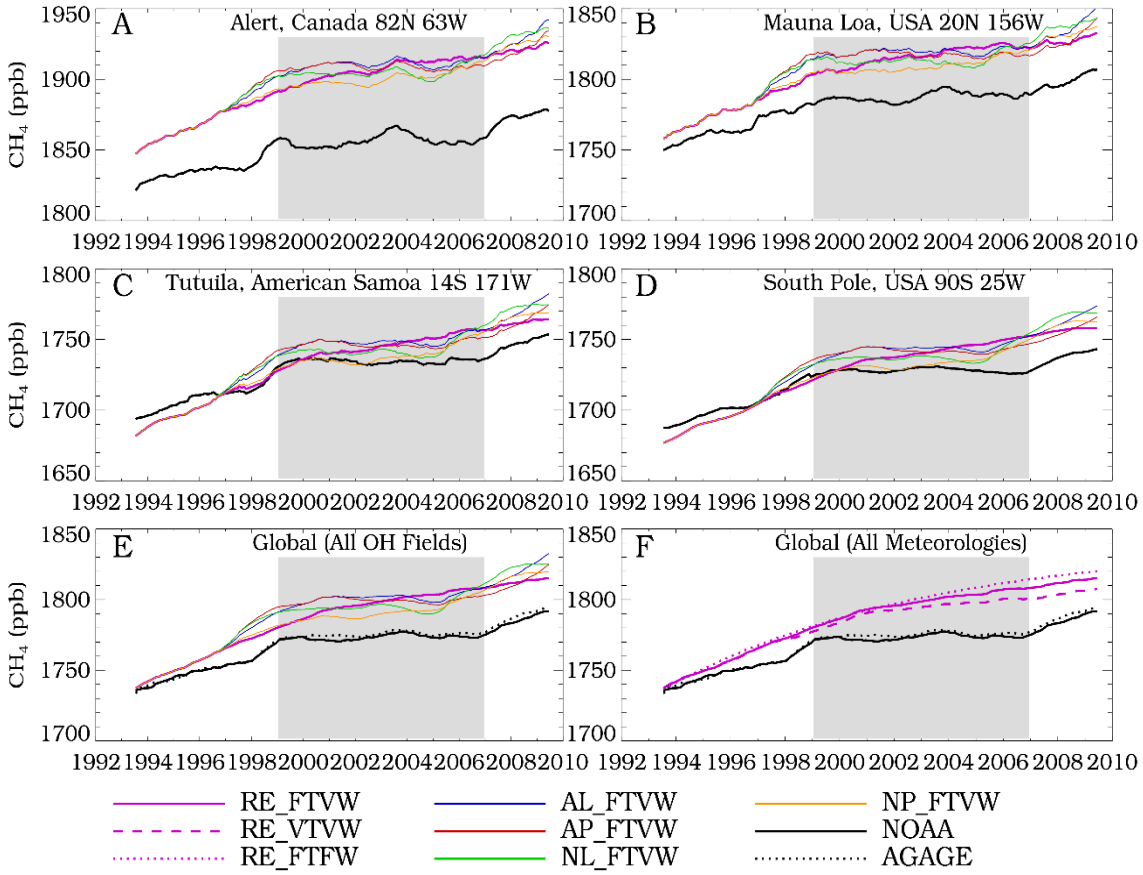


*Figure 4.11 Deseasonalised surface CH4 (ppb) from 4 NOAA sites (black solid line) between 1993 and 2009. Also shown are results from five TOMCAT 3-D CTM simulations with fixed temperatures and varying winds (See Table 4.2) (a-d). Deseasonalised global mean surface CH4 from NOAA (black solid) and AGAGE (black dashed) observations along with the five TOMCAT 3-D CTM simulations used in the previous panels (e). (f) Same as (e) but for TOMCAT simulations using repeating OH (RE) and different treatments of wind and temperature. All panels use observation and model values which are smoothed with a 12-month running average. The shaded region marks the stagnation period in the observed CH4 growth rate.*

| Model or observation | Global mean $\Delta CH_4$ in ppb (ppb/yr) | | | |
|---|---|---|---|---|
| | 1993-2009* | 1993-1998* | 1999-2006 | 2007-2009* |
| RE_FTFW | 85.0 (5.0) | 47.2 (7.9) | 32.9 (4.1) | 4.3 (1.4) |
| RE_FTVW | 82.2 (4.8) | 48.2 (8.0) | 27.8 (3.5) | 5.4 (1.8) |
| RE_VTVW | 74.6 (4.4) | 45.6 (7.6) | 23.1 (2.9) | 5.3 (1.8) |
| AP_FTVW | 97.7 (5.7) | 62.3 (10.4) | 8.2 (1.0) | 26.4 (8.8) |
| AL_FTVW | 104.2 (6.1) | 58.4 (9.7) | 17.3 (2.2) | 27.5 (9.2) |
| NP_FTVW | 86.2 (5.1) | 49.7 (8.3) | 24.8 (3.1) | 10.6 (3.8) |
| NL_FTVW | 91.4 (5.4) | 58.8 (9.8) | 20.1 (2.5) | 11.3 (3.8) |
| NOAA | 56.1 (3.3) | 36.0 (6.0) | 4.8 (0.6) | 14.7 (4.9) |
| AGAGE | 66.3 (3.9) | 42.6 (7.1) | 5.6 (0.7) | 17.4 (5.8) |

*Table 4.4 Calculated $CH_4$ changes over different time periods from selected TOMCAT experiments and, NOAA and AGAGE networks. *Where [OH] data are available.*

Table 4.4 shows that runs NP_FTVW and NL_FTVW (NOAA-derived [OH]) produce a small modelled $CH_4$ growth of 2.5-3.1 ppb/yr during the stagnation period 1999-2006, compared to 1.0 ppb/yr for run AP_FTVW (AGAGE-derived [OH]). The AGAGE results are slightly larger than the observed growth rate of 0.6-0.7 ppb/yr. Runs AL_FTVW, AP_FTVW, NL_FTVW and NP_FTVW capture the observed strong decrease in the $CH_4$ growth rate. Clearly, these runs demonstrate the significant potential for relatively small variations in mean [OH] to affect $CH_4$ growth. Excluding the stagnation period the mean modelled $CH_4$ lifetime in run NP_FTVW is 9.4 years, but this decreases slightly by 0.01 years during the stagnation period. For run AP_FTVW there is a decrease of 0.18 years from 9.6 years between the same intervals. The results from all the CTM simulations during 1999-2006 indicate that the accuracy of modelled $CH_4$ growth is improved by accounting for interannual variability in [OH] as derived from $CH_3CCl_3$ observations, and interannual variability in meteorology.

The variation of [OH] after 2007 cannot be determined from the available NOAA data so runs NP_FTVW and NL_FTVW used the mean [OH] field for all subsequent years. The modelled $CH_4$ increase of 3.8 ppb/yr underestimates the NOAA observations (4.9 ppb/yr). Should the lower [OH] of 2007 have persisted then the model would have produced a larger increase in $CH_4$, in better agreement with the observations. The AGAGE-derived [OH] for 2007-2009 (runs AP_FTVW and AL_FTVW) produces a larger $CH_4$ growth relative to the previous years (8.8 ppb/yr and 9.2 ppb/yr). Runs RE_FTFW (1.4 ppb/yr) and RE_FTVW (1.8 ppb/yr) both show a decreased rate of growth during the final 5 years, consistent with a system approaching steady state.

Figure 4.12 shows the global $CH_4$ growth rate derived from the AGAGE and NOAA networks together with selected model simulations. Figures 4.12b and 4.12c show the differences between the model simulations and the NOAA and AGAGE observations, respectively. The runs which include variations in [OH] agree better with the observed changes, i.e. larger R values in panel (a) and the model lines are closer to the y=0 line in panels (b) and (c), especially in the first 5 years of the stagnation period. It is interesting to note that the relative impacts of wind and temperature variations are larger for $CH_4$ than for $CH_3CCl_3$ (compare simulations RE_FTFW, RE_FTVW and RE_VTVW in Figures 4.8 and 4.12). The temperature dependences of the OH loss reactions are similar for the two species (see equations 4.1 and 4.2) but the impact of transport from emission regions to chemical loss regions is more variable for $CH_4$. This needs to be considered when applying results derived from $CH_3CCl_3$ to $CH_4$.

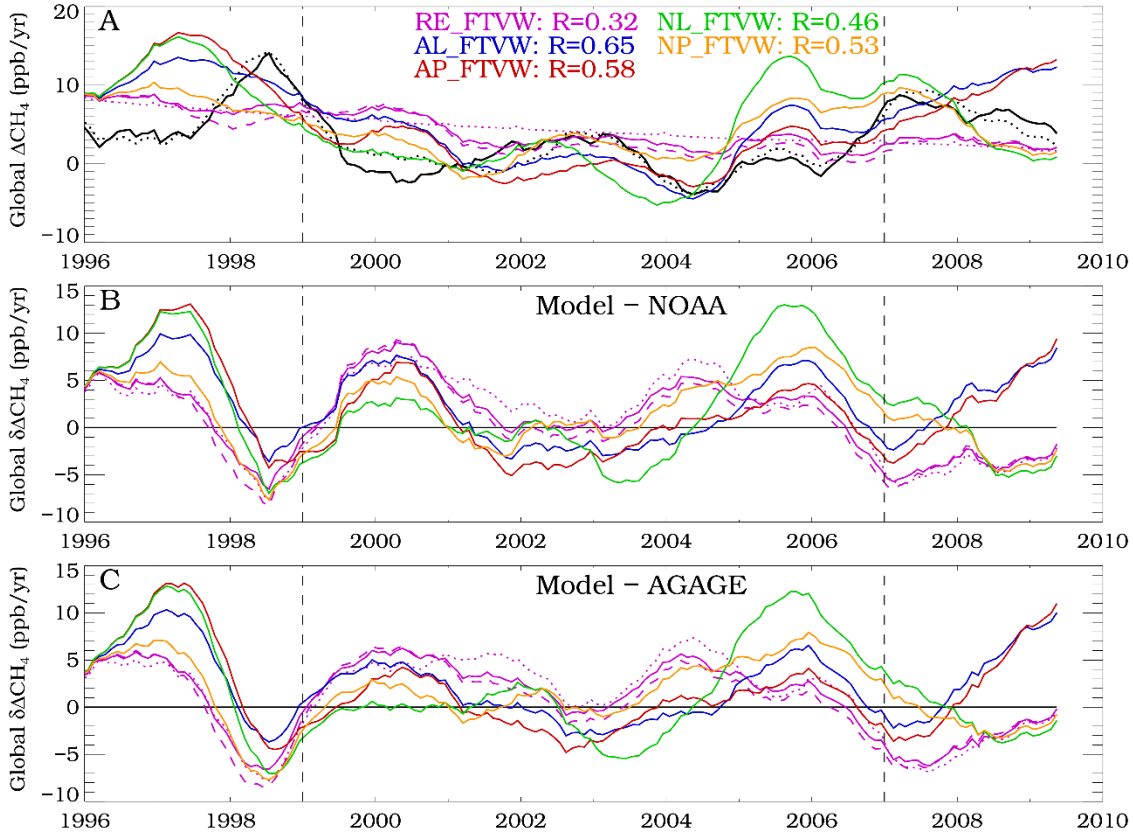


*Figure 4.12 (a) The smoothed variation in the global annual $CH_4$ growth rate (ppb/yr) derived from NOAA (black solid) and AGAGE (black dashed) observations. Also shown are the smoothed growth rates from five TOMCAT 3-D CTM simulations with fixed temperatures and varying winds (See Table 4.2). Values in legend give correlation coefficient between model run and NOAA observations. Also shown are results from runs RE_FTFW and RE_VTVW as a purple dotted line and dashed line, respectively (b) the difference in smoothed growth rate between TOMCAT simulations and NOAA observations shown in panel (a). (c) Same as (b) except using differences compared to AGAGE observations. The vertical dashed lines mark the start and end of the stagnation period in the observed $CH_4$ growth rate (1999 – 2006).*

## 4.6 Summary

This chapter has investigated the atmospheric contribution to recent trends in the global $CH_4$ growth rate with the following key results:

- A simple-one-box model has been used to create global annual anomalies of $CH_3CCl_3$-derived [OH], which is found to be negatively correlated with observed $CH_4$ growth (R = -0.32 (NOAA) and -0.64 (AGAGE)).

- When used in a 3-D CTM the box-model derived [OH] anomalies provide improved correlation of $CH_3CCl_3$ with observations (R = 0.71 – 0.90) compared with using annually repeating [OH] (R = 0.62 – 0.67).

- Box-model derived global [OH] anomalies used in a 3-D CTM accurately predict the $CH_3CCl_3$ decay rate anomaly at individual stations.

- One-box model simulations show that when considering variations in atmospheric [OH], the $CH_4$ emissions required during the stagnation period (1999-2006) are higher (549.7 – 553.8 Tg/yr) than when [OH] anomalies are not considered (546.2 – 548.4 Tg/yr).

- The $CH_4$ growth anomaly agreement between the 3-D CTM model simulations and observations increases when the annually repeating [OH] (R = 0.32) is replaced by the box-model derived global [OH] anomaly (R = 0.58 – 0.65).

- An anomalously high [OH] during the $CH_4$ stagnation period may explain a large fraction of the observed decrease in $CH_4$ growth.

TOMCAT model results suggest that variability in atmospheric [OH] and transport may well have played key roles in the observed recent variations in $CH_4$ growth, particularly during the $CH_4$ stagnation period between 1999 and 2006. The 3-D CTM calculations show that during the stagnation period, variations in [OH], temperature and transport in the tropical lower to mid-troposphere could potentially account for an important component of the observed decrease in global $CH_4$ growth. Within this, small increases in [OH] were the largest contributing factor, while variations in transport made a smaller contribution. Note, however, that the ultimate loss of $CH_4$ is still due to chemistry. The role of atmospheric temperature variations is factored into the observationally derived OH, but model experiments show that changes in the OH concentration itself is most important. The remainder of the $CH_4$ variation can be ascribed to other processes not considered in the model runs such as emission changes. There are also measurement uncertainties to consider and the possible underrepresentation of the global mean $CH_3CCl_3$ which will affect the derived OH concentration. These results are consistent with an earlier budget study which analysed 1991 to 2004 and found that variations in [OH] were the main control of variations in atmospheric $CH_4$ lifetime (65%), with temperature accounting for a smaller fraction (35%) (Fiore *et al.*, 2006). As noted here the $CH_4$ lifetime can also be affected by emissions distributions which affects transport to the main loss regions.

Prior to the stagnation period the TOMCAT simulation using AGAGE-derived [OH] overestimates $CH_4$ growth compared to observations which degrades the agreement with the observed $CH_4$ variations. There are inaccuracies in box-model derived [OH] in 1997 when emissions played a large role in the observed $CH_3CCl_3$ and the e-fold decay had not stabilised (Montzka *et al.*, 2011).

Variations in $CH_4$ emissions are not accounted for in simulations used in this chapter, but are investigated in Chapter 5. The results from this Chapter suggest that although global $CH_4$ emissions do vary year-to-year, the observed trend in $CH_4$ growth between 1999 and 2006 was impacted by changing atmospheric processes that affected $CH_4$ loss. When variations in atmospheric conditions are considered, the required decrease in emissions to match observations is reduced. Changes in emissions are still important and likely to dominate $CH_4$ variations over other time periods. The observed changes in growth rates during ENSO events in e.g. 1998 are poorly captured by the meteorological changes considered here and can be attributed to changes in emissions through changing precipitation and enhanced biomass burning (Hodson *et al.*, 2011). The renewed growth of $CH_4$ in 2007 is also poorly captured by all model simulations without varying [OH]. The observed decrease in AGAGE and NOAA-derived [OH] coincides with the increase in $CH_4$ growth in 2007, although the currently available data do not allow for a more detailed investigation of the possible contribution of [OH] changes in this recent increase.

Improved quantification of the role of OH variability will require efforts to reduce uncertainties associated with estimating [OH]. Estimates of global mean [OH] in recent years from $CH_3CCl_3$ observations is becoming increasingly difficult because $CH_3CCl_3$ levels are currently <5 ppt; hence this may limit the accuracy of derived [OH] and its variability in future years (Lelieveld *et al*., 2006). Wennberg *et al*. (2004) also noted that there can be time variations in the small uptake of $CH_3CCl_3$ by the oceans, which can also affect the derived [OH] concentrations and are not considered here. Future atmospheric trends in $CH_4$ are likely to be strongly influenced by not only emissions but also changes in processes that affect atmospheric loss. The accuracy of predictions would therefore be improved by including variations in [OH] and meteorology.

# 5 Evaluation of Wetland $CH_4$ Models

## 5.1 Introduction

This chapter compares and evaluates $CH_4$ emission predictions from three wetland models. Wetlands are the largest single source of $CH_4$ to the atmosphere (~30%) and have the largest uncertainty surrounding their emissions (Ciais *et al.*, 2014). Model development can improve current and future wetland emission estimates, as well as predictions of possible climate feedbacks associated with these emissions. A second key area of model development concerns the improvement of the spatial and seasonal distribution of $CH_4$ emissions, which can be tested against atmospheric observations. Identification of weaknesses of existing wetland models highlights areas that require development.

This chapter aims to separate the uncertainty in the model forcing parameters (wetland fraction, temperature and carbon) from the structural uncertainty of wetland $CH_4$ emission models, using similar process descriptions for three different models. The recently completed WETland and Wetland $CH_4$ Inter-comparison of Models Project (WETCHIMP) highlighted challenges facing the wetland $CH_4$ modelling community (Melton *et al.*, 2013). That study involved ten wetland $CH_4$ emission models which used a variety of processes and observed driving parameters (e.g. temperature), and showed both structural and parameter uncertainty in the models. Structural uncertainty includes missing processes (e.g transport) and uncertainty in the representation of some processes. The models analysed here were not part of the WETCHIMP study and, in addition to comparing them with each other, this chapter tests their accuracy by performing comparisons using a CTM and observations. The spatial and temporal differences between the models used here highlight parameter uncertainties and the relevant observation comparisons permit some assessment of the process description accuracy. It is assumed that the uncertainty in wetland $CH_4$ emissions outweighs the uncertainties in other emissions and sinks in wetland regions and that any inaccuracies in all three models are a result of missing wetland processes.

Section 5.2 gives a background on the analysis framework. This includes a description of the wetland emission datasets, a comparison of the driving parameters, a brief overview of other $CH_4$ emission sources and the specifications of the TOMCAT simulations. Section 5.3 compares all three wetland emission datasets, generated by the wetland $CH_4$ emission models, prior to them being used to force TOMCAT. Section 5.4 shows comparisons of TOMCAT $CH_4$ simulations with flask, TCCON and GOSAT observations. Section 5.5 summarises the agreement between the wetland emission dataset and the TOMCAT simulations compared with observations.

## 5.2 TOMCAT model simulation specifications

The period 1993-2012 has been simulated using 3 TOMCAT $CH_4$ tracers, all of which were identical except for the wetland emissions. To evaluate the wetland datasets modelled atmospheric $CH_4$ predictions were compared with observations. The non-wetland emissions and loss fields were the same as those used in Chapter 4, except that some were allowed to vary interannually. Model resolution and forcing data was the same as described in Chapter 3. 12-hourly surface $CH_4$ output has been used for flask comparisons and 10-daily profile output is used for GOSAT and TCCON comparisons. A 12-year spin-up was performed using time varying emissions where available from 1980-1991. The global $CH_4$ value was reset in 1992 using the global $CH_4$ observations from the NOAA flask network and spun-up for a further year using climatologies for each inventory.

Anthropogenic emissions were taken from the EDGAR version 3.2 database (2001) between 1993 and 2008, with 2009-2012 emissions set as a repeat of 2008. These are based on linear interpolation and extrapolation of estimates for 1990, 1995 and 2000 (Patra *et al.*, 2009). Biomass burning emissions were taken from the GFED v3.1 inventory (van der Werf *et al.*, 2010) between 1997 and 2010. A climatology was used for emissions between 1993 and 1996, and years 2011-2012 used a repeat of 2010 emissions. Emissions from rice, hydrates, volcanoes, termites, wild animals and ocean were annually repeating and identical to those described in Chapter 4. All emissions were scaled to IPCC estimates described in Chapter 2 and gridded at 1° by 1° resolution.

### 5.2.1 Wetland $CH_4$

Three wetland emission models were used, each with similar process descriptions and all were scaled to average yield annual emissions of 177 Tg/yr. Two models, formulated and parameterised as part of this thesis, are based on the JULES process description shown in equation 5.1 (Gedney

*et al.*, 2004), where $F_{CH4}$ is the $CH_4$ flux in kg $m^{-2}$ $s^{-1}$, $k_{0CH4}$ is a global scaling constant in $s^{-1}$, $f_w$ is wetland fraction in $m^2/m^2$, $C_s$ is carbon substrate in kg $m^{-2}$, $Q_{10}$ describes the temperature dependence of the methanogenesis reaction, $T_{soil}$ is the soil temperature and $T_0$ = 273.15 K is a reference temperature. The third model, taken from Bloom *et al.* (2012), uses equation 5.2, where $F_{bCH4}$ is the $CH_4$ flux in mg $m^{-2}day^{-1}$, $\emptyset$ is a decay constant in $day^{-1}$, $\tau_w$ is the equivalent water height, $D_s$ is the equivalent depth of wetland soil and $C_b$ is the carbon substrate in mg $m^{-2}$. All three models are solely dependent on temperature, wetland and carbon substrate.

$$F_{CH_4} = k_{0CH_4} f_w C_s Q_{10} (T_{soil})^{(T_{soil}-T_0)/10} \qquad \textbf{(5.1)}$$

$$F_{bCH_4} = \emptyset(\tau_w + D_s) C_b Q_{10} (T_{soil})^{(T_{soil}-T_0)/10} \qquad \textbf{(5.2)}$$

The following sections outline the three wetland emission datasets generated by the models, hereafter referred to as JU, JP and BL. Both JULES emission datasets were created as part of this work, the third, the top-down dataset, was taken from Bloom *et al.* (2012).

**JULES Driven by JULES Parameters (JU)**

The first wetland emission dataset, JU, was driven by JULES version 3.4.1 wetland fraction, soil temperature and soil carbon. This section describes the JULES configuration used, a more general model overview is discussed in Chapter 3. The three driving parameters for wetland $CH_4$ emissions in JULES are soil carbon, temperature and wetland fraction (see equation 5.1). WATCH-forcing-data-ERA-interim (WFDEI) was used to force JULES from 1993 to 2012 (Weedon *et al.*, 2014), this meteorological input is provided at 3-hourly time steps and at a horizontal resolution of 0.5° by 0.5°. The forcing data includes 67,209 land points outside Antarctica and provides JULES with long-wave and short-wave downward surface radiation, 2 m air temperature, 10 m wind speed, surface pressure, 2 m specific humidity, rainfall rate and snowfall rate. Monthly JULES output is used.

TRIFFID was enabled in the model, which simulates vegetation and soil carbon dynamics to provide carbon substrate for methanogenesis (Cox *et al.*, 2001). The soil carbon model uses the RothC soil carbon scheme (Coleman and Jenkinson, 1996), where leaf litter from vegetation is first split into two carbon pools, DPM and RPM (Decomposable/Resistant Plant Material), the ratio of which is dependent on the PFT (Plant Functional Type). Then the carbon can be released through respiration or further broken down into the BIO (Biomass) and HUM (Humus) pools.

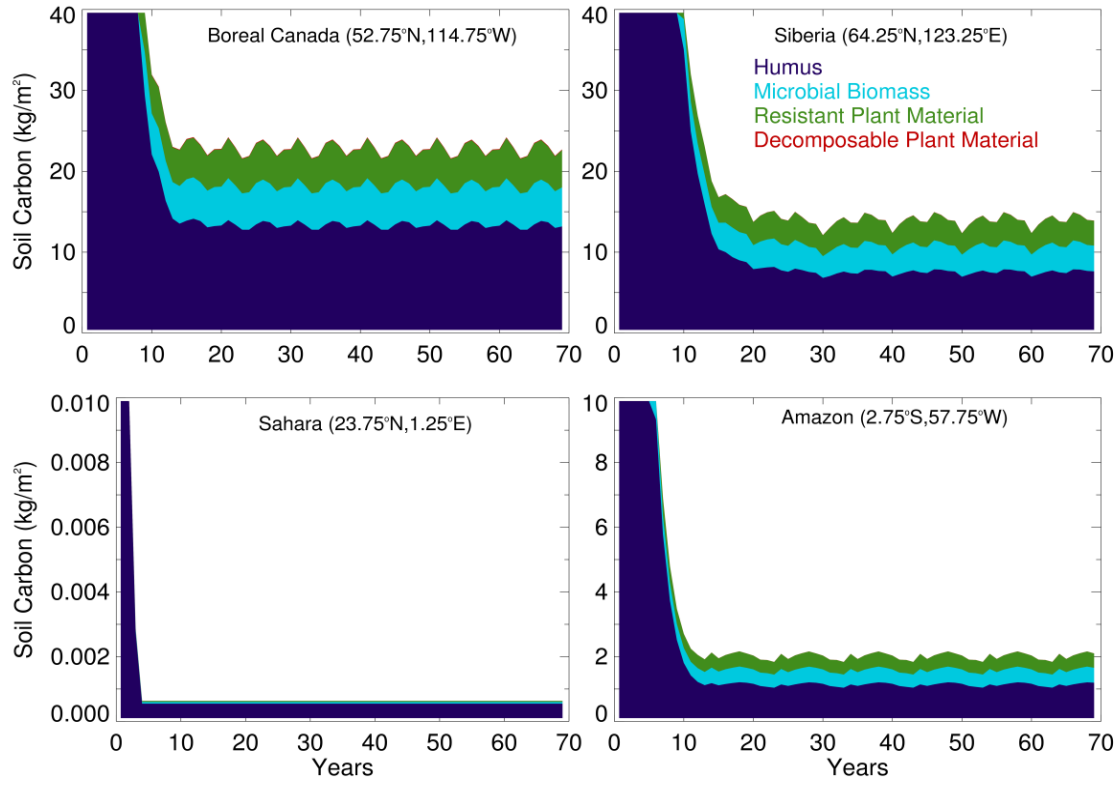


*Figure 5.1 Spin-up of JULES soil carbon at 4 locations using the accelerated method for humus (purple), microbial biomass (blue), and resistant (green) and decomposable plant material (red).*

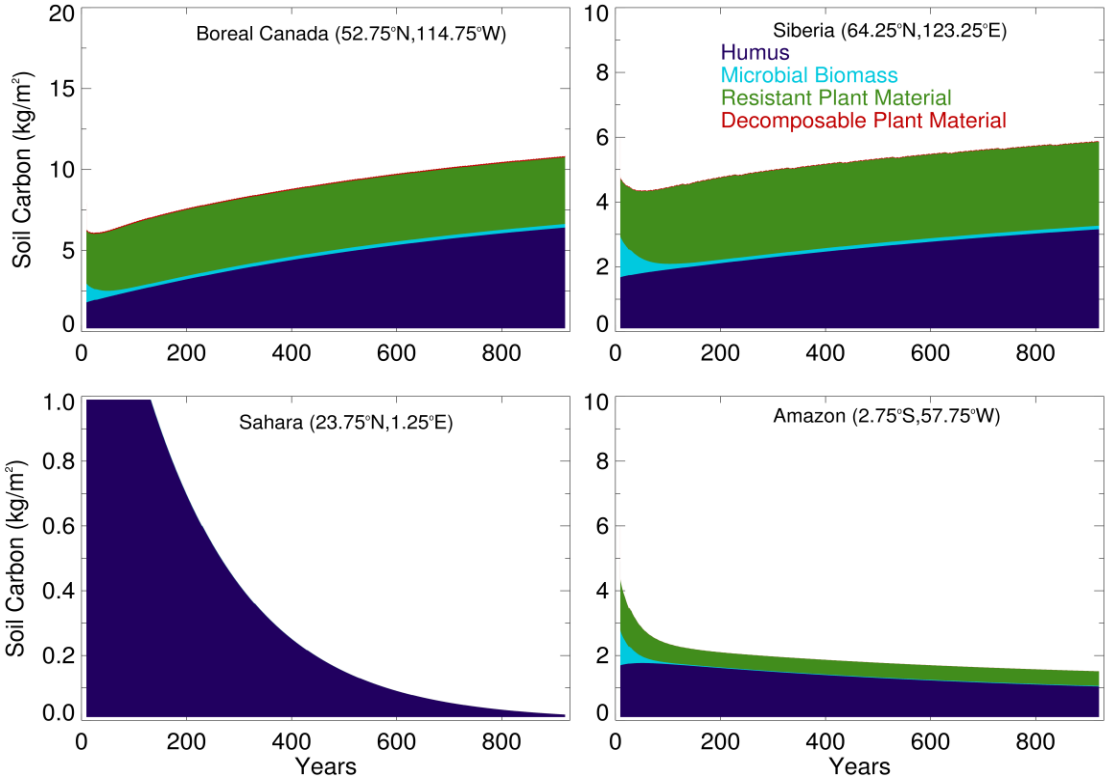


*Figure 5.2 Spin-up of JULES soil carbon at the same 4 locations as Figure 5.1 but using the standard method for humus (purple), microbial biomass (blue), and resistant (green) and decomposable plant material (red).*

The use of the four soil carbon pools requires a long spin-up period (typically >1000 years) because of the slow turnover rate of the humus pool. This can be avoided by applying an accelerated decomposition method described by Koven *et al.* (2013). Once the soil carbon input, from vegetation, is in equilibrium, the size of the soil carbon pool is determined by the decomposition rates. The linear relationship between the size of the pool and the decomposition rate is exploited by accelerating the decomposition rates by a factor, α, and rescaling the pools by α. To assess the accuracy of this approach two spin-up methods were compared. The first, shown in Figure 5.1, used accelerated decomposition by spinning-up the vegetation for 30 years, followed by rescaling and accelerating the decomposition rates for 70 years. The second, shown in Figure 5.2, used a standard TRIFFID setup which is spun-up for 900 years. The standard version of the model had not reached equilibrium after 900 years, in particular the HUM pool. It is assumed that with a longer spin-up the standard version would eventually tend toward the values calculated using the accelerated decomposition method (see Figures 5.1 and 5.2).

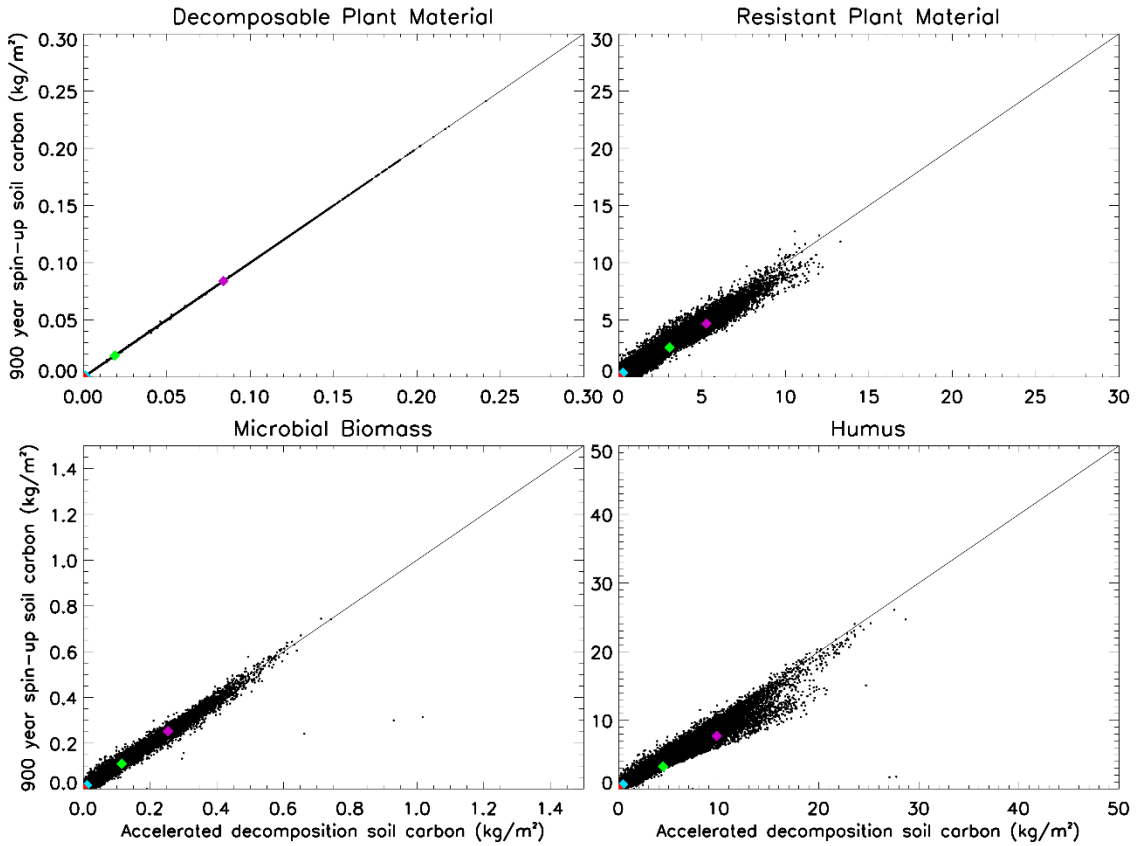


*Figure 5.3 Comparison at all land points of the four JULES soil carbon pools, after a 70-year spin-up using accelerated decomposition and a 900-year spin-up using standard JULES. The four points in Figures 5.1 and 5.2 are represented by the purple (Boreal Canada), green (Siberia), red (Sahara) and blue (Amazon) diamonds.*

Figure 5.3 shows that both spin-up approaches yield similar size pools for each substrate type at all model land points; as a result the accelerated method is used for the rest of this thesis to reduce computational demand. To ensure the model is spun-up for the correct time period, 1993 to 2013, the JULES simulation starts in 1979. This results in the soil carbon not just being in near-equilibrium but also provides the model representation of the global soil carbon state from 1993.

The respiration rate is different for each pool in the RothC scheme, (see Table 5.1) and further details of this are discussed in Chapter 3. For methane production in JU the same methanogenesis rates are applied to each pool, using an overall methane production rate given in equation 5.3, where $C_{dpm,rpm,bio,hum}$ represents the substrate availability of each of the four pools in kg $m^{-2}$, $R_{dpm,rpm,bio,hum}$ represents the methanogensis rate of each pool in $s^{-1}$ and $\Lambda$ is the methane production rate. A modified flux equation shown by equation 5.4 is then used, where $\Lambda$ and a new time-independent scaling factor, $k_{CH4}$, replace $C_s$ and $k_{0CH4}$ of equation 5.1.

$$\Lambda = C_{dpm}R_{dpm} + C_{rpm}R_{rpm} + C_{bio}R_{bio} + C_{hum}R_{hum} \quad \textbf{(5.3)}$$

$$F_{CH_4} = k_{CH_4} f_w \Lambda Q_{10}(T_{soil})^{(T_{soil}-T_0)/10} \quad \textbf{(5.4)}$$

| Carbon Pool | DPM | RPM | BIO | HUM |
|---|---|---|---|---|
| Respiration Rate ($s^{-1}$) | 3.22 x $10^{-7}$ | 9.65 x $10^{-9}$ | 2.12 x $10^{-8}$ | 6.43 x $10^{-10}$ |

*Table 5.1 JULES default respiration rates for each soil carbon pool based on values from Clark et al. (2011). The methanogenesis rates are assumed to equal the respiration rates.*

The soil temperature is calculated for four different layers in JULES. For this experiment all methane production is assumed to occur in the top 10 cm, which is the top soil layer in JULES. The baseline temperature dependence, $Q_{10}(T_0)$, was set at 1.65. This value changes depending on the soil temperature as in equation 5.5 (taken from Gedney *et al.* 2004). This is required because the Arrhenius equation, which describes the temperature dependence of methanogenesis, is only valid over a limited temperature range (Gedney *et al.*, 2004). Where the soil temperature is lower than 273.15 K, emissions are set to zero because the ground is considered frozen with no microbial activity.

$$Q_{10}(T) = Q_{10}(T_0)^{T_0/T} \quad \textbf{(5.5)}$$

Wetland fraction for each model grid cell is given as the fraction of the grid cell that is fully inundated, estimated from the topographic index, which takes into account slope gradient and catchment area. Production and instantaneous emission of $CH_4$ is restricted to saturated regions within the model, where saturated soils are surfaces which can no longer absorb water. In reality

some emissions are also observed at unsaturated sites (Wickland *et al.*, 1999), but these are not accounted for in the model. The $CH_4$ produced is immediately emitted into the atmosphere in the model, neglecting transport pathways and oxidation. JULES only simulates natural wetlands and does not account for agricultural practices, such as fertilisation, altering the biogeochemical processes. Some rice paddies are found in areas of natural wetlands, thus a rice field mask is placed over the JULES wetland and the rice emissions are taken from Yan *et al.* (2009). The mask used is an annually repeating monthly mean rice fraction map taken from MICRA2000, which is a global monthly irrigated and rainfed crop area database (Portmann *et al.*, 2010).

**JULES Driven by Prescribed Parameters (JP)**

The second wetland emission dataset, JP, used equation 5.1 and a prescribed wetland fraction, soil temperature and soil carbon. This is an identical process description to JU but with different driving parameters. Unlike JU, the soil carbon does not vary with time. The prescribed parameters used to generate JP are based on observations.

JP used a single carbon pool that has been spatially regridded from the Harmonised World Soil Database (HWSD) (Fischer *et al.*, 2008). HWSD combines regional and national soil information maps to generate a global data set of multiple parameters which do not vary in time and which have a ~1km resolution. The database includes topsoil organic carbon fraction and density. Carbon is given as a percentage of the total mass in the top 30 cm of the soil column and is multiplied with soil density to obtain an estimate of substrate kg $C/m^2$ available for methanogenesis. Figure 5.4 shows how the HWSD database, with a single carbon pool, compares to the four carbon pools generated estimated with JULES, taken from JU. High values over Greenland can be ignored because there is no respiration or methanogenesis in that region. Total carbon is lower in JULES predictions compared to HWSD, especially in boreal regions. Carbon substrate is also more uniformly distributed in JULES simulations. Based on soil carbon alone, JU would produce more evenly distributed wetland $CH_4$ emissions, than JP. JU also exhibits a more pronounced seasonality because it varies in time.

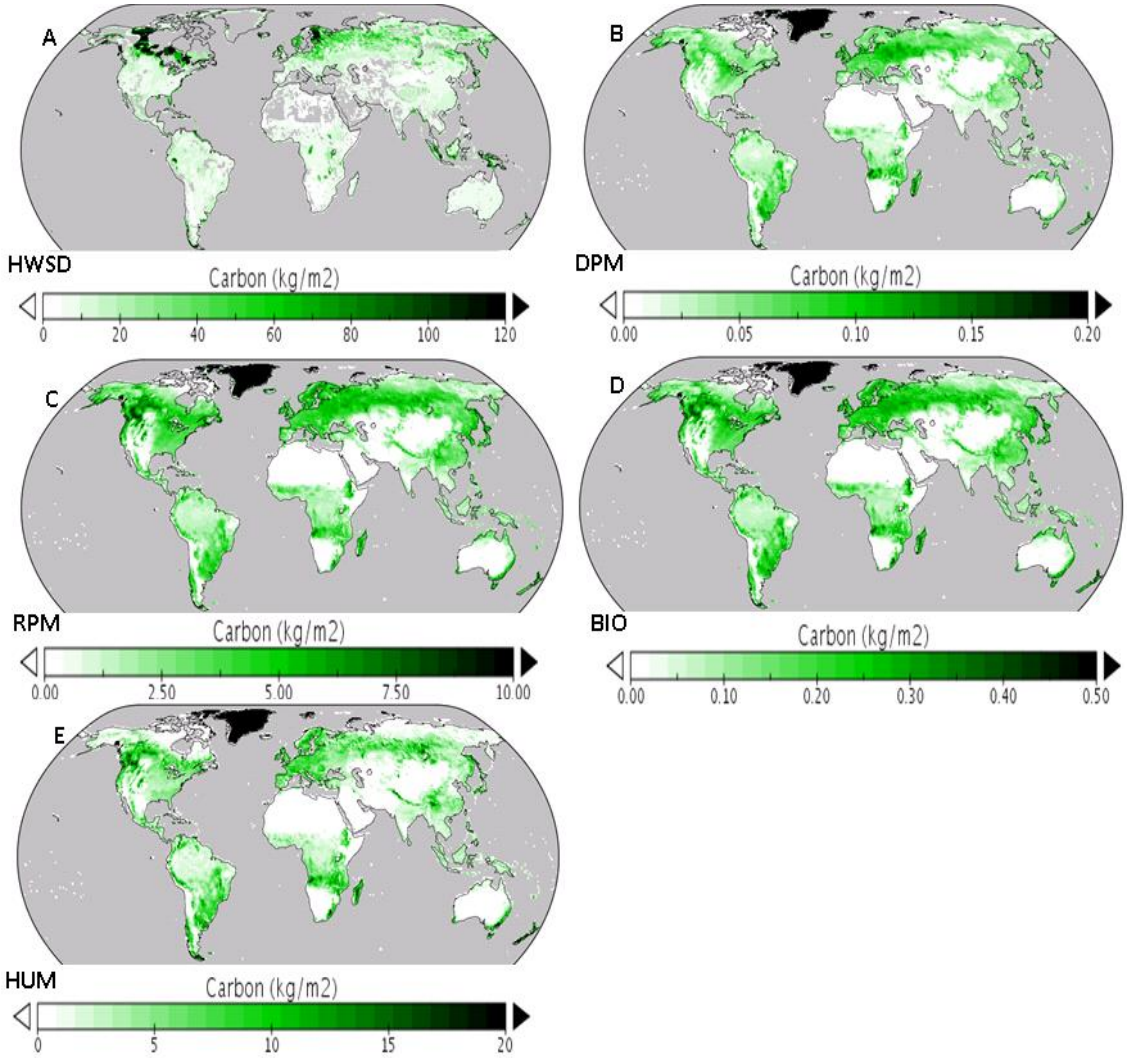


*Figure 5.4 Global substrate carbon used in the wetland emission datasets JU and JP. (a) Global fixed topsoil organic carbon taken from HWSD. (b-e) Global substrate from the four JULES carbon pools, after accelerated decomposition, for September 2005. Note that the scale varies between plots. Large carbon pools over Greenland are a result of no respiration from the initial state.*

The soil temperature for JP is taken from the NCEP Climate Forecast System Reanalysis (Saha *et al*., 2010). The 0-10 cm soil temperature is provided at 6-hourly time steps and at a 0.5° by 0.5° resolution. This has been averaged into monthly means to provide data from 1993 to 2009. Soil temperature values from 2009 were used for 2010 to 2012. Figure 5.5 shows how the NCEP soil temperature compares with the top-layer JULES soil temperature taken from JU. There is good overall agreement between the two temperature datasets both spatially and temporally. This suggests that, based on temperature alone, there should be good agreement between the two datasets or equivalently any differences are unlikely to be caused by differences in soil temperature. The exclusion of Antarctica from JULES will not affect the wetland methane production because of a lack of soil carbon and wetland fraction in that region.

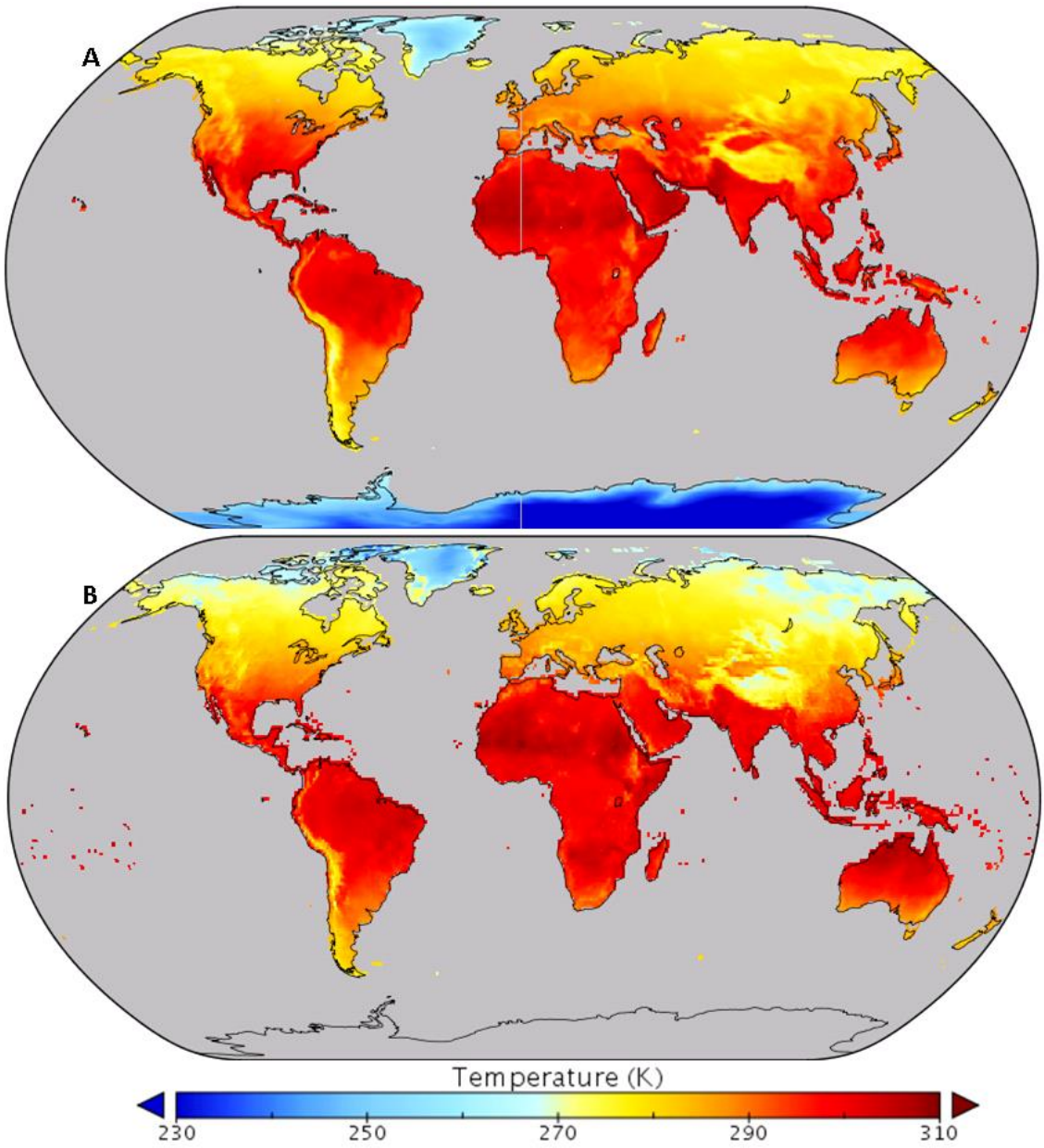


*Figure 5.5 Global 0-10 cm soil temperature (K) used in the wetland emission datasets (a) JP, taken from NCEP Climate Forecast Reanalysis and (b) JU, taken from JULES for September 2005.*

The wetland fraction used in equation 5.1 for JP is taken from the Global Inundation Extent from Multi-Satellites (GIEMS) dataset (Prigent *et al.*, 2012). The data combines passive microwave land surface emissivities from The Special Sensor Microwave Imager (SSM/I) and the International Satellite Cloud Climatology Project (ISCCP) observations, European Remote Sensing (ERS) scatterometer responses, and Advanced Very High Resolution Radiometer (AVHRR) visible and near-infrared reflectances to provide 0.25° by 0.25° global inundated fractions. The data, which are from 1993-2007, are binned into 0.5° by 0.5° gridboxes, with a climatology used for 2008-2012. The same rice paddy distribution mask as for JU is applied to

JP. Figure 5.6 shows a comparison between the JULES wetland fraction used in JU and the GIEMS wetland fraction used in JP for March and September 2005. Spatially, JULES shows a more uniform distribution than GIEMS, with higher fraction in the tropics and lower in boreal regions.

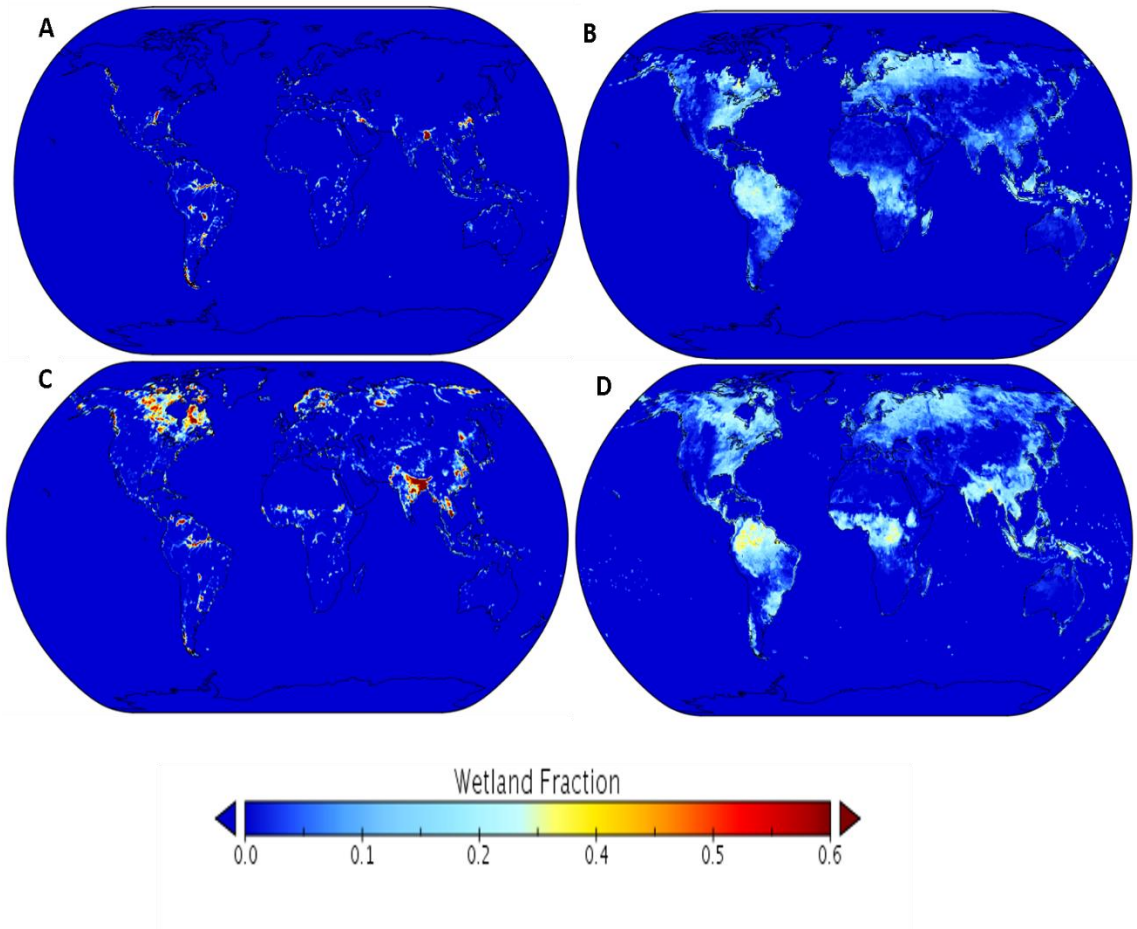


*Figure 5.6 Global wetland fraction from GIEMS (a and c) and JULES (b and d) for March (a and b) and September (c and d) 2005. Note that the wetland fraction shown is before a rice mask is applied.*

Annually the total wetland area is much larger in JULES compared to the GIEMS estimate; however, because the emissions are scaled to a global value the fractional distribution regionally compared to the global value is more important than the total wetland area for $CH_4$ emissions. Figure 5.7b shows that up to approximately 40% of global wetlands can be found in Boreal regions during summer according to the GIEMS database, which is larger than in JULES (~30%). JULES exhibits a higher seasonal peak in wetland fraction in the tropics of up to ~75% compared to GIEMS (~60%) (see Figure 5.7d). GIEMS shows a larger seasonal variability in both the Boreal and Tropical regions as a fraction of the total global amount; however in absolute terms the variability is larger in JULES in the boreal regions. Overall the main differences in $CH_4$ emissions

between JU and JP are likely to occur as a result of differences between the two wetland fractions, both spatially and temporally. Based on wetland fraction, JP is likely to have a more pronounced seasonal cycle than JU with comparably more emissions from the Boreal regions. Both wetland datasets exhibit interannual variability in wetland fraction, which is further investigated in the analysis of the wetland emission datasets in Section 5.3.

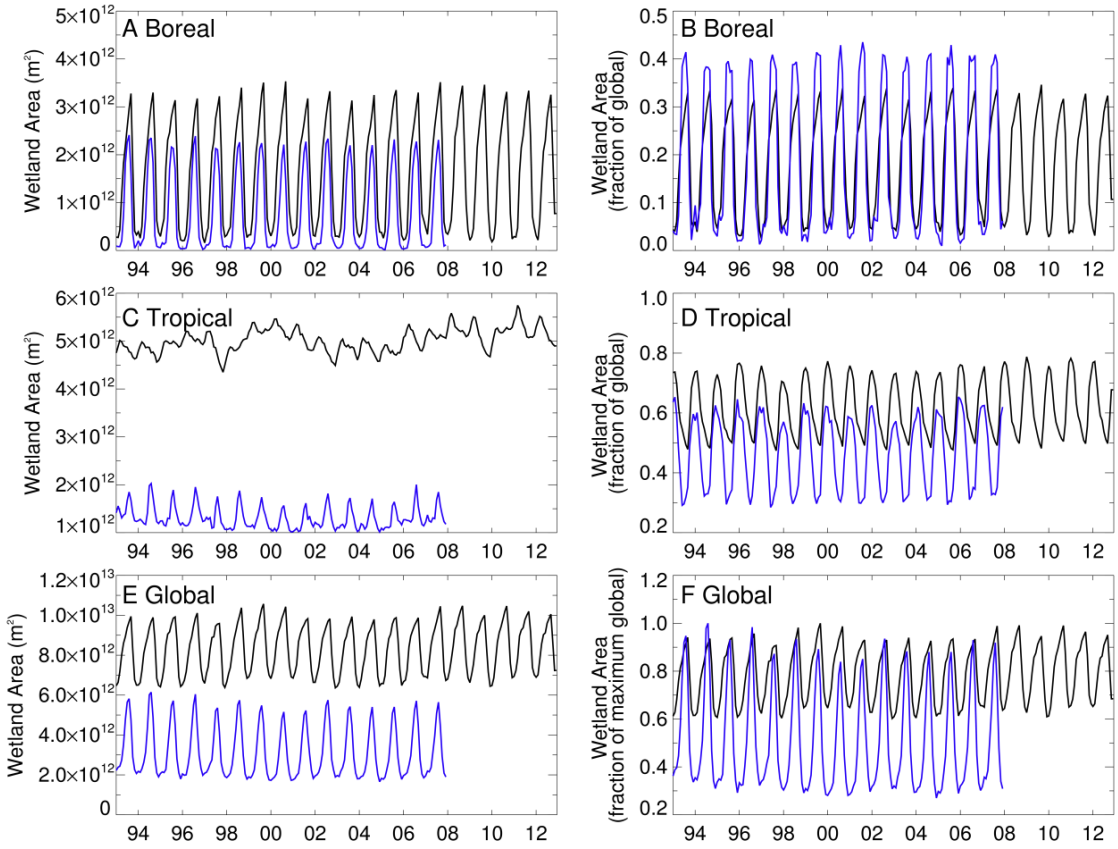


*Figure 5.7 Time series of (a) wetland area and (b) wetland area as a fraction of total global wetland area, for JULES (black) and GIEMS (blue) between 1993 and 2012 in the northern Boreal region (>45°N). (c, d) The same as (a, b), for the Tropical region between 23.5°S and 23.5°N. (e) The same as (a, b), globally. (f) Global wetland area as a fraction of the maximum global value. Note the wetland fraction is after rice mask has been applied.*

**Top-Down Wetland $CH_4$ Dataset (BL)**

The third set of wetland $CH_4$ emissions, BL, were estimated using equation 5.2 together with top-down observations. The dataset, described in this section, was not created as part of this thesis, but was taken directly from Bloom *et al.* (2012). The method isolates wetland and rice contributions to SCIAMACHY $CH_4$ observations based on water-table depth and surface temperature (Bloom *et al.*, 2010). The dataset correlates the variability in atmospheric $CH_4$ over wetland regions with changes in water-table depth and soil temperature to produce the flux equation 5.2 between 2003 and 2011. For 1993-2002 and 2012 a climatology is used.

A dynamic methanogen-available carbon pool is used to limit the methane production and the decay constant provides an estimated methanogenesis turnover rate for the available carbon. The carbon pool is updated daily and is fitted to the SCIAMACHY $CH_4$ observations. The carbon flux into the pool is assumed to be constant in time and balances the net $CH_4$ flux on an annual timescale.

Skin temperature is taken from the NCEP/National Centre for Atmospheric Research (NCAR) reanalysis project (Kalnay *et al.*, 1996) and used as a proxy for soil temperature. This is aggregated from a global 1.9° by 1.88° resolution onto a daily 3° by 3° resolution.

The equivalent water table used in equation 5.2 is derived from two satellites flown as part of The Gravity Recovery and Climate Experiment (GRACE). Changes in the Earth's gravity are measured by GRACE, which provides data at a 1° x 1° resolution (Lemoine *et al.*, 2007). An advantage of using GRACE is that it provides water table height both above and below the surface, which could be advantageous when developing transport processes within the process model.

## 5.3 Wetland $CH_4$ Flux Comparisons

This section compares spatial and temporal differences in the $CH_4$ fluxes of the three datasets (JU, JP and BL). Figure 5.8 shows the total annual emissions of the three datasets for the period 1993 to 2012. It highlights the relative contribution of each emission source and shows that the largest deviation from the mean annual emission of 553 Tg/yr is in 1998, for all datasets (JU: 565.4, JP: 570.3, BL: 561.8 Tg/yr). This was mainly caused by an increase in biomass burning emissions during the 1997/1998 El Niño event (van der Werf *et al.*, 2004). JU has a positive trend in emissions over the 20-year period of 0.49 Tg/yr, BL shows a smaller increase of 0.11 Tg/yr, which is influenced by earlier years having repeat wetland emissions, and JP shows a decreasing trend of -0.16 Tg/yr.

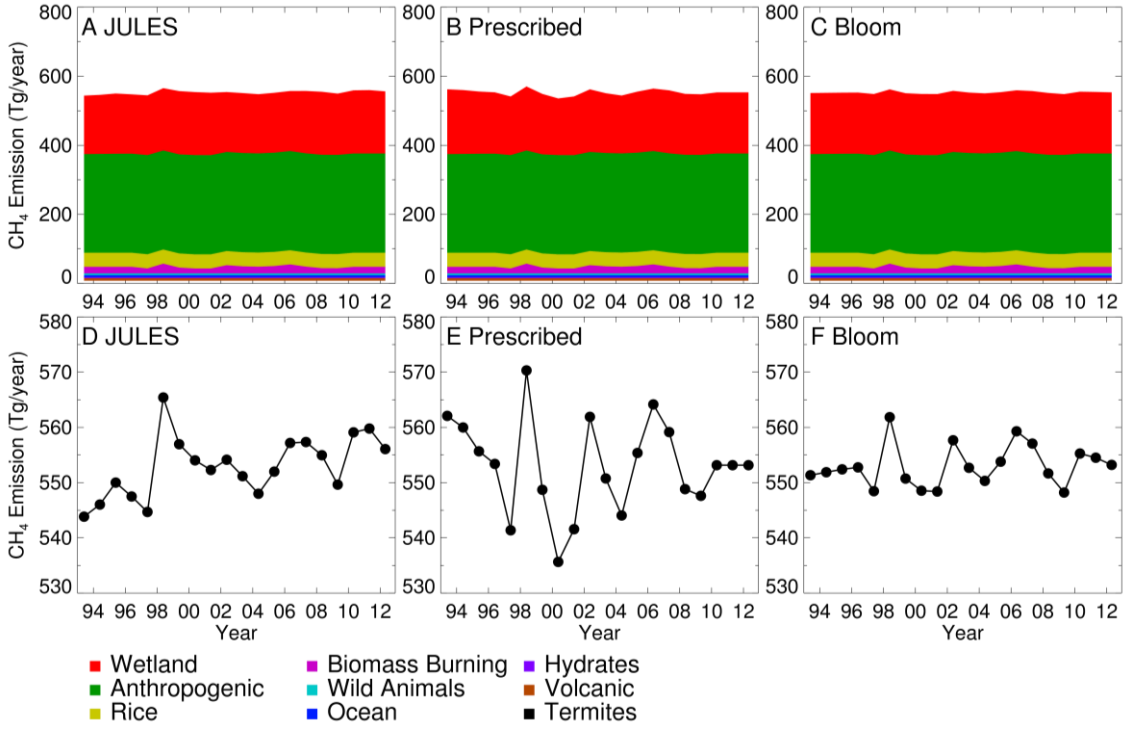


*Figure 5.8 (a-c) Annual emissions of $CH_4$, in Tg/yr, from three different datasets between 1993 and 2012 divided into individual source types. Datasetss have identical non-wetland emissions and different wetlands from (a) JU, (b) JP and (c) BL (Bloom et al., 2012). (d-f) Total annual emissions, same as a-c, with a different scale.*

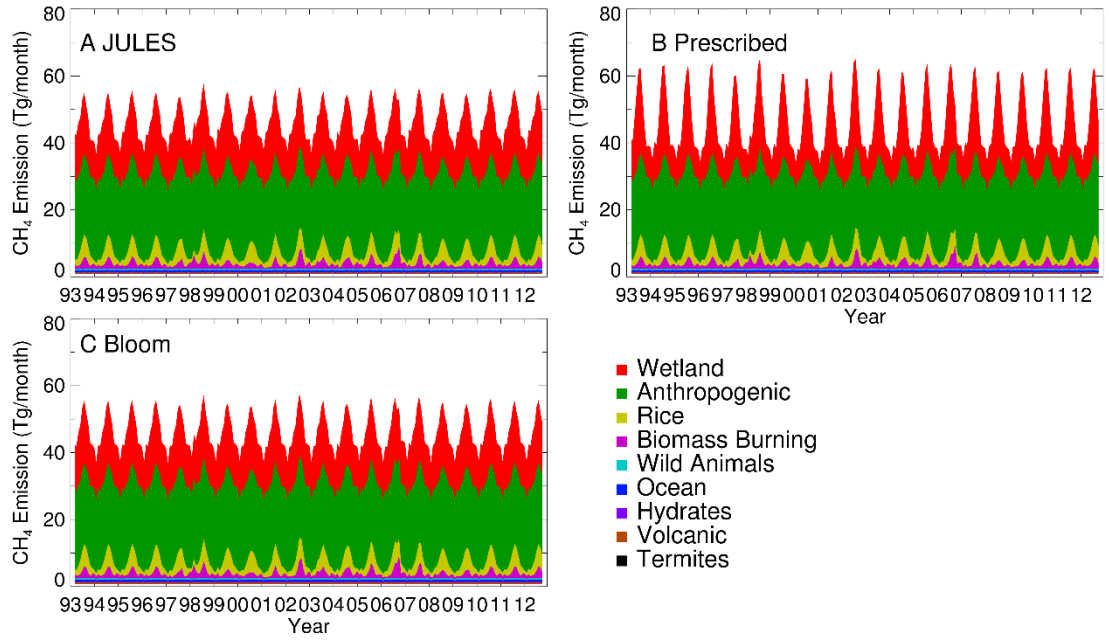


*Figure 5.9 Monthly emissions of $CH_4$, in Tg/yr, from three different datasets between 1993 and 2012 divided into individual source types. Datasets have identical non-wetland emissions and different wetlands from (a) JU, (b) JP and (c) BL (Bloom et al., 2012). Note rice, wild animal, ocean, hydrate, volcanic and termite emissions are all annually-repeating.*

Mirroring the strong seasonality in wetland area, Figure 5.9 shows that the relative variations in emissions are much larger on a seasonal timescale than on an interannual timescale, with peak emissions in August (JU: 55.7, JP: 62.4, BL: 55.7 Tg/month) and low emissions in February (JU: 37.4, JP: 34.9, BL: 37.3 Tg/month). Most of the variability is caused by seasonal changes in emissions from rice paddies and both, seasonal and interannual, changes in biomass burning and wetland emissions. Global rice emissions range from 6.7 Tg/month in August to 1.0 Tg/month in January. Biomass burning ranges from average values of 3.5 Tg/month in August to 0.74 Tg/month in November. Wetland variability is discussed in more detail later.

DeFries and Townshend (1994) defined regions to reflect geographical and mechanistic elements, these have been adapted to the regions used here (see Figure 5.10) and are used for both Chapters 5 and 6. The annual variance in biomass burning emissions is 13.9 Tg, this is smaller than for JU (1993 – 2012), 23.3 Tg, and JP (1993 – 2007), 46.6 Tg, but larger than BL (2003 – 2011), 2.2 Tg. Globally, wetland emissions range from 169.5 Tg/yr (1993) to 183.6 Tg/yr (2011) in JU, 164.1 Tg/yr (2000) to 187.7 Tg/yr (1993) in JP and 173.8 Tg/yr (2004) to 180.3 Tg/yr (2007) in BL. The variation in interannual emissions in JP is caused by changes in wetland fraction, which is less prominent in JU and BL. JP shows the largest interannual variability in Boreal North America and Tropical Asia, with variances of 3.7 Tg/yr and 6.4 Tg/yr, respectively (see Figure 5.11). For BL and JU the interannual variability in regions is typically smaller, the largest being North Africa for BL, 0.57 Tg/yr and Tropical Asia for JU, 2.4 Tg/yr. Figure 5.11 shows datasets agree on the annual emissions in some regions, Temperate North America and Europe, but disagree elsewhere, Boreal North America and Tropical Asia.

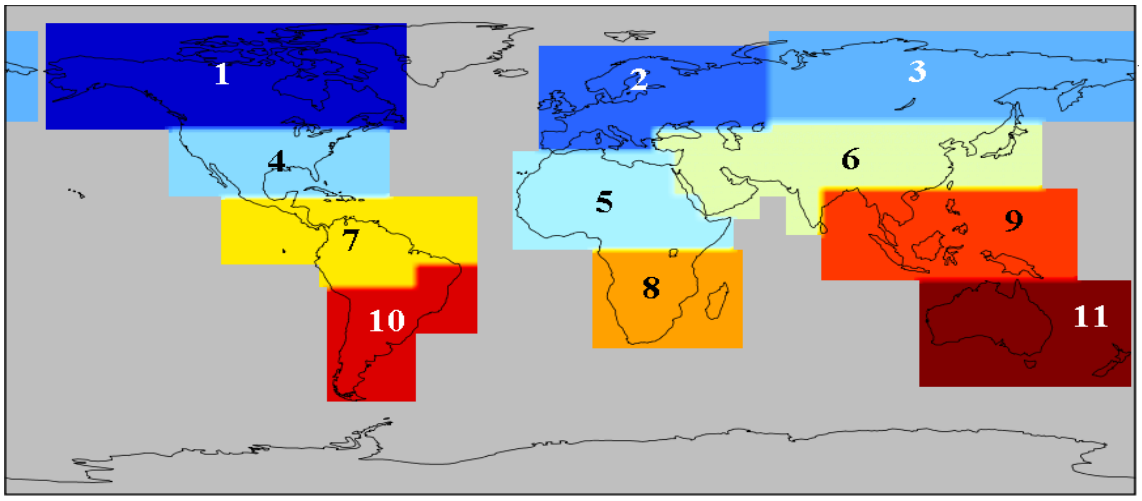


*Figure 5.10 Map showing the regions used in the thesis with Boreal North America (1), Europe (2), Boreal North Asia (3), Temperate North America (4), North Africa (5), Temperate Asia (6), Tropical South America (7), Africa South (8), Tropical Asia (9), Temperate South America (10) and Australia (11).*

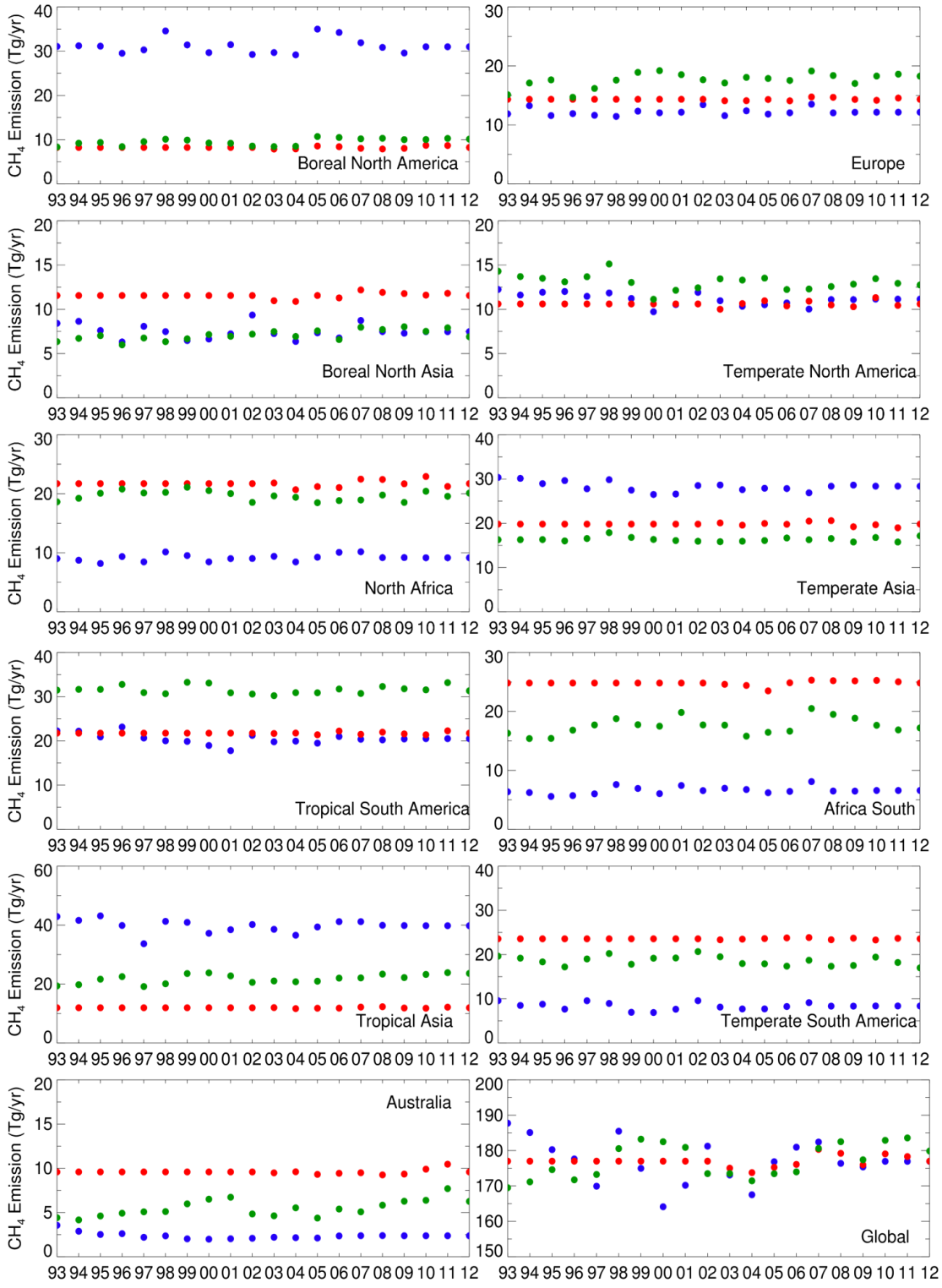


*Figure 5.11 Annual $CH_4$ wetland emissions, in Tg/yr, from JU (green), JP (blue) and BL (Bloom et al., 2012) (red) between 1993 and 2012. Individual panels show regions defined in Figure 5.10 and the bottom right panel shows the global emissions.*

| Wetland $CH_4$ Dataset | Annual Average Emissions (Tg/yr) | | | Region |
|---|---|---|---|---|
| | 1993-1998* | 1999-2006 | 2007-2012* | |
| JU | 173.5 | 176.6 | 181.1 | Global |
| JP | 181.0 | 173.6 | 178.1 | Global |
| BL | - | 175.0 | 178.6 | Global |
| JU | 9.2 | 9.4 | 10.2 | Boreal North America |
| JP | 31.3 | 31.2 | 30.8 | Boreal North America |
| BL | - | 8.2 | 8.3 | Boreal North America |
| JU | 16.4 | 18.1 | 18.3 | Europe |
| JP | 12.0 | 12.2 | 12.6 | Europe |
| BL | - | 14.1 | 14.5 | Europe |
| JU | 6.5 | 7.1 | 7.7 | Boreal Asia |
| JP | 7.8 | 7.2 | 7.8 | Boreal Asia |
| BL | - | 11.2 | 11.9 | Boreal Asia |
| JU | 13.9 | 12.7 | 12.8 | Temperate North America |
| JP | 11.9 | 10.7 | 10.7 | Temperate North America |
| BL | - | 10.5 | 10.7 | Temperate North America |
| JU | 19.8 | 19.6 | 19.6 | North Africa |
| JP | 9.0 | 9.1 | 9.5 | North Africa |
| BL | - | 21.2 | 22.1 | North Africa |
| JU | 16.6 | 16.2 | 16.3 | Temperate Asia |
| JP | 29.4 | 27.6 | 28.0 | Temperate Asia |
| BL | - | 19.8 | 19.8 | Temperate Asia |
| JU | 31.5 | 31.4 | 31.8 | Tropical South America |
| JP | 21.5 | 19.8 | 20.3 | Tropical South America |
| BL | - | 21.8 | 21.7 | Tropical South America |
| JU | 16.7 | 17.4 | 18.4 | Africa South |
| JP | 6.2 | 6.7 | 7.0 | Africa South |
| BL | - | 24.3 | 25.2 | Africa South |
| JU | 20.4 | 21.9 | 23.1 | Tropical Asia |
| JP | 40.4 | 39.1 | 40.3 | Tropical Asia |
| BL | - | 11.8 | 12.1 | Tropical Asia |
| JU | 18.9 | 18.7 | 18.2 | Temperate South America |
| JP | 8.8 | 7.9 | 8.6 | Temperate South America |
| BL | - | 23.6 | 23.6 | Temperate South America |
| JU | 4.7 | 5.5 | 6.2 | Australia |
| JP | 2.7 | 2.1 | 2.4 | Australia |
| BL | - | 9.5 | 9.7 | Australia |

*Table 5.2 Global and regional wetland emissions between 1993 and 1998, 1999 and 2006, and 2007 and 2012, from JULES, JULES driven by prescribed parameters and a top-down estimate (Bloom et al., 2012).*

* Where data are available from JU (1993-2012), JP (1993-2009) and BL (2003-2011).

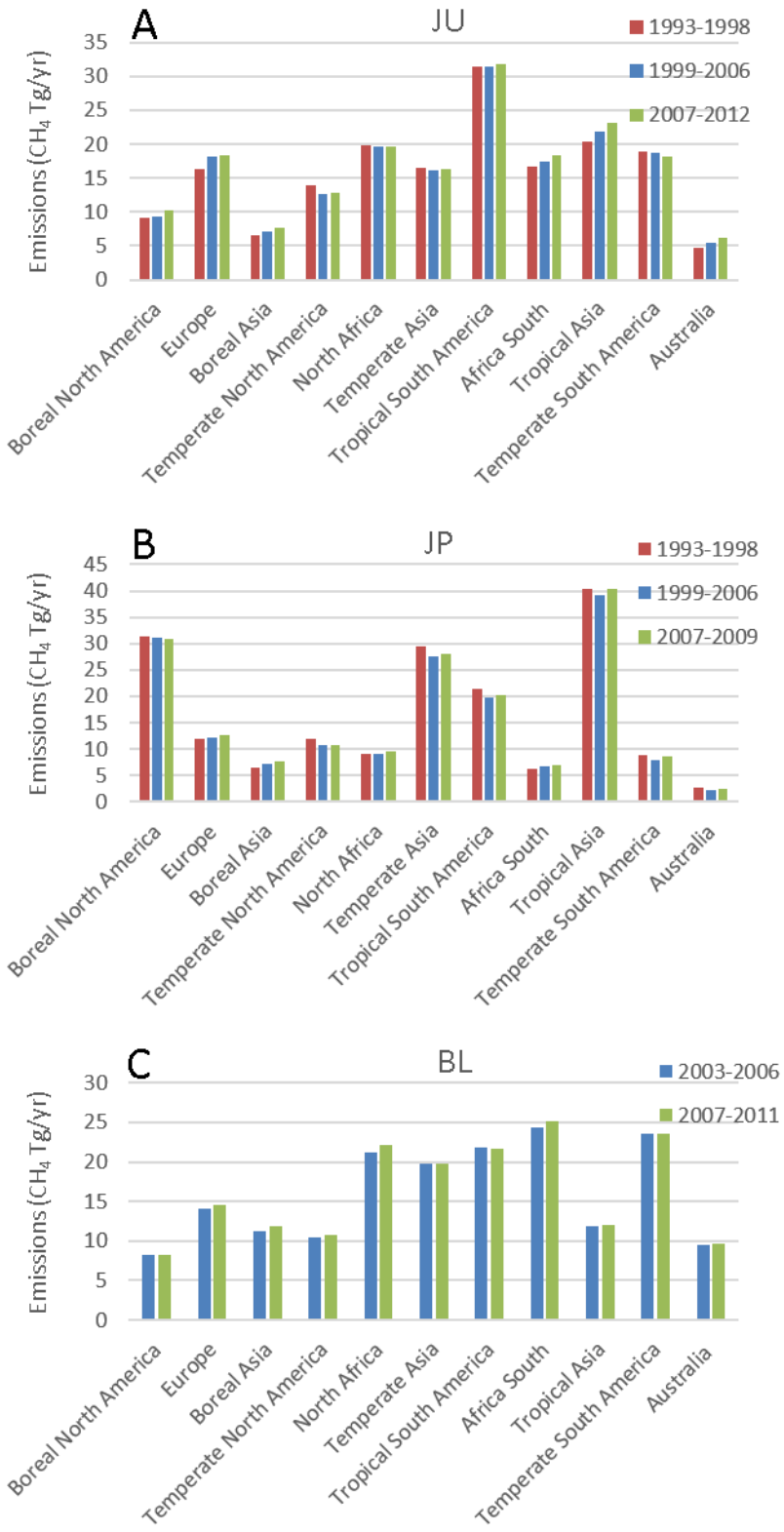


*Figure 5.12 Regional wetland emissions between 1993 and 1998, 1999 and 2006, and 2007 and 2012 where data are available, from (a) JU, (b) JP and (c) BL (Bloom et al., 2012).*

Table 5.2 and Figure 5.12 show how average wetland emissions change over time, bracketing intervals before, during and after the pause in $CH_4$ growth discussed in Chapter 4. JU (1993-2012) and BL (2003-2011) show an overall positive trend in global wetland emissions of 0.43 Tg/yr and 0.56 Tg/yr, respectively, both of which are statistically significant at the 95% level ($p<0.05$). JP (1993-2009) shows a negative trend of -0.35 Tg/yr, which is not statistically significant. This highlights the uncertainty in trend prediction using wetland $CH_4$ modelling. JU emissions decreased by 0.4 Tg/yr during the stagnation period (1999-2006), with the largest decrease in Temperate North America (0.4 Tg/yr). JP emissions decreased by 3.4 Tg/yr during the same period, with the largest decreases in Temperate Asia (0.7 Tg/yr), Tropical South America (0.7 Tg/yr) and Tropical Asia (0.7 Tg/yr). BL emissions decreased by 2 Tg/yr during the same period, with noticeable decreases in Boreal Asia (0.4 Tg/yr), North Africa (0.5 Tg/yr) and Africa South (0.5 Tg/yr). This shows that all datasets predict a decrease in emissions but do not agree on the magnitude or the spatial distribution of the decrease. Since 2007 all three datasets estimate that global wetland emissions are above the 1993-2012 average of 177 Tg/yr by 1.1 Tg/yr (JP) to 4.1 Tg/yr (JU). JU predicts increases in Africa South, Australia and all boreal and tropical regions. JP predicts increases in Europe, Boreal and Tropical Asia, North and Africa South, and Temperate South America. BL predicts increases in Temperate North America, North Africa, Africa South, Tropical Asia, Australia and all boreal regions. All datasets agree that African and boreal emissions have increased since 2007.

Changes in modelled wetland $CH_4$ emissions are dependent on three parameters; wetland fraction, soil temperature and soil carbon content. Figure 5.13 shows how each of these parameters vary with time and the relative coefficient anomaly these changes have on global wetland emissions. Wetland fraction is the largest driver of the reduced emissions during the stagnation period with a mean coefficient anomaly in JU of -0.4% and in JP of -3.3% between 1999 and 2006. Rainfall over the mean wetland area is comparably high in 1999 and 2000 but reduces below the average for the remainder of the stagnation period. Temperature causes less than a 0.1% reduction in emissions in both JU and JP, and soil carbon produces an above average coefficient during the stagnation of 0.1%. Regression analysis reveals a statistically significant (95% level) positive trend in the wetland coefficient anomaly of 0.5%/yr for JU and a negative trend of -0.6%/yr for JP. Both, JU and JP, show a statically significant trend in the temperature coefficient anomaly of 0.5% and 0.4% respectively. JU does not predict a statistically significant trend in emissions due to changes in soil carbon content.

The global seasonal ranges in wetland emissions differ between each dataset (see Figure 5.14). Globally, JU has an average seasonal maximum in August (18.6 Tg/month) and minimum in February (11.3 Tg/month). BL has an almost identical maximum in August (18.6 Tg/month) and

minimum in February (11.3 Tg/month). JP has a much larger seasonal range with an average maximum in August (26.5 Tg/month) and minimum in December (8.8 Tg/month). The large peak in JP emissions in the Northern Hemisphere summer mostly originates from increased emissions over Boreal North America. The datasets show similar seasonal cycles over Europe, Boreal North Asia and Temperate North America.

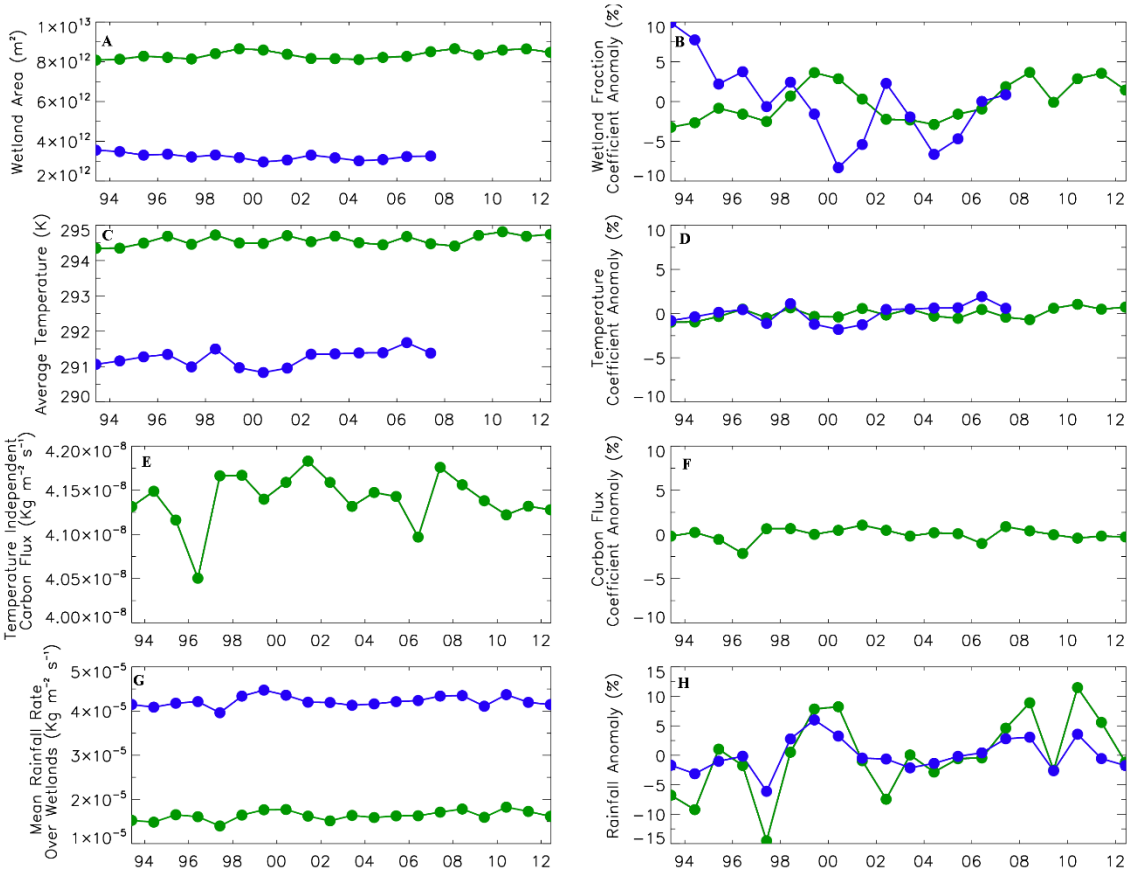


*Figure 5.13 The parameters required to generate the different $CH_4$ wetland flux datasets. (a) Total global mean wetland area in $m^2$, (c) soil temperature in K and (e) temperature independent unscaled soil carbon flux in kg $m^{-2}$ $s^{-1}$ from JU (green) and JP (blue). The relative global anomalies in the coefficients for (b) wetland area, (d) soil temperature and (f) soil carbon. (g) The global average rainfall over the climatological wetland area in kg $m^{-2}$ $s^{-1}$ and (h) the relative anomalies in rainfall. All data is for 1993 to 2011 for JU and 1993 to 2007 for JP.*

Temporal and spatial differences in all three wetland datasets shown here mainly arise because of differences in the wetland fraction. Firstly, the overall long-term trend in emissions is positive in JU and BL but negative in JP. Secondly, JP interannual variations in emissions are larger than for JU and BL. Thirdly, JP predicts a more pronounced seasonal cycle than the other two datasets, which is most evident in Boreal North America. Finally, there are clear differences in the spatial distribution of emissions predicted by JP compared to JU and BL, which have similar distributions to each other. Based on these comparisons there are noticeable differences between datasets even when the same methanogenesis model is applied, highlighting the parameter uncertainty in

wetland models. The parameter information is assessed in Section 5.4 by comparing CTM simulations driven by the wetland datasets with atmospheric $CH_4$ observations.

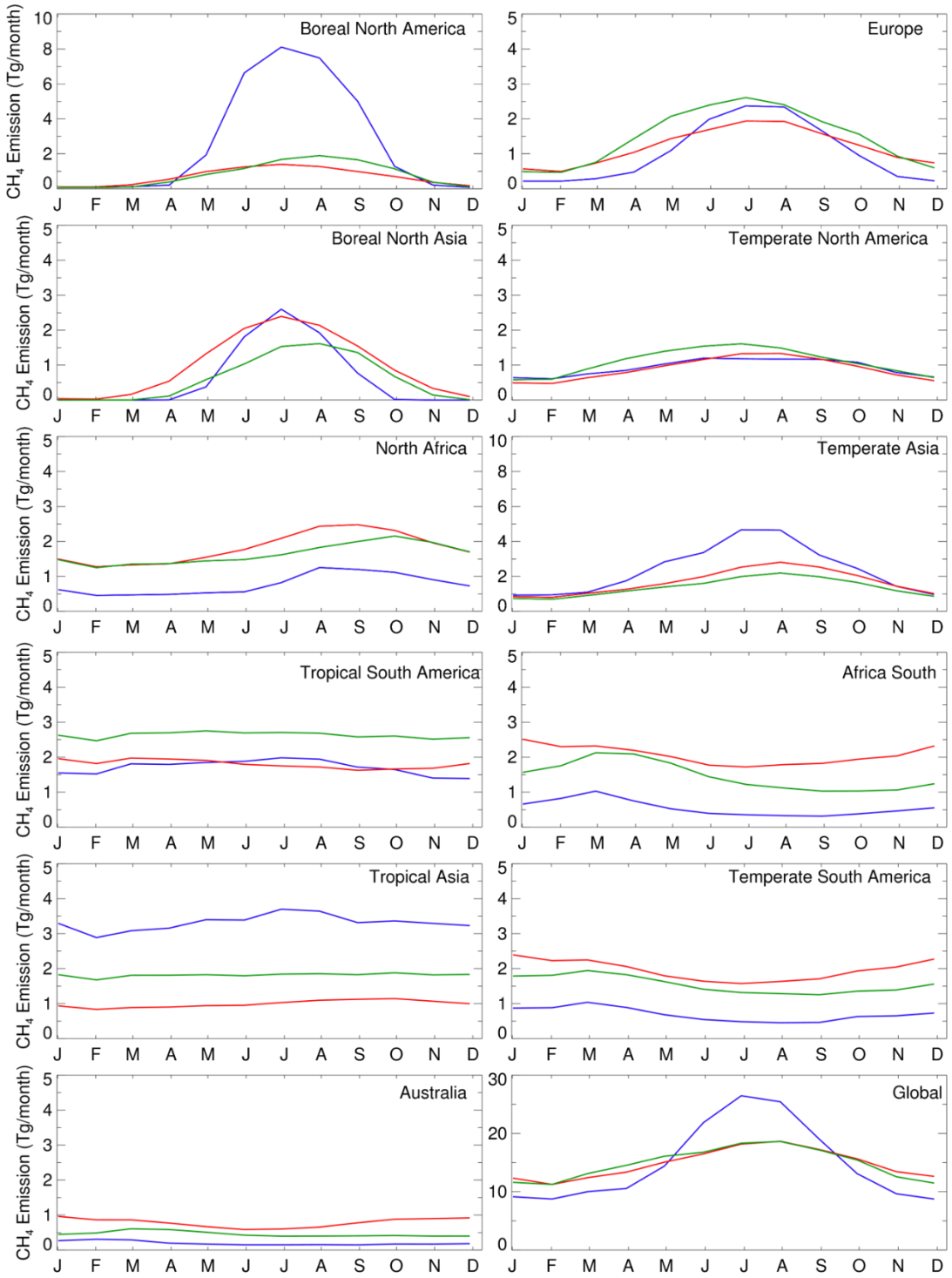


*Figure 5.14 Seasonal cycle of $CH_4$ wetland emissions, in Tg/month, from JU (green), JP (blue) and BL (Bloom et al., 2012) (red). Monthly averages are taken from years where data are available, JU (1993-2012), JP (1993-2009) and BL (2003-2011). Individual panels show regions defined in Figure 5.10 and the bottom right panel shows the global emissions.*

## 5.4 Comparisons of TOMCAT $CH_4$ with Observations

The three emission inventories were used as the $CH_4$ flux boundary conditions in TOMCAT each with three different OH loss fields, RE, AO and NO, as described in Chapter 4. These were then compared with surface, TCCON and GOSAT observations. The length of the flask record used (1993-2012) allows for the assessment of long-term trends in the TOMCAT simulations, whilst the TCCON and GOSAT observations allow for the assessment of column $CH_4$.

### 5.4.1 Flask Comparisons

The results of the TOMCAT simulations have been compared to the NOAA surface sites listed in Chapter 4 (see Figure 5.15). The model predicted $CH_4$ fields have been linearly interpolated to the latitude, longitude and altitude of the surface sites. Monthly mean observations and model output are used when available between 1993 and 2012. At high-latitude southern hemisphere sites the difference between simulations using JU, JP and BL is small. These sites observe well-mixed background $CH_4$ concentrations, because there are little or no local emission sources. The difference between the model runs becomes more apparent at low-latitude and high-latitude northern hemisphere sites, where JP exhibits high seasonality.

The initial global $CH_4$ concentration in the model is scaled to match the observation network global mean, although the concentrations do not match at individual sites (see Chapter 4). The initial model average $CH_4$ concentration at the 7 high-latitude northern sites (>60° N) is 1867 ppb, which is 29 ppb higher than observed (1838 ppb). This is balanced out in the southern hemisphere where the model average at the 3 high-latitude southern sites (>60° S) is 1659 ppb, which is 24 ppb lower than observed (1683 ppb). Assuming the source and sink distributions are broadly accurate during the spin-up phase, this would suggest that the interhemispheric transport in the model is too slow from the northern hemisphere, where a majority of emissions occur, to the southern hemisphere. This was previously noted in the TransCom study (Patra *et al*., 2011), in which the TOMCAT model predicted larger inter-hemispheric gradients of $CH_4$, $CH_3CCl_3$ and $SF_6$ concentrations compared to both observed values and other models involved in the intercomparison.

The RMSE and correlation coefficient are calculated for each model simulation and observation (see Table 5.3). Simulations with NOAA OH are selected for subsequent analysis because they result in the lowest RMSE and highest correlation coefficients, hereafter referred to as TOM_JU, TOM_JP and TOM_BL. RMSE is taken by calculating the residual error between the model and

observation, which is squared, averaged, and then square-rooted as given by equation 5.6, where $n$ is the number of months, and $CH_{4m}$ and $CH_{4o}$ are the modelled and observed $CH_4$, respectively.

$$RMSE = \sqrt{\frac{\sum(CH_{4m} - CH_{4o})^2}{n}} \qquad \textbf{(5.6)}$$

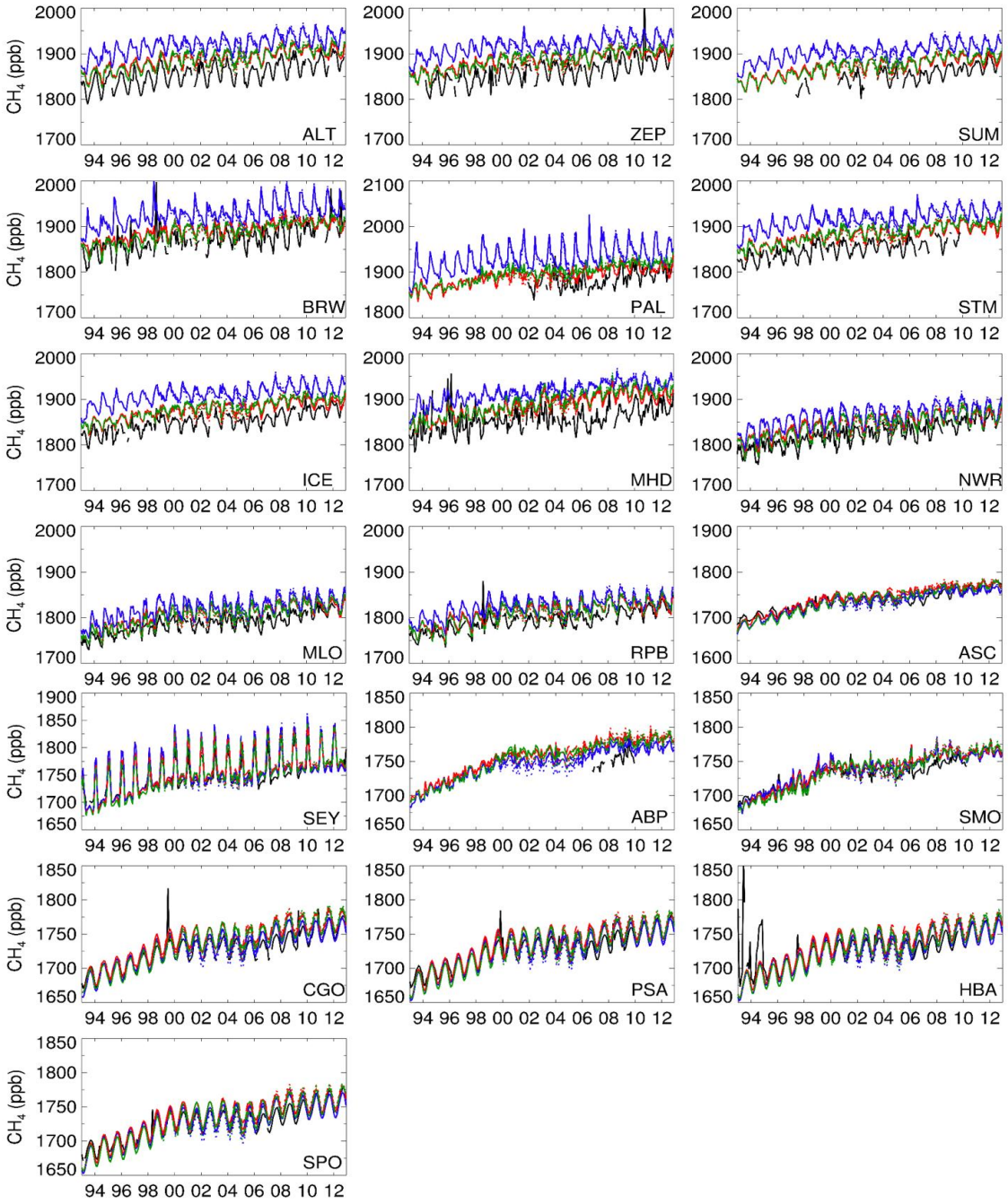


*Figure 5.15 Monthly mean surface $CH_4$ (ppb) from 19 NOAA observation sites (black) from 1993 to 2012, where data are available. Also shown are results from three TOMCAT 3-D CTM simulations, TOM_JU (green), TOM_JP (blue) and TOM_BL (Bloom et al., 2012) (red). Different line styles represent simulations with different OH fields, Rigby et al. (2013) AGAGE OH anomalies (dotted), Montzka et al. (2011) NOAA OH anomalies (solid) and repeat OH field (dashed).*

Table 5.3 shows that TOM_JU predictions correlate the best with observations at all but two sites and that both TOM_JU (22.8 ppb) and TOM_BL (22.6 ppb) produce lower average RMSE values than TOM_JP (37.6 ppb). This suggests that when the interannual and the seasonal variability are both taken into account, TOM_JU and TOM_BL agree comparably well with observations. The large RMSE values in the northern high latitudes are, in part, due to the initial state having high concentrations at those sites.

| Station | TOMCAT simulation | | | | | |
|---|---|---|---|---|---|---|
| | TOM_JU | | TOM_JP | | TOM_BL | |
| | Correlation Coefficient | RMSE (ppb) | Correlation Coefficient | RMSE (ppb) | Correlation Coefficient | RMSE (ppb) |
| ALT | 0.89 | 31.9 | 0.58 | 65.7 | 0.87 | 32.2 |
| ZEP | 0.80 | 30.6 | 0.53 | 61.0 | 0.76 | 30.3 |
| SUM | 0.82 | 29.6 | 0.48 | 59.2 | 0.77 | 27.5 |
| BRW | 0.62 | 26.9 | 0.31 | 61.5 | 0.52 | 30.3 |
| PAL | 0.47 | 31.0 | 0.18 | 61.6 | 0.56 | 23.9 |
| STM | 0.81 | 29.6 | 0.47 | 61.9 | 0.80 | 28.5 |
| ICE | 0.87 | 29.0 | 0.53 | 61.0 | 0.85 | 26.1 |
| MHD | 0.63 | 41.5 | 0.54 | 63.3 | 0.64 | 36.4 |
| NWR | 0.91 | 21.6 | 0.85 | 39.4 | 0.89 | 24.0 |
| MLO | 0.93 | 18.8 | 0.87 | 33.1 | 0.92 | 18.7 |
| RPB | 0.86 | 20.3 | 0.82 | 32.4 | 0.85 | 19.8 |
| ASC | 0.94 | 11.9 | 0.92 | 11.8 | 0.92 | 12.3 |
| SEY | 0.95 | 12.1 | 0.94 | 15.1 | 0.95 | 12.5 |
| ABP | 0.69 | 30.9 | 0.64 | 23.7 | 0.60 | 34.1 |
| SMO | 0.95 | 10.3 | 0.92 | 10.6 | 0.94 | 10.6 |
| CGO | 0.93 | 14.0 | 0.92 | 10.8 | 0.93 | 15.2 |
| PSA | 0.95 | 11.5 | 0.93 | 10.5 | 0.94 | 12.5 |
| HBA | 0.70 | 21.9 | 0.68 | 21.4 | 0.68 | 22.1 |
| SPO | 0.96 | 10.7 | 0.95 | 9.5 | 0.96 | 11.6 |
| Average | 0.83 | 22.8 | 0.69 | 37.6 | 0.81 | 22.6 |

*Table 5.3 Correlation coefficient and RMSE values for $CH_4$ flask observations compared with TOMCAT model output using NOAA-derived OH field between 1993 and 2012, where TOM_JU uses JULES wetland emissions, TOM_JP uses JULES wetland emissions driven by prescribed parameters and TOM_BL uses a top-down wetland dataset (Bloom et al., 2012).*

The mean absolute percentage error (MAPE) (Equation 5.7) is used in Figure 5.16 to assess model performance. This highlights the large error in the northern high latitude in TOM_JP and the similarity between TOM_JU and TOM_BL. At most sites the choice of wetland inventories produces a larger difference in error than the OH field; however there is some overlap with TOM_JU and TOM_BL at some sites.

$$MAPE = \frac{1}{n}\sum\left|\frac{CH_{4o}-CH_{4m}}{CH_{4o}}\right| \qquad \textbf{(5.7)}$$

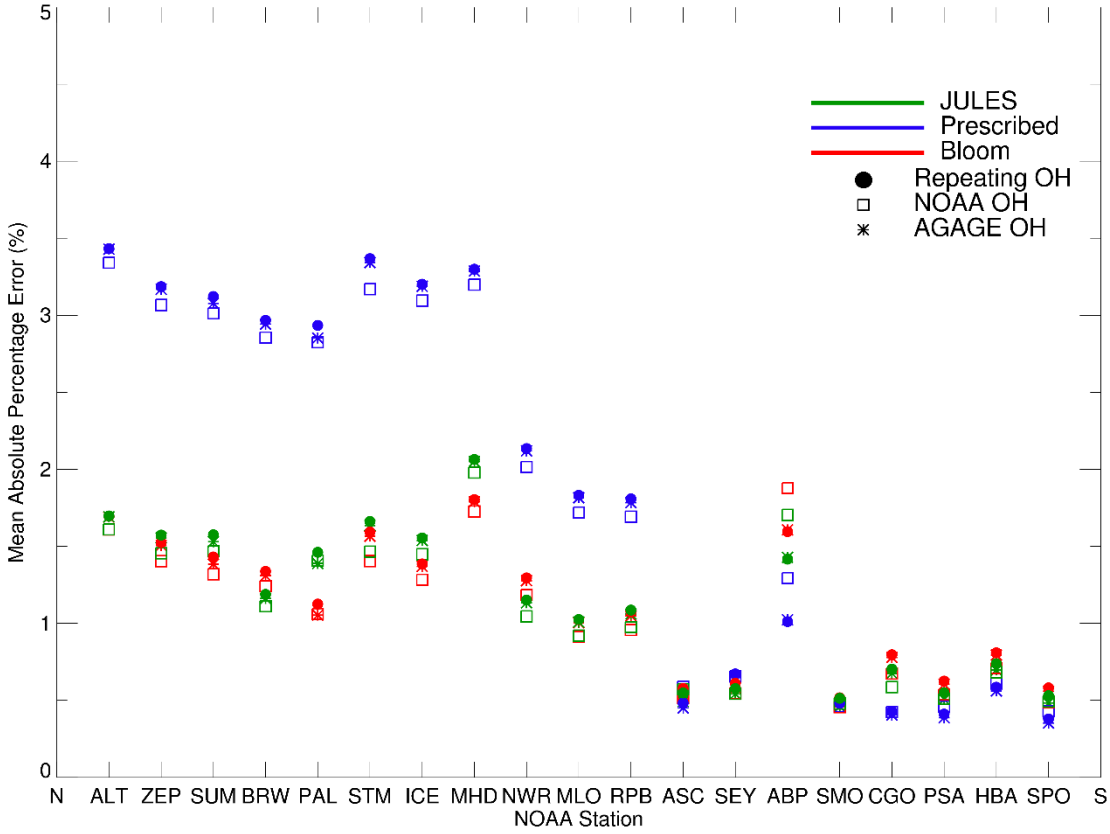


*Figure 5.16 The mean absolute percentage error (%) between observations and TOMCAT simulations, TOM_JU (green), TOM_JP (blue) and TOM_BL (Bloom et al., 2012)*

The ability of the TOMCAT model simulations to capture the interannual and seasonal variability separately is displayed in Figure 5.17 and Figure 5.18. All three model simulations capture the interannual variability of $CH_4$ well. Notably, the pause from 1999 to 2006 is captured by all three model simulations due, not only to an increase in OH loss (see Chapter 4), but also decreased wetland emissions. The observed continued growth between 2010 and 2012 is not captured by the model simulations, however over this period TOM_JP (2009-2012) and TOM_BL (2012) use climatological wetland emissions that would not capture a potential increase in emissions. TOM_JU predicts above average wetland emissions in 2010 (182.9 Tg), 2011 (183.6 Tg) and 2012 (179.9 Tg) but this is not sufficient to reproduce the observed growth. A possible increase in anthropogenic (2009-2012) and biomass burning (2011-2012) emissions (see Chapter 2) is not accounted for in the model simulations and could contribute to this increase.

The relatively large seasonal cycle at high-latitude southern hemisphere stations is a result of a reduction in loss during southern hemisphere winter because of a decrease in sunlight and slower

photochemistry (see Figure 5.18). The same is observed, to a lesser extent, at northern hemisphere high-latitude sites, where the reduction in oxidative loss coincides with a decrease in wetland emissions as a result of a reduction in surface temperatures. TOM_JP fails to capture the seasonal cycle at most northern sites, with the timing and magnitude of the cycle not comparable to the observations. TOM_JU and TOM_BL both capture the seasonal cycle at most sites, even when the seasonal cycle is small (ABP). The background seasonal cycle over the Antarctic stations (PSA, HBA and SPO) is well captured in all model simulations.

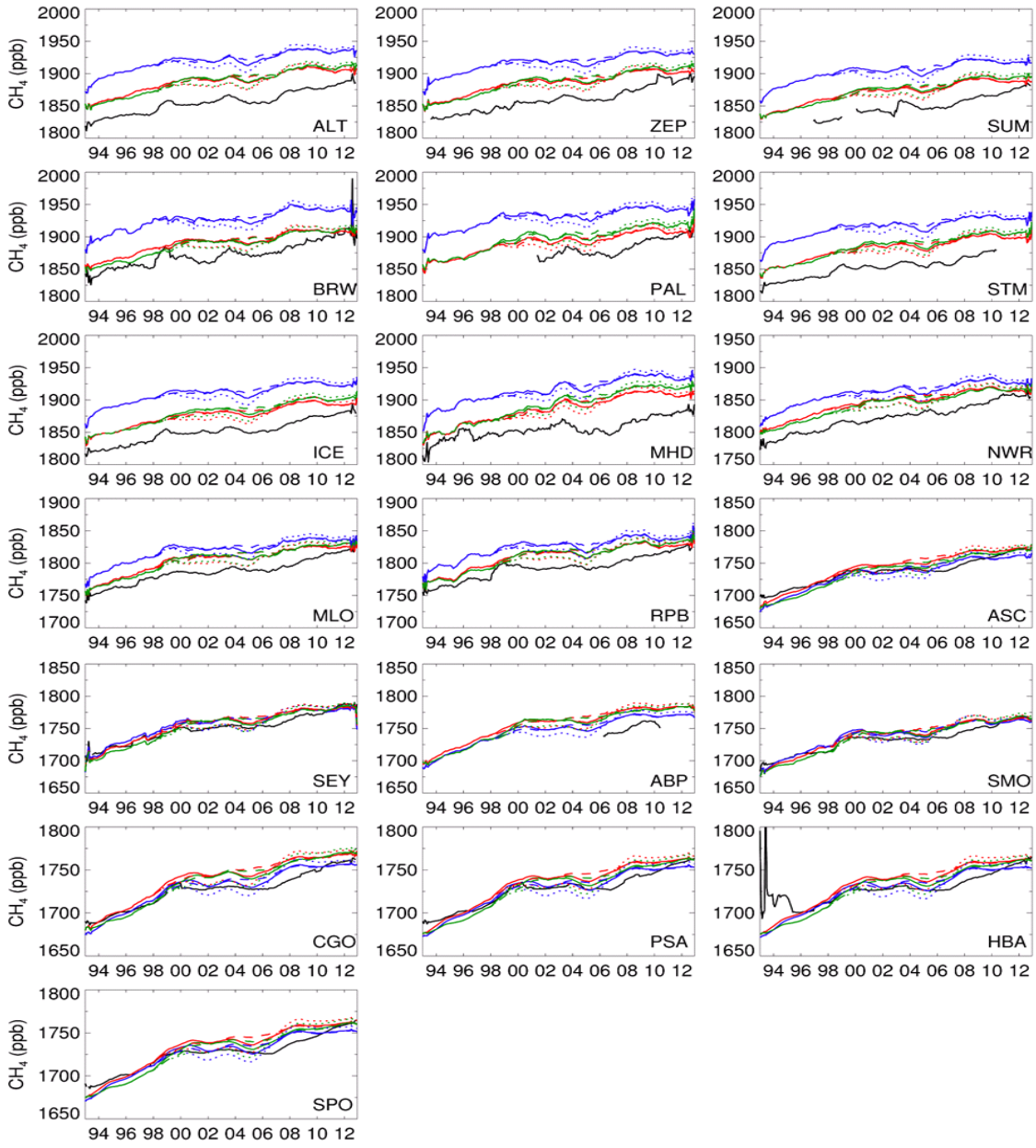


*Figure 5.17 Deseasonalised monthly mean surface $CH_4$ (ppb) from 19 NOAA observations (black) and TOMCAT from 1993 to 2012, where data are available. Labelling is the same as Figure 5.15.*

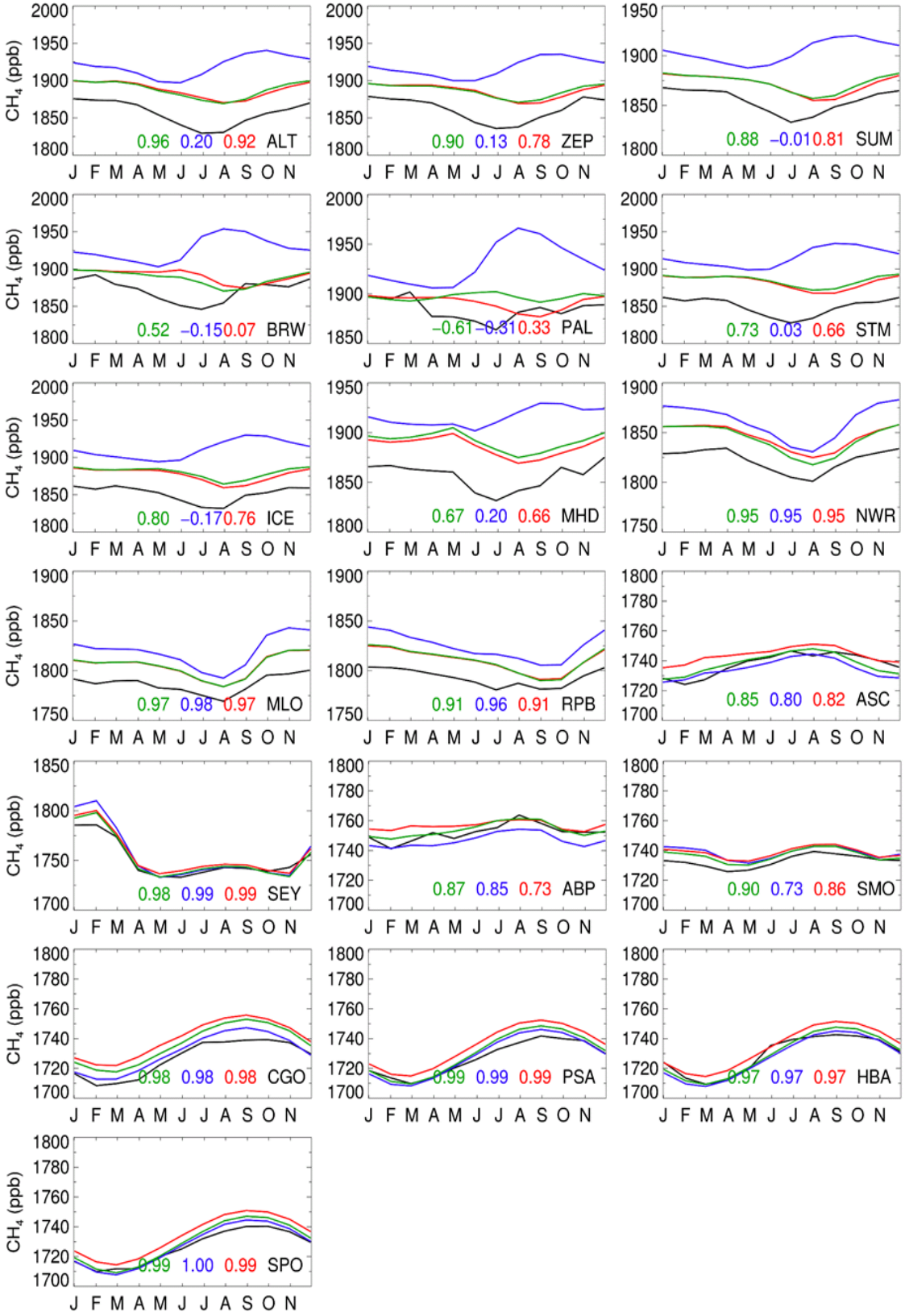


*Figure 5.18 Seasonal cycle of monthly mean surface $CH_4$ (ppb) from 19 NOAA observation sites (black) from 1993 to 2012, where data are available. Also shown are results from three TOMCAT 3-D CTM simulations TOM_JU (green), TOM_JP (blue) and TOM_BL (red), all using the Montzka et al. (2011) NOAA OH anomalies. Correlation coefficients of model and observations are displayed for TOM_JU (green), TOM_JP (blue) and TOM_BL (red).*

The comparisons show that all model simulations capture the interannual variability for most of the time series except the observed growth in the final three years. The average annual emissions of 177 Tg/yr seem reasonable because the overall growth over the 20 year period is comparable to observed growth. TOM_JP emissions in the boreal northern hemisphere are likely too high, resulting in a bias between the model and observations. The seasonal cycle is well captured at all sites by TOM_JU and TOM_BL but not by TOM_JP. Tropical wetland regions remain untested because of a lack of NOAA observations.

## 5.4.2 Satellite Comparisons

GOSAT measures weighted air column mixing ratios of $CH_4$, $XCH_4$, which are sensitive in the mid to lower troposphere, at a high spatial resolution. The $XCH_4$ estimates used here are from a proxy retrieval method described by Parker *et al.* (2011), which have a weighted averaging kernel applied to account for differing sensitivities throughout the atmosphere. The remaining retrieval information is provided by an a priori profile, taken from model simulations. To account for this weighting the averaging kernel is applied to the TOMCAT model. The sensitivity of the averaging kernel is not only dependent on height but also on the solar zenith angle (SZA) (see Figure 5.19). The retrievals typically have most sensitivity between 200 hPa and 900 hPa.

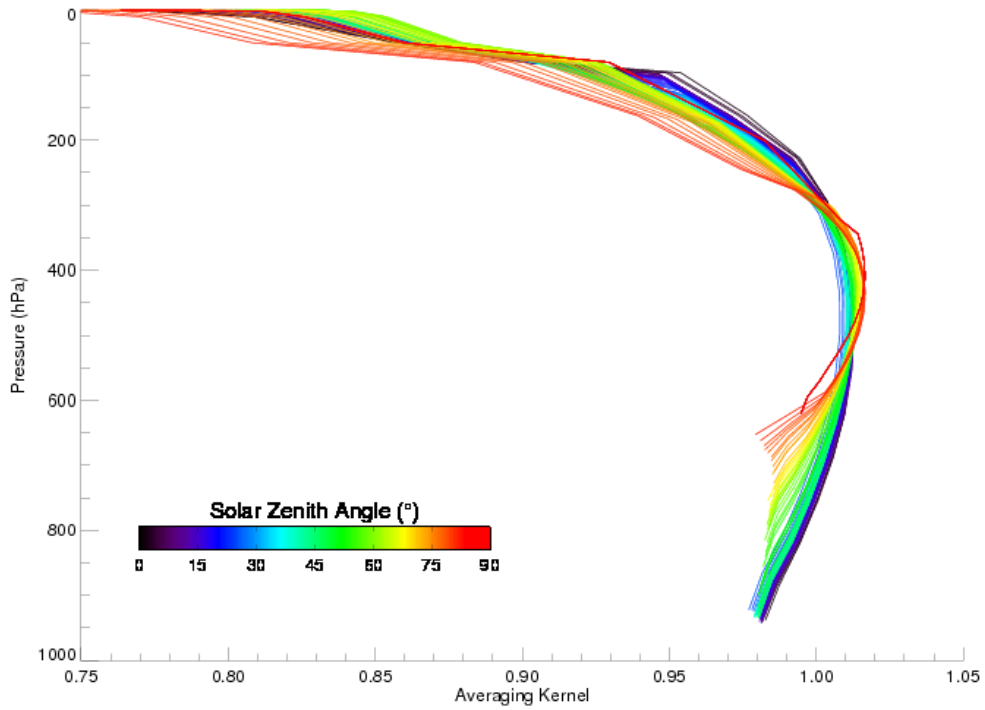


*Figure 5.19 Typical GOSAT averaging kernel across 20 pressure levels and 90, 1° solar zenith angle bins. Colour range represents solar zenith angles from 0° to 90°.*

The averaging kernel and satellite column $CH_4$ a priori vertical profile are used with the model output to produce an $XCH_4$ for each retrieval, shown in equation 5.8 adapted from Wunch *et al*. (2010), where $p_{wfn}$ is the pressure weighting function at level n, n_max is the number of levels, $CH_{4ap}$ is the a priori, $A_n$ is the averaging kernel at level n and $CH_{4m}$ is the model $CH_4$. Model output is interpolated horizontally, temporally and from 60 levels to 20 levels so the averaging kernel can be applied using the method described by Connor *et al*. (2008). The model profile would not be maintained if direct interpolation methods were used because the model column profile does not vary linearly. To ensure the model profile is accurately interpolated, to conserve the column, several steps are required. First, the profile volume mixing ratio (VMR) is converted into partial columns. These are then vertically integrated to provide a cumulative column, which is the total column below the pressure level. The cumulative column is then interpolated onto the satellite retrieval levels, where it can be converted back into a VMR.

$$XCH_4 = \sum_{n=1}^{n\_max} p_{wf_n}(CH_{4ap} + A_n(CH_{4m} - CH_{4ap})) \quad \textbf{(5.8)}$$

GOSAT data are used from April 2009 to December 2012, providing a full seasonal cycle for almost 3 years. These are used to analyse trends in $XCH_4$ concentration and seasonal cycles, both globally and locally. Figure 5.20 highlights the spatial coverage of satellite retrievals, showing poor coverage over boreal regions in northern hemisphere winter.

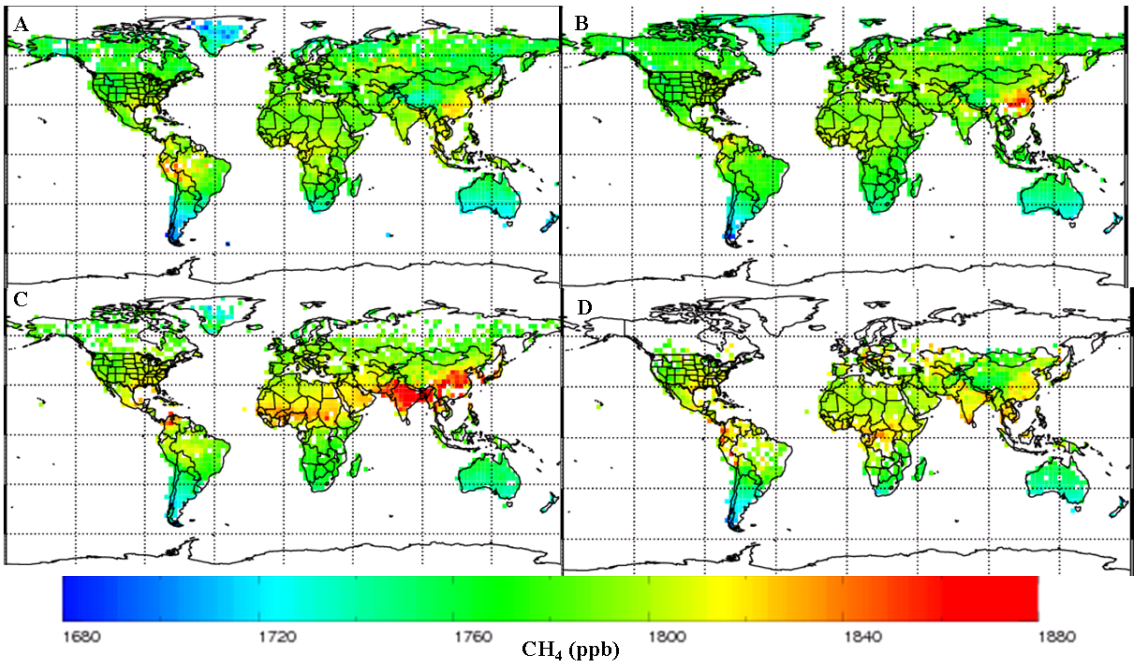


*Figure 5.20 Global monthly mean $XCH_4$ concentrations (ppb) from GOSAT in 2.8° by 2.8° bins for (a) March, (b) June, (c) September and (d) December, 2010.*

The comparisons of TOMCAT simulations with GOSAT $XCH_4$ are performed using annually repeating OH fields (see Chapter 4) because there are little or no OH anomaly data available over the GOSAT period (2009-). Figures 5.21, 5.22 and 5.23 show the differences between the model simulations, with the averaging kernel applied, and GOSAT for the same months as shown in Figure 5.20. These show overall good agreement with GOSAT observations. All three simulations show a slightly high higher in the boreal northern hemisphere and lower in the tropics. This is most evident in simulation TOM_JP, which frequently differs by more than 50 ppb, particularly in September. Over the entire GOSAT period there is reasonable model agreement, GOSAT estimates a global average $CH_4$ concentration of 1790.3 ppb, whilst TOM_JU, TOM_JP and TOM_BL estimate averages, after the averaging kernel is applied, of 1789.9 ppb, 1795.3 ppb and 1787.8 ppb, respectively. This suggests that the model emissions are well balanced with the sinks. The mean bias values between TOM_JU, TOM_JP and TOM_BL, and GOSAT are 11.8 ppb, 19.2 ppb and 11.8 ppb, respectively, showing that overall TOM_JU and TOM_BL agree better with GOSAT observations than TOM_JP. Similarly, the RMSE values are lower for TOM_JU (6.7 ppb) and TOM_BL (6.6 ppb), than for TOM_JP (10.4 ppb).

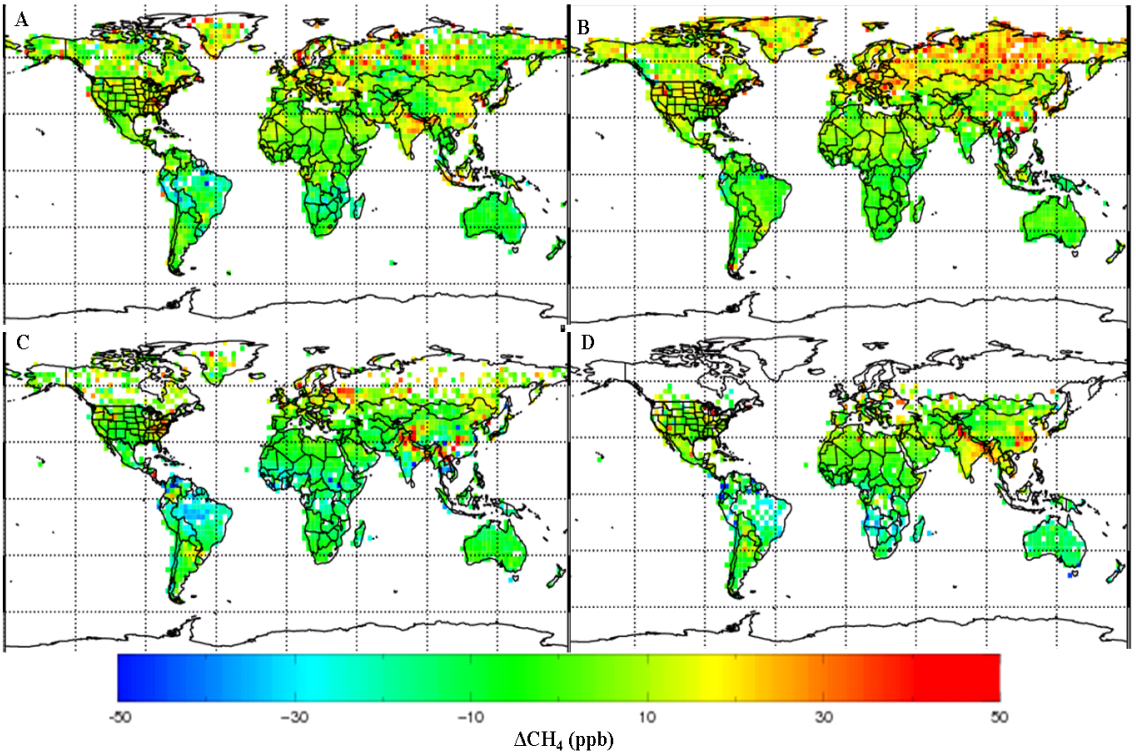


*Figure 5.21 Difference in global monthly mean $XCH_4$ concentrations (ppb) between TOM_JU and GOSAT observations (TOM_JU – GOSAT) for (a) March, (b) June, (c) September and (d) December, 2010. A GOSAT averaging kernel has been applied to the model data. Note that all non-wetland emissions are the same for each model simulation.*

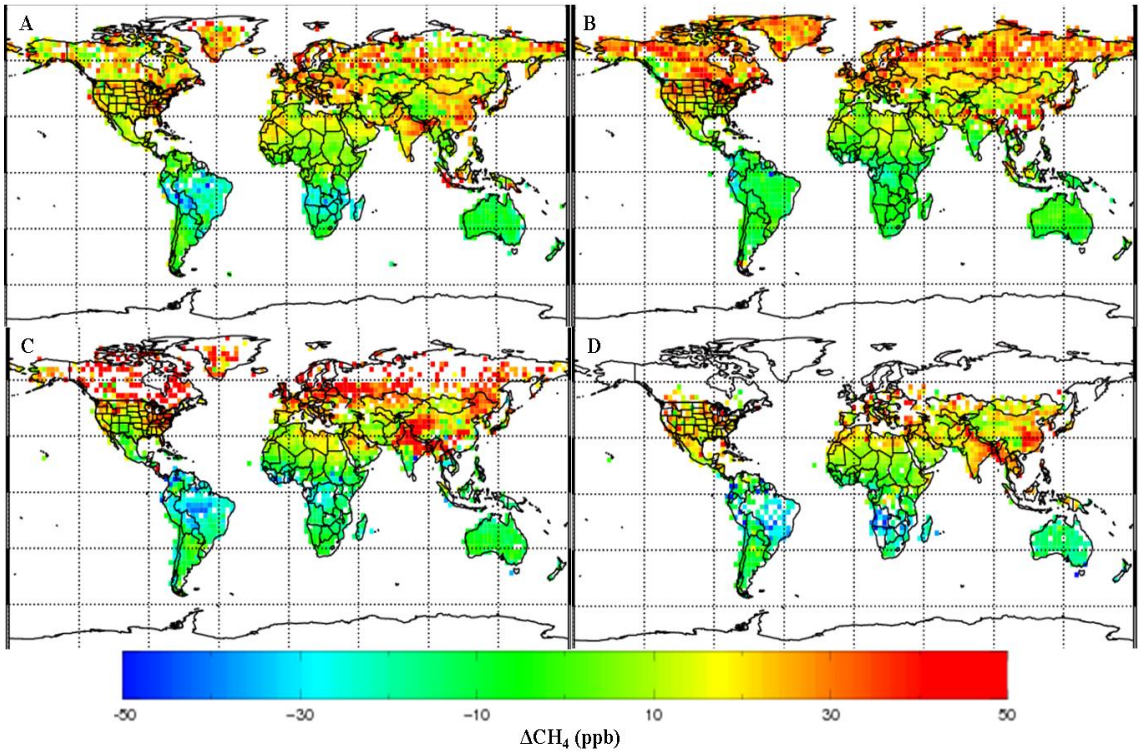


*Figure 5.22 As Figure 5.21 but comparison between GOSAT observations and TOM_JP.*

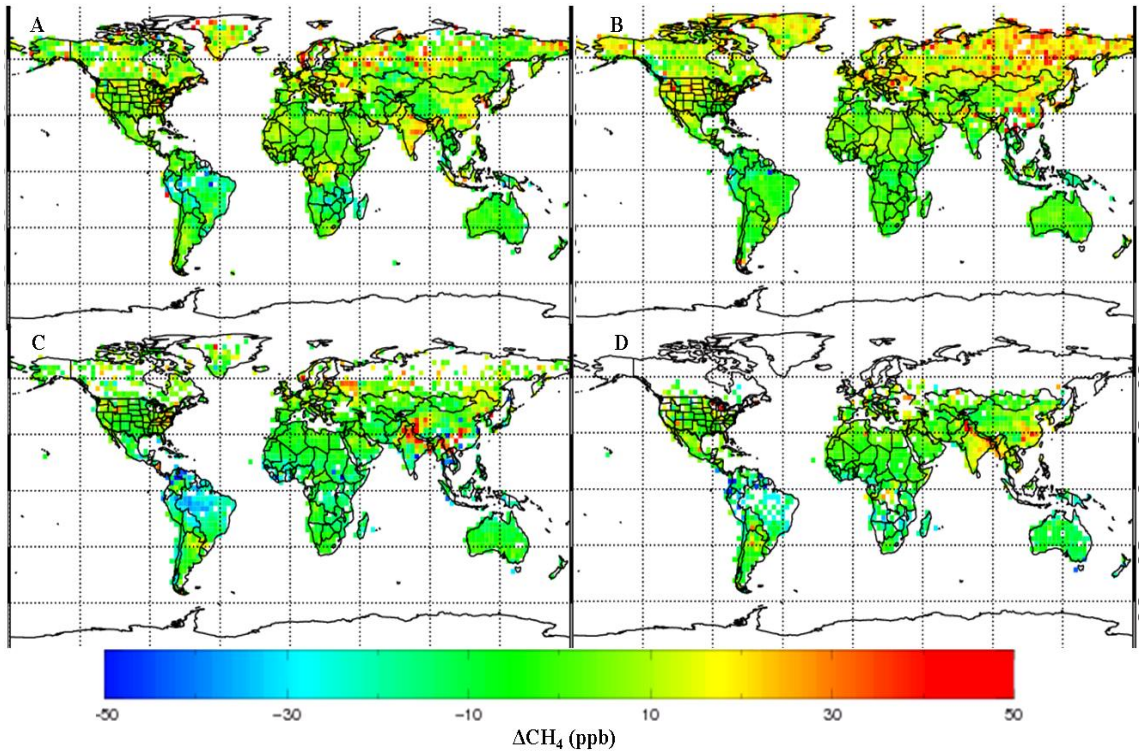


*Figure 5.23 As Figure 5.21 but comparisons between GOSAT observations and TOM_BL.*

To assess the regional and temporal differences between the three TOMCAT simulations and GOSAT observations, data are split into the regions defined by Figure 5.10 and shown in Figure 5.24 with the correlation coefficients labelled. Overall all three simulations capture the variability in $XCH_4$ concentrations in each region well (R>0.6); however the correlation coefficients between simulations and observations reveal that differences in wetland emissions are the main cause of the model data differences.

The seasonal ranges in TOM_JP in Boreal North America (31.6 ppb), Europe (24.4 ppb), Boreal North Asia (31.8 ppb), Temperate North America (32.2 ppb) and Temperate Asia (41.8 ppb) are 25-58% larger than the observed range (22.1 ppb, 17.0 ppb, 25.0 ppb, 20.4 ppb and 33.5 ppb). TOM_JU provides the highest correlation with observations in all five of these northern hemisphere regions, suggesting that boreal wetland emissions are well represented in TOM_JU. The high correlation coefficients for all simulations for the Temperate Asia region is influenced by the annually repeating rice emissions, which reproduce the observed seasonal cycle well.

The lowest correlation coefficients for both TOM_JU (R = 0.69) and TOM_JP (R = 0.63) are observed over both the Amazon and Orinoco Basin in Tropical South America, TOM_BL correlates similarly in this region (R = 0.61). Assuming biomass burning emissions are accurate and at least one of the parameter sets used to drive the $CH_4$ flux estimates are reasonable, this suggests that the process description used to described wetland emissions is not sufficient to capture the seasonal cycle accurately. A possible alternative explanation is that all three inventories are driven by inaccurate wetland fractions for the Amazon and/or the Orinoco basin.

All three model simulations fail to capture the trend in global growth observed by GOSAT observations between 2009 and 2012. From the start of the GOSAT time series till the end the global $CH_4$ increased at a rate of 6.8 ppb/yr, this compares to 2.8 ppb/yr in TOM_JU and only 1.6 ppb/yr and 1.5 ppb/yr in TOM_JP and TOM_BL, respectively. This could be a result of an increase in emissions and/or a decrease in sinks. Increased non-wetland emissions are most likely due to increased anthropogenic or biomass burning sources, which are not accounted for in any of the model simulations. Only JU extends for long enough to fully account for a potential increase in emissions from wetlands. A rise in wetland emissions in later years could have been caused by the increased ground water storage that occurred over Australia, northern South America and Southeast Asia during the 2011 La Niña event (Boening *et al.*, 2012). Based on the results presented here an increase in wetland emissions since 2009 can explain only a comparably small fraction (~20%) of the observed increase in growth between 2009 and 2012. The highest observed growth trend in GOSAT is in Tropical Asia (8.2 ppb/yr), this is also the case for TOM_JU (4.6 ppb/yr), TOM_JP (3.2 ppb/yr) and TOM_BL (3.2 ppb/yr).

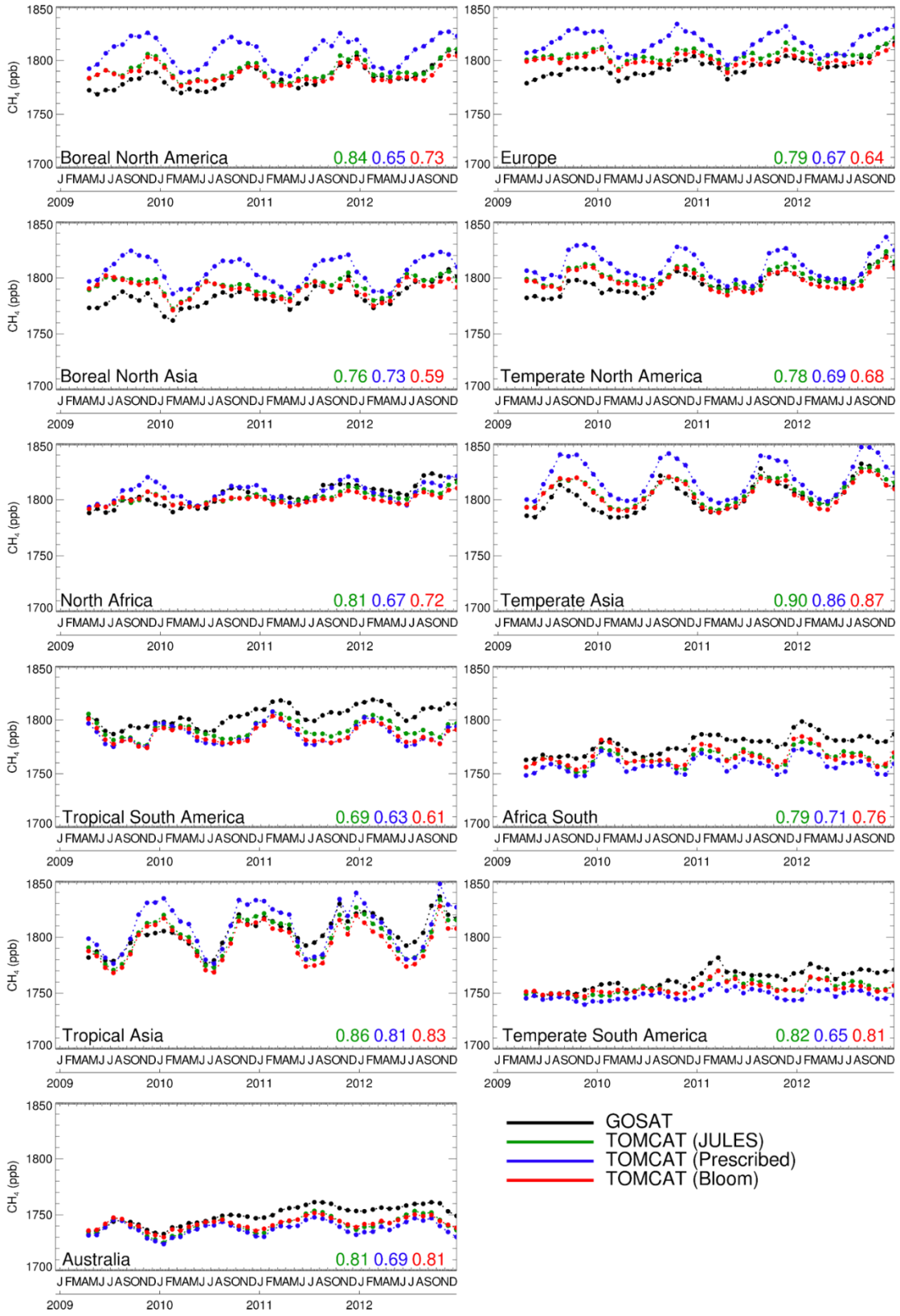


*Figure 5.24 Regional monthly mean $XCH_4$ concentrations (ppb) from GOSAT between April 2009 and December 2012 (black). Also shown are regional monthly mean $XCH_4$ concentrations from three TOMCAT simulations with GOSAT averaging kernels applied, TOM_JU (green), TOM_JP (blue) and TOM_BL (red). Correlation coefficients of model and observations are displayed for TOM_JU (green), TOM_JP (blue) and TOM_BL (red).*

Comparisons of all GOSAT retrievals with each of the TOMCAT simulations after the averaging kernel has been applied shows that TOM_JU and TOM_BL correlate equally well when compared to GOSAT (R = 0.84) while TOM_JP correlated less well (R = 0.76) (see Figure 5.25). The RMSE and mean difference are also similar for both JU and BL and both are lower than values for JP.

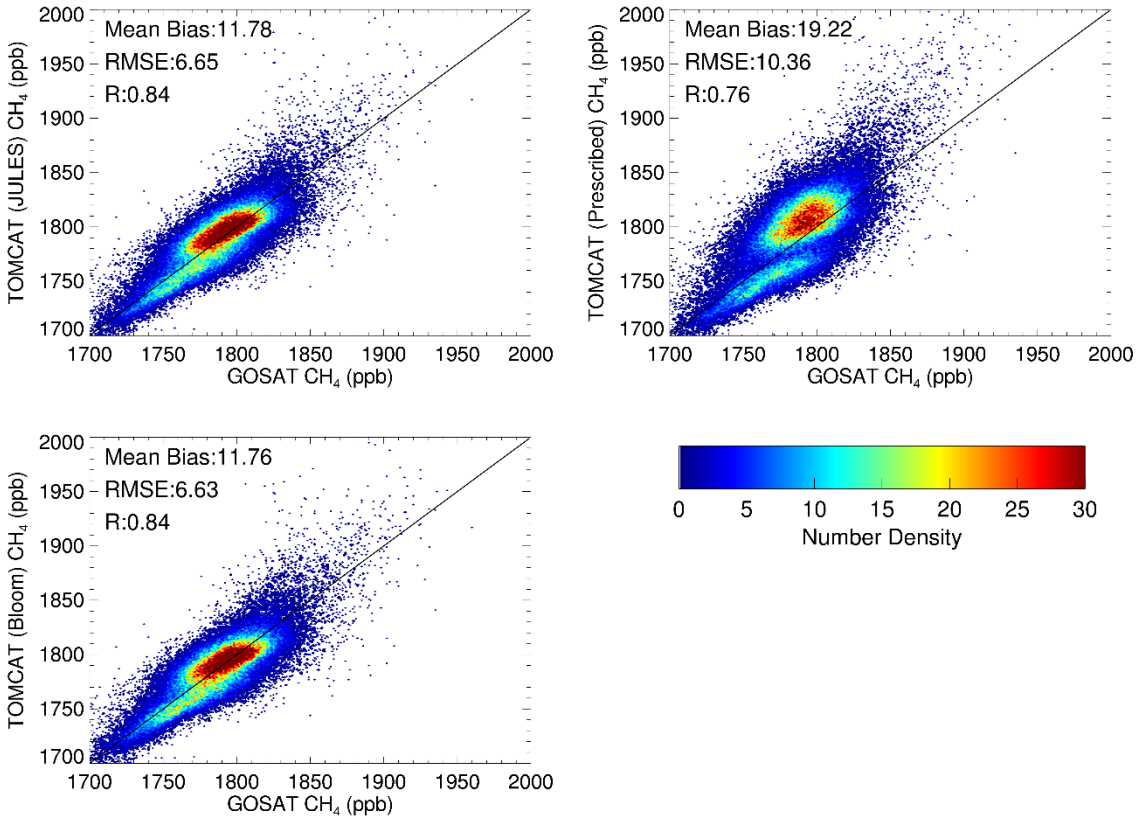


*Figure 5.25 Number density correlation of GOSAT with TOMCAT model output driven by three different wetland emission inventories between April 2009 and December 2012. Points are gridded into 1 ppb by 1 ppb bins. Also shown are the mean bias, RMSE and correlation coefficient of each comparison.*

Overall GOSAT comparisons suggest that TOM_JU and TOM_BL produce the most accurate seasonal cycle in most regions and provide the lowest bias. The overall results are in agreement with those found previously in the surface site comparisons. The results suggest that an improved process description is required to capture the observed seasonality in the Amazon, Orinoco and Pantanal, this might include the addition of $CH_4$ transport or oxidation within the soil. The observed increase in $CH_4$ growth is not captured by any of the TOMCAT simulations suggesting missing sources or sinks within the model simulations.

## 5.4.3 TCCON Comparisons

As a final analysis the three TOMCAT simulations were compared with atmospheric $CH_4$ measurements from 15 TCCON stations listed in Table 5.3. Further details of the TCCON sites and retrieval method are discussed in Chapter 2. The sites surface elevation varies from sea-level, DB and WG (0.03 km), to over 2 km, IZ (2.37 km), and over a range of land types. Three TCCON sites were not included in this analysis because their time series length were considered too short (<6 months). The data provide weighted column mean $CH_4$ concentrations at high northern latitudes, EU and SO, mid northern latitudes, BI, GM, JC, JF, KA, OC, OR and PA, and mid southern latitudes, LH, LL, WG, but not at latitudes below 45.04°S. The lack of coverage at high southern latitudes should not effect this study as there are no wetlands in that region. The network only provides data at one low-latitude northern hemisphere site, IZ, and one low-latitude southern hemisphere site, DB. A map of the sites used is shown in Figure 5.26, which reveals the lack of coverage over major wetland regions, such as the Amazon River basin, the Congo and the West Siberian Plain. This hinders the ability to differentiate between errors in the wetland and non-wetland emissions.

| Site Code | Site Name | Latitude | Longitude | Altitude (km) | Start Date | End Date |
|---|---|---|---|---|---|---|
| BI | Bialystok, Poland | 53.23 | 23.03 | 0.18 | 01/03/2009 | Ongoing |
| DB | Darwin, Australia | -12.42 | 130.89 | 0.03 | 28/08/2005 | Ongoing |
| EU | Eureka, Canada | 80.05 | -86.42 | 0.61 | 24/07/2010 | Ongoing |
| GM | Garmisch, Germany | 47.48 | 11.06 | 0.74 | 16/07/2007 | Ongoing |
| IZ | Izana, Spain | 28.3 | -16.5 | 2.37 | 18/05/2007 | Ongoing |
| JC | Pasadena, USA | 34.2 | -118.18 | 0.39 | 08/01/2007 | 23/06/2008 |
| JF | Pasadena, USA | 34.2 | -118.18 | 0.39 | 20/05/2011 | 31/01/2012 |
| KA | Karlsruhe, Germany | 49.1 | 8.44 | 0.12 | 19/04/2010 | Ongoing |
| LH | Lauder, New Zealand | -45.04 | 169.68 | 0.37 | 20/06/2004 | 28/02/2011 |
| LL | Lauder, New Zealand | -45.04 | 169.68 | 0.37 | 02/02/2010 | Ongoing |
| OC | Lamont, USA | 36.6 | -97.49 | 0.32 | 06/072008 | Ongoing |
| OR | Orleans, France | 47.97 | 2.11 | 0.13 | 29/08/2009 | Ongoing |
| PA | Park Falls, USA | 45.95 | -90.27 | 0.44 | 26/05/2004 | Ongoing |
| SO | Sodankyla, Finland | 67.37 | 26.63 | 0.19 | 06/02/2009 | Ongoing |
| WG | Wollongong, Australia | -34.41 | 150.88 | 0.03 | 26/06/2008 | Ongoing |

*Table 5.4 Information about the 15 TCCON $XCH_4$ observation sites used in this study. Data are used up until the end of 2012 where available. Note that Pasadena and Lauder have used two different instruments at each site for retrievals, which are treated as separate time series.*

The vertical sensitivity of TCCON instruments to atmospheric $CH_4$ varies at each station and site specific averaging kernels are applied to model data before any comparisons are made. The final model comparisons are a combination of an a priori and the original model data. The averaging kernel is applied in the same way for TCCON as for GOSAT but the sensitivity of the sites differ with altitude and SZA, as shown in Figure 5.27. This also includes the same interpolation method and averaging kernel equation (5.6). The TCCON averaging kernels are provided on 71 vertical levels and across 16, 5° SZA bins from 10° to 90°. The retrieval sensitivity for TCCON is typically much more dependent on the SZA than GOSAT.

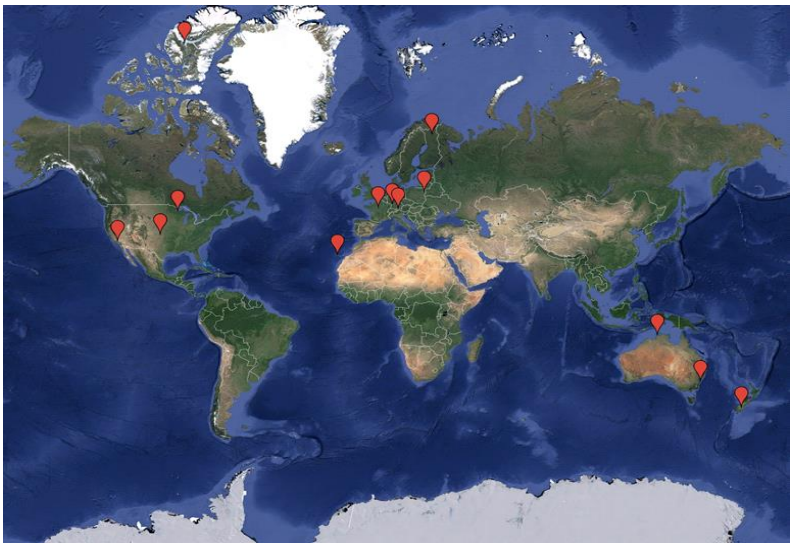

*Figure 5.26 Map showing spatial distribution of the 15 TCCON measurement sites used.*

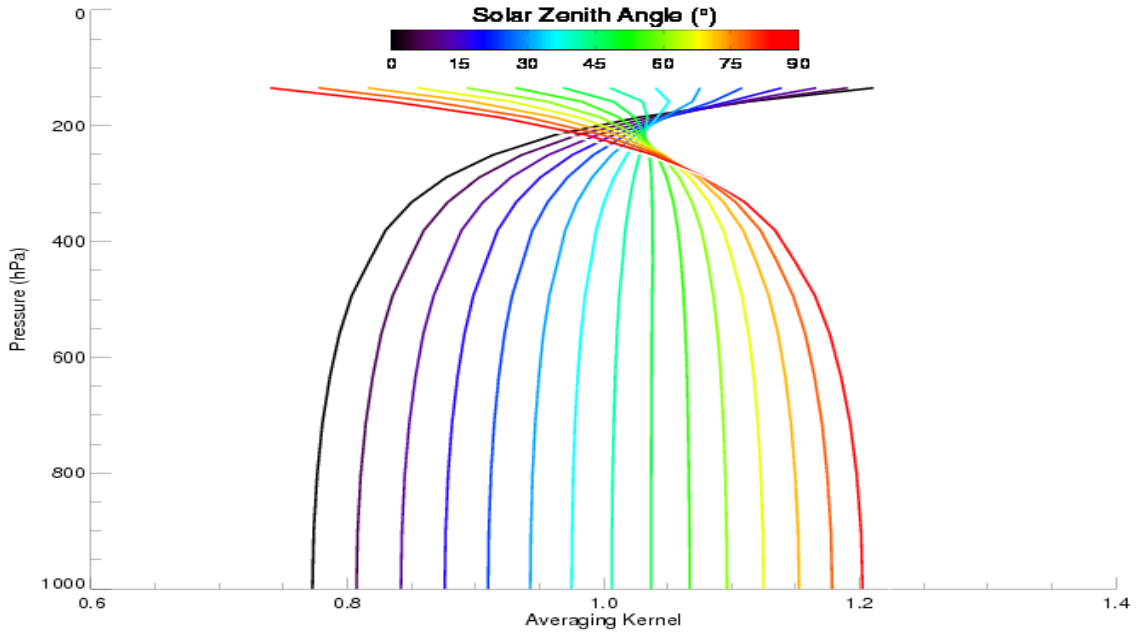


*Figure 5.27 Typical TCCON averaging kernel across 71 pressure levels and 16, 5° solar zenith angle bins from 10° to 90°. Colour range represents solar zenith angles from 10° to 90°.*

The length of the TCCON time series varies at different sites, PA provides almost continuous data from 2004, whilst JC and JF provide less than a year of continuous data. EU and SO operate seasonally and so the data is fragmented and only available in certain months. For an accurate representation of the seasonal cycle at a site continuous data are required over multiple years.

Figure 5.28 shows comparisons of all three TOMCAT simulations with repeating OH fields, with TCCON observations. The TCCON times are matched with the nearest available 10-day average TOMCAT $CH_4$ predictions before the averaging kernel is applied. The data are then binned into monthly bins. TOM_JU predictions correlate the best with TCCON averaged over all sites (R = 0.63), followed by TOM_JP (R = 0.59) and TOM_BL (R = 0.56). When compared with TCCON models provide correlation coefficients within 0.1 of each other at 7 of the 15 stations and only differ by more than 0.2 at one station (KA), suggesting that the inventories are performing comparably to each other.

All models over-predict $CH_4$ concentrations at the two seasonal high-latitude stations, EU and SO, but all models do capture the seasonal variability (R > 0.7) at those sites with TOM_JP over predicting the seasonal amplitude. The correlation coefficients for the three sites most closely associated with northern boreal and temperate wetland emissions, PA, EU and SO, reveal that TOM_JU predicts seasonal wetland emissions in this region the best. At the four European sites, BI, KA, OR and GM, all models fail to capture the seasonal variability, with relatively low average correlation coefficients of R = 0.44 (TOM_JU), R = 0.52 (TOM_JP) and R = 0.35 (TOM_BL). There are no major wetlands close to these sites, suggesting that other sources or sinks might be missing, for example, anthropogenic emissions. At southern hemisphere sites the monthly mean model concentrations fall within the distribution of individual observations for most months, suggesting the total model concentrations are reasonable in all three simulations.

The lack of continuous data means that it is difficult to compare global $CH_4$ changes in observations and model simulations; however at individual sites, discrepancies in growth rates are observed when compared to model simulations. The growth rate observed at most sites is larger than that observed by all model simulations, particularly in later years. PA, which provides the longest, almost continuous, record shows that the average growth rate for the entire period between 2004 and 2012 is 4.8 ppb/yr, this is larger than in all model simulations which use the NOAA OH field at the same location (TOM_ JU: 4.4 ppb/yr, TOM_JP: 3.6 ppb/yr and TOM_BL: 3.8 ppb/yr). The NOAA OH field is chosen because it produces the highest correlation coefficient for all three inventories. This suggests that either a potential trend in wetland emissions is missing or that a trend in non-wetland emissions or sinks is not accounted for.

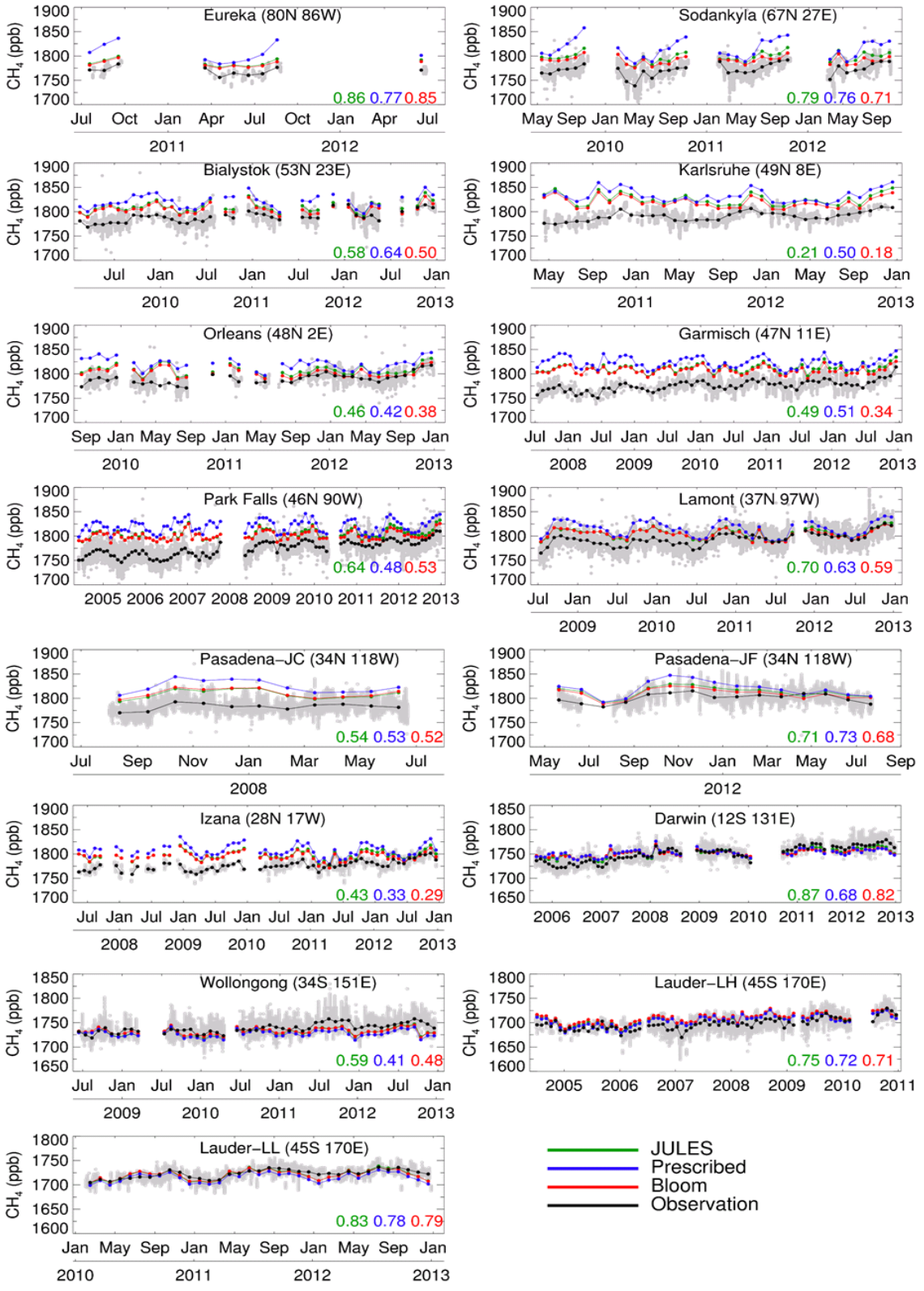


*Figure 5.28 Monthly mean $XCH_4$ concentrations (ppb) from 15 TCCON sites when data are available (black). Also shown are concentrations from three TOMCAT simulations with TCCON averaging kernels applied. TOMCAT simulations are driven by JULES wetland $CH_4$ (green), JULES wetland $CH_4$ driven by prescribed parameters (blue) and a top-down wetland $CH_4$ dataset (Bloom et al., 2012) (red). Correlation coefficients of model and observations are displayed for TOM_JU (green), TOM_JP (blue) and TOM_BL (red). Individual observations are also shown (grey).*

## 5.5 Summary

This chapter has evaluated three wetland $CH_4$ models with similar process descriptions and investigated the role of wetlands in causing recent variations of the $CH_4$ growth rate. The key results are:

- Although parameters (wetland area, temperature and soil carbon) are a limitation in wetland $CH_4$ model accuracy, two methods which use different parameter sets produce similar wetland $CH_4$ flux estimates, both in their spatial pattern and seasonality (JULES and Bloom *et al.*, 2012).

- TOMCAT driven by the JULES wetland dataset performs well when compared with NOAA surface flask $CH_4$ observations (R = 0.47 – 0.96), TCCON column $CH_4$ observations (R = 0.21 – 0.87) and GOSAT column $CH_4$ observations (R = 0.84).

- Between 1993 and 2012 $CH_4$ wetland emissions estimated by the JULES model increase by 0.43 Tg/yr.

- JULES predictions of wetland emissions decreased by 0.4 Tg/yr during the $CH_4$ stagnation period (1999-2006), mainly due to a decrease in wetland fraction.

- The increased global atmosphere $CH_4$ growth rate between 2010 and 2012 is not captured in any model simulation.

- TOMCAT simulations show the poorest correlation with GOSAT in the Amazon and Orinoco region (R = 0.61 – 0.69), suggesting missing processes within the wetland model or other inaccurate sources (e.g. biomass burning).

Three TOMCAT simulations have been used to evaluate the recent trends in atmospheric $CH_4$, all of which were dependent on wetland fraction, temperature and soil carbon. The first, JU, used parameters from JULES, the second, JP, used observations and the third, BL, used a top-down approach. Observations from GOSAT, TCCON and flask sites have been used to investigate the limitation of these wetland $CH_4$ models, both bottom-up and top-down. It was found that inaccuracy in wetland $CH_4$ models originate from a combination of both parameter and process uncertainty.

Over the boreal wetlands there is large uncertainty in the parameters used by the wetland models, this is particularly evident in JP which uses satellite-derived wetlands to produce an emission dataset that does not agree with BL and JU. Flask, GOSAT and TCCON comparisons show that JULES parameters (TOM_JU) produce reasonable $CH_4$ emissions over boreal wetlands and that a simple process approach is sufficient for simulating wetland dynamics, assuming the parameters are accurate. This is the case on a seasonal and interannual scale for a majority of the time series, with two exceptions. Firstly, for the final period of the model simulation, 2010-2012, there is an observed growth in atmospheric $CH_4$, which is not captured by the model. These years use repeat anthropogenic emissions from 2008 and 2012 and use biomass burning emissions from 2011. Therefore, any increase in these emission sources are not accounted for in the model. An increase in wetland emissions that are not accounted for is an alternative possibility, as is a change in the atmospheric sink in these later years. Secondly, when compared with GOSAT, the seasonal cycle is poorly captured by all three datasets over the Amazon and Orinoco. Assuming at least one of the datasets used a reasonably accurate parameter set in the region, this suggests that there are missing wetland processes not accounted for or other emissions and sinks are poorly represented.

The overall long-term trend in wetland emissions differs between the three datasets used, with one bottom-up (JU) and the top-down (BL) dataset showing a positive trend in emissions and the other bottom-up (JP) dataset showing a negative one. The dataset which uses emissions driven by JULES parameters (TOM_JU) produces the strongest agreement with observations and shows a statistically significant ($p < 0.05$) positive trend in wetland emissions between 1993 and 2012 of 0.43 Tg/yr. Analysis of the meteorological driving data suggests that increased precipitation caused increases in wetland fraction, which caused a positive trend in emissions. Datasets with lower interannual and seasonal variability in emissions, JU and BL, perform better than the dataset with a higher interannual and seasonal variability, JP. More details of wetland processes are explored in Chapter 6.

# 6 Improvement of the JULES Wetland $CH_4$ Model

## 6.1 Introduction

This chapter introduces additional wetland processes to the JULES wetland $CH_4$ model and tests the new model using *in-situ* $CH_4$ flux observations. The current process description in JULES ignores potentially important processes including $CH_4$ production in soils which are not saturated, oxidation of $CH_4$, sulphate suppression and transport mechanisms. The aim is to improve the JULES representation of the spatial and temporal wetland $CH_4$ emissions by including these processes into the model. If model accuracy is increased by including additional processes then improved future flux estimates can be made, and previous trends in atmospheric $CH_4$ concentrations can be more accurately attributed to wetland emissions. If model-observation agreement does not improve this suggests a negligible contribution to emission variations from the additional processes, assuming that they are incorporated accurately.

The current version of the JULES wetland $CH_4$ scheme predicts emissions based on only soil temperature, wetland fraction and soil carbon (Gedney *et al.*, 2004). Additional processes have been included in other LSMs, including oxidation of soil $CH_4$ and transport (Wania *et al.*, 2010; Riley *et al.*, 2011), which were found to show good agreement with flux observations. These LSMs were not tested against simpler models nor have they been compared to atmospheric observations using an atmospheric model. Here, a perturbed parameter ensemble is used to optimise the JULES model using flux observations. The updated JULES model is tested against the original version using TOMCAT simulations and atmospheric observations. The evaluation of model performance follows the same methodology used in Chapter 5.

Section 6.2 explains the biogeochemical aspects of wetland $CH_4$, detailing methanogen microbial activity, productivity and transport pathways of $CH_4$ to the atmosphere. Section 6.3 describes the inclusion of additional processes into the JULES wetland model, which are typically adapted from

previous studies. Section 6.4 optimises model parameters using a perturbed parameter ensemble for $CH_4$ production, temperature sensitivity of $CH_4$ production, oxidation of $CH_4$ and $CH_4$ transport from the soil and water column to the atmosphere. Section 6.5 compares the updated flux estimates with the fluxes generated from the original version of the model and flux observations. Section 6.6 details the TOMCAT setup, outlining emission and loss fields. Section 6.7 shows comparisons of TOMCAT simulations with flask, TCCON and GOSAT observations. Finally, Section 6.8 summarises the overall performance of the additional process descriptions and resulting trends in wetland $CH_4$ emissions between 1993 and 2012 given by the original and updated versions of the model.

## 6.2 Wetland $CH_4$ Processes

The emission of $CH_4$ from wetlands is dependent on the production of $CH_4$, methanogenesis, the oxidation of $CH_4$, methanotrophy, and the transport through the soil and water column to the atmosphere (see Figure 2.6). This is discussed only briefly here as more detail has been given in Chapter 2. Methanogens, which produce $CH_4$, use organic carbon as an electron donor to drive their metabolism (Bridgham *et al.*, 2013). Past studies have suggested that the quality of organic carbon correlates with the decomposition rates (Updegraff *et al.*, 1995; Chanton *et al.*, 2008). Previous versions of JULES consider only the quantity and not the quality (ease with which it is broken down) of organic carbon when generating an emission estimate (Gedney *et al.*, 2004; Hayman *et al.*, 2014). The version of JULES used in Chapter 5 accounts for the quality of soil carbon by partitioning the total carbon pool into 4 individual pools for the first time. The $CH_4$ production within wetlands is also dependent on the anaerobic fraction of the soil column and soil temperature. Temperature dependence is accounted for in JULES by a $Q_{10}$ temperature coefficient, set to 1.65. Currently, the anaerobic fraction is assumed to be either 1 or 0 in JULES. Competition between bacteria for the fermentation end products, $H_2/CO_2$ and acetate, should also be considered when calculating wetland $CH_4$ production (Bridgham *et al.*, 2013). Sulphate reduction typically outcompetes methanogenesis, and as a result sulphate ($SO_4^{2-}$) deposition should be, but is not currently, considered in JULES (Gauci *et al.*, 2004). Other factors, not considered here, include both the pH dependence and plant productivity correlations to $CH_4$ production (see Chapter 2).

The oxidation of $CH_4$ in soils and surface water is estimated to be between 40 and 70% of the total $CH_4$ production (Megonigal *et al.*, 2005), but this is not accounted for in the current version of JULES. Methanotrophs can oxidise $CH_4$ in the soil/water column, depending on oxygen and

$CH_4$ availability. Water table height, soil porosity and oxygen drawn down by plant root activity are all controls on the availability of oxygen and as a result, the oxidation of $CH_4$.

Transport of $CH_4$ from the site of methanogenesis into the atmosphere can occur via diffusion, ebullition and/or plant-mediated transport. The current version of JULES assumes that emissions of $CH_4$ from the surface immediately follow on from production without accounting for transport mechanisms. The diffusion rate of $CH_4$ is dependent on the temperature and is different for water and air (Broecker and Peng, 1974). When considering the diffusion through the soil column, the porosity of the soil must be taken into account. The rate of $CH_4$ ebullition is controlled by the temperature-dependent solubility of the water column (Yamamoto *et al.*, 1976) and the volume of water. When maximum solubility is exceeded the $CH_4$ is released into the atmosphere. The final mechanism, plant-mediated transport, occurs as either a passive diffusion process or as an active pump process. This process is dependent on the temperature and, the abundance, biomass, phenology and rooting depth of aerenchymatous plants, which are described in Chapter 2 (Wania *et al.*, 2010).

## 6.3 Process Developments

This section describes additions to the existing JULES model, JU (see Chapter 5), in an attempt to make the model more realistic. The new version of the model, hereafter referred to as JN, includes process descriptions of sulphate suppression and transport mechanisms. Additionally, JN has a representation of $CH_4$ pools, production and oxidation in both saturated and unsaturated regions. The developments introduced to JULES in this chapter are adapted from several other studies (Gauci *et al.*, 2004; Zhuang *et al.*, 2004; Wania *et al.*, 2010; Riley *et al.*, 2011).

### 6.3.1 Methanogenesis in Unsaturated Soils

The production of $CH_4$ in soils is assumed to be limited to anaerobic environments, which not only includes fully saturated soils, but also a fraction of partially saturated soils. Currently JULES only considers production in fully water saturated soils. In these soils the ratio of $CO_2$:$CH_4$ production is assumed to be constant because organic carbon is available to both processes, $CO_2$ respiration and methanogenesis, at all depths. The $CO_2$:$CH_4$ production ratio in unsaturated soils is larger than in saturated soils because less carbon is allocated to the anaerobic fraction where the production of $CH_4$ occurs. As a result the production rate of $CH_4$ in unsaturated soils is dependent on both the production ratio and the moisture content. The moisture content is used as

a proxy for anaerobic fraction, see equations 6.1 and 6.2, where $f_{moi}$ is the non-wetland anaerobic fraction of the grid cell, $s_{moi}$ is the grid cell soil moisture fraction, $P_{uns\_CH4}$ is the unsaturated $CH_4$ production rate in kg $m^{-2}$ $s^{-1}$ and $\varphi_{uns}$ is the unsaturated $CO_2$:$CH_4$ production ratio. For production under saturated conditions, equation 5.4 is updated using a production ratio, $\varphi_{sat}$.

$$f_{moi} = \frac{(s_{moi} - f_w)}{(1 - f_w)} \qquad \textbf{(6.1)}$$

$$P_{uns\_CH4} = (1 - f_w) f_{moi} \varphi_{uns} \Lambda Q_{10} (T_{soil})^{(T_{soil} - T_0)/10} \qquad \textbf{(6.2)}$$

## 6.3.2 $CH_4$ Pools

Current emissions of $CH_4$ in JULES instantaneously follow production. Bloom *et al.* (2010) showed that there is a lag between water table height and $CH_4$ emissions, suggesting that an instantaneous relationship between water height and emissions might not be accurate. For JN a $CH_4$ 2-pool system has been introduced whereby $CH_4$ can accumulate in saturated and unsaturated soils before being transported and/or oxidised. One aim of these changes is to simulate ebullition pulse events that have been previously observed (Tokida *et al.*, 2007). For each grid cell the unsaturated, $CH_{4uns}$, and saturated, $CH_{4sat}$, pools, which represent $CH_4$ contained within the soil and/or water column, are updated with each time step; by first accounting for changes in wetland area (see equations 6.3, 6.4, 6.5 and 6.6).

$For f_{wet,t} - f_{wet,t-1} > 0$:

$$CH_{4sat,t} = CH_{4sat,t-1} + CH_{4uns,t-1}(f_{wet,t} - f_{wet,t-1}) \qquad \textbf{(6.3)}$$

$$CH_{4uns,t} = CH_{4uns,t-1}(1 + f_{wet,t-1} - f_{wet,t}) \qquad \textbf{(6.4)}$$

$For f_{wet,t} - f_{wet,t-1} < 0$:

$$CH_{4sat,t} = CH_{4sat,t-1}(1 - f_{wet,t-1} + f_{wet,t}) \qquad \textbf{(6.5)}$$

$$CH_{4uns,t} = CH_{4uns,t-1} + CH_{4sat,t-1}(f_{wet,t-1} - f_{wet,t}) \qquad \textbf{(6.6)}$$

After the $CH_4$ production, transport and oxidation terms are calculated the pools are then updated again by considering fluxes in and out of the pool, shown in equations 6.7 and 6.8, where

$CH_{4prod/aer/ebu/dif/oxi}$ are $CH_4$ production, plant-mediated transport, ebullition, diffusion and oxidation, respectively, in kg $m^{-2}$ $d^{-1}$.

$$CH_{4uns,t+1} = CH_{4uns,t} + CH_{4uns,prod,t} - CH_{4uns,aer,t} - CH_{4uns,dif,t} - CH_{4uns,oxi,t} \quad \textbf{(6.7)}$$

$$CH_{4sat,t+1} = CH_{4sat,t} + CH_{4sat,prod,t} - CH_{4sat,aer,t} - CH_{4sat,ebu,t} - CH_{4sat,dif,t} \quad \textbf{(6.8)}$$

## 6.3.3 Sulphate Suppression and Oxidation of $CH_4$

In JULES there is currently no competition with methanogens for available organic carbon. However, Gauci *et al.* (2004) described the importance of sulphur deposition in the suppression of methanogenesis from surface soils. To take this process into account for JN, a sulphur deposition rate estimate is taken from the coupled chemistry-climate model HadGEM3-UKCA (Turnock *et al.*, 2015), which includes sulphur chemistry from Mann *et al.* (2010). Deposited sulphur is then used to suppress the production of $CH_4$ in JN using equation 6.9, which is adapted from Gauci *et al.* (2004). Here *SS* is suppression in percent, $V_{max}$ is the maximum suppression in percent, which is set to 38.6 %, $S_{dep}$ is the sulphate deposition in kg $ha^{-1}$ $yr^{-1}$. For $CH_4$ production, equation 5.4 is updated to include *SS*.

$$SS = \frac{(V_{max} \times S_{dep})}{(S_{dep} + 8.71)} \quad \textbf{(6.9)}$$

The removal of $CH_4$ from the unsaturated pool via oxidation by methanotrophs is included in JN but not in JU. Oxidation is only considered in unsaturated soils because methanotroph activity peaks at a soil moisture content of around 33% after which it declines (Czepiel *et al.*, 1995). The oxidation rate is dependent on temperature, soil moisture content, $O_2$ concentration and $CH_4$ concentration. For the temperature dependence, *f(T)*, the same $Q_{10}$ factor as for $CH_4$ production is used. The soil moisture dependence, $f(f_{moi})$, is calculated using equation 6.10 taken from Zhuang *et al.* (2004), where $M_{min,}$ $M_{max}$ and $M_{opt}$ are the minimum, maximum and optimum volumetric soil moistures for oxidation set at 0, 1 and 0.33, respectively. The $CH_4$ concentration is taken from $CH_{4uns}$ and the $O_2$ concentration is calculated based on an assumed surface $O_2$concentration and soil porosity from the HWSD. These individual elements are combined to calculate the oxidation at each time step using equation 6.11, which is adapted from Zhuang *et al.* (2004). Here, $f_{ox}$ is the fraction of $CH_4$ available for oxidation, $O_{max}$ is the maximum oxidation coefficient in mol $m^{-3}$ $s^{-1}$ and, $k_{CH4}$ and $k_{O2}$ are the half-saturation coefficients of $CH_4$ and $O_2$, respectively, in mol $m^{-3}$.

$$f(f_{moi}) = \frac{(f_{moi}-M_{min})(f_{moi}-M_{max})}{[(f_{moi}-M_{min})(f_{moi}-M_{max})]-(f_{moi}-M_{opt})^2} \quad \textbf{(6.10)}$$

$$CH_{4uns,oxi} = O_{max}\left[\frac{[CH_4]}{K_{CH_4}+[CH_4]}\right]\left[\frac{[O_2]}{K_{O_2}+[O_2]}\right] f(T) f(f_{moi})\, f_{ox} \quad \textbf{(6.11)}$$

## 6.3.4 Transport Mechanisms

Following the accumulation of $CH_4$ in pools, transport mechanisms to the atmosphere have been introduced, which provides a model flux. The total flux at each time step is a sum of the diffusion, plant-mediated transport and ebullition.

Diffusion in JN occurs in both saturated and unsaturated soils, through both soil and water. The diffusivity of $CH_4$ in water and air is given by equations 6.12 and 6.13, taken from Wania *et al.* (2010), which was adapted from earlier studies (Broecker and Peng, 1974; Lerman, 1979). Here, $D_{CH4,water/air}$ are the diffusivities of $CH_4$ in water and air in units of $10^{-9}$ $m^2$ $s^{-1}$ and $10^{-4}$ $m^{-2}$ $s^{-1}$, respectively.

$$D_{CH4,water} = 0.9798 + 0.02986T + 0.0004381T^2 \quad \textbf{(6.12)}$$

$$D_{CH4,air} = 0.1875 + 0.0013T \quad \textbf{(6.13)}$$

For the diffusion of $CH_4$ through soils, the porosity of the soil is accounted for by considering the soil composition taken from the HWSD (Harmonised World Soil Database). The $CH_4$ diffusion rate from soils is calculated using equation 6.14 taken from Zhuang *et al.* (2004), where *$CH_4$_diff* is the diffusion rate in kg $m^{-2}$ $s^{-1}$, γ is the tortuosity coefficient, set at 0.66, and, $f_{clay/sand/silt}$ and $PV_{clay/sand/silt}$ are the fractions and porosities of clay, sand and silt, respectively.

$$CH_4\_diff = \gamma D_{CH4,air}\left(f_{sand}PV_{sand} + f_{silt}PV_{silt} + f_{clay}PV_{clay}\right)CH_{4uns} \quad \textbf{(6.14)}$$

Equation 6.15 considers only $CH_4$ diffusion from saturated soils, $D_{CH4,water}$. Diffusion from unsaturated soils is dependent on soil moisture content and uses a combination of both $D_{CH4,water}$ and $D_{CH4,air}$ (see equation 6.16).

$$CH_{4sat,dif} = CH_{4sat}D_{CH4,water} \quad \textbf{(6.15)}$$

$$CH_{4uns,dif} = f_{moi}CH_{4uns}D_{CH4,water} + (1 - f_{moi})CH_4\_diff \quad \textbf{(6.16)}$$

Emissions of $CH_4$ via aerenchyma (see Chapter 2 for details) in plants is assumed to be via diffusion and occurs in both C3 and C4 grasses in JN. The total aerenchyma diameter is based on both the number of tillers (segmented stems) within the grid cell and an assumed average cross-sectional area per tiller. To calculate the total number of tillers, $N_{till}$, an average tiller biomass of 0.22 g C is assumed (Wania *et al.*, 2010) and the total C3 and C4 leaf biomass for the grid cell is calculated using equation 6.17, taken from Clark *et al.* (2011), where $R$ is leaf biomass in kg C $m^{-2}$, $L_b$ is the leaf area index (LAI) and $\sigma$ is the specific leaf density, which is set to 0.025 kg C $m^{-2}$ and 0.05 kg C $m^{-2}$ for C3 and C4 grasses, respectively. Leaf biomass is assumed to equal tiller biomass (Clark *et al.*, 2011).

$$R = \sigma L_b \qquad \textbf{(6.17)}$$

The aerenchyma percentage of the tiller surface area is assumed to be 19.7% for saturated and 2.5% for unsaturated conditions (Insausti *et al.*, 2001), which can be scaled based on an assumed PFT porosity, $C_{por}$. The average cross-sectional area, $A_{till}$, is assumed to be $2.6 \times 10^{-5}$ $m^2$, based on Wania *et al.* (2010). Using these values the aerenchyma flux from the saturated ($CH_{4sat,aer}$) and unsaturated ($CH_{4uns,aer}$) pool is calculated using equations 6.18 and 6.19.

$$CH_{4sat,aer} = 0.197 C_{por} A_{till} N_{till} CH_{4sat} D_{CH4,air} \qquad \textbf{(6.18)}$$

$$CH_{4uns,aer} = 0.025 C_{por} A_{till} N_{till} CH_{4uns} D_{CH4,air} \qquad \textbf{(6.19)}$$

The transport of $CH_4$ via soil/water/aerenchyma diffusion is considered as a flux in JN, whereas ebullition is represented as an instantaneous pulse once the $CH_4$ pool in saturated soils exceeds the maximum solubility. This threshold is temperature-dependent following Yamamoto *et al.* (1976) and using a best-fit curve from Wania *et al.* (2010) shown in equation 6.20, where $S_B$ is the Bunsen solubility coefficient, defined as volume of $CH_4$ per volume of water at atmospheric pressure.

$$S_B = 0.05708 - 0.001545T + 0.00002069T^2 \qquad \textbf{(6.20)}$$

The water volume, $V_{H2O,}$ for $CH_4$ storage is assumed to be proportional to the wetland area within the grid cell, with an assumed maximum depth, $Max_d$, (see equation 6.21).

$$V_{H2O} = Max_d f_{wet} \qquad \textbf{(6.21)}$$

Following Wania *et al.* (2010), the ideal gas law is used to calculate the maximum $CH_4$ storage capacity of saturated soils, *SC*, shown in equation 6.22, where $p_s$ is the surface pressure. If $CH_{4,sat}$ exceeds this capacity then the difference between $CH_{4,sat}$ and *SC* is emitted via ebullition.

$$SC = \frac{16.04 V_{H2O} p_s S_B}{8.3145 T} \qquad \textbf{(6.22)}$$

## 6.3.5 Overview of Updated JULES

The updated version of the model is used to produce a daily $CH_4$ emission inventory at a 0.5° by 0.5° resolution. An overview of the model is provided in Figure 6.1, which shows the inclusion of saturated/unsaturated $CH_4$ pools, oxidation, sulphate suppression and transport. The model is driven by JULES output parameters where available, e.g. surface pressure, but also requires some ancillary information taken from HWSD, e.g. soil composition.

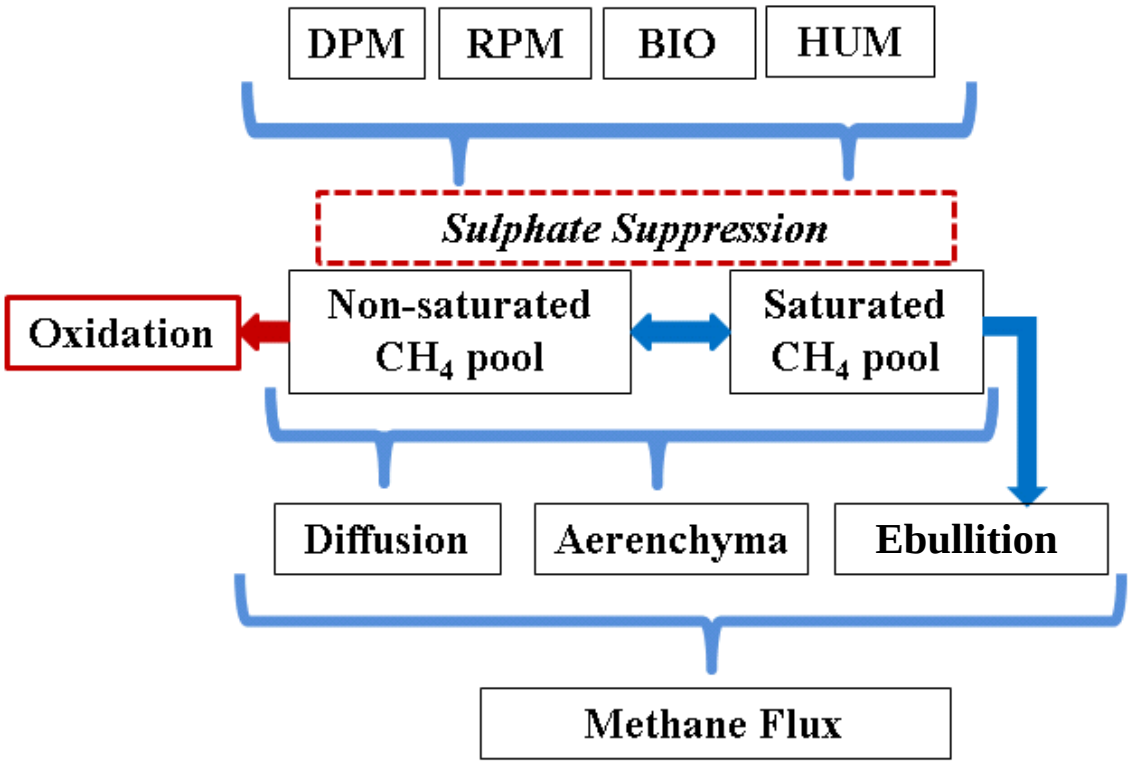


*Figure 6.1 Schematic representation of the updated JULES wetland $CH_4$ model. Carbon is taken from four pools (DPM, RPM, BIO and HUM) for methanogenesis. Carbon availability is limited by sulphur deposition. $CH_4$ is stored and transferred between two pools, saturated and unsaturated. A fraction of the unsaturated pool is oxidised by methanotrophs. Diffusion through the soil and water creates a surface $CH_4$ flux. $CH_4$ is also diffused through aerenchyma within plants. When the saturated $CH_4$ pool exceeds the maximum solubility of $CH_4$ then the surplus $CH_4$ is immediately released through ebullition.*

## 6.4 Sensitivity Testing of Updated JULES $CH_4$

To tune the new version of JULES, a Latin Hypercube design was used to create a perturbed parameter ensemble to explore parameter space (Lee *et al.*, 2013). In this method, X number of parameters are each given N number of values within a suitable range and each parameter combination is modelled, requiring $N^X$ simulations. This is done in two stages to reduce computational demand; the first set of perturbed parameters control the production and temperature dependence of $CH_4$ and the second set control the transport. The perturbed parameters are evaluated against flux observations taken from Riley *et al.* (2011) and are used to produce an optimised parameter set across all observation sites.

### 6.4.1 Methanogenesis Parameter Estimation

The first perturbed parameter ensemble varies parameters relating to the $CH_4$ production rate and production temperature dependence. These are listed in Table 6.1, using a range of estimated values, some of which are based on previous studies (Zhuang *et al.*, 2004; Wania *et al.*, 2010; Riley *et al.*, 2011; Yvon-Durocher *et al.*, 2014).

| | | Sensitivity Values | | | | |
|---|---|---|---|---|---|---|
| Parameter | Units | Value 1 | Value 2 | Value 3 | Value 4 | Value 5 |
| $R_{dpm}$ | $s^{-1}$ | $7.5\times10^{-7}$ | $1.5\times10^{-6}$ | $3\times10^{-6}$ | $6\times10^{-6}$ | $1.2\times10^{-5}$ |
| $R_{rpm}$ | $s^{-1}$ | $2.510^{-8}$ | $5\times10^{-8}$ | $1\times10^{-7}$ | $2\times10^{-7}$ | $4\times10^{-7}$ |
| $R_{bio}$ | $s^{-1}$ | $5\times10^{-8}$ | $1\times10^{-7}$ | $2\times10^{-7}$ | $4\times10^{-7}$ | $8\times10^{-7}$ |
| $R_{hum}$ | $s^{-1}$ | $1.5\times10^{-9}$ | $3\times10^{-9}$ | $6\times10^{-9}$ | $1.2\times10^{-8}$ | $2.4\times10^{-8}$ |
| $Q_{10}(T_0)$ | - | 1 | 1.65 | 2 | 3 | 4.4 |
| $\varphi_{uns}$ | - | $2\times10^{-4}$ | $2\times10^{-3}$ | $2\times10^{-2}$ | 0.2 | 0.4 |
| $\varphi_{sat}$ | - | $5\times10^{-2}$ | 0.1 | 0.2 | 0.5 | 1 |

*Table 6.1 Parameter sensitivity analysis ranges for $CH_4$ production and temperature dependence applied to updated JULES model, JN, and tested against observations.*

The ensembles are compared to 13 observations previously collated by Riley *et al.* (2011) to assess model performance. Measurements typically exist over a 12-month period at varying time intervals using static chamber measurements. A basic overview of each measurement site is provided in Table 6.2, with further information provided in Riley *et al.* (2011). No other site information is used in this thesis and all parameter information is taken from model output and other ancillary data (e.g. soil moisture content). The model simulates a flux over the entire grid

cell whereas the flux observation typically represents a localised area, as a result this increases parameter uncertainty at the site in the model. Measurement sites are typically placed in wetland regions of the grid cell; as a result scaled fluxes are expected to be lower in the model than observed (see Section 6.5).

| Site Location | Latitude | Longitude | Observation Year(s) | Site Description |
|---|---|---|---|---|
| Abisko, Sweden | 68.3 | 18.7 | 2002 | Sub-Arctic mire; grass and a moss layer |
| Alaska, USA | 65.0 | -148.0 | 1989 | Tundra underlain by permafrost |
| Degero, Sweden | 64.0 | 20.0 | 1996 | Oligotrophic lawn in a boreal mire |
| Salmisuo, Finland | 62.5 | 30.6 | 1993 | Minerogenic oligotrophic fen |
| Boreas, Canada | 55.9 | -98.4 | 1996 | Fen with peat and brown mosses |
| Sanjiang, China | 47.4 | 133.3 | 2002 | Peatland |
| Minnesota, USA | 47.3 | -93.3 | 1989 | Transitional between poorly minerotrophic fen and oligotrophic bog |
| Michigan, USA | 42.3 | -84.0 | 1991 | Peatland bog |
| Ruoergai, China | 32.5 | 102.3 | 2001 | Freshwater marsh |
| Panama | 9.0 | -80.0 | 1987 | Tropical swamp |
| Orinoco, Venezuela | 8.3 | -63.2 | 1991 | Flooded forest and floodplain |
| Central Amazonia, Brazil | -3.2 | -59.9 | 1988-1989 | Flooded forest |
| Pantanal, Brazil | -19.5 | -57.0 | 1998 | Tropical wetland |

*Table 6.2 Description of the $CH_4$ flux sites and measurements used to assess model performance. Adapted from Riley et al. (2011).*

The results from all 78,125 ($5^7$) simulations, none of which are scaled to a global value, are shown at each site and compared to observations in Figure 6.2. The results show that low-latitude simulations and observations produce little or no seasonal cycle in $CH_4$ emissions. At Ruoergai in China no model simulation reproduces the maximum fluxes observed. At the high-latitude sites the onset of the seasonal flux due to the spring time melt is typically well represented, although

the duration of the seasonal emission is typically too long at some sites (Degero, Salmisuo and Sanjiang). At a majority of sites, most model simulations underestimate the observed flux, with a high number density (red colour) producing fluxes that rarely exceed 200 $mgCH_4\ m^{-2}\ d^{-1}$. The influence of perturbing model parameters is noticeably more evident at some sites, e.g. Central Amazonia, than at others, e.g. Ruoergai.

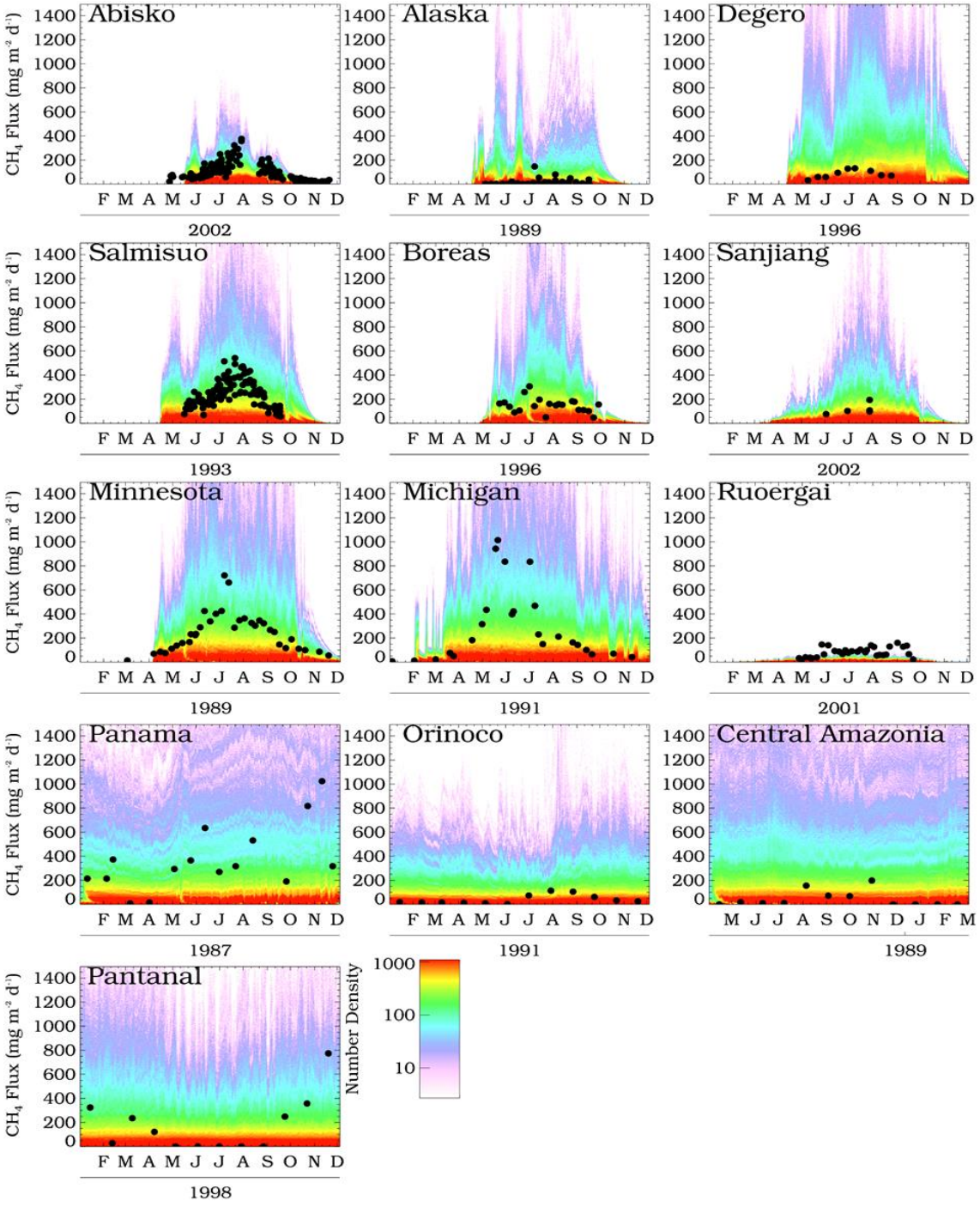


*Figure 6.2 $CH_4$ flux ($mgCH_4\ m^{-2}\ day^{-1}$) from 13 measurement sites when data are available, some of which are binned monthly (black circles). Also shown are daily number density results from the JN production perturbed parameter ensemble at each site, with simulation results binned into 5 $mgCH_4\ m^{-2}\ day^{-1}$ bins. Note that years differ at each site and colour scale is logarithmic.*

To evaluate model performance Taylor diagrams are used (see Figures 6.3 and 6.4), which quantify the observations and simulations in terms of their correlation, centred RMSE and the ratio of standard deviations (Taylor *et al.*, 2001). From this information a model skill score can be determined between 0 (least skilful) and 1 (most skilful) using equation 6.23, taken from Taylor *et al.* (2001), where $S$ is skill, $R_0$ is the maximum correlation attainable, which is assumed to be 1, $R$ is the correlation coefficient, and $\sigma_f$ is the ratio of model to observed standard deviation.

$$S = \frac{4(1+R)}{(\sigma_f+1/\sigma_f)^2(1+R_0)} \quad \textbf{(6.23)}$$

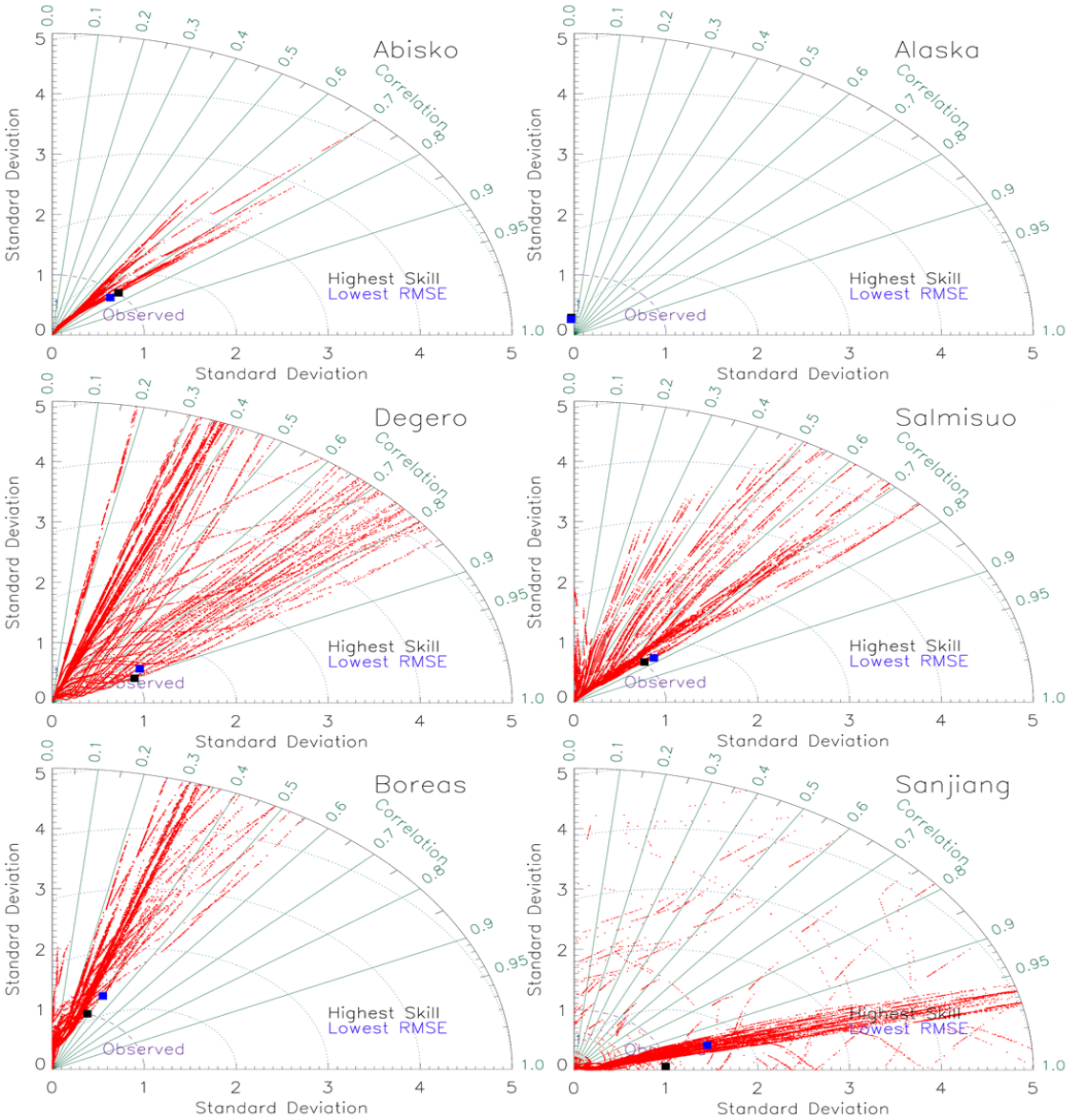


*Figure 6.3 Taylor diagrams comparing the perturbed parameter ensemble and observed $CH_4$ flux at the 6 most northern sites from Table 6.2 (red circles). Standard deviation provided as a ratio of simulated to observed flux deviation. Simulations with the highest site-specific skill (black) and lowest site-specific RMSE (blue) are indicated (squares).*

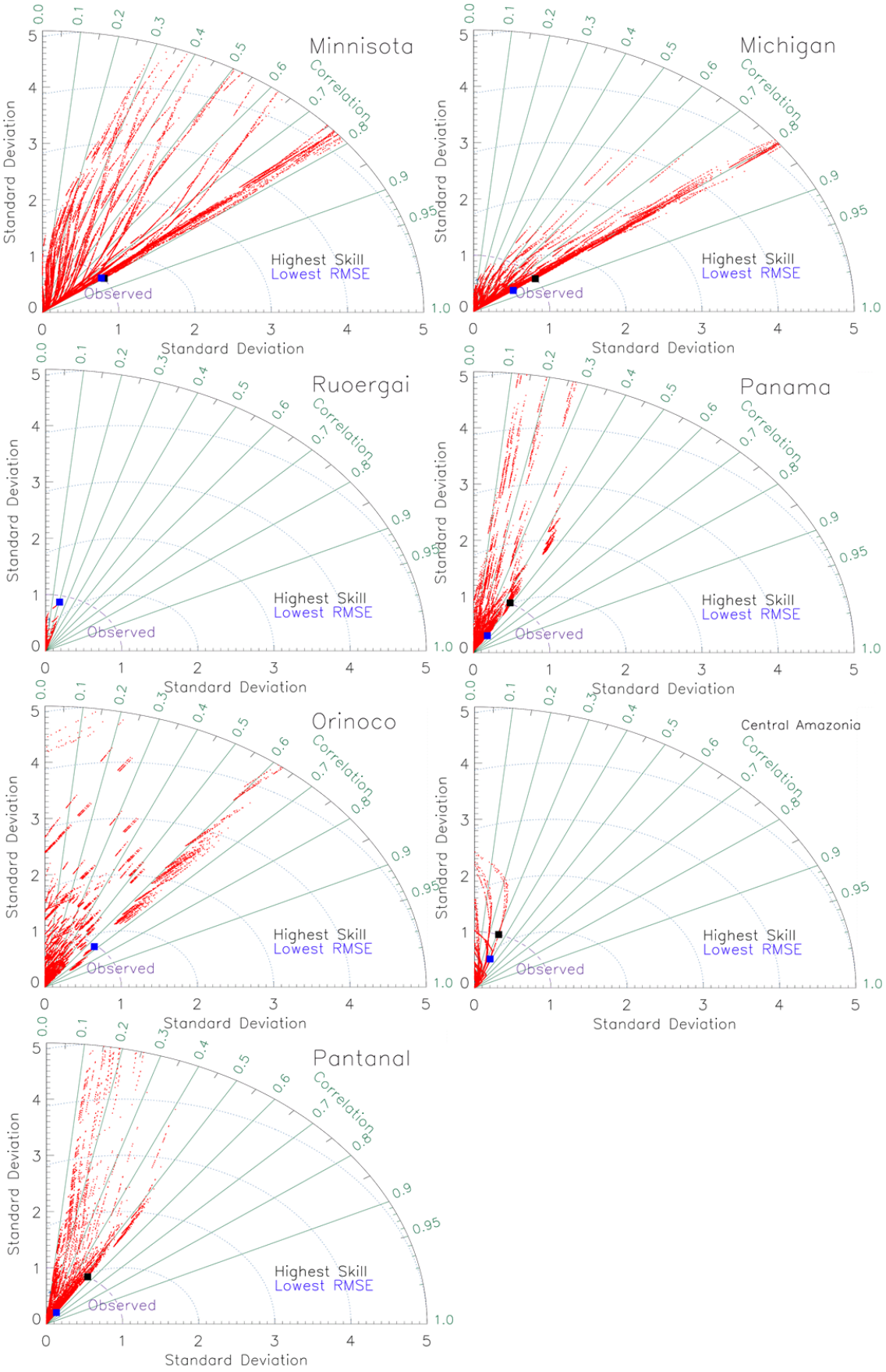


*Figure 6.4 As Figure 6.3 but for the 7 southern most sites from Table 6.2.*

Both RMSE and skill can be used as metrics to assess model performance although the suitability of either is somewhat subjective and dependent on the model requirements. For most sites the choice of metric makes only a small difference when considering the most suitable parameter set. The flux difference is typically more noticeable between the parameter set with the lowest site specific RMSE and the set with the lowest all-site mean RMSE (see Figure 6.5). The parameter set that simulates the lowest all-site mean RMSE is adopted for use for global model simulations of JN.

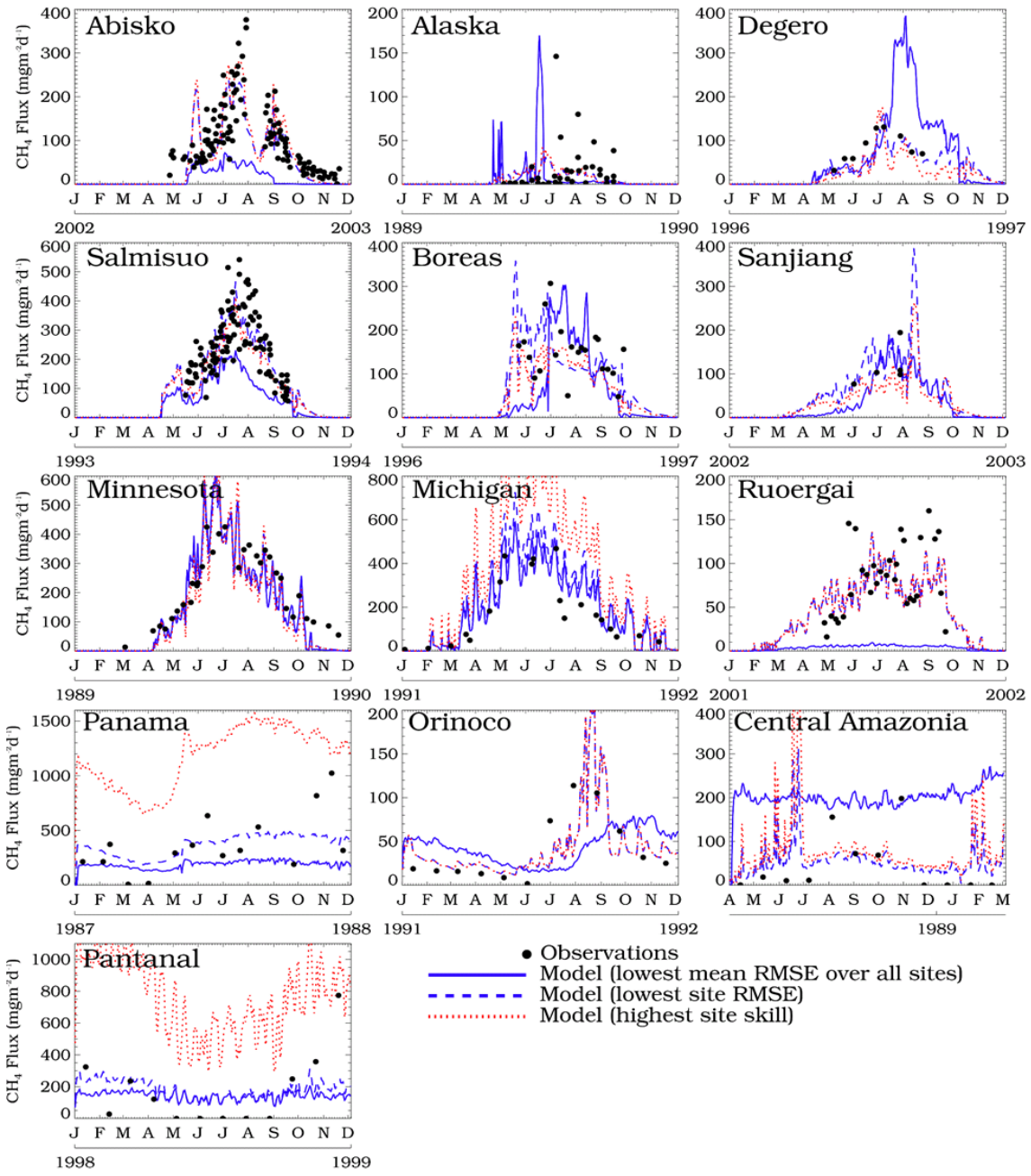


*Figure 6.5 $CH_4$ flux ($mgCH_4\ m^{-2}\ day^{-1}$) from 13 measurement sites when data are available (black circles). Also shown are daily results from JN, for the parameter configuration that provides the lowest mean RMSE over all sites (blue solid line), lowest site-specific RMSE (blue dashed line) and the highest site-specific skill (red dashed line). Note that years differ at each site.*

Each perturbed parameter affects not just the magnitude of the flux but also the timing (see Figure 6.6). Salmisuo is selected as an example site because it has the highest number of flux measurements (128) and here the influence of varying the HUM and BIO methanogenesis rate is small. This is the same at other stations because a majority of $CH_4$ production originates from the DPM and RPM pools. Increasing $\varphi_{uns}$ results in higher fluxes towards the end of the year, whereas increasing $\varphi_{sat}$ shows increased fluxes earlier. The observed fluxes are within the limits of the selected parameter ranges, suggesting that the values chosen are reasonable. For the remainder of this chapter all results shown use the parameter set with the lowest all-site mean RMSE (see Table 6.3).

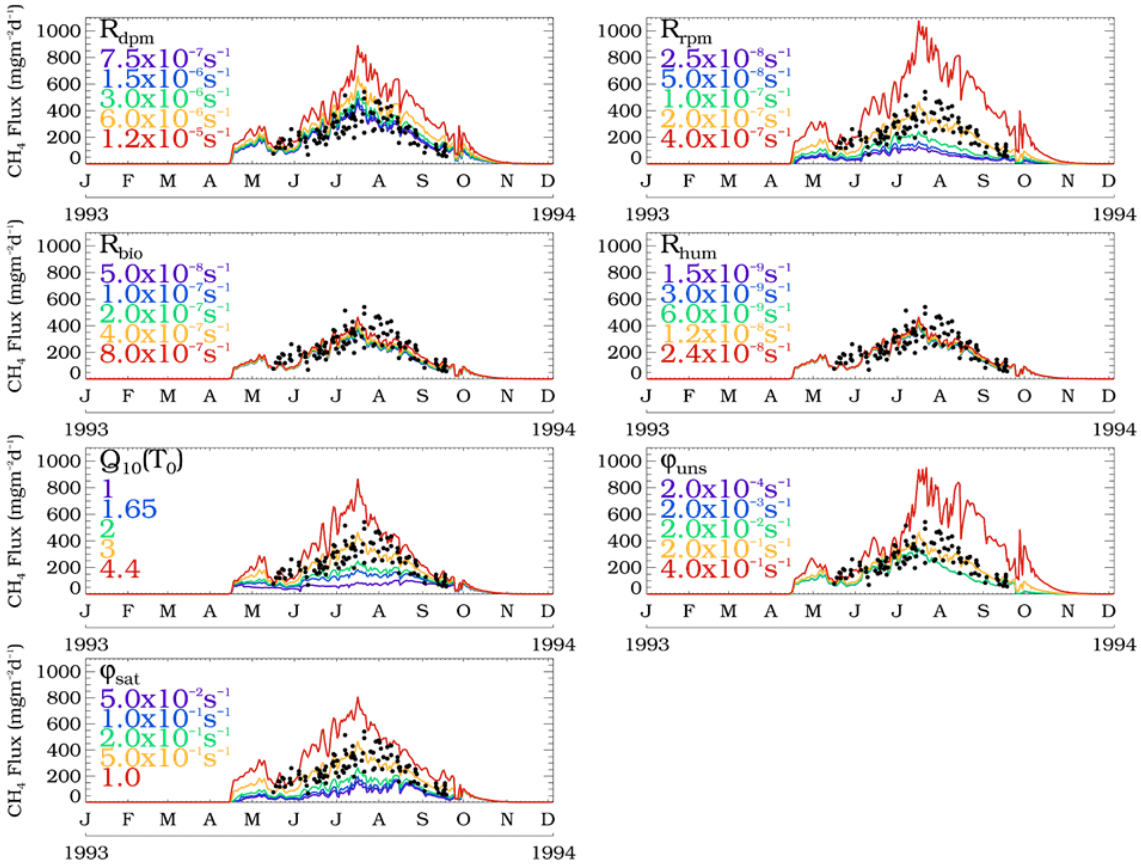


*Figure 6.6 $CH_4$ flux ($mgCH_4\ m^{-2}\ day^{-1}$) from the Salmisuo measurement site when data are available (black circles). Also shown are JN $CH_4$ flux sensitivities for 7 parameters using the optimised configuration based on the lowest site-specific RMSE.*

| Parameter | $R_{dpm}$ ($s^{-1}$) | $R_{rpm}$ ($s^{-1}$) | $R_{bio}$ ($s^{-1}$) | $R_{hum}$ ($s^{-1}$) | $Q_{10}(T_0)$ | $\varphi_{sat}$ | $\varphi_{und}$ |
|---|---|---|---|---|---|---|---|
| Lowest all-site mean RMSE | $1.2\times10^{-5}$ | $2.5\times10^{-8}$ | $5.0\times10^{-8}$ | $1.5\times10^{-9}$ | 3 | $2\times10^{-2}$ | $5\times10^{-1}$ |
| Lowest site-specific RMSE | $7.5\times10^{-7}$ | $2.0\times10^{-7}$ | $8.0\times10^{-7}$ | $2.4\times10^{-8}$ | 3 | $2\times10^{-1}$ | $5\times10^{-1}$ |

*Table 6.3 Parameter fitting summary at Salmisuo showing the parameter configurations which produce the lowest all-site RMSE and lowest site-specific RMSE for first ensemble.*

## 6.4.2 Transport and Oxidation Parameter Estimation

The second perturbed parameter ensemble used the parameter configuration with the lowest all-site mean RMSE from the first ensemble and perturbed 6 further parameters which influence oxidation and transport. Some of the parameter value ranges, shown in Table 6.4, originate from previous studies (Zhuang *et al.*, 2004; Wania *et al.*, 2010; Riley *et al.*, 2011).

| | | Sensitivity Values | | | | |
|---|---|---|---|---|---|---|
| Parameter | Units | Value 1 | Value 2 | Value 3 | Value 4 | Value 5 |
| $f_{ox}$ | - | 0.25 | 0.5 | 0.75 | 0.9 | 1.0 |
| $O_{max}$ | mol $m^{-3}$ $s^{-1}$ | $1.25\times10^{-7}$ | $7.5\times10^{-7}$ | $1.25\times10^{-6}$ | $7.5\times10^{-6}$ | $1.25\times10^{-5}$ |
| $K_{CH4}$ | mol $m^{-3}$ | $5\times10^{-4}$ | $1\times10^{-3}$ | $5\times10^{-3}$ | $1\times10^{-2}$ | $5\times10^{-2}$ |
| $K_{O2}$ | mol $m^{-3}$ | $7\times10^{-3}$ | $2\times10^{-2}$ | $7\times10^{-2}$ | 0.2 | 0.7 |
| $Max_d$ | m | $5\times10^{-3}$ | $1\times10^{-2}$ | $5\times10^{-2}$ | 0.1 | 0.5 |
| $C_{por}$ | - | 0.1 | 0.2 | 0.3 | 0.4 | 0.5 |

*Table 6.4 Parameter sensitivity analysis ranges for $CH_4$ transport and oxidation applied to JN and tested against observations.*

A repeat of the analysis used in section 4.2.1 is used for the second ensemble, with the unscaled fluxes from 15,625 ($5^6$) simulations and observations shown as a density plot (see Figure 6.7). The results show that the transport and oxidation parameters affect the pathway for the flux but have only a minor influence on the total flux with time. This could either be a result of an inaccurate model description, the parameter ranges being too limited or the transport mechanisms not playing a key role in the total emission of $CH_4$. The influence of varying transport and oxidation parameters is more evident at some sites, e.g. Panama, than at others, e.g. Pantanal.

The same approach for model evaluation is performed for the second ensemble, where the configuration which produced the lowest all-site mean RMSE is selected for further analysis. Perturbing individual parameters using this configuration shows that at the example site, Salmisuo, only $O_{max}$ and $Max_d$ have a noticeable impact on the flux (see Figure 6.8). Both $F_{ox}$ and $O_{max}$ are temporally and spatially constant coefficients of oxidation, but the influence of $O_{max}$ is more noticeable in the sensitivity analysis because the parameter range is larger. At some other sites the influence of $Max_d$ is even larger, for example, Panama (see Figure 6.9). The higher $Max_d$ values at Panama suggest less frequent but larger ebullition pulse events than the simulations with lower $Max_d$. The low temporal frequency of observations limits the ability to observe these ebullition pulse events and improved parameterisations are dependent on improved observations.

This section has outlined the developments made to produce JN. In subsequent sections JN refers to the model parameter configuration that produced the lowest all-site mean RMSE from the first (see Table 6.3) and second (see Table 6.5) ensemble.

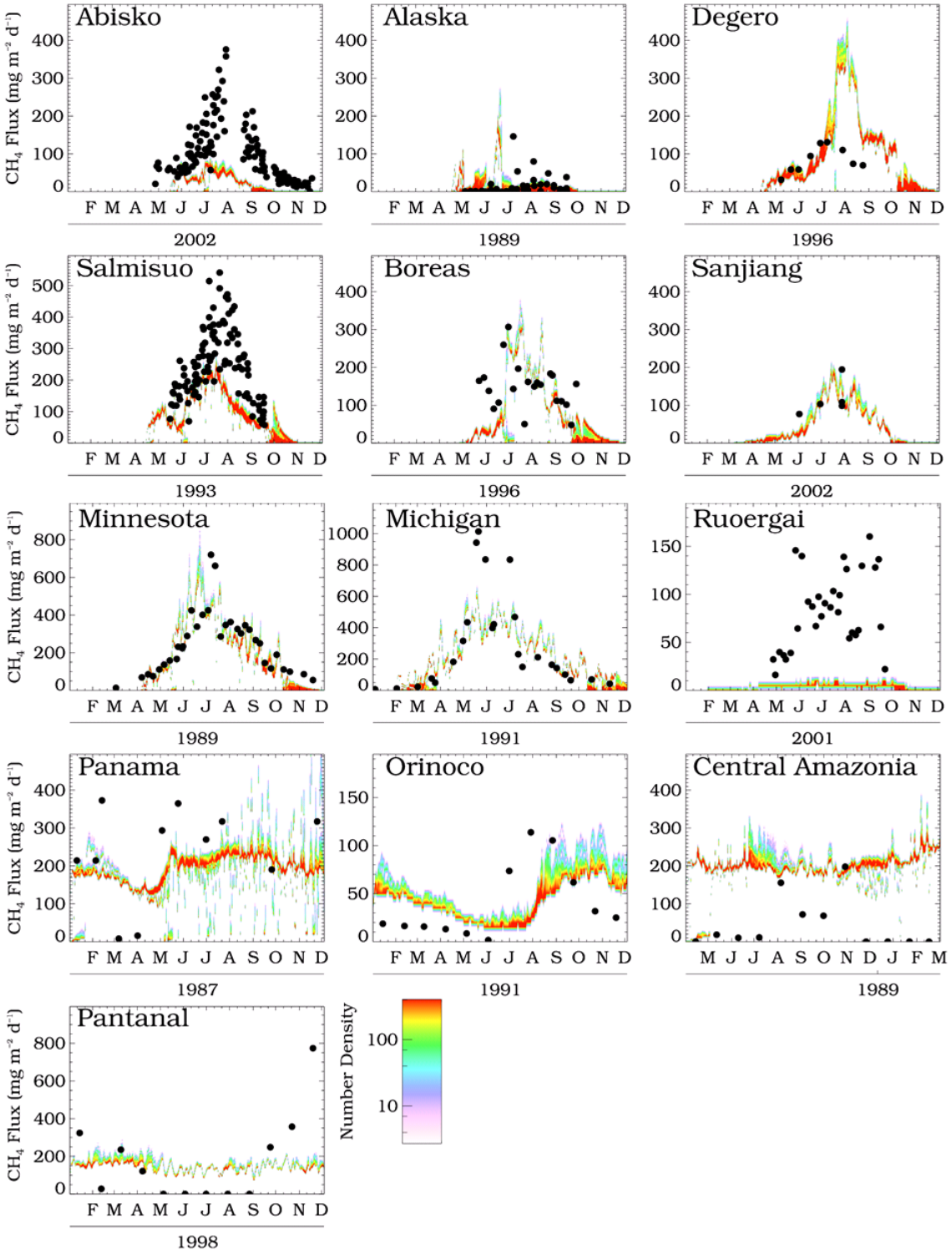


*Figure 6.7 $CH_4$ flux ($mgCH_4\ m^{-2}\ day^{-1}$) from 13 measurement sites when data are available (black circles). Also shown are daily results from the JN transport and oxidation perturbed parameter ensemble at each site, with simulation results binned into 5 $mgCH_4\ m^{-2}\ day^{-1}$ bins. Note that years differ at each site and colour scale is logarithmic.*

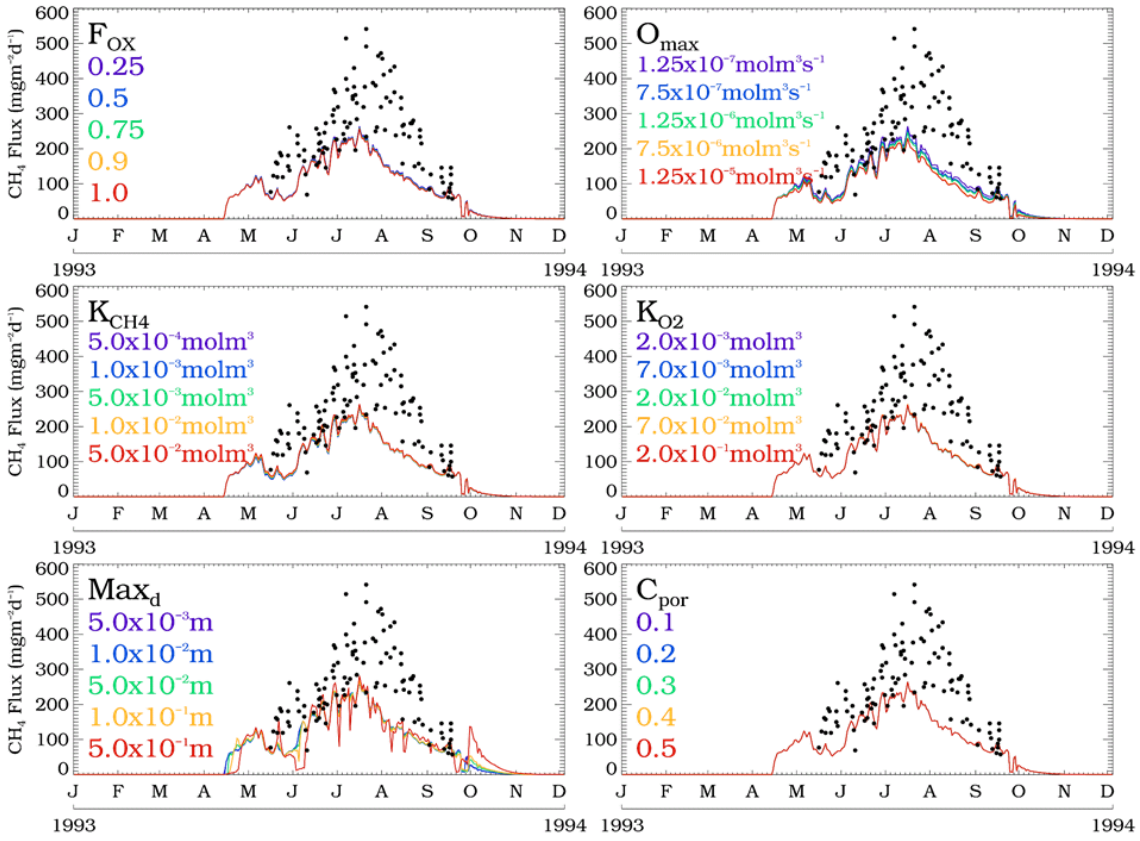


*Figure 6.8 $CH_4$ flux ($mgCH_4\ m^{-2}\ day^{-1}$) from the Salmisuo measurement site when data are available (black circles). Also shown are JN $CH_4$ sensitivities for 6 parameters using the lowest all-site RMSE from the first ensemble and the site-specific RMSE from the second ensembles (see Tables 6.3 and 6.5).*

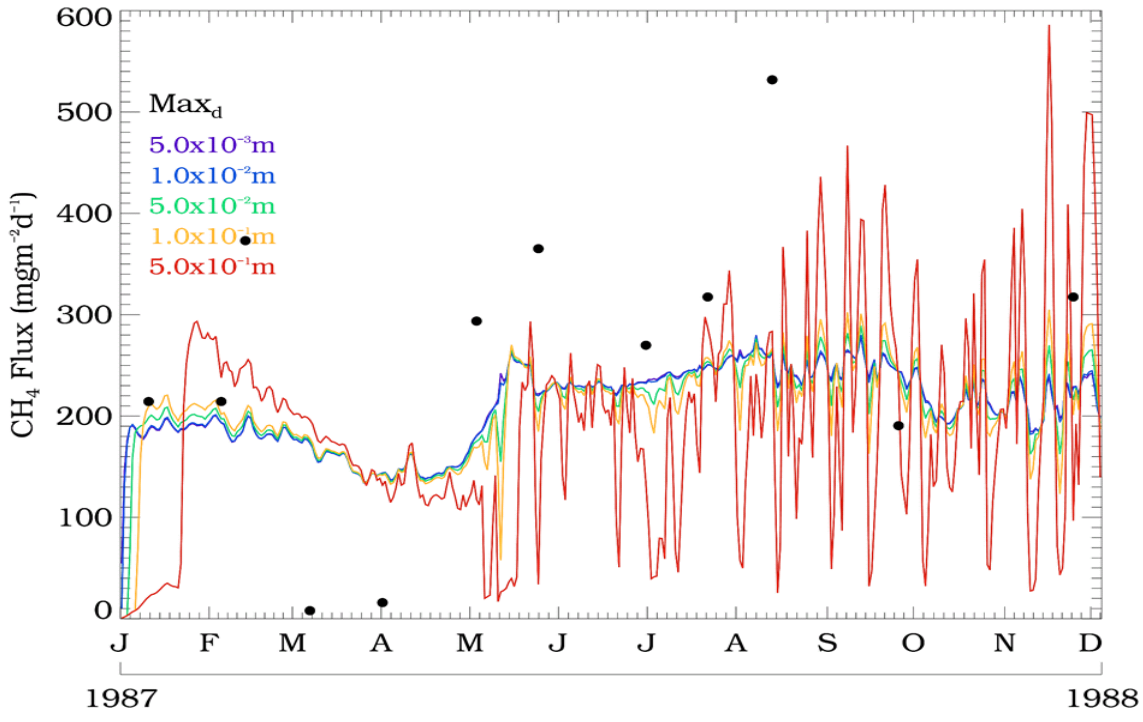


*Figure 6.9 As Figure 6.8 but only showing parameter sensitivities of $Max_d$ at Panama.*

| Parameter | $f_{ox}$ | $O_{max}$ (mol $m^{-3}$ $s^{-1}$) | $K_{CH4}$ (mol $m^{-3}$) | $K_{O2}$ (mol $m^{-3}$) | $Max_d$ | $C_{por}$ |
|---|---|---|---|---|---|---|
| Lowest all-site mean RMSE | 0.25 | $1.25\times10^{-6}$ | $5\times10^{-2}$ | 0.7 | $5\times10^{-3}$ | 0.1 |
| Lowest site-specific RMSE | 0.25 | $1.25\times10^{-7}$ | $5\times10^{-2}$ | 0.7 | $5\times10^{-3}$ | 0.1 |

*Table 6.5 Parameter fitting summary at Salmisuo showing the parameter configurations which produce the lowest all-site RMSE and lowest site-specific RMSE for second ensemble.*

## 6.5 Comparisons of Updated JULES with Flux Observations

This section compares the spatial and temporal differences in the wetland $CH_4$ emissions from JN and JU, prior to their use in TOMCAT. Both inventories were derived using the same JULES parameters, with JN using some additional ones from JULES and HWSD. As a result any differences between them are the result of the additional process descriptions included in JN.

The horizontal resolution of both models is 0.5° by 0.5°, which is far larger than the flux chamber observation area. As a result, scaled model emissions are likely to be far smaller than observations because they will include non-wetland regions with negligible emissions. Considering this, model performance is analysed based on the timing and not the magnitude of emissions. Therefore, scaled comparisons with flux observations are no longer evaluated using RMSE, but instead using the correlation coefficient. Figure 6.10 shows a comparison of JN and JU with observations, where the modelled emissions are increased by a factor of 20 so that the seasonal cycle comparison can be clearly observed on the same scale. Results show that JN produces an improved correlation at 9 of the 13 sites when compared with JU. Both models fail to capture the seasonality at the Alaska and Central Amazonia sites, showing negative correlations. The model developments show a slight deterioration in model performance at the Sanjiang site from R = 0.52 to R = 0.51; however the correlations are limited by the lack of observational data. The other two sites where JU produces a higher correlation, Orinoco and Panama, only have a small seasonal signal and as a result do not produce a statistically significant correlation coefficient at the 90%-level. When averaged over all observation sites JN (R = 0.34) produces a slightly higher correlation coefficient than JU (R = 0.32). This the difference becomes slightly larger when only the statistically significant, at the 90%-level, sites are used (JN: R = 0.43, JU: R = 0.37). These results suggest that at a site level the JULES process additions improve the temporal distributions of emissions only slightly, and that further analysis using a CTM and atmospheric observations is required to assess the spatial and temporal emission distribution on a larger scale.

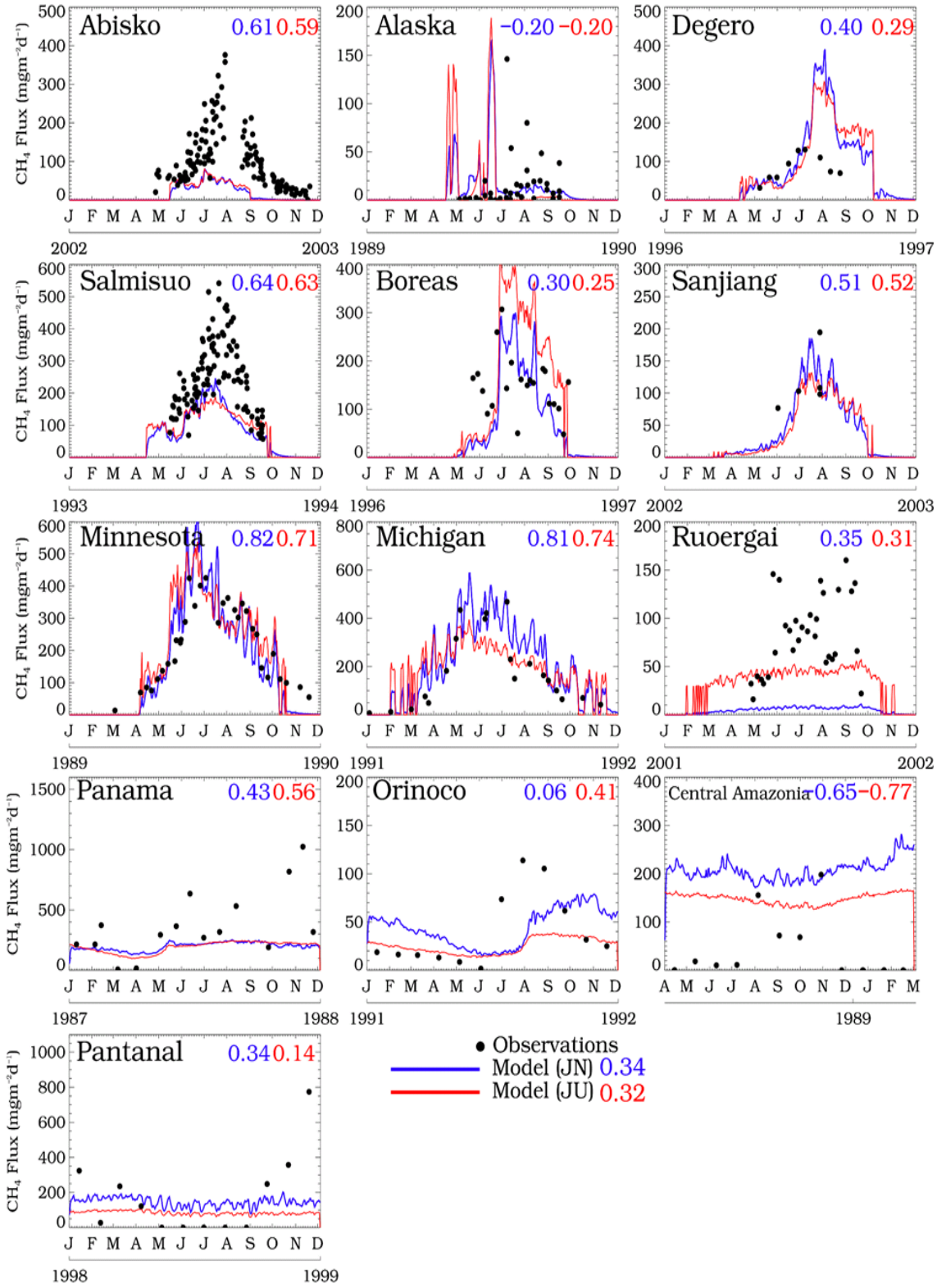


*Figure 6.10 $CH_4$ flux ($mgCH_4\ m^{-2}\ day^{-1}$) from 13 measurement sites when data are available (black circles). Also shown are daily results from JN, for the parameter configuration that provides the lowest mean RMSE over all sites (blue solid line) and emissions from JU (red solid line), both of which have been scaled to produce global emissions of 177 Tg/yr and are increased by a factor of 20. Note that years differ at each site. Correlation coefficients for JN (blue) and JU (red) compared with observations are displayed for each site and as an all-site mean.*

Global comparisons of emission inventories show that the interannual variability is larger in JN (variance = 31.8 Tg/yr) than JU (variance = 23.3 Tg/yr). This is a result of years with unusually high, 2001(189 Tg), and low, 1993 (170 Tg), emissions in the JN inventory. The regions responsible for these unusually high/low emission periods can be determined, for example in 2001 JN emissions in Africa South and Australia increase from the annual means of 20.4 Tg/yr and 6.2 Tg/yr to 25.1 Tg and 9.3 Tg, respectively (see Figure 6.11). Typically JU produces higher boreal emissions, which is offset by higher tropical emissions in JN. As a percentage change in mean emissions this is most evident in Boreal North America where on average JU emissions (9.6 Tg/yr) are 2.4 times larger than JN emissions (3.9 Tg/yr). The inventories show good agreement on the global interannual variability of emissions, with both showing below average emissions for the final 5 years of the atmospheric growth stagnation period (2002-2006) of 173.2 Tg/yr (JU) and 173.7 Tg/yr (JN). Neither inventory suggests wetland emissions were the cause of the initial decline in atmospheric $CH_4$ growth (1999-2001). Since 2007, JN emissions were above average in all years, in agreement with previous findings shown in Chapter 5, which suggests an increase in wetland emissions played a role in the observed increase in atmospheric $CH_4$. This is in part the result of a noticeable change in Africa South in both inventories between 2006 and 2007 with emissions increasing by 4.5 Tg/yr and 3.8 Tg.yr in JN and JU, respectively. There is an overall statistically significant ($p<0.05$) positive trend in wetland emissions in JN of 0.40 Tg/yr, which is in agreement with the trend in JU (0.43 Tg/yr) discussed in Chapter 5. In agreement with JU, JN shows the largest overall trend in emissions over Tropical Asia (0.17 Tg/yr), followed by Australia (0.1 Tg/yr).

Globally, the seasonal ranges in JN and JU are very similar ($R = 0.99$), with maxima in August of 18.0 Tg/month and 18.6 Tg/month (see Figure 6.12). The seasonal low occurs in December in JN (12.3 Tg/yr) and February in JU (11.3 Tg/yr), resulting in JN having a slightly smaller seasonal range. This is mainly caused by the seasonal range of JU emissions in Boreal North America (1.8 Tg/month) being approximately double that of JN (0.9 Tg/month).

On a global scale, the additional process description affected wetland $CH_4$ emissions more on an interannual basis, than seasonally. However, on a regional scale the influence of additional processes is observable both interannually and seasonally. The differences between JN and JU may not necessarily indicate model improvement, but it does highlight the influence of model complexity on emission inventories.

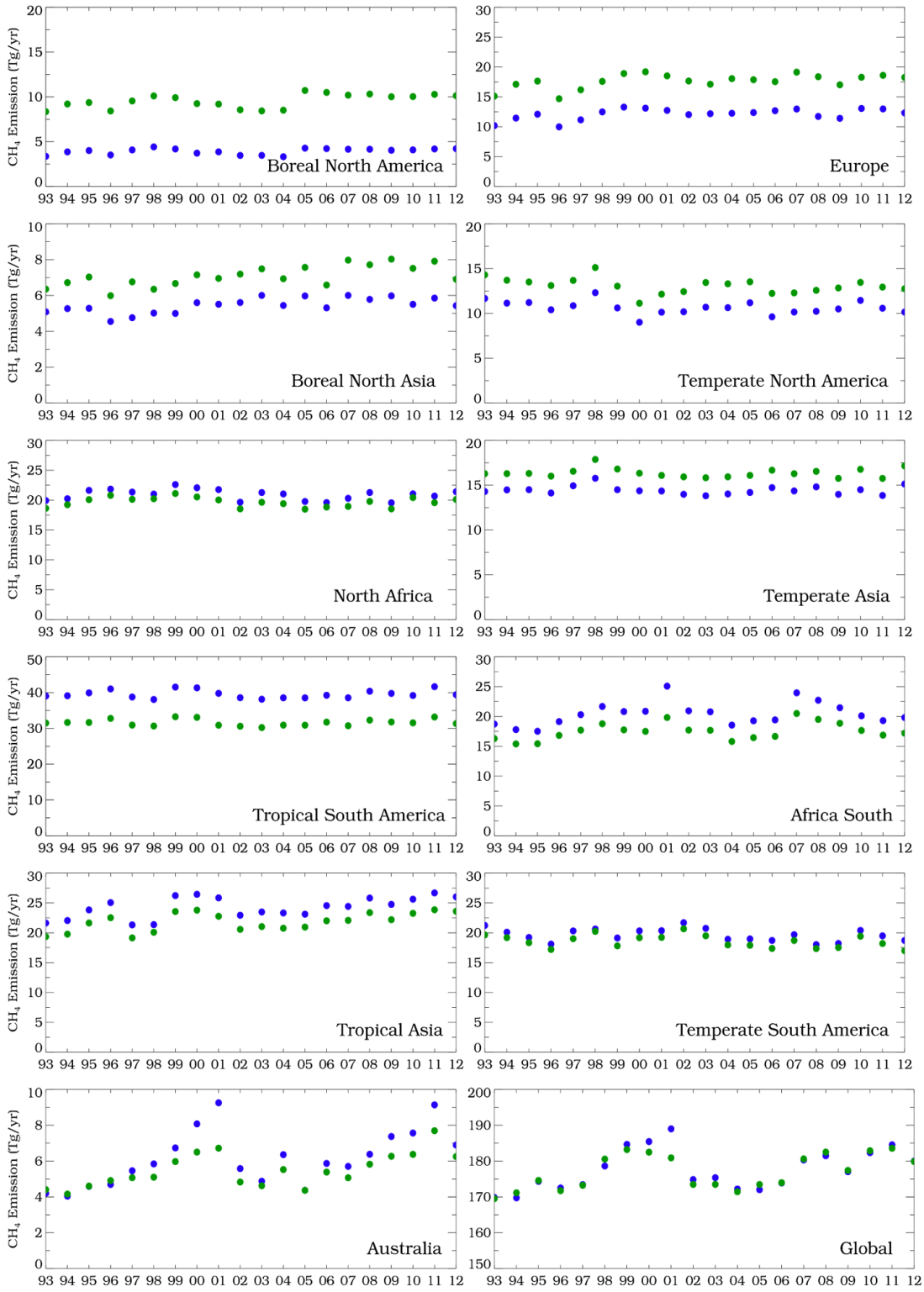


*Figure 6.11 Annual $CH_4$ wetland emissions, in Tg/yr, from JULES simulations, JU (green) and JN (blue) between 1993 and 2012. Individual panels show regions previously defined (Figure 5.10) and the bottom right panel shows the global emissions. Note the difference in y-axis values and that the x-axis values correspond to years.*

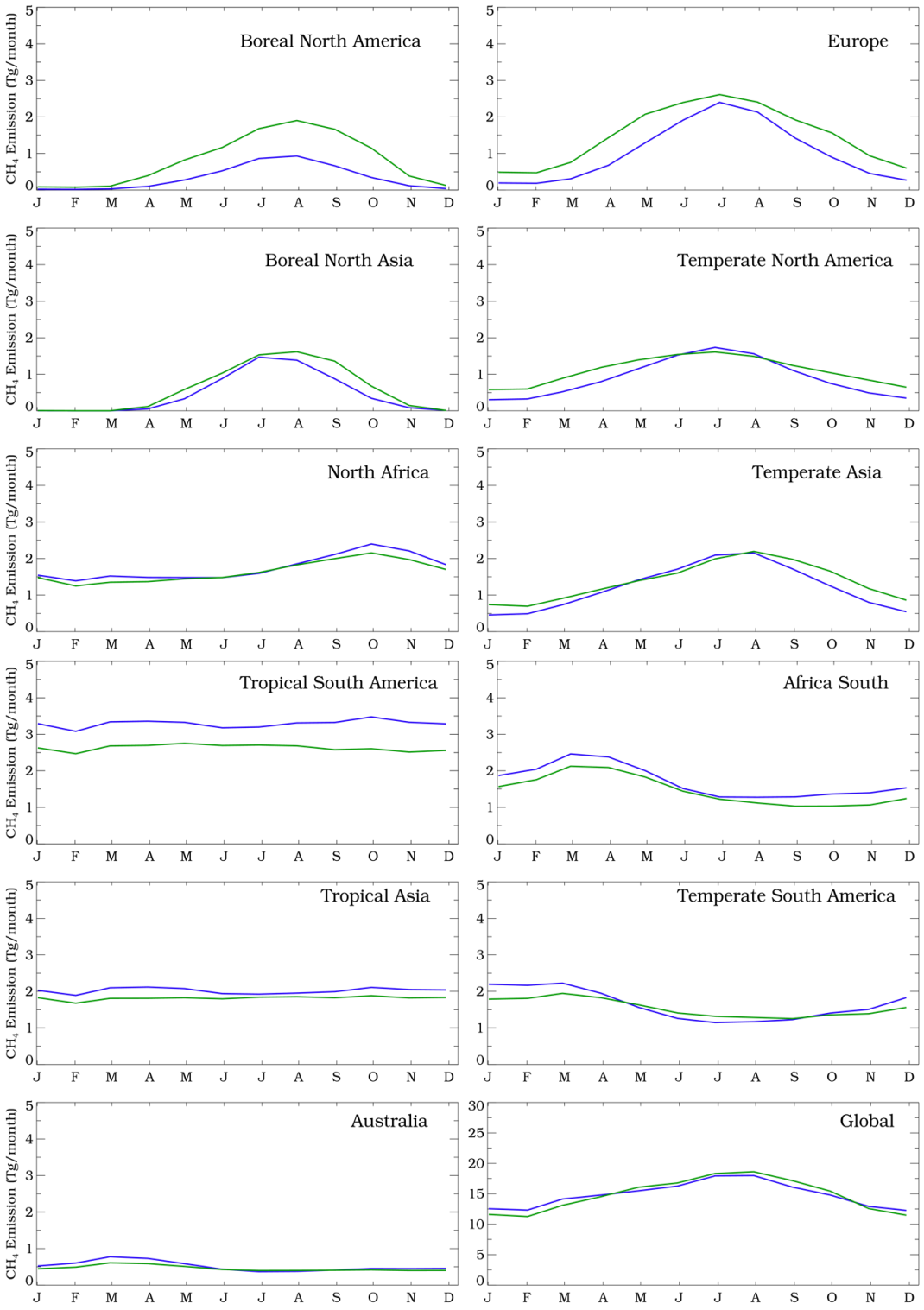


*Figure 6.12 Seasonal cycle of $CH_4$ wetland emissions, in Tg/month, from JULES simulations, JU (green) and JN (blue) averaged between 1993 and 2012. Individual panels show regions previously defined (Figure 5.10) and the bottom right panel shows the global emissions.*

## 6.6 Model Set-up

TOMCAT was used to simulate 2 $CH_4$ tracers from 1993-2012, both of which were identical except for the wetland emissions. The first tracer, which used JU wetland emissions, hereafter referred to as TOM_JU, was identical to the JULES tracer previously used (see Chapter 5). The second tracer used JN wetland emissions, hereafter referred to as TOM_JN. All other $CH_4$ emissions and loss fields were the same as those used in Chapter 5, although, only the NOAA-derived OH field (1997-2007) was used. As a result TOM_JU comparisons with GOSAT and TCCON will differ slightly from those in Chapter 5, which used a repeating OH field. The initial atmospheric state, model resolution, meteorological driving data and output frequency was otherwise identical to the setup from Chapter 5.

## 6.7 Comparisons of TOMCAT $CH_4$ with Observations

### 6.7.1 Flask Comparisons

The results from the two TOMCAT simulations have been compared to surface NOAA sites (see Figure 5.15) between 1993 and 2012, using previously defined spatial and temporal interpolation methods (see Chapters 4 and 5). Model performance is not only dependent on the wetland inventories, but also the accuracy of other emission inventories and loss fields which are not always time-varying, and model transport. A potential issue in model evaluation may occur if for example, incorrect hemispheric emission estimates are offset by incorrect model transport resulting in the model agreeing with the observations but for the wrong reason.

The increased southern hemisphere emissions used in TOM_JN, which are offset by the decreased northern hemisphere emissions, are observable in the comparisons with TOM_JU (see Figure 6.13). TOM_JN captures the observed pause in atmospheric $CH_4$ growth rate, which was previously shown to be well captured by TOM_JU, and is the result of a change in OH and a slight reduction in wetland emissions. Of the two simulations TOM_JU shows stronger agreement with the observed growth rate at northern high-latitude stations (see Table 6.6); however, the model $CH_4$ is biased high in this region, which would result in an overestimation of atmospheric $CH_4$ loss. This might explain why TOM_JN underestimates the high-latitude $CH_4$ growth rate. Averaged over all sites, TOM_JN (20.5 ppb) produces a lower RMSE than TOM_JU (22.8 ppb) when compared to observations, which might also be as a result of the initial model bias in the northern hemisphere. From these long-term smoothed comparisons it is difficult to isolate the

influence of wetland emissions on the observed growth rate. However, the site averaged growth rate falls between the two model simulations, suggesting reasonable model performance on a long-term global scale.

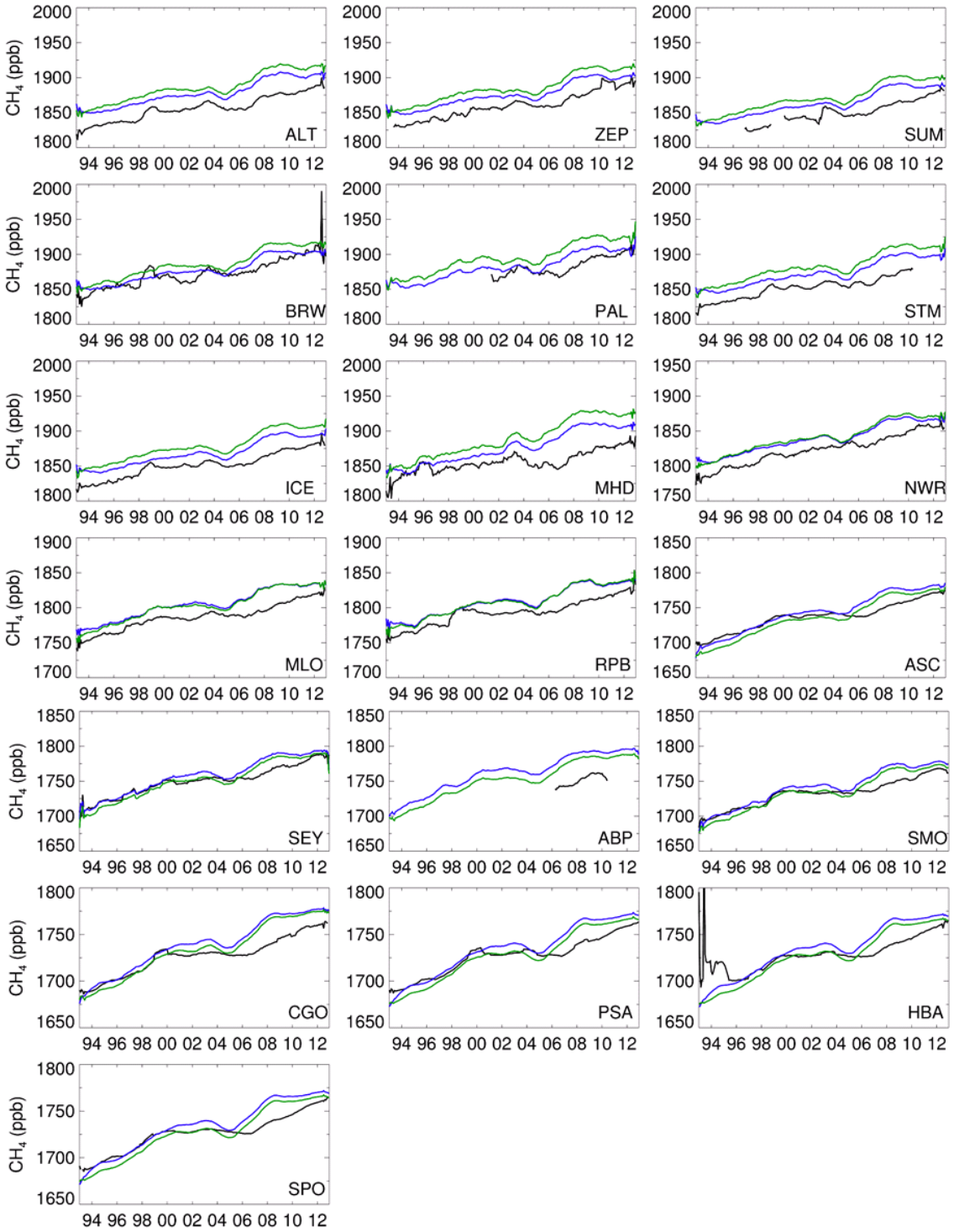


*Figure 6.13 Deasonalised monthly mean surface $CH_4$ (ppb) from 19 NOAA observation sites (black) from 1993 to 2012, where data are available. Also shown are results from two TOMCAT 3-D CTM simulations, TOM_JU (green) and TOM_JN (blue).*

| Station | TOMCAT simulation | | | | | | |
|---|---|---|---|---|---|---|---|
| | TOM_JU | | | TOM_JN | | | NOAA |
| | Correlation Coefficient | RMSE (ppb) | Growth (ppb/yr) | Correlation Coefficient | RMSE (ppb) | Growth (ppb/yr) | Growth (ppb/yr) |
| ALT | 0.89 | 31.9 | 3.2 | 0.90 | 23.8 | 2.2 | 3.5 |
| ZEP | 0.80 | 30.6 | 3.1 | 0.80 | 22.8 | 2.0 | 3.5 |
| SUM | 0.82 | 29.6 | 3.1 | 0.83 | 20.9 | 2.1 | 3.4 |
| BRW | 0.62 | 26.9 | 3.0 | 0.59 | 24.4 | 1.9 | 2.7 |
| PAL | 0.47 | 31.0 | 4.5 | 0.56 | 19.9 | 3.1 | 3.6 |
| STM | 0.81 | 29.6 | 4.1 | 0.82 | 21.3 | 2.8 | 3.7 |
| ICE | 0.87 | 29.0 | 3.7 | 0.87 | 20.1 | 2.6 | 3.2 |
| MHD | 0.63 | 41.5 | 4.6 | 0.64 | 30.9 | 2.3 | 3.9 |
| NWR | 0.91 | 21.6 | 4.0 | 0.90 | 19.7 | 3.1 | 4.4 |
| MLO | 0.93 | 18.8 | 3.8 | 0.92 | 20.1 | 3.2 | 4.6 |
| RPB | 0.86 | 20.3 | 3.6 | 0.85 | 20.3 | 2.7 | 3.9 |
| ASC | 0.94 | 11.9 | 5.0 | 0.93 | 13.2 | 5.4 | 3.8 |
| SEY | 0.95 | 12.1 | 3.9 | 0.95 | 13.9 | 3.5 | 4.0 |
| ABP | 0.69 | 30.9 | 4.2 | 0.60 | 39.4 | 4.4 | 2.9 |
| SMO | 0.95 | 10.3 | 4.7 | 0.95 | 13.1 | 4.8 | 3.9 |
| CGO | 0.93 | 14.0 | 4.7 | 0.93 | 16.6 | 5.0 | 3.8 |
| PSA | 0.95 | 11.5 | 4.5 | 0.95 | 13.7 | 4.9 | 3.7 |
| HBA | 0.70 | 21.9 | 4.4 | 0.69 | 22.6 | 4.8 | 3.8 |
| SPO | 0.96 | 10.7 | 4.5 | 0.96 | 12.9 | 4.9 | 3.9 |
| Average | 0.83 | 22.8 | 4.0 | 0.82 | 20.5 | 3.5 | 3.7 |

*Table 6.6 Correlation coefficient and RMSE values for $CH_4$ flask observations compared with TOM_JU and TOM_JN between 1993 and 2012. Also shown are modelled and observed annual $CH_4$ growth rates in ppb/yr, where observation data are available.*

The seasonality of wetland emissions is not always captured by a simple process description (see Chapter 5), which provided a justification for introducing new model processes in an attempt to better represent the observed seasonal cycle. The seasonal cycles of both TOM_JU and TOM_JN have been evaluated against NOAA observations and shown to perform almost identically at most sites (see Figure 6.14). There are two exceptions to this, BRW and PAL, neither of which exhibits a noticeable seasonal cycle in the observations. At BRW the correlation coefficient decreases when the additional wetland processes are introduced from R = 0.52 to R = 0.44 and at PAL it increases from R = -0.16 to R = 0.17. The results from the remaining stations suggest that the additional wetland processes, which result in a change in $CH_4$ emissions, only have a minor influence on the observed $CH_4$concentration where the sites are located. It is possible that the influence is more noticeable over tropical wetlands which are not included in the NOAA network.

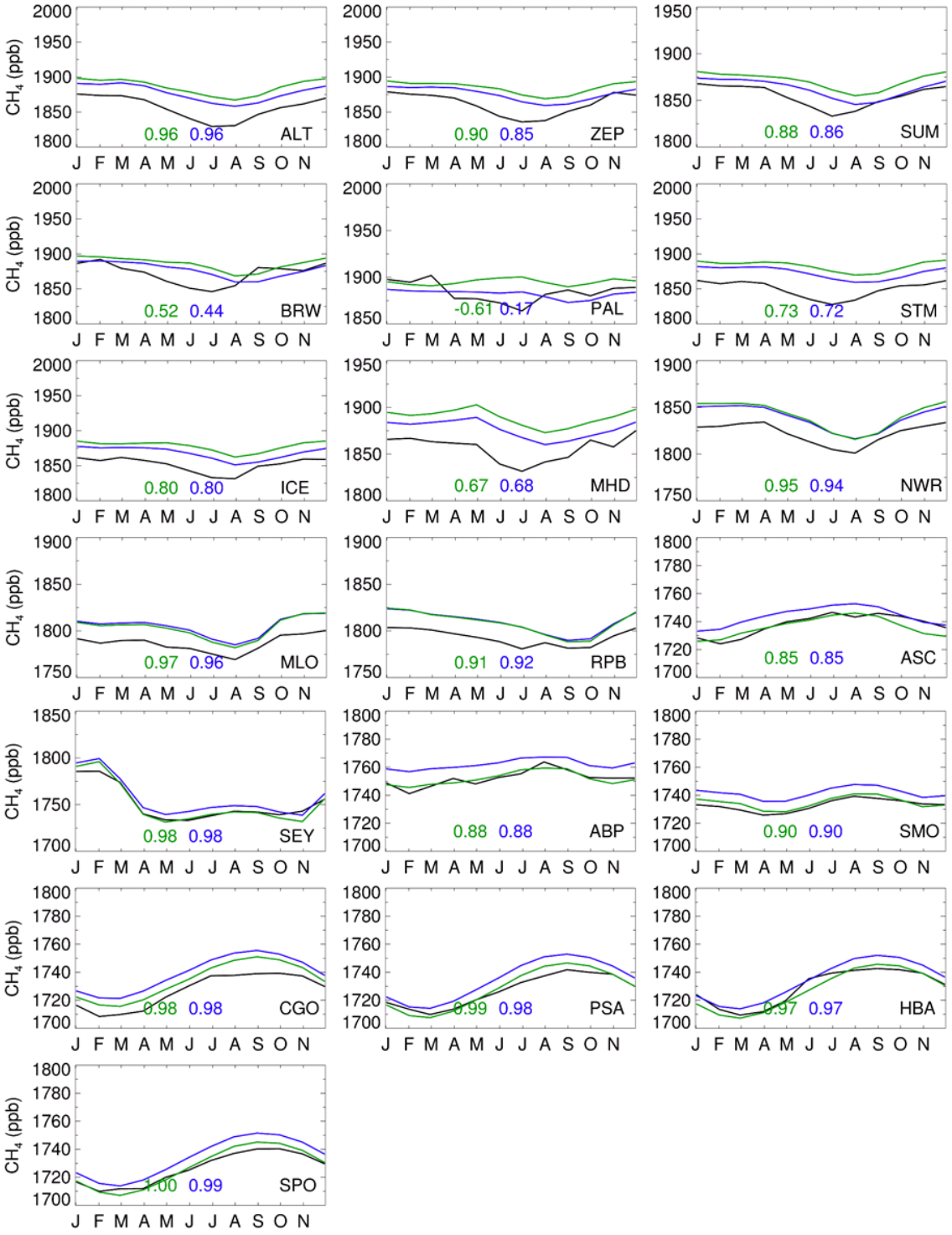


*Figure 6.14 Seasonal cycle of monthly mean surface $CH_4$ (ppb) from 19 NOAA observation sites (black) from 1993 to 2012, where data are available. Also shown are results from two TOMCAT 3-D CTM simulations TOM_JU (green) and TOM_JN (blue). Correlation coefficients of model and observations are displayed for TOM_JU (green) and TOM_JN (blue).*

## 6.7.2 Satellite Comparisons

GOSAT observations, discussed in more detail in Chapters 2 and 5, have been used to evaluate the two TOMCAT simulations. The GOSAT averaging kernel was applied to both simulations, and comparisons were made using the same methodology outlined in Chapter 5. TOMCAT and GOSAT comparisons in Chapter 5 used a repeating OH field, whereas in these simulations both TOM_JU and TOM_JN used the NOAA-derived OH field from 1997-2007.

The positive northern hemisphere bias in June 2010 in TOM_JU, when compared to GOSAT, is reduced, but still present, in TOM_JN (see Figures 6.15 and 6.16). The negative southern hemisphere bias in September and December in TOM_JU is also reduced in TOM_JN. Across all locations and times studied, the mean bias with GOSAT is higher for TOM_JU (13.2 ppb) than for TOM_JN (11.3 ppb). The RMSE from GOSAT comparisons is also higher for TOM_JU (7.4 ppb) than for TOM_JN (6.5 ppb).

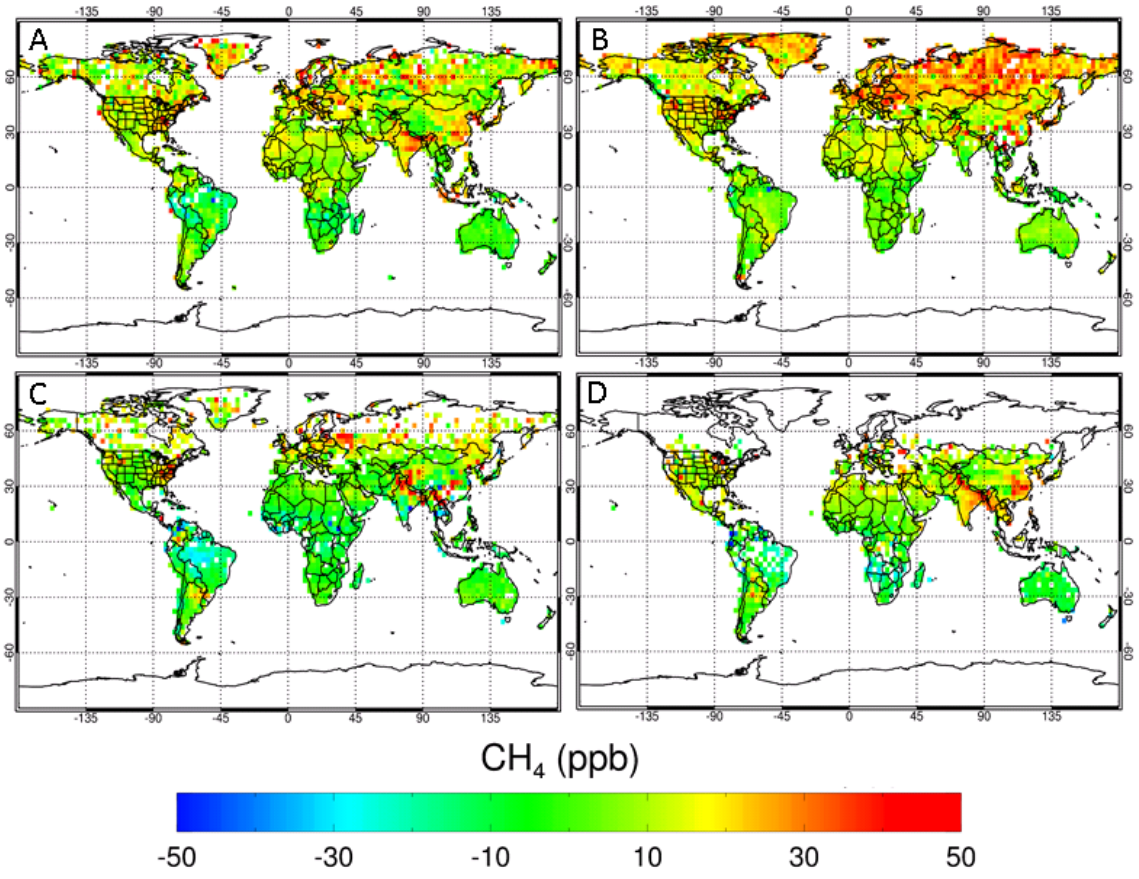


*Figure 6.15 Difference in global monthly mean $XCH_4$ concentrations (ppb) between TOM_JU and GOSAT observations for (a) March, (b) June, (c) September and (d) December, 2010. A GOSAT averaging kernel has been applied to the model data. Note that TOM_JU here is different than in Figure 5.21, which does not use the NOAA-derived OH field.*

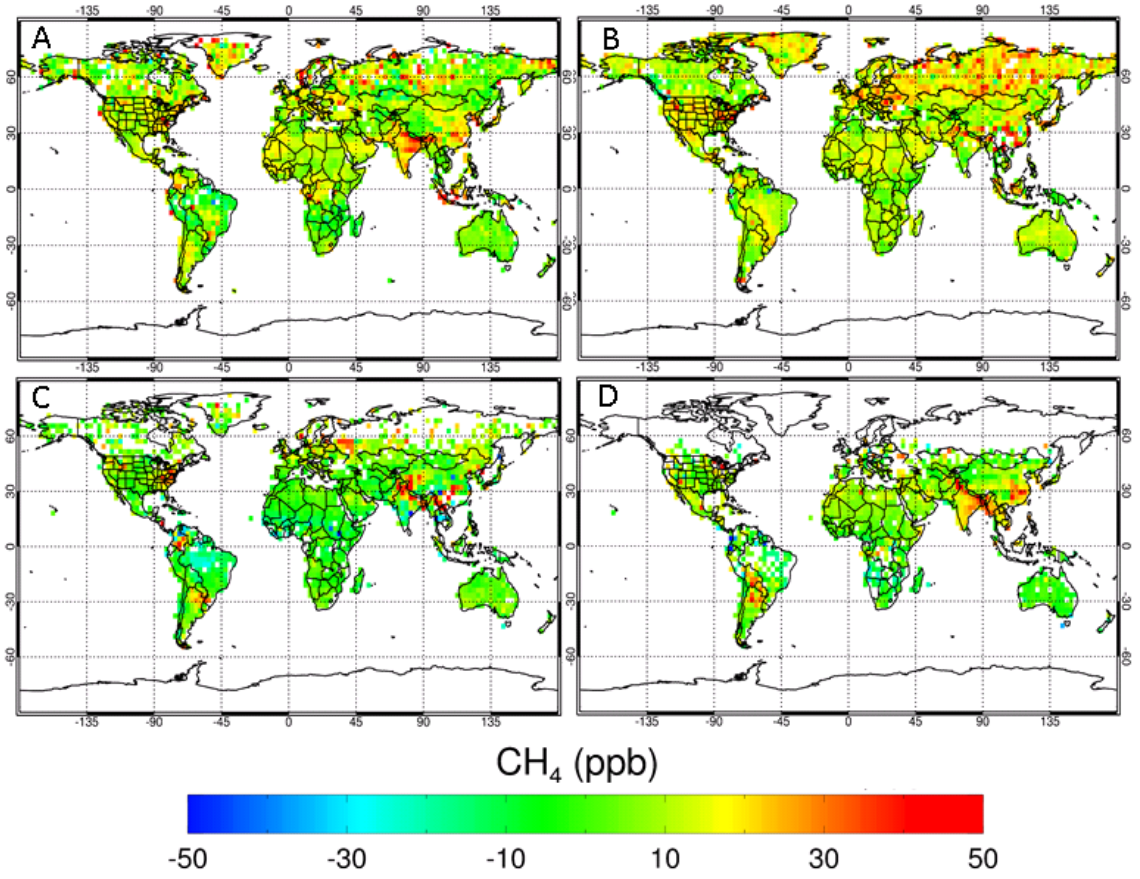


*Figure 6.16 As Figure 6.15 but comparison between GOSAT observations and TOM_JN.*

Previously defined regions (see Figure 5.10) are used to assess spatial and temporal differences between TOM_JU, TOM_JN and GOSAT and the correlation coefficients between TOMCAT and GOSAT are used as a metric for model performance (see Figure 6.17). TOM_JN and TOM_JU produce the same correlation coefficients with GOSAT in 4 out of the 11 regions. In 5 regions TOM_JN correlation coefficients are slightly higher (difference of <0.05) and in the remaining 2 regions TOM_JU correlation coefficients are 0.01 higher. The similarities between the correlation coefficients are in agreement with the NOAA site comparisons, which suggests that the additional wetland process present in JN have only a small influence on the modelled atmospheric $CH_4$ in most regions. The slight model correlation improvement in TOM_JN in Tropical (+0.01) and Temperate (+0.04) South America suggests that aspects of the Amazon, Orinoco and Pantanal wetland emissions are improved by the inclusion of the more complex processes present in JN. The GOSAT observed global growth rate (6.6 ppb/yr) for the entire time series is larger than both TOM_JN (2.5 ppb/yr) and TOM_JU (2.5 ppb/yr), suggesting an incorrect balance between sources and sinks in the model. Both wetland inventories have above average wetland emissions over the TOMCAT time series; however they could still be underestimating total emissions. Other explanations include increased biomass burning or anthropogenic emissions, or a decrease in the atmospheric sink through a reduction in [OH].

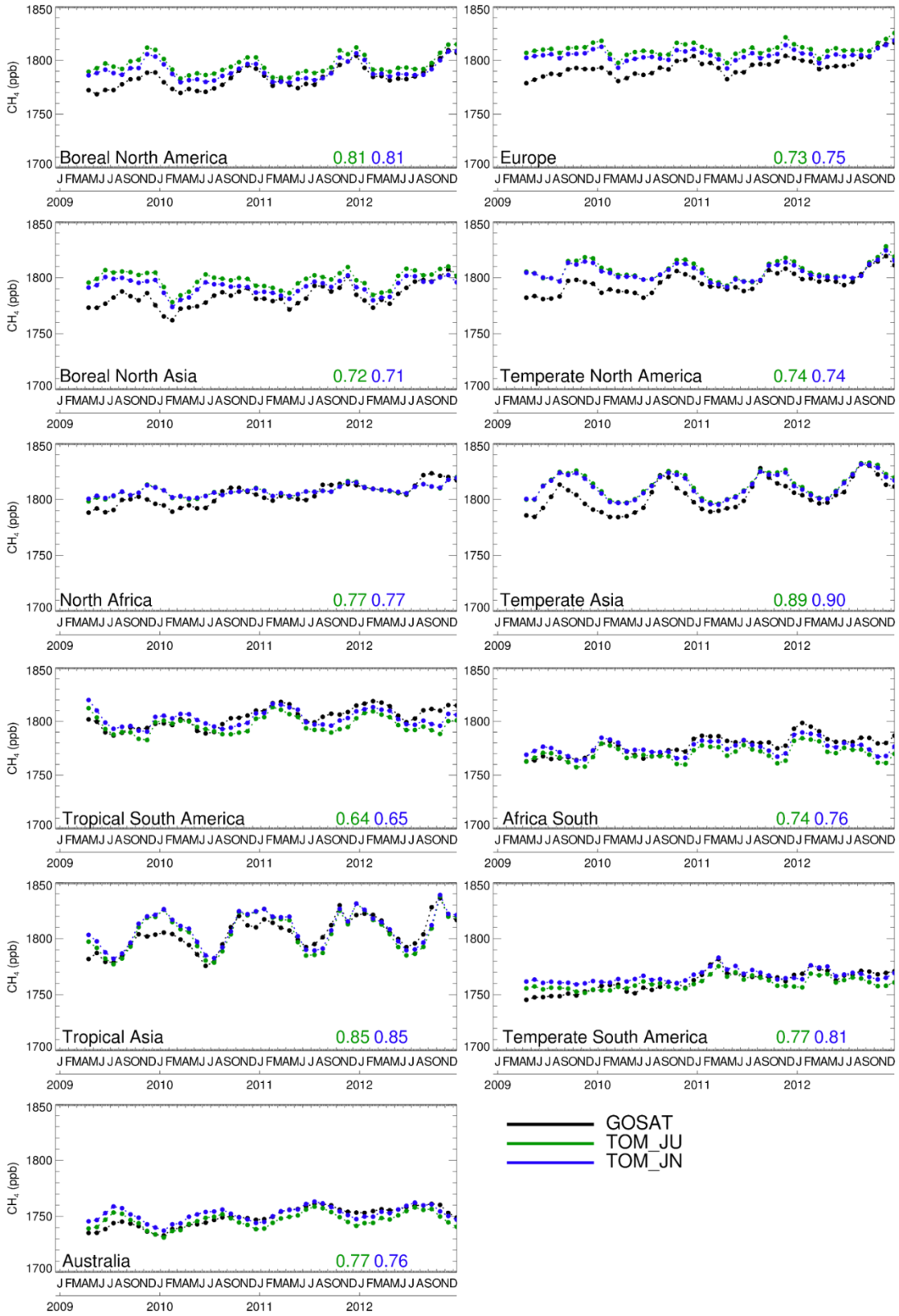


*Figure 6.17 Regional monthly mean $XCH_4$ concentrations (ppb) from GOSAT between April 2009 and December 2012 (black). Also shown are regional monthly mean $XCH_4$ concentrations from two TOMCAT simulations with GOSAT averaging kernels applied, TOM_JU (green) and TOM_JN (blue). Correlation coefficients of model and observations are displayed for TOM_JU (green) and TOM_JN (blue).*

All GOSAT retrievals have been correlated with both TOM_JN and TOM_JU $XCH_4$ after the averaging kernel has been applied (see Figure 6.18). Results show that TOM_JN produces a lower mean bias, RMSE and a higher correlation than TOM_JU. This suggests that when all GOSAT retrieval points are considered TOMCAT produces a more accurate $XCH_4$ when driven by JN.

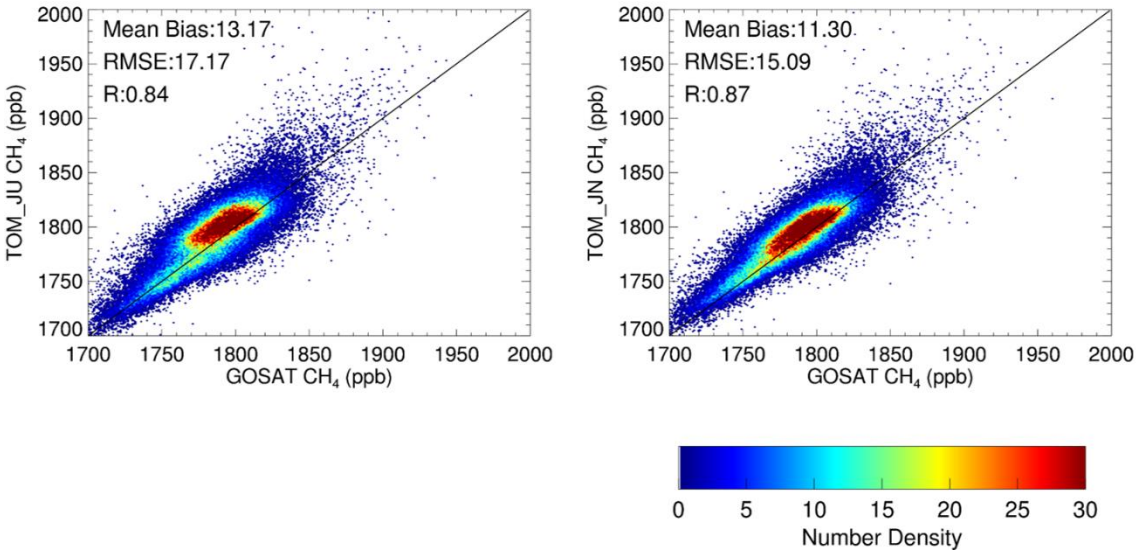


*Figure 6.18 Number density correlation of GOSAT with TOMCAT model output driven by two different wetland emission inventories between April 2009 and December 2012. Points are gridded into 1 ppb by 1 ppb bins. Also shown are the mean bias, RMSE and correlation coefficient of each comparison.*

## 6.7.3 TCCON Comparisons

The final observation comparisons are made with 15 TCCON stations, which are described in Chapters 2 and 5. The averaging kernel is applied to both TOMCAT simulations using the method from Chapter 5 and all comparisons are made using monthly TCCON and TOMCAT data. The TOM_JU comparisons use the NOAA-derived OH field, which differs from those shown using a repeating OH field in Chapter 5. Typically the correlation coefficients calculated are similar for both TOM_JU and TOM_JN when compared with the TCCON observations (see Figure 6.19). This is unsurprising because, as noted earlier, the majority of TCCON stations are not near wetland emission regions. TOM_JU produces a higher correlation coefficient at 11 of the 15 stations, while TOM_JN only produces a higher correlation at Eureka, a station limited by infrequent observations. This suggests that TOM_JU more accurately captures the seasonality of $XCH_4$ at TCCON stations. The comparisons would profit from increased TCCON coverage of wetland regions. TOM_JN produces a lower mean bias (20.0 ppb) and RMSE (9.1 ppb) than TOM_JU (22.4 ppb and 9.9 ppb).

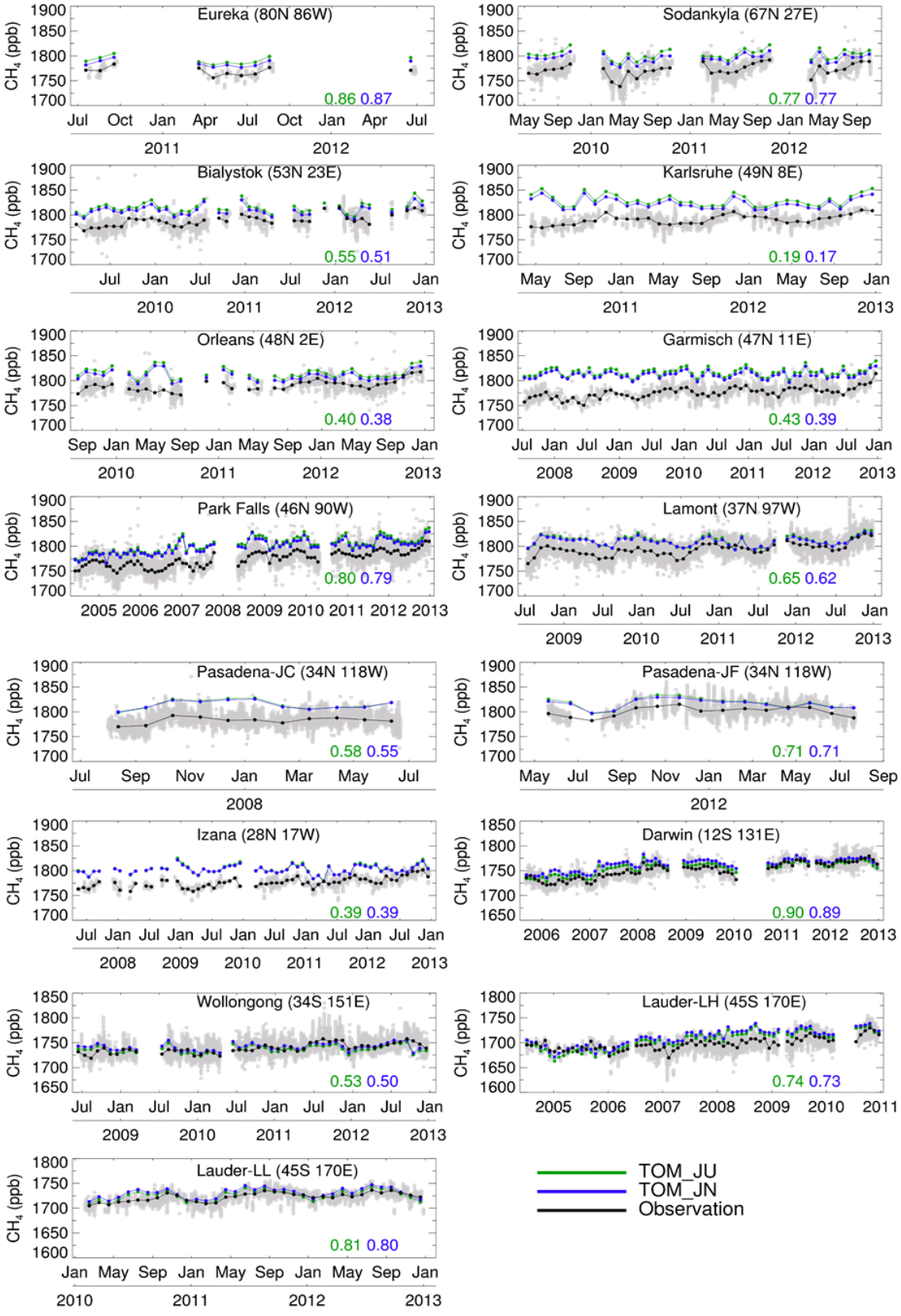


*Figure 6.19 Monthly mean $XCH_4$ concentrations (ppb) from 15 TCCON sites when data are available (black). Also shown are concentrations from TOM_JU (green) and TOM_JN (blue), both with TCCON averaging kernels applied. Correlation coefficients of model and observations are displayed for TOM_JU (green) and TOM_JN (blue). Individual observations are also shown (grey).*

## 6.8 Summary

This chapter has introduced additional processes to the JULES wetland $CH_4$ emissions model and compared both the updated and original version with flux measurements. Emissions from the updated model have also been used to force TOMCAT for comparisons with atmospheric measurements. The key results are:

- The methanogenesis rate of the fast turnover pools (Decomposable/Resistant Plant Material), the temperature dependence, and the fraction of carbon available for methanogenesis were all identified as parameters potentially controlling the timing and magnitude of $CH_4$ emissions.

- In the updated JULES model, transport and oxidation parameters had a small impact on the timing of $CH_4$ emissions with the exception of the ebullition parameters at some flux sites.

- When $CH_4$ was globally scaled to 177 Tg/yr, both versions of JULES (standard and updated) underestimated observed fluxes by approximately a factor of 20 because of the coarse model resolution.

- Average model correlation with $CH_4$ flux observations increased from R = 0.32 in the standard version to R = 0.34 in the updated version of JULES, i.e. there was only a marginal improvement.

- Comparisons with flask measurements showed almost no change in the updated version of JULES compared to the standard version.

- Comparisons of GOSAT column $CH_4$ estimates with TOMCAT showed a slight improvement with respect to time-correlation (R = 0.87), mean bias (11.30 ppb) and RMSE (15.09 ppb) compared with the standard version of JULES (R = 0.84, mean bias = 13.17 ppb and RMSE = 17.17 ppb).

- Comparisons with TCCON column $CH_4$ estimates showed that the mean bias and RMSE were reduced when using the updated version of JULES compared to the standard version, from 22.4 ppb to 20.0 ppb and 9.9 ppb to 9.1 ppb. However, the correlation also decreased slightly from R = 0.62 to R = 0.60.

The first part of this chapter explored increasing the complexity of the JULES wetland $CH_4$ model by adding processes. This included the production of $CH_4$ in non-saturated soils, sulphate suppression of $CH_4$ production, storage and transfer of $CH_4$ between a saturated and non-saturated pool, transport of $CH_4$ via diffusion, ebullition and aerenchyma, and oxidation within the soils. These processes, implemented largely based on previous studies, were optimised using a perturbed parameter ensemble and flux observations. From this the methanogenesis rate of the fast turnover carbon pools (DPM and RPM), the temperature dependence ($Q_{10}$) and the fraction of carbon available for methanogenesis ($\varphi_{sat/uns}$) were all identified as parameters which noticeably influenced $CH_4$ flux. The updated model showed a slightly improved agreement (R = 0.34) with $CH_4$ flux observations than the standard version (R = 0.32); however, when scaled to top-down global estimates both versions underestimated the observed flux. This is most likely because the modelled emissions represented a much larger area than the observed fluxes, which were typically chosen in specific areas with known wetlands. To improve model evaluation it is recommended that comparisons are made with flux measurements taken over a larger area (e.g. tower observations).

The emission inventories produced from the standard version of JULES (JU) and the updated version (JN) were then used alongside other emissions in TOMCAT (TOM_JU and TOM_JN). Both, JU and JN, showed a decrease in emissions to 173.2 Tg/yr and 173.7 Tg/yr during the final 5 years of the observed stagnation in atmospheric $CH_4$ growth (2002-2006); however, neither inventory showed a decrease in emissions in the initial 3 years of the stagnation (1999-2001) These simulations were evaluated using observations from GOSAT, TCCON and flask sites and a model assessment was made by analysing the temporal and spatial distribution of atmospheric $CH_4$ using the correlation, mean bias and RMSE values. The previously observed northern hemisphere positive bias in TOM_JU is reduced in TOM_JN, this suggests that either latitudinal wetland emissions are better represented in JN or that a slow latitudinal transport in TOMCAT is offset by under predicted northern hemisphere $CH_4$ emissions. TOM_JN produced a lower average mean bias and RMSE than TOM_JU in comparisons with all three observation types, although correlation coefficient changes were less noticeable. Previous comparisons suggest that South American emissions are poorly represented in wetland $CH_4$ models (see Chapter 5). TOM_JN showed a slight correlation improvement over TOM_JU in the Amazon and Orinoco wetland region (Tropical South America) and the Pantanal wetland region (Temperate South America), when compared with GOSAT of +0.01 and +0.04, respectively. The model evaluation showed that the additional processes introduced to JULES slightly improve model performance. It is recommended that an improved understanding of wetland biogeochemistry and more surface $CH_4$ flux observations are required to further develop the model.

# 7 Summary

## 7.1 Completion of Aims

The overall objective of this thesis was to improve understanding of recent trends in atmospheric $CH_4$ using a combination of the JULES land surface model (LSM), the TOMCAT atmospheric chemical transport model (CTM), flux measurements and atmospheric concentration observations. These atmospheric $CH_4$ trends depend on the spatial and temporal distribution of the sources, sinks and atmospheric transport. As a result, a detailed understanding of these individual components is required to accurately constrain the past and to predict future changes in $CH_4$. The atmospheric loss of $CH_4$ through the reaction with OH and variations in wetland $CH_4$ emissions were specifically targeted for investigation by utilising recent advancements in remote sensing capabilities and other observations. Uncertainties in wetland $CH_4$ models were also investigated and process developments made to the wetland component of the existing JULES LSM. The remainder of this section focuses on the completion of individual aims that were outlined in Chapter 1.

**Assess the role of atmospheric processes in the pause in $CH_4$ growth between 1999 and 2006.**

As a first step, the atmospheric contribution to trends in the $CH_4$ growth rate was investigated, with a particular focus on the period between 1999 and 2006, where there was a pause in the growth. This was achieved using a combination of both TOMCAT and a simple one-box model to simulate multiple configurations of atmospheric conditions with differing meteorology and OH loss fields, and then by comparing those simulations with observations. These experiments did not account for any year-to-year changes in emissions. With the exception of an annually repeating OH field, the suite of OH fields used were derived from $CH_3CCl_3$ measurements using either a simple one-box model or taken from previous studies (Montzka *et al*., 2011; Rigby *et al*., 2013). In addition, model simulations included every combination of varying/repeating temperature and transport to assess the individual contributions of these to $CH_4$ growth.

When used to perturb an existing mean [OH] field, derived global [OH] anomalies were shown to capture the observed $CH_3CCl_3$ decay rate anomaly, which demonstrated the suitability of using $CH_3CCl_3$-derived global annual [OH] anomalies in TOMCAT to study $CH_4$ loss. Model $CH_4$ growth agreement with observations improved from R = 0.32, with an annually repeating [OH], to R = 0.58-0.65, with an annually varying [OH]; indicating the importance of [OH] variability on the growth rate. When accounting for [OH] variability, results from the one-box model showed that annual emissions needed only to drop between 0 Tg/yr and 3 Tg/yr during the stagnation period. In contrast, when [OH] variability was not accounted for the results from the one-box model showed emissions were required to decrease by between 5 Tg/yr and 7 Tg/yr. This suggests that the emission changes required during the stagnation period, to explain the decrease in $CH_4$ growth, were smaller than previously considered, and that anomalously high [OH] may explain a large fraction of the observed growth decrease. The influence of both temperature and transport changes are also shown to have reduced the growth rate of $CH_4$, albeit to a lesser extent than [OH]. Given the very low current abundance of current $CH_3CCl_3$, measurements are not accurate enough to investigate the period of resumed growth since 2007; however, there are indications of a decrease in [OH] between 2007 and 2012.

**Use a global atmospheric chemistry transport model, TOMCAT, and observations to investigate limitations of current wetland $CH_4$ emissions models.**

The next step introduced varying emissions to the TOMCAT simulations, with the aim of quantifying the role of wetland emissions on the observed trends in $CH_4$ growth. This was achieved using three different wetland inventories, all of which used the same process description but different driving parameters. As a result, these simulations separated parameter uncertainty from process uncertainty, with wetland fraction emerging as the most influential parameter. Spatial and temporal distributions were analysed and comparisons were made with observations to evaluate model performance. Finally, long-term trends were identified in each of the wetland emission inventories.

Two wetland $CH_4$ emission inventories, one based on top-down estimates (BL) and the other derived from JULES (JU), produced similar temporal and spatial distributions. The third inventory, based on observed variables (JP), showed noticeable differences. When used in TOMCAT, BL and JU both showed reasonable agreement with observations, whereas the simulation using JP showed a weaker correlation with observations, suggesting inaccuracy in the observed driving variables. When compared with satellite observations all model versions produced the lowest correlation in South America, suggesting either missing processes within the wetland models, misrepresentation of non-wetland emissions or model transport issues. All three

inventories showed a slight decrease in average wetland emissions during the stagnation period (1999-2006), which implied that wetland emissions contributed to the slowdown of atmospheric $CH_4$ growth. The models did not agree on the regions which were responsible for the decrease in emissions. During this time period emission decreases were largest in Temperate North America (0.4 Tg/yr) in JU, Temperate Asia (0.7 Tg/yr), Tropical South America (0.7 Tg/yr) and Tropical Asia (0.7 Tg/yr) in JP and Boreal Asia (0.4 Tg/yr), North Africa (0.5 Tg/yr) and Africa South (0.5 Tg/yr) in BL. Meteorological driving data in JULES suggests that the reduced emissions were, in part, a result of reduced precipitation over wetland regions during the latter stages of this time period (2001-2006). Over the entire time series both JU (1993-2012: +0.43 Tg/yr) and BL (2003-2011: +0.56 Tg/yr) showed a statistically significant (95%-level) trend in wetland $CH_4$ emissions, extrapolating this trend into the future would imply a continued increase in wetland $CH_4$ emissions. Both JU and BL indicated that a fraction of the observed increase in atmospheric $CH_4$ growth post-2007 was caused by an increase in wetland emissions.

**Improve understanding of processes which drive wetland $CH_4$ emissions and use this in the development of the JULES land surface model.**

Additional processes were introduced to the JULES wetland $CH_4$ model as a final step to improve emission estimates, which was achieved with the aid of surface flux observations. Further, descriptions introduced included production in non-saturated soils, pool storage, sulphate suppression, oxidation and transport. In addition to this, pre-existing parameters were tuned using a perturbed parameter ensemble to fit observed fluxes. Both the standard version (JU) and the updated version (JN) of JULES were then used to drive TOMCAT with a $CH_3CCl_3$-derived OH field. The same comparisons as used in previous experiments were performed on both versions of the model to evaluate whether the inclusion of additional processes to JULES improved agreement with observations.

From the perturbed parameter ensemble the methanogenesis rate of two of the carbon pools (DPM and RPM), the temperature dependence and the fraction of carbon available for methanogenesis emerged as the dominant parameters when considering the magnitude and timing of $CH_4$ emissions. The transport and oxidation parameters were observed to only have a small impact, although at some sites when the water depth parameter was varied, ebullition pulse events noticeably altered emissions. In total 13 parameters were tuned to optimise the model fit with observations. The flux correlation between JULES and observations improved slightly on addition of these processes from $R = 0.32$ to $R = 0.34$. When used in TOMCAT the updated JULES (JN) dataset produced a lower RMSE and mean bias when compared with three separate observation types (NOAA flask, TCCON and GOSAT). For GOSAT comparisons the correlation

was also improved, suggesting that the additional processes introduced improved the spatial and temporal representation of wetland emissions slightly. The small bias in all model simulations suggested that the top-down average emission estimate of 177 Tg/yr for wetland $CH_4$ is reasonable.

**Synthesis**

Recent trends in observed atmospheric $CH_4$ show a slowdown in growth between 1999 and 2006 followed by a post-2007 increase in growth. Results using $CH_3CCl_3$ measurements, JULES, TOMCAT and observations, showed that both an increase in OH and a decrease in wetland emissions contributed to this initial pause in growth. Additionally, the observed increase in atmospheric $CH_4$ between 2007 and 2012 can be partly, but not entirely, attributed to an increase in wetland emissions. Model results suggested a positive trend in recent years of wetland $CH_4$ emissions, which may have implications for predicted atmospheric $CH_4$. An evaluation of existing wetland $CH_4$ inventories show that a combination of process and parameter uncertainty lead to uncertainties in the spatial and temporal distribution of emissions. The JULES model was shown to reproduce similar emissions to an earlier top-down study (Bloom *et al.*, 2012) and these emissions produced a reasonable model agreement with observations when used in TOMCAT. Comparisons between TOMCAT and observations suggested that developments made to JULES, including both $CH_4$ oxidation and transport improved the modelled representation of $CH_4$ emissions.

## 7.2 Future Work

The $CH_3CCl_3$-derived OH anomaly used as part of this work currently only exists for a limited timeframe (1997-2009) and relies on a sparse network of surface observations. Accurate $CH_3CCl_3$ measurements made from an increased number of sites could provide an extended OH anomaly time series, although the phase out of $CH_3CCl_3$ due to the Montreal Protocol will limit its use. The community will need to search for alternative gases from which to derive global mean OH, possible candidates include anthropogenic hydrofluorocarbons (HFCs). Either way, these observations can then be used to produce an extended derived OH anomaly suitable for use in future studies. This would help explain whether a decreased [OH] had a role in the observed $CH_4$ growth post-2009. An alternative direction would involve incorporating online OH fields into the model evaluation; however, currently too much uncertainty surrounds the use of an online OH field (Voulgarakis *et al.*, 2013).

Current model evaluation performed using TOMCAT relies on anthropogenic and biomass burning emissions which are only available up until 2008 and 2011, respectively. An update to these emission inventories would improve the models ability to accurately represent recent interannual variations in atmospheric $CH_4$. The same is also true for many other emission fields currently used within the model, which typically do not vary interannually, e.g. rice, termites. In the future, further TOMCAT evaluations could be performed for more recent years which overlap more with the GOSAT time series (2009- ), by extending the JULES simulations beyond 2012.

The additional process descriptions developed for use in JULES could be included in the standard version of the JULES model and be used in climate prediction scenarios. These emission estimates could be forecast using modelled meteorological fields (e.g. Unified Model). To build upon this work, further development using additional processes (e.g. pH) and more observations over a larger area (e.g. tower measurements) would be required.

Several areas not specifically investigated in this thesis could be introduced to further this work, including the use of inverse modelling and isotope observations to identify emission source types from atmospheric $CH_4$ measurements. $CH_4$ sources have distinct isotopic signatures, for example, biogenic sources have a mean isotopic signature of $\delta^{13}C = -60 \pm 5‰$, whereas pyrogenic sources have a heavier mean isotopic signature of $\delta^{13}C = -22 \pm 3‰$ (Sapart *et al.*, 2012). By using inversion techniques on observed $CH_4$ isotope concentrations the source location and type can be identified. This would help constrain individual sources and attribute changes in observed atmospheric $CH_4$ to those individual sources.

# References

Akagi, S.K., Yokelson, R.J., Wiedinmyer, C., Alvarado, M.J., Reid, J.S., Karl, T., Crounse, J.D. and Wennberg, P.O., 2011. Emission factors for open and domestic biomass burning for use in atmospheric models. *Atmospheric Chemistry and Physics*, 11(9), 4039-4072.

Allan, W., Struthers, H. and Lowe, D.C., 2007. Methane carbon isotope effects caused by atomic chlorine in the marine boundary layer: Global model results compared with Southern Hemisphere measurements. *Journal of Geophysical Research: Atmospheres*, 112(D4).

Anderson, B., Bartlett, K., Frolking, S., Hayhoe, K., Jenkins, J. and Salas, W., 2010. Methane and nitrous oxide emissions from natural sources. *United States Environmental Protection Agency*, Office of Atmospheric Programs, Washington.

Andreae, M.O. and Merlet, P., 2001. Emission of trace gases and aerosols from biomass burning. *Global biogeochemical cycles*, 15(4), 955-966.

Archer, D., 2007. Methane hydrate stability and anthropogenic climate change. *Biogeosciences Discussions*, 4(2), 993-1057.

Archer, D., Eby, M., Brovkin, V., Ridgwell, A., Cao, L., Mikolajewicz, U., Caldeira, K., Matsumoto, K., Munhoven, G., Montenegro, A. and Tokos, K., 2009. Atmospheric lifetime of fossil fuel carbon dioxide. *Annual Review of Earth and Planetary Sciences*, 37(1), p.117.

Bastviken, D., Cole, J., Pace, M. and Tranvik, L., 2004. Methane emissions from lakes: Dependence of lake characteristics, two regional assessments, and a global estimate. *Global biogeochemical cycles*, 18(4).

Bastviken, D., Tranvik, L.J., Downing, J.A., Crill, P.M. and Enrich-Prast, A., 2011. Freshwater methane emissions offset the continental carbon sink. *Science*, 331(6013), 50.

Bergamaschi, P., Frankenberg, C., Meirink, J.F., Krol, M., Dentener, F., Wagner, T., Platt, U., Kaplan, J.O., Körner, S., Heimann, M. and Dlugokencky, E.J., 2007. Satellite chartography of atmospheric methane from SCIAMACHY on board ENVISAT: 2. Evaluation based on inverse model simulations. *Journal of Geophysical Research: Atmospheres*, 112(D2).

Bergamaschi, P., Frankenberg, C., Meirink, J.F., Krol, M., Villani, M.G., Houweling, S., Dentener, F., Dlugokencky, E.J., Miller, J.B., Gatti, L.V. and Engel, A., 2009. Inverse modeling of global and regional $CH_4$ emissions using SCIAMACHY satellite retrievals. *Journal of Geophysical Research: Atmospheres*, 114(D22).

Beven, K.J., Kirkby, M.J., Schofield, N. and Tagg, A.F., 1984. Testing a physically-based flood forecasting model (TOPMODEL) for three UK catchments. *Journal of Hydrology*, 69(1-4), 119-143.

Blaxter, K.L. and Clapperton, J.L., 1965. Prediction of the amount of methane produced by ruminants. *British journal of nutrition*, 19(01), 511-522.

Bloom, A.A., Palmer, P.I., Fraser, A., Reay, D.S. and Frankenberg, C., 2010. Large-scale controls of methanogenesis inferred from methane and gravity spaceborne data. *Science*, 327(5963), 322-325.

Bloom, A.A., Palmer, P.I., Fraser, A. and Reay, D.S., 2012. Seasonal variability of tropical wetland CH 4 emissions: the role of the methanogen-available carbon pool. *Biogeosciences*, 9(8), 2821-2830.

Boening, C., Willis, J.K., Landerer, F.W., Nerem, R.S. and Fasullo, J., 2012. The 2011 La Niña: So strong, the oceans fell. *Geophysical Research Letters*, 39(19).

Bogner, J. and Matthews, E., 2003. Global methane emissions from landfills: new methodology and annual estimates 1980–1996. *Global Biogeochemical Cycles*, 17(2).

Bousquet, P., Ciais, P., Miller, J.B., Dlugokencky, E.J., Hauglustaine, D.A., Prigent, C., Van der Werf, G.R., Peylin, P., Brunke, E.G., Carouge, C. and Langenfelds, R.L., 2006. Contribution of anthropogenic and natural sources to atmospheric methane variability. *Nature*, 443(7110), 439-443.

Bousquet, P., Ringeval, B., Pison, I., Dlugokencky, E.J., Brunke, E.G., Carouge, C., Chevallier, F., Fortems-Cheiney, A., Frankenberg, C., Hauglustaine, D.A. and Krummel, P.B., 2011. Source attribution of the changes in atmospheric methane for 2006–2008. *Atmospheric Chemistry and Physics*, 11(8), 3689-3700.

Bovensmann, H., Burrows, J.P., Buchwitz, M., Frerick, J., Noël, S., Rozanov, V.V., Chance, K.V. and Goede, A.P.H., 1999. SCIAMACHY: Mission objectives and measurement modes. *Journal of the Atmospheric Sciences*, 56(2), 127-150.

Bridgham, S.D., Cadillo-Quiroz, H., Keller, J.K. and Zhuang, Q., 2013. Methane emissions from wetlands: biogeochemical, microbial, and modeling perspectives from local to global scales. *Global Change Biology*, 19(5), 1325-1346.

Broecker, W.S. and Peng, T.H., 1974. Gas exchange rates between air and sea1. *Tellus*, 26(1-2), 21-35.

Buchwitz, M.D., Beek, R.D., Burrows, J.P., Bovensmann, H., Warneke, T., Notholt, J., Meirink, J.F., Goede, A.P.H., Bergamaschi, P., Körner, S. and Heimann, M., 2005. Atmospheric methane and carbon dioxide from SCIAMACHY satellite data: initial comparison with chemistry and transport models. *Atmospheric Chemistry and Physics*, 5(4), 941-962.

Cao, M., Marshall, S. and Gregson, K., 1996. Global carbon exchange and methane emissions from natural wetlands: Application of a process-based model. *Journal of Geophysical Research: Atmospheres*, 101(D9), 14399-14414.

Carn, S.A., Yang, K., Prata, A.J. and Krotkov, N.A., 2015. Extending the long-term record of volcanic SO2 emissions with the Ozone Mapping and Profiler Suite nadir mapper. *Geophysical Research Letters*, 42(3), 925-932.

Chen, Y.H. and Prinn, R.G., 2005. Atmospheric modeling of high-and low-frequency methane observations: Importance of interannually varying transport. *Journal of Geophysical Research: Atmospheres*, 110(D10).

Chen, Y.H. and Prinn, R.G., 2006. Estimation of atmospheric methane emissions between 1996 and 2001 using a three-dimensional global chemical transport model. *Journal of Geophysical Research: Atmospheres*, 111(D10).

Chipperfield, M.P., Cariolle, D., Simon, P., Ramaroson, R. and Lary, D.J., 1993. A three-dimensional modeling study of trace species in the Arctic lower stratosphere during winter 1989–1990. *Journal of Geophysical Research: Atmospheres*, 98(D4), 7199-7218.

Chipperfield, M.P., 2006. New version of the TOMCAT/SLIMCAT off-line chemical transport model: Intercomparison of stratospheric tracer experiments. *Quarterly Journal of the Royal Meteorological Society*, 132(617), 1179-1203.

Christensen, T.R. and Cox, P., 1995. Response of methane emission from Arctic tundra to climatic change: results from a model simulation. *Tellus B*, 47(3), 301-309.

Ciais, P., Sabine, C., Bala, G., Bopp, L., Brovkin, V., Canadell, J., Chhabra, A., DeFries, R., Galloway, J., Heimann, M. and Jones, C., 2014. Carbon and other biogeochemical cycles. In *Climate Change 2013: The Physical Science Basis. Contribution of Working Group I to the Fifth Assessment Report of the Intergovernmental Panel on Climate Change* ( 465-570). Cambridge University Press.

Cicerone, R.J. and Oremland, R.S., 1988. Biogeochemical aspects of atmospheric methane. *Global biogeochemical cycles*, 2(4), 299-327.

Cicerone, R.J. and Shetter, J.D., 1981. Sources of atmospheric methane: measurements in rice paddies and a discussion. *Journal of Geophysical Research: Oceans*, 86(C8), 7203-7209.

Clark, D.B., Mercado, L.M., Sitch, S., Jones, C.D., Gedney, N., Best, M.J., Pryor, M., Rooney, G.G., Essery, R.L.H., Blyth, E. and Boucher, O., 2011. The Joint UK Land Environment Simulator (JULES), model description–Part 2: carbon fluxes and vegetation dynamics. *Geoscientific Model Development*, 4(3), 701-722.

Coleman, K. and Jenkinson, D.S., 1996. RothC-26.3-A Model for the turnover of carbon in soil. In *Evaluation of soil organic matter models* ( 237-246). Springer Berlin Heidelberg.

Coleman, K. and Jenkinson, D.S., 1999. ROTHC-26.3. A Model for the Turnover of Carbon in Soil. Model Description and Windows Users Guide. Harpenden.

Colmer, T.D., 2003. Long-distance transport of gases in plants: a perspective on internal aeration and radial oxygen loss from roots. *Plant, Cell & Environment*, 26(1), 17-36.

Connor, B.J., Boesch, H., Toon, G., Sen, B., Miller, C. and Crisp, D., 2008. Orbiting Carbon Observatory: Inverse method and prospective error analysis. *Journal of Geophysical Research: Atmospheres*, 113(D5).

Conrad, R., Schütz, H. and Babbel, M., 1987. Temperature limitation of hydrogen turnover and methanogenesis in anoxic paddy soil. *FEMS Microbiology Ecology*, 3(5), 281-289.

Conrad, R., 2009. The global methane cycle: recent advances in understanding the microbial processes involved. *Environmental Microbiology Reports*, 1(5), 285-292.

Cox, P.M., Betts, R.A., Bunton, C.B., Essery, R.L.H., Rowntree, P.R. and Smith, J., 1999. The impact of new land surface physics on the GCM simulation of climate and climate sensitivity. *Climate Dynamic*s, 15(3), 183-203.

Cox, P.M., 2001. *Description of the TRIFFID dynamic global vegetation model* ( 1-16). Technical Note 24, Hadley Centre, United Kingdom Meteorological Office, Bracknell, UK.

Cunnold, D.M., Steele, L.P., Fraser, P.J., Simmonds, P.G., Prinn, R.G., Weiss, R.F., Porter, L.W., O'Doherty, S., Langenfelds, R.L., Krummel, P.B. and Wang, H.J., 2002. In situ measurements of atmospheric methane at GAGE/AGAGE sites during 1985–2000 and resulting source inferences. *Journal of Geophysical Research: Atmospheres*, 107(D14).

Curry, C.L., 2007. Modeling the soil consumption of atmospheric methane at the global scale. *Global Biogeochemical Cycles*, 21(4).

Czepiel, P.M., Crill, P.M. and Harriss, R.C., 1995. Environmental factors influencing the variability of methane oxidation in temperate zone soils. *Journal of Geophysical Research: Atmospheres*, 100(D5), 9359-9364.

Dee, D.P., Uppala, S.M., Simmons, A.J., Berrisford, P., Poli, P., Kobayashi, S., Andrae, U., Balmaseda, M.A., Balsamo, G., Bauer, P. and Bechtold, P., 2011. The ERA-Interim reanalysis: Configuration and performance of the data assimilation system. *Quarterly Journal of the Royal Meteorological Society*, 137(656), 553-597.

DeFries, R.S. and Townshend, J.R.G., 1994. NDVI-derived land cover classifications at a global scale. *International Journal of Remote Sensing*, 15(17), 3567-3586.

Denman, K.L., Brasseur, G.P., Chidthaisong, A., Ciais, P., Cox, P.M., Dickinson, R.E., Hauglustaine, D.A., Heinze, C., Holland, E.A., Jacob, D.J. and Lohmann, U., 2007. Couplings between changes in the climate system and biogeochemistry. *Climate change 2007: The physical science basis.*

Dentener, F., Peters, W., Krol, M., van Weele, M., Bergamaschi, P. and Lelieveld, J., 2003. Interannual variability and trend of $CH_4$ lifetime as a measure for OH changes in the 1979–1993 time period. *Journal of Geophysical Research: Atmospheres*, 108(D15).

Dentener, F., Stevenson, D., Cofala, J., Mechler, R., Amann, M., Bergamaschi, P., Raes, F. and Derwent, R., 2005. The impact of air pollutant and methane emission controls on tropospheric ozone and radiative forcing: CTM calculations for the period 1990-2030. *Atmospheric Chemistry and Physics*, 5(7), 1731-1755.

Dhomse, S., Chipperfield, M.P., Feng, W. and Haigh, J.D., 2011. Solar response in tropical stratospheric ozone: a 3-D chemical transport model study using ERA reanalyses. *Atmospheric Chemistry and Physics*, 11(24), 12773-12786.

Dickens, G.R., 2003. A methane trigger for rapid warming?. *Science*, 299(5609), 1017-1017.

Dlugokencky, E.J., Masaire, K.A., Lang, P.M., Tans, P.P., Steele, L.P. and Nisbet, E.G., 1994. A dramatic decrease in the growth rate of atmospheric methane in the northern hemisphere during 1992. *Geophysical Research Letters*, 21(1), 45-48.

Dlugokencky, E.J., Dutton, E.G., Novelli, P.C., Tans, P.P. and Masarie, K.A., 1996. Changes in CH 4 and CO growth rates after the eruption of Mt. Pinatubo and their link with changes in tropical. *Geophysical Research Letters*, 23(20), 2761-2764.

Dlugokencky, E.J., Houweling, S., Bruhwiler, L., Masarie, K.A., Lang, P.M., Miller, J.B. and Tans, P.P., 2003. Atmospheric methane levels off: Temporary pause or a new steady-state?. *Geophysical Research Letters*, 30(19).

Dlugokencky, E.J., Myers, R.C., Lang, P.M., Masarie, K.A., Crotwell, A.M., Thoning, K.W., Hall, B.D., Elkins, J.W. and Steele, L.P., 2005. Conversion of NOAA atmospheric dry air $CH_4$ mole fractions to a gravimetrically prepared standard scale. *Journal of Geophysical Research: Atmospheres*, 110(D18).

Dlugokencky, E.J., Nisbet, E.G., Fisher, R. and Lowry, D., 2011. Global atmospheric methane: budget, changes and dangers. *Philosophical Transactions of the Royal Society of London A: Mathematical, Physical and Engineering Sciences*, 369(1943), 2058-2072.

Dlugokencky, E.J., P.M. Lang, A.M. Crotwell, K.A. Masarie, and M.J. Crotwell (2015), Atmospheric Methane Dry Air Mole Fractions from the NOAA ESRL Carbon Cycle Cooperative Global Air Sampling Network, 1983-2014, Version: 2015-08-03, Path: ftp://aftp.cmdl.noaa.gov/data/trace_gases/ch4/flask/surface/.

Dunfield, P., Dumont, R. and Moore, T.R., 1993. Methane production and consumption in temperate and subarctic peat soils: response to temperature and pH. *Soil Biology and Biochemistry*, 25(3), 321-326.

Dutton, E.G. and Christy, J.R., 1992. Solar radiative forcing at selected locations and evidence for global lower tropospheric cooling following the eruptions of El Chichón and Pinatubo. *Geophysical Research Letters*, 19(23), 2313-2316.

EDGAR, 2001. EUROPA - EDGAR - Archived datasets. [online] Available at: http://edgar.jrc.ec.europa.eu/archived_datasets.php [Accessed 27 Nov. 2015].

EDGAR, 2009. EUROPA - EDGAR - Archived datasets. [online] Available at: http://edgar.jrc.ec.europa.eu/archived_datasets.php [Accessed 27 Nov. 2015].

EPA, 2010. Methane and nitrous oxide emissions from natural sources. [online] Available at: https://www.epa.gov/outreach/pdfs/Methane-and-Nitrous-Oxide-Emissions-From-Natural-Sources.pdf [Accessed 27 Nov. 2015].

EPA, 2012. Global anthropogenic non-$CO_2$ greenhouse gas emissions: 1990-2030 [online] Available at: http://www3.epa.gov/climatechange/Downloads/EPAactivities/EPA_Global_NonCO2_Projections_Dec2012.pdf [Accessed 27 Nov. 2015].

Etheridge, D.M., Steele, L., Francey, R.J. and Langenfelds, R.L., 1998. Atmospheric methane between 1000 AD and present: Evidence of anthropogenic emissions and climatic variability. *Journal of Geophysical Research: Atmospheres*, 103(D13), 15979-15993.

Etiope, G., Lassey, K.R., Klusman, R.W. and Boschi, E., 2008. Reappraisal of the fossil methane budget and related emission from geologic sources. *Geophysical Research Letters*, 35(9).

Fiore, A.M., Horowitz, L.W., Dlugokencky, E.J. and West, J.J., 2006. Impact of meteorology and emissions on methane trends, 1990–2004. *Geophysical Research Letters*, 33(12).

Fischer, G., Nachtergaele, F., Prieler, S., Van Velthuizen, H.T., Verelst, L. and Wiberg, D., 2008. Global agro-ecological zones assessment for agriculture (GAEZ 2008). *IIASA, Laxenburg, Austria and FAO, Rome, Italy*.

Fraser, A., Palmer, P.I., Feng, L., Boesch, H., Cogan, A., Parker, R., Dlugokencky, E.J., Fraser, P.J., Krummel, P.B., Langenfelds, R.L. and O'Doherty, S., 2013. Estimating regional methane surface fluxes: the relative importance of surface and GOSAT mole fraction measurements. *Atmospheric Chemistry and Physics*, 13(11), 5697-5713.

Fung, I., John, J., Lerner, J., Matthews, E., Prather, M., Steele, L.P. and Fraser, P.J., 1991. Three-dimensional model synthesis of the global methane cycle. *Journal of Geophysical Research: Atmospheres*, 96(D7), 13033-13065.

Gauci, V., Matthews, E., Dise, N., Walter, B., Koch, D., Granberg, G. and Vile, M., 2004. Sulfur pollution suppression of the wetland methane source in the 20th and 21st centuries. *Proceedings of the National Academy of Sciences of the United States of America*, 101(34), 12583-12587.

Gedney, N., Cox, P.M. and Huntingford, C., 2004. Climate feedback from wetland methane emissions. *Geophysical Research Letters*, 31(20).

Guilyardi, E., Cai, W., Collins, M., Fedorov, A., Jin, F.F., Kumar, A., Sun, D.Z. and Wittenberg, A., 2012. New strategies for evaluating ENSO processes in climate models. *Bulletin of the American Meteorological Society*, 93(2), 235.

gosat.nies.go.jp. 2015. GOSAT PROJECT. [online] Available at: http://www.gosat.nies.go.jp. [Accessed 27 Nov. 2015].

Hansen, J., Sato, M., Ruedy, R., Lacis, A. and Oinas, V., 2000. Global warming in the twenty-first century: An alternative scenario. *Proceedings of the National Academy of Sciences*, 97(18), 9875-9880.

Hansen, J.E. and Sato, M., 2001. Trends of measured climate forcing agents. *Proceedings of the National Academy of Sciences*, 98(26), 14778-14783.

Hao, W.M. and Ward, D.E., 1993. Methane production from global biomass burning. *Journal of Geophysical Research: Atmospheres*, 98(D11), 20657-20661.

Hartmann, D.L., Klein Tank, A.M.G., Rusicucci, M., Alexander, L.V., Broenniman, B., Charabi, Y., Dentener, F.J., Dlugokencky, E.J., Easterling, D.R., Kaplan, A. and Soden, B.J., 2013. Observations: atmosphere and surface. In: *Climate Change 2013: The Physical Science Basis. Contribution of Working Group I to the Fifth Assessment Report of the Intergovernmental Panel on Climate Change* ( 465-570). Cambridge University Press.

Hayman, G.D., O'Connor, F.M., Dalvi, M., Clark, D.B., Gedney, N., Huntingford, C., Prigent, C., Buchwitz, M., Schneising, O., Burrows, J.P., Wilson, C., Richards, N. and Chipperfield, M., 2014. Comparison of the HadGEM2 climate-chemistry model against in situ and SCIAMACHY atmospheric methane data. *Atmospheric Chemistry and Physics*, 14(23), 13257-13280.

Hodson, E.L., Poulter, B., Zimmermann, N.E., Prigent, C. and Kaplan, J.O., 2011. The El Niño–Southern Oscillation and wetland methane interannual variability. *Geophysical Research Letters*, 38(8).

Hoelzemann, J.J., Schultz, M.G., Brasseur, G.P., Granier, C. and Simon, M., 2004. Global Wildland Fire Emission Model (GWEM): Evaluating the use of global area burnt satellite data. *Journal of Geophysical Research: Atmospheres*, 109(D14).

Holmes, C.D., Prather, M.J., Søvde, O.A. and Myhre, G., 2013. Future methane, hydroxyl, and their uncertainties: key climate and emission parameters for future predictions. *Atmospheric Chemistry and Physics*, 13(1), 285-302.

Holtslag, A.A.M. and Boville, B.A., 1993. Local versus nonlocal boundary-layer diffusion in a global climate model. *Journal of Climate*, 6(10), 1825-1842.

Hossaini, R., Chipperfield, M.P., Montzka, S.A., Rap, A., Dhomse, S. and Feng, W., 2015. Efficiency of short-lived halogens at influencing climate through depletion of stratospheric ozone. *Nature Geoscience*. 8, 186-190.

Huang, Y., Zhang, W., Zheng, X., Han, S. and Yu, Y., 2006. Estimates of methane emissions from Chinese rice paddies by linking a model to GIS database. *Acta Ecologica Sinica*, 26(4), 980-987.

Huijnen, V., Williams, J., Weele, M.V., Noije, T.V., Krol, M., Dentener, F., Segers, A., Houweling, S., Peters, W., Laat, J.D. and Boersma, F., 2010. The global chemistry transport model TM5: description and evaluation of the tropospheric chemistry version 3.0. *Geoscientific Model Development*, 3(2), 445-473.

Insausti, P., Grimoldi, A.A., Chaneton, E.J. and Vasellati, V., 2001. Flooding induces a suite of adaptive plastic responses in the grass Paspalum dilatatum. *New Phytologist*, 152(2), 291-299.

Ito, A. and Inatomi, M., 2012. Use of a process-based model for assessing the methane budgets of global terrestrial ecosystems and evaluation of uncertainty. *Biogeosciences*, 9(2), 759-773.

Ito, A. and Penner, J.E., 2004. Global estimates of biomass burning emissions based on satellite imagery for the year 2000. *Journal of Geophysical Research: Atmospheres*, 109(D14).

Jamali, H., Livesley, S.J., Dawes, T.Z., Cook, G.D., Hutley, L.B. and Arndt, S.K., 2011. Diurnal and seasonal variations in CH 4 flux from termite mounds in tropical savannas of the Northern Territory, Australia. *Agricultural and Forest Meteorology*, 151(11), 1471-1479.

Johnson, K.A. and Johnson, D.E., 1995. Methane emissions from cattle. *Journal of animal science*, 73(8), 2483-2492.

Kai, F.M., Tyler, S.C., Randerson, J.T. and Blake, D.R., 2011. Reduced methane growth rate explained by decreased Northern Hemisphere microbial sources. *Nature*, 476(7359), 194-197.

Kalnay, E., Kanamitsu, M., Kistler, R., Collins, W., Deaven, D., Gandin, L., Iredell, M., Saha, S., White, G., Woollen, J. and Zhu, Y., 1996. The NCEP/NCAR 40-year reanalysis project. *Bulletin of the American meteorological Society*, 77(3), 437-471.

Kirschke, S., Bousquet, P., Ciais, P., Saunois, M., Canadell, J.G., Dlugokencky, E.J., Bergamaschi, P., Bergmann, D., Blake, D.R., Bruhwiler, L. and Cameron-Smith, P., 2013. Three decades of global methane sources and sinks. *Nature Geoscience*, 6(10), 813-823.

Kobayashi, H., Shimota, A., Yoshigahara, C., Yoshida, I., Uehara, Y. and Kondo, K., 1999. Satellite-borne high-resolution FTIR for lower atmosphere sounding and its evaluation. *Geoscience and Remote Sensing, IEEE Transactions o*n, 37(3), 1496-1507.

Koppmann, R., Czapiewski, K.V. and Reid, J.S., 2005. A review of biomass burning emissions, part I: gaseous emissions of carbon monoxide, methane, volatile organic compounds, and nitrogen containing compounds. *Atmospheric Chemistry and Physics Discussions*, 5(5), 10455-10516.

Koven, C.D., Riley, W.J., Subin, Z.M., Tang, J.Y., Torn, M.S., Collins, W.D., Bonan, G.B., Lawrence, D.M. and Swenson, S.C., 2013. The effect of vertically resolved soil biogeochemistry and alternate soil C and N models on C dynamics of CLM4. *Biogeosciences*, 10(11), 7109-7131.

Kvenvolden, K.A. and Rogers, B.W., 2005. Gaia's breath—global methane exhalations. *Marine and Petroleum Geology*, 22(4), 579-590.

Lamarque, J.F., Shindell, D.T., Josse, B., Young, P., Cionni, I., Eyring, V., Bergmann, D., Cameron-Smith, P., Collins, W.J., Doherty, R.M. and Dalsoren, S.B., 2013. The Atmospheric Chemistry and Climate Model Intercomparison Project (ACCMIP): overview and description of models, simulations and climate diagnostics. *Geoscientific Model Development*, 6(1), 179-206.

Le Mer, J. and Roger, P., 2001. Production, oxidation, emission and consumption of methane by soils: a review. *European Journal of Soil Biology*, 37(1), 25-50.

Lee, L.A., Pringle, K.J., Reddington, C.L., Mann, G.W., Stier, P., Spracklen, D.V., Pierce, J.R. and Carslaw, K.S., 2013. The magnitude and causes of uncertainty in global model simulations of cloud condensation nuclei. *Atmospheric Chemistry and Physics*, 13(17), 8879-8914.

Lelieveld, J., Peters, W., Dentener, F.J. and Krol, M.C., 2002. Stability of tropospheric hydroxyl chemistry. *Journal of Geophysical Research: Atmospheres*, 107(D23).

Lelieveld, J., Dentener, F.J., Peters, W. and Krol, M.C., 2004. On the role of hydroxyl radicals in the self-cleansing capacity of the troposphere. *Atmospheric Chemistry and Physics*, 4(9/10), 2337-2344.

Lelieveld, J., 2006. Climate change: a nasty surprise in the greenhouse. *Nature*, 443(7110), 405-406.

Lerman, A., 1979. *Geochemical processes. Water and sediment environments*. John Wiley and Sons, Inc..

Lemoine, J.M., Bruinsma, S., Loyer, S., Biancale, R., Marty, J.C., Perosanz, F. and Balmino, G., 2007. Temporal gravity field models inferred from GRACE data. *Advances in Space Research*, 39(10), 1620-1629.

Levin, I., Veidt, C., Vaughn, B.H., Brailsford, G., Bromley, T., Heinz, R., Lowe, D., Miller, J.B., Poß, C. and White, J.W.C., 2012. No inter-hemispheric $\delta^{13}CH_4$ trend observed. *Nature*, 486(7404), 3-4.

Mann, G.W., Carslaw, K.S., Spracklen, D.V., Ridley, D.A., Manktelow, P.T., Chipperfield, M.P., Pickering, S.J. and Johnson, C.E., 2010. Description and evaluation of GLOMAP-mode: a modal global aerosol microphysics model for the UKCA composition-climate model. *Geoscientific Model Development*, 3(2), 519-551.

Marthews, T.R., Dadson, S.J., Lehner, B., Abele, S. and Gedney, N., 2015. High-resolution global topographic index values for use in large-scale hydrological modelling. *Hydrology and Earth System Sciences*, 19(1), 91-104.

Matthews, E. and Fung, I., 1987. Methane emission from natural wetlands: Global distribution, area, and environmental characteristics of sources. *Global biogeochemical cycles*, 1(1), 61-86.

Masarie, K.A., Langenfelds, R.L., Allison, C.E., Conway, T.J., Dlugokencky, E.J., Francey, R.J., Novelli, P.C., Steele, L.P., Tans, P.P., Vaughn, B. and White, J.W.C., 2001. NOAA/CSIRO Flask Air Intercomparison Experiment: A strategy for directly assessing consistency among atmospheric measurements made by independent laboratories. *Journal of Geophysical Research: Atmospheres*, 106(D17), 20445-20464.

McCulloch, A. and Midgley, P.M., 2001. The history of methyl chloroform emissions: 1951–2000. *Atmospheric Environment*, 35(31), 5311-5319.

McElroy, M.B., 2002. *The atmospheric environment: effects of human activity*. Princeton University Press.

Megonigal, J.P., Mines, M.E. and Visscher, P.T., 2005. Linkages to Trace Gases and Aerobic Processes. *Biogeochemistry*, 8, 350-362.

Melton, J.R., Wania, R., Hodson, E.L., Poulter, B., Ringeval, B., Spahni, R., Bohn, T., Avis, C.A., Beerling, D.J., Chen, G. and Eliseev, A.V., 2013. Present state of global wetland extent and

wetland methane modelling: conclusions from a model intercomparison project (WETCHIMP). *Biogeosciences*, 10, 753-788.

Myhre, G., Shindell, D., Bréon, F.M., Collins, W., Fuglestvedt, J., Huang, J., Koch, D., Lamarque, J.F., Lee, D., Mendoza, B. and Nakajima, T., 2013. Anthropogenic and Natural Radiative Forcing In: *Climate Change 2013: The Physical Science Basis. Contribution of Working Group I to the Fifth Assessment Report of the Intergovernmental Panel on Climate Change* ( 659-740). Cambridge University Press.

Mieville, A., Granier, C., Liousse, C., Guillaume, B., Mouillot, F., Lamarque, J.F., Grégoire, J.M. and Pétron, G., 2010. Emissions of gases and particles from biomass burning during the 20th century using satellite data and an historical reconstruction. *Atmospheric Environment*, 44(11), 1469-1477.

Mikaloff Fletcher, S.E., Tans, P.P., Bruhwiler, L.M., Miller, J.B. and Heimann, M., 2004. $CH_4$ sources estimated from atmospheric observations of $CH_4$ and its 13C/12C isotopic ratios: 2. Inverse modeling of $CH_4$ fluxes from geographical regions. *Global biogeochemical cycles*, 18(4).

Mills, M.J., Schmidt, A., Easter, R., Solomon, S., Kinnison, D.E., Ghan, S.J., Neely, R.R., Marsh, D.R., Conley, A., Bardeen, C.G. and Gettelman, A., 2016. Global volcanic aerosol properties derived from emissions, 1990-2014, using CESM1 (WACCM). *Journal of Geophysical Research: Atmospheres.* (Accepted).

Montzka, S.A., Spivakovsky, C.M., Butler, J.H., Elkins, J.W., Lock, L.T. and Mondeel, D.J., 2000. New observational constraints for atmospheric hydroxyl on global and hemispheric scales. *Science*, 288(5465), 500-503.

Montzka, S.A., Krol, M., Dlugokencky, E., Hall, B., Jöckel, P. and Lelieveld, J., 2011. Small interannual variability of global atmospheric hydroxyl. *Science*, 331(6013), 67-69.

Neef, L., van Weele, M. and van Velthoven, P., 2010. Optimal estimation of the present-day global methane budget. *Global biogeochemical cycles*, 24(4).

Newhall, C.G. and Self, S., 1982. The volcanic explosivity index (VEI) an estimate of explosive magnitude for historical volcanism. *Journal of Geophysical Research: Oceans*, 87(C2), 1231-1238.

Nisbet, E.G., Dlugokencky, E.J. and Bousquet, P., 2014. Methane on the rise—again. *Science*, 343(6170), 493-495.

Nouchi, I., Mariko, S. and Aoki, K., 1990. Mechanism of methane transport from the rhizosphere to the atmosphere through rice plants. *Plant Physiology*, 94(1), 59-66.

O'Connor, F.M., Boucher, O., Gedney, N., Jones, C.D., Folberth, G.A., Coppell, R., Friedlingstein, P., Collins, W.J., Chappellaz, J., Ridley, J. and Johnson, C.E., 2010. Possible role of wetlands, permafrost, and methane hydrates in the methane cycle under future climate change: A review. *Reviews of Geophysics*, 48(4).

OECD, Development Assistance Committee Organisation for Economic Co-operation and Development, 1996. *Guidelines for aid agencies for improved conservation and sustainable use of tropical and sub-tropical wetlands*.

Oleson, K.W., Lawrence, D.M., Gordon, B., Flanner, M.G., Kluzek, E., Peter, J., Levis, S., Swenson, S.C., Thornton, E., Feddema, J. and Heald, C.L., 2010. *Technical description of version 4.0 of the Community Land Model (CLM).* NCAR Tech. Note NCAR/TN-478+ STR, 257.

Olivier, J.G., Van Aardenne, J.A., Dentener, F.J., Pagliari, V., Ganzeveld, L.N. and Peters, J.A., 2005. Recent trends in global greenhouse gas emissions: regional trends 1970–2000 and spatial distribution of key sources in 2000. *Environmental Sciences*, 2(2-3), 81-99.

Oremland, R.S. and Culbertson, C.W., 1992. Importance of methane-oxidizing bacteria in the methane budget as revealed by the use of a specific inhibitor. *Nature*, 356(6368), 421-423.

Parker, R., Boesch, H., Cogan, A., Fraser, A., Feng, L., Palmer, P.I., Messerschmidt, J., Deutscher, N., Griffith, D.W., Notholt, J. and Wennberg, P.O., 2011. Methane observations from the Greenhouse Gases Observing SATellite: Comparison to ground-based TCCON data and model calculations. *Geophysical Research Letters*, 38(15).

Patra, P.K., Takigawa, M., Ishijima, K., Choi, B.C., Cunnold, D., Dlugokencky, E.J., Fraser, P.J., Gomez-Pelaez, A.J., Goo, T.Y., Kim, J.S. and Krummel, P.B., 2009. Growth rate, seasonal, synoptic, diurnal variations and budget of methane in the lower atmosphere. *Journal of the Meteorological Society of Japan*, 87(4).

Patra, P.K., Houweling, S., Krol, M., Bousquet, P., Belikov, D., Bergmann, D., Bian, H., Cameron-Smith, P., Chipperfield, M.P., Corbin, K. and Fortems-Cheiney, A., 2011. TransCom

model simulations of $CH_4$ and related species: linking transport, surface flux and chemical loss with $CH_4$ variability in the troposphere and lower stratosphere. *Atmospheric Chemistry and Physics*, 11(24), 12813-12837.

Pison, I., Ringeval, B., Bousquet, P., Prigent, C. and Papa, F., 2013. Stable atmospheric methane in the 2000s: key-role of emissions from natural wetlands. *Atmospheric Chemistry and Physics*, 13(23), 11609-11623.

Portmann, F.T., Siebert, S. and Döll, P., 2010. MIRCA2000—Global monthly irrigated and rainfed crop areas around the year 2000: A new high-resolution data set for agricultural and hydrological modeling. *Global Biogeochemical Cycles*, 24(1).

Prather, M.J., Holmes, C.D. and Hsu, J., 2012. Reactive greenhouse gas scenarios: Systematic exploration of uncertainties and the role of atmospheric chemistry. *Geophysical Research Letters*, 39(9).

Prigent, C., Papa, F., Aires, F., Jimenez, C., Rossow, W.B. and Matthews, E., 2012. Changes in land surface water dynamics since the 1990s and relation to population pressure. *Geophysical Research Letters*, 39(8).

Prinn, R.G., Weiss, R.F., Fraser, P.J., Simmonds, P.G., Cunnold, D.M., Alyea, F.N., O'Doherty, S., Salameh, P., Miller, B.R., Huang, J. and Wang, R.H.J., 2000. A history of chemically and radiatively important gases in air deduced from ALE/GAGE/AGAGE. *Journal of Geophysical Research: Atmospheres*, 105(D14), 17751-17792.

Prinn, R.G., Huang, J., Weiss, R.F., Cunnold, D.M., Fraser, P.J., Simmonds, P.G., McCulloch, A., Harth, C., Reimann, S., Salameh, P. and O'Doherty, S., 2005. Evidence for variability of atmospheric hydroxyl radicals over the past quarter century. *Geophysical Research Letters*, 32(7).

Reshetnikov, A.I., Paramonova, N.N. and Shashkov, A.A., 2000. An evaluation of historical methane emissions from the Soviet gas industry. *Journal of Geophysical Research: Atmospheres*, 105(D3), 3517-3529.

Rhee, T.S., Kettle, A.J. and Andreae, M.O., 2009. Methane and nitrous oxide emissions from the ocean: A reassessment using basin-wide observations in the Atlantic. *Journal of Geophysical Research: Atmospheres*, 114(D12).

Rigby, M., Prinn, R.G., Fraser, P.J., Simmonds, P.G., Langenfelds, R.L., Huang, J., Cunnold, D.M., Steele, L.P., Krummel, P.B., Weiss, R.F. and O'Doherty, S., 2008. Renewed growth of atmospheric methane. *Geophysical Research Letters*, 35(22).

Rigby, M., Prinn, R.G., O'Doherty, S., Montzka, S.A., McCulloch, A., Harth, C.M., Mühle, J., Salameh, P.K., Weiss, R.F., Young, D. and Simmonds, P.G., 2013. Re-evaluation of the lifetimes of the major CFCs and $CH_3$ $CCl_3$ using atmospheric trends. *Atmospheric Chemistry and Physics*, 13(5), 2691-2702.

Ringeval, B., Friedlingstein, P., Koven, C., Ciais, P., Noblet-Ducoudré, N.D., Decharme, B. and Cadule, P., 2011. Climate-$CH_4$ feedback from wetlands and its interaction with the climate-$CO_2$ feedback. *Biogeosciences*, 8(8), 2137-2157.

Russell, J.M., Gordley, L.L., Park, J.H., Drayson, S.R., Hesketh, W.D., Cicerone, R.J., Tuck, A.F., Frederick, J.E., Harries, J.E. and Crutzen, P.J., 1993. The halogen occultation experiment. *Journal of Geophysical Research: Atmospheres*, 98(D6), 10777-10797.

Saad, K.M., Wunch, D., Toon, G., Bernath, P., Boone, C., Connor, B.J., Deutscher, N., Griffith, D.W., Kivi, R., Notholt, J. and Roehl, C., 2014. Derivation of tropospheric methane from TCCON $CH_4$ and HF total column observations. *Atmospheric Measurement Techniques*, 7(9), 2907-2918.

Saha, S., Moorthi, S., Pan, H.L., Wu, X., Wang, J., Nadiga, S., Tripp, P., Kistler, R., Woollen, J., Behringer, D. and Liu, H., 2010. The NCEP climate forecast system reanalysis. *Bulletin of the American Meteorological Society*, 91(8), 1015-1057.

Sander, S.P., Abbatt, J., Barker, J. R., Burkholder, J. B., Friedl, R. R., Golden, D. M., Huie, R. E., Kolb, C. E., Kurylo, M. J., Moortgat, G. K., Orkin, V. L. and Wine, P. H., 2011. Chemical Kinetics and Photochemical Data for Use in Atmospheric Studies, Evaluation No. 17, *JPL Publication*, 10-6.

Sanderson, M.G., 1996. Biomass of termites and their emissions of methane and carbon dioxide: A global database. *Global Biogeochemical Cycles*, 10, 543-558.

Sapart, C.J., Monteil, G., Prokopiou, M., Van de Wal, R.S.W., Kaplan, J.O., Sperlich, P., Krumhardt, K.M., Van der Veen, C., Houweling, S., Krol, M.C. and Blunier, T., 2012. Natural and anthropogenic variations in methane sources during the past two millennia. *Nature*, 490(7418), 85-88.

Schneising, O., Buchwitz, M., Burrows, J.P., Bovensmann, H., Bergamaschi, P. and Peters, W., 2009. Three years of greenhouse gas column-averaged dry air mole fractions retrieved from satellite–Part 2: Methane. *Atmospheric Chemistry and Physics*, 9(2), 443-465.

Seinfeld, J.H. and Pandis, S.N., 2012. *Atmospheric chemistry and physics: from air pollution to climate change*. John Wiley & Sons.

Sepúlveda, E., Schneider, M., Hase, F., Barthlott, S., Dubravica, D., Garcia, O., Gomez-Pelaez, A., González, Y., Guerra, J.C., Gisi, M. and Kohlhepp, R., 2014. Tropospheric $CH_4$ signals as observed by NDACC FTIR at globally distributed sites and comparison to GAW surface in situ measurements. *Atmospheric Measurement Techniques*, 7, 2337-2360.

Shakhova, N., Semiletov, I., Salyuk, A., Yusupov, V., Kosmach, D. and Gustafsson, Ö., 2010. Extensive methane venting to the atmosphere from sediments of the East Siberian Arctic Shelf. *Science*, 327(5970), 1246-1250.

Shibata, M., Terada, F., Kurihara, M., Nishida, T. and Iwasaki, K., 1993. Estimation of methane production in ruminants. *Animal Science and Technology*, 64, 1221-1227.

Simpson, I.J., Rowland, F.S., Meinardi, S. and Blake, D.R., 2006. Influence of biomass burning during recent fluctuations in the slow growth of global tropospheric methane. *Geophysical Research Letters*, 33(22).

Spahni, R., Wania, R., Neef, L., Weele, M.V., Pison, I., Bousquet, P., Frankenberg, C., Foster, P.N., Joos, F., Prentice, I.C. and Velthoven, P.V., 2011. Constraining global methane emissions and uptake by ecosystems. *Biogeosciences*, 8(6), 1643-1665.

Spivakovsky, C.M., Logan, J.A., Montzka, S.A., Balkanski, Y.J., Foreman-Fowler, M., Jones, D.B.A., Horowitz, L.W., Fusco, A.C., Brenninkmeijer, C.A.M., Prather, M.J. and Wofsy, S.C., 2000. Three-dimensional climatological distribution of tropospheric OH: Update and evaluation. *Journal of Geophysical Research: Atmospheres*, 105(D7), 8931-8980.

Stockwell, D.Z. and Chipperfield, M.P., 1999. A tropospheric chemical-transport model: Development and validation of the model transport schemes. *Quarterly Journal of the Royal Meteorological Society*, 125(557), 1747-1783.

Sugimoto, A., Inoue, T., Tayasu, I., Miller, L., Takeichi, S. and Abe, T., 1998. Methane and hydrogen production in a termite-symbiont system. *Ecological Research*, 13(2), 241-257.

Svensson, B.H., 1984. Different temperature optima for methane formation when enrichments from acid peat are supplemented with acetate or hydrogen. *Applied and Environmental Microbiology*, 48(2), 389-394.

Taylor, K.E., 2001. Summarizing multiple aspects of model performance in a single diagram. *Journal of Geophysical Research: Atmospheres*, 106(D7), 7183-7192.

Tccon.ornl.gov, (2016). TCCON Data Archive. [online] Available at: http://tccon.ornl.gov/ [Accessed 23 Nov. 2015].

Thonicke, K., Spessa, A., Prentice, I.C., Harrison, S.P., Dong, L. and Carmona-Moreno, C., 2010. The influence of vegetation, fire spread and fire behaviour on biomass burning and trace gas emissions: results from a process-based model. *Biogeosciences*, 7(6), 1991-2011.

Tiedtke, M., 1989. A comprehensive mass flux scheme for cumulus parameterization in large-scale models. *Monthly Weather Review*, 117(8), 1779-1800.

Tokida, T., Miyazaki, T., Mizoguchi, M., Nagata, O., Takakai, F., Kagemoto, A. and Hatano, R., 2007. Falling atmospheric pressure as a trigger for methane ebullition from peatland. *Global Biogeochemical Cycles*, 21(2).

Trenberth, K.E., 1997. The definition of el nino. *Bulletin of the American Meteorological Society*, 78(12), 2771-2777.

Trenberth, K.E., 2011. Changes in precipitation with climate change. *Climate Research*, 47(1), 123.

Turnock, S.T., Spracklen, D.V., Carslaw, K.S., Mann, G.W., Woodhouse, M.T., Forster, P.M., Haywood, J., Johnson, C.E., Dalvi, M., Bellouin, N. and Sánchez-Lorenzo, A., 2015. Modelled and observed changes in aerosols and surface solar radiation over Europe between 1960 and 2009. *Atmospheric Chemistry and Physics*, 15(16), 9477-9500.

UNEP, (2015). United Nations Environment Programme – Environmental Data Explorer. [online] Available at: http://geodata.grid.unep.ch/ [Accessed 13 Sep. 2015].

van Der Werf, G.R., Randerson, J.T., Collatz, G.J., Giglio, L., Kasibhatla, P.S., Arellano, A.F., Olsen, S.C. and Kasischke, E.S., 2004. Continental-scale partitioning of fire emissions during the 1997 to 2001 El Nino/La Nina period. *Science*, 303(5654), 73-76.

van der Werf, G.R., Randerson, J.T., Giglio, L., Collatz, G.J., Kasibhatla, P.S. and Arellano Jr, A.F., 2006. Interannual variability in global biomass burning emissions from 1997 to 2004. *Atmospheric Chemistry and Physics*, 6(11), 3423-3441.

van der Werf, G.R., Randerson, J.T., Giglio, L., Collatz, G.J., Mu, M., Kasibhatla, P.S., Morton, D.C., DeFries, R.S., Jin, Y.V. and van Leeuwen, T.T., 2010. Global fire emissions and the contribution of deforestation, savanna, forest, agricultural, and peat fires (1997–2009). *Atmospheric Chemistry and Physics*, 10(23), 11707-11735.

Vardag, S.N., Hammer, S., O'Doherty, S., Spain, T.G., Wastine, B., Jordan, A. and Levin, I., 2014. Comparisons of continuous atmospheric $CH_4$, $CO_2$ and $N_2O$ measurements–results from a travelling instrument campaign at Mace Head. *Atmospheric Chemistry and Physics*, 14(16), 8403-8418.

Velders, G.J.M., 1995. *Scenario Study of the Effects of CFC, HCFC, and HFC Emissions on Stratospheric Ozone*. RIVM Report 722201006, National Institute of Public Health and the Environment.

Voulgarakis, A., Naik, V., Lamarque, J.F., Shindell, D.T., Young, P.J., Prather, M.J., Wild, O., Field, R.D., Bergmann, D., Cameron-Smith, P. and Cionni, I., 2013. Analysis of present day and future OH and methane lifetime in the ACCMIP simulations. *Atmospheric Chemistry and Physics*, 13(5), 2563-2587.

Wallace, J.M. and Hobbs, P.V., 2006. *Atmospheric Chemistry. Atmospheric Science, Second Edition: An Introductory Survey*, edited by: Dmowska, R., Hartmann, D., and Rossby, HT, Elsevier, 153-207.

Wallmann, K., Pinero, E., Burwicz, E., Haeckel, M., Hensen, C., Dale, A. and Ruepke, L., 2012. The global inventory of methane hydrate in marine sediments: A theoretical approach. *Energies*, 5(7), 2449-2498.

Walter, B.P., Heimann, M., Shannon, R.D. and White, J.R., 1996. A process-based model to derive methane emissions from natural wetlands. *Geophysical Research Letters*, 23(25), 3731-3734.

Walter, B.P. and Heimann, M., 2000. A process-based, climate-sensitive model to derive methane emissions from natural wetlands: Application to five wetland sites, sensitivity to model parameters, and climate. *Global Biogeochemical Cycles*, 14(3), 745-765.

Walter, K.M., Smith, L.C. and Chapin, F.S., 2007. Methane bubbling from northern lakes: present and future contributions to the global methane budget. *Philosophical Transactions of the Royal Society of London A: Mathematical, Physical and Engineering Sciences*, 365(1856), 1657-1676.

Wang, K.Y., Pyle, J.A., Sanderson, M.G. and Bridgeman, C., 1999. Implementation of a convective atmospheric boundary layer scheme in a tropospheric chemistry transport model. *Journal of Geophysical Research: Atmospheres*, 104(D19), 23729-23745.

Wania, R., Ross, I. and Prentice, I.C., 2010. Implementation and evaluation of a new methane model within a dynamic global vegetation model: LPJ-WHyMe v1. 3.1. *Geoscientific Model Development*, 3(2), 565-584.

Warwick, N.J., Bekki, S., Law, K.S., Nisbet, E.G. and Pyle, J.A., 2002. The impact of meteorology on the interannual growth rate of atmospheric methane. *Geophysical Research Letters*, 29(20).

Wayne, R.P., 1993. *Chemistry of Atmosphere*. Oxford University Press.

Weedon, G.P., Balsamo, G., Bellouin, N., Gomes, S., Best, M.J. and Viterbo, P., 2014. The WFDEI meteorological forcing data set: WATCH Forcing Data methodology applied to ERA-Interim reanalysis data. *Water Resources Research*, 50(9), 7505-7514.

Wennberg, P.O., Peacock, S., Randerson, J.T. and Bleck, R., 2004. Recent changes in the air-sea gas exchange of methyl chloroform. *Geophysical Research Letters*, 31(16).

Wickland, K.P., Striegl, R.G., Schmidt, S.K. and Mast, M.A., 1999. Methane flux in subalpine wetland and unsaturated soils in the southern Rocky Mountains. *Global Biogeochemical Cycles*, 13(1), 101-113.

Williams, J.E., Strunk, A., Huijnen, V. and Weele, M.V., 2012. The application of the Modified Band Approach for the calculation of on-line photodissociation rate constants in TM5: implications for oxidative capacity. *Geoscientific Model Development*, 5(1), 15-35.

Wilson, C., Chipperfield, M.P., Gloor, M. and Chevallier, F., 2014. Development of a variational flux inversion system (INVICAT v1. 0) using the TOMCAT chemical transport model. *Geoscientific Model Development*, 7(5), 2485-2500.

Wunch, D., Toon, G.C., Wennberg, P.O., Wofsy, S.C., Stephens, B.B., Fischer, M.L., Uchino, O., Abshire, J.B., Bernath, P., Biraud, S.C. and Blavier, J.F., 2010. Calibration of the Total Carbon Column Observing Network using aircraft profile data. *Atmospheric Measurement Techniques*, 3(5), 1351-1362.

Wunch, D., Toon, G.C., Blavier, J.F.L., Washenfelder, R.A., Notholt, J., Connor, B.J., Griffith, D.W., Sherlock, V. and Wennberg, P.O., 2011. The total carbon column observing network. *Philosophical Transactions of the Royal Society of London A: Mathematical, Physical and Engineering Sciences*, 369(1943), 2087-2112.

Yamamoto, S., Alcauskas, J.B. and Crozier, T.E., 1976. Solubility of methane in distilled water and seawater. *Journal of Chemical and Engineering Data*, 21(1), 78-80.

Yan, X., Akiyama, H., Yagi, K. and Akimoto, H., 2009. Global estimations of the inventory and mitigation potential of methane emissions from rice cultivation conducted using the 2006 Intergovernmental Panel on Climate Change Guidelines. *Global Biogeochemical Cycles*, 23(2).

Zhuang, Q., Melillo, J.M., Kicklighter, D.W., Prinn, R.G., McGuire, A.D., Steudler, P.A., Felzer, B.S. and Hu, S., 2004. Methane fluxes between terrestrial ecosystems and the atmosphere at northern high latitudes during the past century: A retrospective analysis with a process-based biogeochemistry model. *Global Biogeochemical Cycles*, 18(3).